Composants et Systèmes Térahertz

Stéphane Blin

MÉMOIRE POUR L'HABILITATION À DIRIGER DES RECHERCHES
DE L'UNIVERSITÉ DE MONTPELLIER

Composants et Systèmes TéraHertz

présenté par : Stéphane Blin

Institut d'Électronique et des Systèmes
Univ Montpellier - UMR CNRS 5214

le 02 Octobre 2017

Devant le jury composé de :

Roland TEISSIER, Directeur de recherche (IES, Montpellier)	Président
Marc BRUNEL, Professeur des universités (IPR, Rennes)	Rapporteur
Béatrice CABON, Professeur des universités (INP, Grenoble)	Rapporteur
Juliette MANGENEY, Directeur de recherche (LPA, Paris)	Rapporteur
Gilles FEUGNET, Ingénieur (TRT, Palaiseau)	Membre du jury
Arnaud GARNACHE, Directeur de recherche (IES, Montpellier)	Membre du jury

UNIVERSITÉ
DE MONTPELLIER

Table des matières

Première partie

Activités et contexte

Chapitre 1

Curriculum Vitae

Nous allons présenter ici succinctement mon CV, avant de détailler les activités de recherche et d'enseignement.

1.1 État Civil

Nom :	Blin
Prénom :	Stéphane
Né le :	06 Janvier 1977 à Saint-Nazaire (44), 40 ans
Nationalité :	Française
Situation familiale :	PACSé, sans enfant
Contact :	Stephane.Blin@umontpellier.fr
	+33 (0)4 67 14 34 73

1.2 Education

2000–2003	**Doctorat en cotutelle**
	Université de Rennes 1 & Université Laval (Qc, Ca)
1999–2000	**DEA en Optronique / Communications Optiques**
	Enssat, Université de Rennes 1
1997–2000	**Ingénieur en Optronique**
	Enssat, Université de Rennes 1
1994–1997	**Classes préparatoires option Physique Chimie**
	Lycée Aristide Briand, Saint-Nazaire
1994	**BAC C**
	Lycée Galilée, Guérande

1.3 Parcours professionnel en enseignement

1.3.1 Déroulement de carrière

2009– **Maître de conférences**, section CNU 63
Codirecteur de la mention *Composants et Systèmes pour télécoms* (M2)
Département EEA, Faculté des Sciences, Université de Montpellier
Enseignement principalement en master, mais aussi en licence, particulièrement pour la mention *Composants et Systèmes pour Télécoms*

2008–2009 **Enseignement supérieur en optique**
IUT Réseaux et Télécoms, Université de Rennes 1
Encadrement de travaux pratiques en optique et télécoms.

2007–2009 **Enseignement supérieur en optique**
Enssat, Université de Rennes 1
Interventions ponctuelles en cours magistral, encadrement de projets pluri-disciplinaires.

2003–2004 **Attaché Temporaire d'Enseignement et de Recherche** (demi-service)
Enssat, Université de Rennes 1
Cours magistral (optique anisotrope), travaux dirigés (optique linéaire, optique anisotrope, optique guidée, propagation guidée, physique des lasers, optique physique), travaux pratiques, encadrement de projets étudiants

2000–2003 **Enseignant vacataire**
Enssat, Université de Rennes 1
Travaux dirigés (optique guidée, physique des lasers, optique physique), travaux pratiques, encadrement de projets étudiants

2001 **Enseignement en milieu industriel**
Alcatel Optronics
Cours magistral et travaux pratiques aux opérateurs du site travaillant sur la caractérisation de filtres égalisateurs de gain pour amplificateurs à fibres optiques

1.3.2 Activités particulières

Responsabilités

Depuis 2015, je suis **codirecteur de la mention *Composants et systèmes pour télécoms*** du département EEA (master 2), et de fait **membre du bureau du département EEA**.

Je suis aussi **responsable des salles de travaux pratique en optique**, de la sécurité au matériel en passant par la logistique et le montage de travaux pratiques.

Je suis enfin **responsable d'un adjoint technique** (N+1), Benjamin Fêtré, affecté à 50% au département. Benjamin est en charge de la gestion des salles de simulation pour le département EEA.

Financements

Je réponds aux appels d'offre pour le financement des salles de travaux pratiques, j'ai notamment obtenu un financement du Labex NUMEV de 39 k€ en 2013 pour la mise en place de travaux pratiques sur la thématique des *Mesures optique et hyperfréquences pour l'environnement*.

Diffusion

J'ai pu participer aux journées portes ouvertes de la Faculté des Sciences en 2017, afin de présenter les travaux pratiques en optique réalisés au département.

1.4 Parcours professionnel en recherche

1.4.1 Déroulement de carrière

2009– **Maître de conférences**, section CNU 63
Responsable adjoint du département *Photonique & Ondes*
Institut d'Électronique et des systèmes, Université de Montpellier
Composants et Systèmes THz

2007–2009 **Ingénieur de recherche**
Laboratoire Foton, Lannion
Lasers à fibre de puissance cohérent à base de fibre photonique

2007–2009 **Consultant**
iXFiber
Réseaux de capteurs acoustiques sous-marins à bases
de lasers à fibre monofréquences

2004–2007 **Post-doctorat**
Ginzton Laboratory, Stanford University (CA, USA)
Étude de capteurs à fibre optique basés sur l'interféromètre de Sagnac :
réseau de capteurs acoustiques, gyroscope à fibre photonique à cœur creux

Été 2004 **Stage de recherche**
DiCOS Technologies (Qc, CA)
Stabilisation du bruit de fréquence du laser de synchronisation
des antennes du radiotélescope ALMA (Chili)

2003–2004 **Attaché Temporaire d'Enseignement et de Recherche**
ENSSAT, Laboratoire Foton, Université de Rennes 1
Injection optique d'un laser à fibre à contre-réaction distribuée

2000–2003 **Doctorat en Génie Électrique & Doctorat en Physique**
COPL, Univ. Laval (Qc, CA) & ENSSAT, Laboratoire Foton, Univ. de Rennes 1
Réalisation de lasers à fibre à contre-réaction répartie
pour l'étude de l'injection optique : comparaison à l'injection
avec des lasers à semi-conducteurs

1.4.2 Activités particulières

Responsabilités

Depuis 2016, je suis **représentant adjoint du Département Photonique & Ondes**, un des trois départements de recherche de l'Institut d'Électronique et des systèmes, siégeant de fait aux conseils de direction et conseils de laboratoire.

Depuis 2016, je suis **membre de la plateforme Europe/Région GEPETO Hermes-Obi-@ de l'IES** à hauteur de 5%, pour la partie *Développement des systèmes THz*.

En terme de responsabilité collective, je suis **membre de la commission bâtiment**, créée suite à l'emménagement dans un bâtiment neuf, et dont l'objectif est d'assurer une bonne installation logistique du personnel (tableaux, restauration, etc.).

Organisation de conférences (5)

J'ai pu participer au comité d'organisation de 5 conférences, à savoir :

1. 3^{rd} European Workshop on VeCSEL (2015)
2. 2^{nd} European Workshop on VeCSEL (2013)
3. International conference on noise and fluctuation ICNF (2013)
4. 1^{st} European Workshop on VeCSEL (2012)
5. Journées Nationales d'Optiques Guidée (2009)

Relecteur pour journaux scientifiques (10)

Je suis aussi régulièrement sollicité pour relecture (*review*) d'articles scientifiques, notamment pour les 10 journaux suivants :

1. Applied Optics,
2. Optics Letters,
3. Optics and Laser Technology,
4. Journal of Optics,
5. Optics Letters,
6. Optics Express,
7. Measurement Science and Technology,
8. Journal of Physics,
9. Journal of Lightwave Technology,
10. Optical Fiber Technology.

Reviewer ANR (3)

J'ai aussi accepté l'évaluation des 3 ANR suivantes :

1. ANR 2015 ASTRID,
2. ANR 2015 Micro et nanotechnologies pour l'Information et la Communication,
3. ANR 2014 Nanosciences et Nanotechnologies pour l'Information et la Communication.

Jury de Thèse

J'ai été examinateur pour le jury de thèse d'Arnaud Peigné (soutenue le 25 Février 2016 à Thalès Research & Technologies (Palaiseau)) sur le sujet *Holographie adaptative pour la réalisation de capteurs à fibres optiques de très grande sensibilité. Application à la détection d'ondes acoustiques sous-marines.*

Diffusion

Plusieurs activités de diffusion sont à relever, notamment la participation aux **journées portes ouvertes du laboratoire en 2015** (démonstration expérimentale de la transmission d'une vidéo haute-définition sans fil sur porteuse THz), la **participation aux journées du pôle de compétitivité** Optitech sur les *Disruptive photonics technologies* le 4 novembre 2015, ou les **journées portes ouvertes du laboratoire en 2010** avec des démonstrations expérimentales autour de l'analogie ondulatoire entre hyperfréquences, acoustique, optique et mécanique.

Chapitre 2

Contrats de recherche (10)

Les contrats de recherche obtenus sont précisés ci-dessous, et classés en fonction des contrats en tant que porteur, coordinateur scientifique, ou participant.

2.1 Porteur de contrats de recherche (3)

1. Labex NUMEV (2015)
   Accueil de chercheur étranger (V. Apostopoulos, Univ. de Southampton, UK) sur la thématique *Étude exploratoire de mesures physiologiques non destructrices en agronomie par spectroscopie THz*, 3 séjours de 5 jours financés par le Labex.
2. Labex NUMEV (2015, 18,5 k€)
   Équipement sur la thématique *Étude exploratoire de mesures physiologiques non destructrices en agronomie par spectroscopie THz* en collaboration avec C. Romieu (INRA, Montpellier).
3. Maturation Initiale AxLR (2015–2016, 72 k€)
   Étude du laser à fibre bi-fréquence pour la génération THz.

2.2 Coordinateur scientifique de contrats de recherche (2)

1. ANR Nadia (2013–2017, 60 k€), Appel à projet Nanotechnologies et Nanosystèmes 2013, porté D. Coquillat (L2C)
2. Région Côtes d'Armor HIPPOCAMP (2007–2009), porté par T. Chartier (Foton).

2.3 Participant à des contrats de recherche (5)

1. ANR ASTRID TAPPAS (2016–2019, 36 k €)
2. Contrat UM-Canon CRF (2012–2015, 325 k€)

3. Contrat UM-St Gobain (2013, 11 k€)
4. ANR WITH (2010–2014, 172 k€)
5. ANR SNS (2011–2015, 97 k€)

2.4 Demandes de financements

Je souhaite préciser, compte tenu de l'aspect chronophage associé, que j'ai participé à de nombreuse demandes de financement, notamment :

- **En tant que porteur (4)**

1. ANR, Appel Jeune-chercheur JCJC 2013 V4T : refusée,
2. Porteur potentiel : ANR, Appel Jeune-chercheur JCJC 2014 THASEL : refusée,
3. Porteur scientifique potentiel : ANR ASTRID 2017 SCOTT (IES, collaboration LPL) : refusée,
4. Porteur scientifique potentiel : ANR, Appel générique 2017 COTUNERA (IES, collaboration C2N, Innoptics) : refusée au 1er tour.

- **En tant que coordinateur scientifique (3)**

1. Coordinateur scientifique potentiel : ANR, Appel générique 2015 STACCATO (Porteur IMEP-LAHC, collaboration IES, NEEL, Innoptics) : refusée au 2nd tour,
2. Coordinateur scientifique potentiel : ANR, Appel générique 2016 STACCATO (Porteur IMEP-LAHC, collaboration IES, NEEL, Innoptics) : refusée au 2nd tour,
3. Coordinateur scientifique potentiel : ANR, Appel générique 2016 NECTERA(Porteur Canon CRF, collaboration IES, IEMN) : acceptée au 1er tour, non soumise au 2nd tour (désengagement industriel).

- Les **participations** à des demandes en tant que participant ne sont pas reportées.

Chapitre 3

Collaborations et stages

3.1 Stages dans des laboratoires étrangers (3)

Deux stages de deux semaines ont été effectués au laboratoire de T. Nagatsuma à l'Univ. d'Osaka (JP), il est à noter que ma doctorante, L. Tohme, a participé au stage de 2013 sur une semaine. J'ai aussi effectué un stage chez DicOS Technologies (Qc, CA).

1. **Université d'Osaka (JP)** sur la période 3–20 avril 2013
   Sujet : Étude de communications sans fil très haut-débit sur porteuse THz
2. **Université d'Osaka (JP)** sur la période 2–16 mars 2012
   Sujet : Étude de communications sans fil très haut-débit sur porteuse THz
3. **DiCOS Technologies (CA)** de deux mois l'été 2004
   Sujet : Stabilisation d'un laser pour synchronisation des antennes ALMA

3.2 Collaborations

Les collaborations seront dans un premier temps présentées par thématiques de recherche, afin de détailler les collaborations productives internationales puis nationales, en ne retenant que la productivité de ces cinq dernières années.

3.2.1 Communications THz

Concernant la thématique des communications THz, j'ai pu développer plusieurs collaborations de recherche, tant académique qu'industrielles, nationales et internationales, notamment :

1. T. Nagatsuma et al., Université d'Osaka (JP) : communications sans fil très haut-débit à base de transistors comme détecteurs THz,
2. J. Hesler, Virginia Diodes Inc.(USA) : systèmes de communications THz hétérodynes,

3. M. Hella, RPI (USA) : transistors CMOS pour détection THz,
4. W. Knap et al., L2C (FR) : transistors pour détection THz,
5. V. Nodjiajim et al., Nokia–Alcatel III-V (FR) : transistors bipolaires pour détection THz,
6. P. Lebars et al., Canon CRF (FR) : communications THz à base de transistors,
7. G. Ducournau et al., IEMN (FR) : composants et systèmes pour communications THz,
8. J.-F. Roux et al., IMEP-LAHC (FR) : méthodes de caractérisation de détecteurs THz,
9. J.-P. Portal et al., LCMI Grenoble (FR) : études des détecteurs *ratchet* pour les communications THz.

3.2.2 Sources THz par photo-mélange

En ce qui concerne la thématique des sources THz par photo-mélange, les collaborations sont les suivantes :

1. M. Jarrahi, UCLA (USA) : antennes plasmoniques pour la génération THz,
2. V. Apostopoulos, Southampton Univ. (UK) : émission THz par photomélange,
3. G. Ducournau, IEMN (FR) : photo-diodes UTC [1] pour émission THz
4. I. Sagnes et al., C2N Marcoussis (FR) : croissance pour sources lasers,
5. J.-F. Roux, IMEP-LAHC (FR) : sources lasers bifréquences,
6. P. Besnard et al., FOTON (FR) : études lasers pour émission bifréquences,
7. V. Lecocq et al., INNOPTICS (FR) : intégration et prototypage de lasers bifréquences.

3.2.3 Autres thématiques

Nous noterons enfin d'autres collaborations sur des thématiques variées et/ou plus exploratoires :

1. P. Boistel et al., St Gobain (FR) : réflectométrie THz,
2. C. Archier et al., T-WAVE (FR) : systèmes THz,
3. J.-P. Guillet, IMS, Univ. de Bordeaux (FR) : caractérisation TDS [2] d'échantillons pour l'agronomie,
4. C. Romieu, INRA Montpellier (FR) : études physiologique par THz en agronomie.

1. UTC : *Uni-Travelling Carrier* pour photodiode à transport unipolaire.
2. TDS : *Time-Domain Spectroscopy* pour spectroscopie dans le domaine temporel.

3.3 Collaborations productives internationales

Les collaborations internationales productives sont les suivantes, nous ne listons ici que les revues internationales à comité de lecture (toutes les publications sont listées au chapitre 9) :

1. **UM – Univ. Osaka (JP)** : 4 revues internationales (et 3 conférences internationales à comité de lecture avec acte)
   (R:7) Tohme L. et al., *IET Electronics Letters* (2014)
   (R:8) Blin S. et al., *IEEE Journal of Communications and Networks* (2013)
   (R:9) Knap W. et al., *IOP Nanotechnology* (2013)
   (R:11) Blin S. et al., *IEEE Electron Device Letter* (2012)
2. **UM – VDI (USA)** : 1 revue internationale
   (R:2) Blin S. et al., *IEEE Electron Device Letter* (2017)
3. **UM – RPI (USA)** : 1 revue internationale (et 2 conférences internationales à comité de lecture avec acte)
   (R:4) Nahar S. et al., *The European Physical Journal Applied Physics* (2016)

3.4 Collaborations productives nationales

Les collaborations nationales productives sont les suivantes, nous ne listons ici que les revues internationales à comité de lecture (toutes les publications sont listées au chapitre 9) :

1. **UM – C2N** : 2 revues internationales (et 6 conférences internationales à comité de lecture avec acte)
   (R:1) Blin S. et al., *Journal of Selected Topics in Quantum Electronics* (2017)
   (R:5) Paquet R. et al., *Optics Letters* (2016)
2. **UM – IEMN** : 3 revues internationales (et 4 conférences internationales à comité de lecture avec acte)
   (R:1) Blin S. et al., *Journal of Selected Topics in Quantum Electronics* (2017)
   (R:6) Ducournau G. et al., *Electronics Letters* (2014)
   (R:7) Tohme L. et al., *Electronics Letters* (2014)
3. **UM – L2C** : 7 revues internationales (et 11 conférences internationales à comité de lecture avec acte)
   (R:3) Coquillat D. et al., *Intern. J. of High Speed Electronics and Systems* (2016)
   (R:4) Nahar S. et al., *Int. J. of High Speed Electronics and Systems* (2016)
   (R:7) Tohme L. et al., *Electronics Letters* (2014)
   (R:8) Blin S. et al., *IEEE Journal of Communications and Networks* (2013)

(R:9) Knap W. et al., *IOP Nanotechnology* (2013)
(R:11) Blin S. et al., *IEEE Electron Device Letter* (2012)
(R:12) Nouvel P. et al., *Journal of Applied Physics* (2012)

Chapitre 4

(Co)Direction d'étudiants de Master 2 ou de Doctorat

4.1 Thèses encadrées (3–11)

Nous détaillons ici les **3** thèses co-encadrées, ainsi que les autres participations.

Thèse soutenue de Lucie Tohme (encadrement à 70%)

• Intitulé : Communication térahertz sans fil à haut débit avec un transistor à haute mobilité électronique comme détecteur
• Directeur : Luca Varani (encadrement 30%)
• Financement ministériel débuté le 1 octobre 2011
• Soutenue le 17 décembre 2014
• **4 publications dans des revues internationales** avec la doctorante, **8 conférences internationales à comité de lecture avec acte**, **3 brevets** et **4 conférences nationales ou workshop**. Nous rappelons ici la liste des revues seulement, voir la liste de publications au chapitre 9 pour les autres types de publications avec la doctorante :

(R:11) Blin S., Teppe F., Tohme L. et al., « Plasma-Wave Detectors for Terahertz Wireless Communication », *IEEE Electron Device Letters* (2012)

(R:8) Blin S., Tohme L. et al., « Wireless communication at 310 GHz using GaAs high-electron-mobility transistors for detection », *IEEE Journal of Communications and Networks* (2013)

(R:7) Tohme L., Blin S. et al., « Terahertz wireless communication using GaAs transistors as detectors », *IET Electronics Letters* (2014)

(R:6) Ducournau G., Pavanello F., Beck A., Tohme L., Blin S. et al., « High-definition television transmission at 600 GHz combining THz photonics hotspot and high-sensitivity heterodyne receiver », *IET Electronics Letters* (2014)

Thèse soutenue de Romain Paquet (encadrement à 70%)

• Intitulé : Nouvelles sources lasers pour génération THz
• Directeur : Luca Varani (encadrement 30%)
• Financement ministériel débuté le 1 octobre 2013
• Soutenue le 9 décembre 2016
• **2 publications dans des revues internationales** avec le doctorant, **4 conférences internationales à comité de lecture avec acte (dont 2 invitées)**, **1 brevet** et **6 conférences nationales ou workshop**. Nous rappelons ici la liste des revues seulement, voir la liste de publications au chapitre 9 pour les autres types de publications avec le doctorant :

(R:5) Paquet R., Blin S. et al., « Coherent continuous-wave dual-frequency high-Q external-cavity semiconductor laser for GHz–THz applications », *OSA Optics Letters* (2016)

(R:1) Blin S., R. Paquet et al., « Coherent and Tunable THz Emission Driven by an Integrated III-V Semiconductor Laser », *IEEE Journal of Selected Topics in Quantum Electronics*, (2017)

Thèse en cours de Isidore Diouf (encadrement à 70%)

• Intitulé : Étude, Conception et Caractérisation d'un système de télécommunications THz
• Directeur : Luca Varani (encadrement 30%)
• Financement ministériel débuté le 1 octobre 2016 (thèse en cours)

Autres participations aux encadrements de thèses

Nous remarquerons particulièrement l'encadrement expérimental de la thèse de **Amine Bassli** sur l'imagerie THz par réflectométrie à modulation de fréquence, Amine étant un étudiant inscrit à l'Université de Fès au Maroc sous la direction de J. Belkadid, mais effectuant ses campagnes expérimentales à l'IES dans le cadre d'échanges Erasmus. Nous remarquerons une première publication récente en conférence :

(CI:6) A. Bassli, A. Pénarier, S. Blin et al., « Reflectometer THz for imaging 3D at 100 GHz», *IEEE International conference on Wireless technologies, embedded and intelligent system (WITS)*, 2017.

Par implication décroissante, nous noterons aussi l'encadrement officieux des thèses des doctorants suivants : **Olivier Vaudel, Julien Poëtte, Minh Nguyen, Baptiste Chomet, Nam Nugyen, Mohammed Sellahi, Vinayak Dangui, Rémi Dardaillon, Attia Benselama** ; nous relèverons les travaux effectués avec ces étudiants dans le document.

4.2 Stagiaire de niveau M2 encadrés (10)

10 stagiaires de niveau M2 (stages de 5 mois) ont été encadrés :

— Anwar Kerchaoui (M2 EEA, 2017),

— Isidore Diouf (Ingénieur Polytech' Marseille, 2016),

— Amine Bassli (M2 EEA, 2015),

— Steeve Tehaamoana (M2 EEA, 2015),

— Gaël Martin (M2 EEA, 2014),

— Soulimane Kerboua (M2 EEA, 2014),

— Romain Paquet (M2 EEA, 2013),

— Lucie Tohme (Univ. Libanaise Fanar, M2 Laser et Applications Médicales et Industrielles, 2011),

— Olivier Vaudel (Ingénieur ENSSAT, 2003),

— Julien Poëtte (Ingénieur ENSSAT, 2002).

Deuxième partie

Analyse et Perspectives de Recherche

Contexte général

Les travaux scientifiques réalisés se structurent autour de deux thématiques principales qui seront synthétisées dans les sections *Lasers et métrologie optique* et *Composants et systèmes THz*.

Le parcours scientifique et son interaction avec les doctorants encadrés est représenté sur le diagramme de Gant, Fig. 4.1. Sur ce diagramme, j'ai représenté et distingué les étudiants officiellement encadrés, ceux pour lesquels un encadrement significatif est à relever, et ceux pour lesquels l'encadrement ou l'interaction n'était que ponctuelle.

Si nous ne comptabilisons **seulement les publications dans des articles de revues internationales avec comité de lecture**, nous relevons des publications avec 10 de ces doctorants :

1. Thibault Laurent : 5 publications (R:10)(R:12)(R:14)(R:15)(R:16)
2. Lucie Tohme : 4 publications (R:6)(R:7)(R:8)(R:11)
3. Romain Paquet : 2 publications (R:1)(R:5)
4. Minh Nguyen : 2 publications (R:13)(R:17)
5. Baptiste Chomet : 2 publications (R:1)(R:5)
6. Nam Nguyen : 2 publications (R:13)(R:17)
7. Mohammed Sellahi : 2 publications (R:1)(R:5)
8. Olivier Vaudel : 1 publication (R:18)
9. Julien Poëtte : 1 publication (R:24)
10. Vinayak Dangui : 1 publication (R:19)

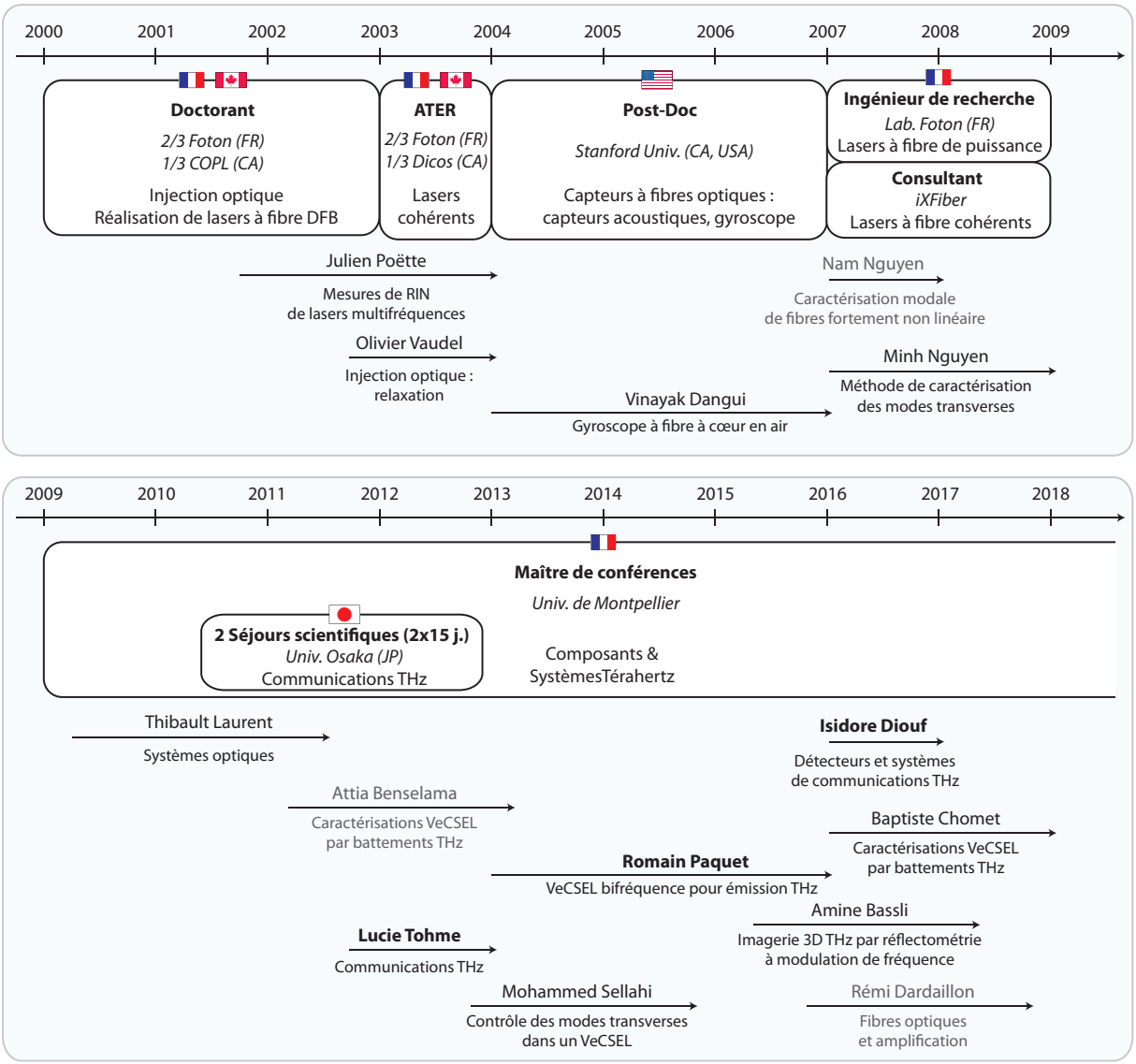

FIGURE 4.1 – Parcours de recherche et (co)encadrements de thèses.
Le nom des étudiants officiellement encadrés sont en caractères gras, ceux que j'ai encadrés de manière significative sont en caractères normaux, ceux pour lesquels l'interaction n'a été que ponctuelle sont en caractères grisés.

Chapitre 5

Lasers et métrologie optique

5.1 Contexte

Tel que nous avons pu l'observer sur le diagramme représenté Fig. 4.1, les travaux effectués autour de cette thématique ont été menés chronologiquement dans les contextes suivants :
• Trois années de **doctorat** (cotutelle), entre le laboratoire **Foton** (ENSSAT, Univ. de Rennes 1, FR) et le **COPL** (Univ. Laval, Qc, CA).
• Une année d'**ATER** [1] au Laboratoire **Foton** dont un stage de recherche chez DiCOS Technologies (Qc, CA).
• Trois années de **post-doctorat** au Ginzton Laboratory (Univ. de **Stanford**, CA, USA).
• Deux années d'**ingénieur de recherche** au laboratoire **Foton**.

Nous relèverons dans ce document une interaction avec les doctorants suivants :
• **Olivier Vaudel** (Foton) pour l'encadrement des cartographies des régimes d'injection, particulièrement le régime relaxé et la dépendance en polarisation,
• **Julien Poëtte** (Foton) pour l'étude du bruit d'intensité dans les lasers multifréquences à fibre,
• **Duc Minh Nguyen** (Foton) pour l'encadrement de l'analyse des modes transverses dans les fibres optiques,
• **Vinayak Dangui** (Stanford) pour l'étude théorique de l'effet Shupe dans le gyroscope à fibre optique photonique à cœur creux,
• **Tanh Nam Nguyen** (Foton) pour la caractérisation d'une fibre non linéaire à petit cœur.
Notons que j'ai aussi encadré Olivier Vaudel et Julien Poëtte lors de leur stage de fin d'étude (ingénieurs ENSSAT).

1. Attaché temporaire d'enseignement et de recherche

5.2 Injection optique

5.2.1 Introduction

En 1665, C. Huygens observait la synchronisation des pendules de deux horloges suspendues sur une même poutre [1] comme le montre la Fig. 5.1. Cette synchroni-

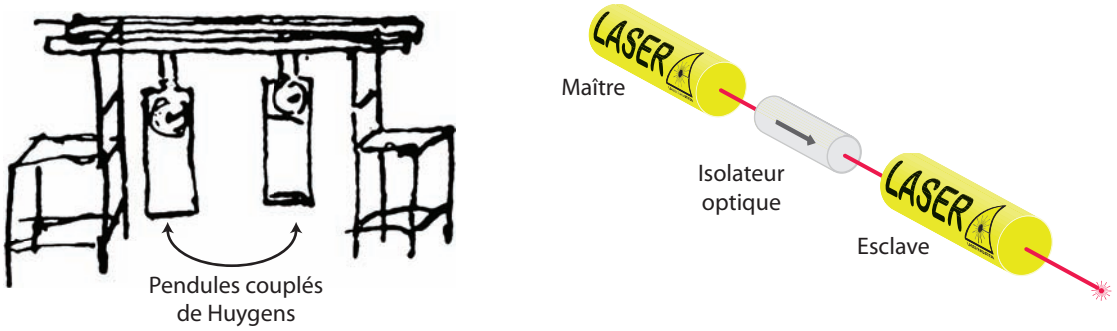

FIGURE 5.1 – Oscillateurs synchronisés.
À gauche : *Croquis de C. Huygens représentant son expérience de synchronisation de deux pendules.* ***À droite :*** *Schéma expérimental d'une expérience d'injection optique.*

sation s'explique par un faible couplage entre ces deux oscillateurs, via les vibrations acoustiques transmises par l'intermédiaire des poutres auxquelles sont accrochés les deux pendules. Depuis, les oscillateurs synchronisés sont devenus la base de nombreux systèmes de communication, de positionnement, de métrologie. Pour plus de contrôle, un oscillateur de référence est couplé de manière *unidirectionnelle* dans un second ou dans de multiples oscillateurs. L'application usuelle consiste à accrocher en fréquence et en phase les oscillateurs secondaires à l'oscillateur de référence. Comme le montre la Fig. 5.1, les expériences d'injection optique présentées dans ce manuscrit consistent à injecter de manière uni-directionnelle un laser dit *maître*, dans un deuxième laser que nous appellerons *esclave*, et à observer le comportement de ce laser esclave perturbé. L'étude de cet oscillateur perturbé est intéressante à de multiples titres selon les caractéristiques de la perturbation (amplitude, fréquence, polarisation), et ce d'autant plus que les oscillateurs ici étudiés sont actifs. Pour un *désaccord* faible entre les fréquences des les lasers maître et esclave(non injecté), et pour une amplitude faible mais suffisante de la perturbation, nous retrouvons généralement la synchronisation observée par Huygens avec des oscillateurs mécaniques. Outre la fréquence, nous verrons que la cohérence spectrale est aussi transférée du laser maître vers le laser esclave. Nous parlons alors d'accrochage optique, ce phénomène étant largement utilisé pour transmettre la cohérence d'un laser maître à un laser esclave moins cohérent mais plus puissant, afin de bénéficier in fine d'un faisceau laser puissant et cohérent.

L'étude de l'atmosphère par LIDAR [2] requiert par exemple des lasers puissants pour une grande portée (plusieurs dizaine de kilomètres), mais aussi cohérents pour permettre de déterminer sa composition par spectroscopie.

Les études originales synthétisées dans ce document ont été observées dans des conditions particulières d'injection optique : nous étudierons les très faibles injections et observerons pour la première fois le transfert progressif de cohérence du maître vers l'esclave, ainsi que les fortes injections et les phénomènes non linéaires et bistables associés. Enfin, ces expériences d'injection optique seront menées avec deux types de lasers esclaves de classe B mais dont les dynamiques (fréquences de relaxation) sont très différentes, l'instrumentation disponible nous permettra ainsi d'observer le comportement d'un laser *rapide* (fréquence de relaxation élevée (> GHz)) dans le domaine spectral, alors que le laser *lent* (fréquence de relaxation lente (< MHz)) sera observé dans le domaine temporel, permettant ainsi une compréhension plus globale des phénomènes physiques observés lors de l'injection de ces oscillateurs optiques.

5.2.2 Oscillateurs optiques utilisés pour les expériences d'injection

Les caractéristiques clefs des lasers utilisés lors des études sur l'injection optique sont présentés dans le tableau 5.1, et seront décrits par la suite.

TABLE 5.1 – Caractéristiques clefs des lasers utilisés pour les expériences d'injection optique. Les DFB à semi-conducteur et à fibre sont utilisés comme lasers esclave, alors que le laser à cavité externe (ECDL) est utilisé comme laser maître.

	DFB semiconducteur	DFB à fibre	ECDL
Taux d'émission spontanée	10 ns	10 ms	-
Produit des réflectivités $R_1\,R_2$	0,1	0,998	-
Longueur	300 μm	3 cm	-
Indice optique	3,5	1,5	1
Temps A/R	3,5 ps	150 ps	-
Temps de cavité	1,5 fs	75 ns	-
Largeur spectrale	3 MHz	10 kHz	125 kHz
Fréquence de relaxation	8 GHz	36 kHz	-

Les deux lasers esclaves sont dits DFB, nous les représentons schématiquement sur la Fig. 5.2. Pour le laser à semi-conducteur, nous observons un guide enterré dont les

2. LIght Detection And Ranging

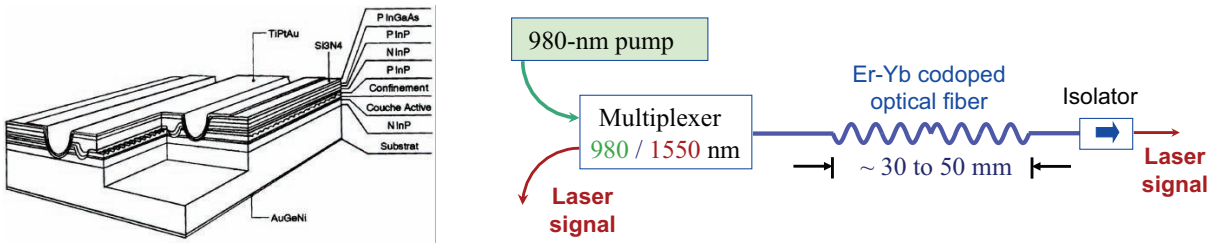

FIGURE 5.2 – Lasers esclaves utilisés.
À gauche *un laser DFB à semi-conducteur (emprunté de [2]).*
À droite *un laser à fibre.*

deux extrémités sont clivées, avec un réseau de Bragg inscrit au dessus de la zone de guidage. Ce laser est pompé électriquement. Pour le laser à fibre, nous observons une fibre copdopée Er-Yb dans laquelle j'ai photo-inscrit un réseau de Bragg avec saut de phase. Le laser est pompé par une diode de pompe fibrée à 980 nm.

Pour les lasers esclaves dits *rapides*, nous utilisons des composants commerciaux gracieusement fournis par Alcatel, à savoir des lasers InGaAs/InP DFBs [3] massifs de type double-hétérojonction à ruban enterré pompés électriquement. La longueur de la cavité optique est de 300 μm. Ces lasers sont monomodes (longitudinal, transverse et polarisation) et émettent continûment autour de 1550 nm, avec typiquement une puissance optique de 5 mW et une largeur spectrale de quelques MHz pour un courant de polarisation de 150 mA. La fréquence de relaxation de ces lasers de classe B est de l'ordre de 8 GHz.

Pour les lasers esclaves dits *lents*, j'ai pu réaliser **au cours de ma thèse** des lasers à fibre continus à 1550 nm pour les expériences d'injection optique grâce à l'équipement disponible au COPL (Université Laval, Qc, Canada). Les lasers fabriqués sont en grande partie des lasers à fibre co-dopée erbium-ytterbium à contre-réaction répartie pompés à 980 nm. Ils ont été fabriqués par photo-inscription d'un réseau de Bragg avec saut de phase le long du milieu actif à l'image des travaux réalisés quelques années plus tôt par d'autres équipes [3]. Les derniers lasers fabriqués répondent parfaitement aux exigences requises pour les expériences d'injection optique : les sources sont monomodes robustes avec un seul mode de polarisation (rapport de suppression de mode > 28 dB), accordables en longueur d'onde par étirement (sur plusieurs nm), et stables en fréquence (gigue inférieure à 3 MHz sur quelques secondes). La fréquence de relaxation de ces lasers de classe B est de l'ordre de la centaine de kHz. Ce travail de recherche a été une amorce au développement de composants actifs pour le laboratoire d'accueil, dont l'expertise se concentrait auparavant sur les composants passifs. De nouvelles

3. *Distributed FeedBack* pour contre-réaction distribuée

configurations lasers ont été explorées par la suite, avec des avancées excitantes telle la fabrication de lasers à fibre multifréquence par photo-inscription de deux réseaux de Bragg à pas variable (*chirpés*) superposés mais longitudinalement décalés, pour lesquels nous avons étudié les propriétés originales en termes de bruit relatif d'intensité avec J. Poëtte (R:24). Nous avons pu montrer que le bruit de chaque mode laser était indépendant, assurant ainsi une grande stabilité de ce laser multifréquence.

Outre la dynamique (lente versus rapide) des lasers étudiés, une différence majeure entre ces deux oscillateurs concerne la finesse de leur cavité optique, soit leur robustesse à l'injection d'un signal extérieur. Les lasers DFBs à semi-conducteurs présentent une très faible finesse, alors que cette finesse est très grande pour le laser à fibre. En effet, la cavité du laser à semi-conducteur n'est constituée que d'une interface semi-conducteur/air. Le réseau de Bragg n'a pas d'impact sur la finesse de la cavité car ce dernier est court, et il est inscrit en dehors du guide d'onde, son rôle n'étant pas de réfléchir mais de favoriser un mode de la cavité, le coefficient de couplage κ est de l'ordre de 1 à 2. Pour le laser à fibre, la cavité dépend uniquement du réseau de Bragg. Afin d'assurer un fonctionnement monomode, la cavité est courte. Le gain linéique étant faible pour une fibre dopée erbium, le réseau de Bragg doit être très réflectif afin d'assurer l'effet laser. Le coefficient de couplage du réseau de Bragg est ainsi de l'ordre de la dizaine, avec une réflectivité de l'ordre de 99,8%, soit une grande finesse de cavité.

Enfin, nous utiliserons une source accordable à cavité étendue (ECDL [4]) commerciale pour l'étude du transfert de cohérence, avec une largeur spectrale typique de 125 kHz.

5.2.3 Caractérisation spectrale des régimes d'injection

L'injection optique a été étudiée expérimentalement et théoriquement sous une approche fondamentale, pour des lasers monofréquences à contre-réaction répartie à semi-conducteurs ou à fibre optique, au cours de ma thèse et de l'encadrement du stage M2 et de la thèse d'O. Vaudel [4]. Compte tenu de la faible finesse de la cavité à semi-conducteur, il est plus facile de l'exciter et ainsi d'observer de manière plus exhaustive les différentes régimes de fonctionnement de l'oscillateur injecté. Compte tenu des grandes fréquences de relaxation du laser à semi-conducteur, l'observation et l'identification des différents régimes d'injection a été effectuée dans le domaine spectral (cf. Fig. 5.3), à l'aide d'analyseurs de spectre Fabry-Perot.

4. *External-Cavity Diode Laser*

(Loading video...)

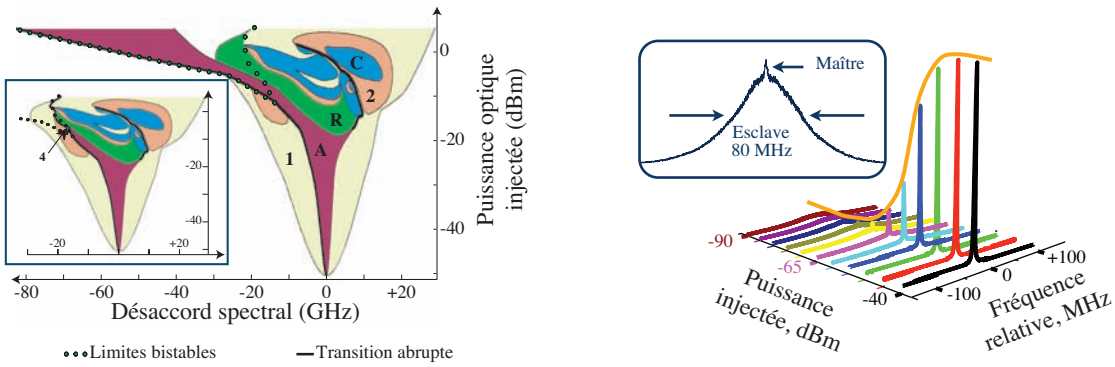

FIGURE 5.3 – États physiques d'un laser à semi-conducteur injecté.
En haut : *régimes d'injection et bistabilité pour un laser à semi-conducteur injecté : vidéo issue de (R:18) pour consultation électronique seulement.*
En bas (gauche) : *forte injection pour un laser polarisé loin du seuil. Les régimes d'accrochage total (A), de relaxation (R), de mélanges d'onde simple (1) et double (2) ou de chaos (C) sont cartographiés expérimentalement pour des désaccords décroissants et croissants (encart), montrant ainsi le comportement bistable du laser.*
En bas (droite) : *très faibles injections d'un laser esclave injecté près du seuil par un laser plus cohérent. Le transfert progressif de cohérence spectrale et la saturation de l'amplification du laser esclave sont clairement mis en évidence. L'encart montre le spectre optique pour une très faible injection.*

J'ai pu définir les paramètres de contrôle de l'injection optique (R:25), et montrer que l'injection optique se comporte différemment selon que le gain du laser esclave est saturé ou non (R:26). Pour un gain saturé, régime couramment étudié dans la littérature, nous avons cartographié les différents régimes d'injection (accrochage, chaos, mélanges d'ondes, relaxation) dans le plan défini par la puissance injectée et le désaccord spectral entre les deux lasers, tel que présenté dans la vidéo associée à la Fig. 5.3 (visible sur support électronique seulement), et/ou sur la cartographie représentée sur cette même figure. Notons que le régime de relaxation a plus particulièrement été étudié dans le cadre de la thèse d'O. Vaudel [4].

L'intérêt de la vidéo est de montrer les transitions abruptes d'un régime à un autre lors d'une variation du désaccord, ces transitions étant typiques des frontières d'une zone de bistabilité. J'ai pu montrer un comportement bistable largement étendu pour la zone d'accrochage, sur plusieurs dizaines de GHz en variant le désaccord spectral, mais aussi, pour des puissances injectées importantes, un fonctionnement du laser esclave en régime d'accrochage sur plusieurs intervalles spectral libre (R:18). Nous avons aussi clairement identifié l'influence du taux de pompage du laser esclave [5] et l'importance de la polarisation du signal maître dans le cadre de la thèse d'O. Vaudel [4]. Ces travaux ont mené à plusieurs perspectives, notamment l'étude de la synchronisation de chaos par injection optique pour la cryptographie optique [4], ou encore l'utilisation de l'injection optique pour assigner à distance les longueurs d'ondes des lasers dans le cadre du multiplexage FTTH (*fiber to the home*) dans le cadre de collaborations industrielles.

Pour de faibles signaux injectés, l'accrochage apparaît progressivement avec la puissance injectée (R:26), tel que présenté Fig. 5.3 (à droite). Pour cette expérience, j'ai injecté un signal cohérent issu de l'ECDL de largeur spectrale de 125 kHz, dans le laser esclave de largeur spectrale de 80 MHz (polarisé proche du seuil). L'esclave, dont le gain n'est pas saturé, agit comme un amplificateur optique de fort gain (cinquantaine de dB), sélectif en longueur d'onde, autour de la résonance de la cavité esclave. Le comportement spectral du laser esclave a principalement été étudié autour du désaccord nul, montrant comment l'esclave acquiert progressivement la cohérence du maître lorsque la puissance injectée augmente. Ce transfert de cohérence apparaît à des puissances injectées d'autant plus faibles que le laser maître est cohérent, offrant une méthode comparative originale pour la mesure de largeur de raie de lasers très cohérents (de largeurs inférieures au kHz) (CI:38). Lorsque les lasers maître et esclave sont légèrement désaccordés, j'ai pu montrer (R:26) une attraction de fréquence du laser esclave par le laser maître pour la première fois, confirmant ainsi le modèle théorique d'Adler [6] ; et d'un point de vue théorique, la fonction d'Airy généralisée au laser [7] a permis de décrire avec précision le comportement du laser injecté en régime non saturé. Finalement, notons que plusieurs applications métrologiques ont été tirées de ces

recherches [5], notamment les mesures du facteur de Henry d'un laser (l'originalité est de l'appliquer aux lasers à fibres), de la largeur de raie du laser maître, mais aussi potentiellement du taux d'émission spontanée du laser esclave.

5.2.4 Caractérisation temporelle des régimes d'injection

La caractérisation temporelle des régimes d'injection a été menée en injectant un laser plus lent, à savoir le laser DFB à fibre optique. J'ai pu présenter ces travaux lors d'une conférence invitée (A:14), travaux issus de mes travaux de thèse et du stage M2 d'O. Vaudel. Compte tenu de la force et de la sélectivité spectrale du miroir distribué, la perturbation de ce laser par injection optique est plus difficile que pour un laser à semi-conducteur dont la cavité froide est nettement moins cohérente. Les cartographies de l'état physique du laser injecté sont donc moins riches que pour l'injection des lasers à semi-conducteurs, tel que représenté Fig. 5.4, nous retrouvons cependant la bistabilité et l'asymétrie de la zone d'accrochage permettant une estimation du facteur de Henry. Nous notons que le facteur de Henry est de signe opposé pour les lasers à fibre, à comparer aux lasers à semi-conducteurs étudiés.

Tel qu'annoncé, l'étude de la réponse temporelle du signal en sortie du laser esclave montre une dynamique intéressante qui n'est que partiellement comprise à ce jour. En effet, l'injection d'un signal maître (ECDL) continu dans le laser à fibre DFB continu montre une réponse dynamique pseudo-amortie périodique tel que montré sur la Fig. 5.4. Nous sommes donc probablement en présence d'un régime stable oscillant autour d'un point de fonctionnement du laser. La période de ce régime de 87 μs n'est pas expliqué à ce jour, nous retrouvons par contre une décroissance exponentielle et des impulsions caractéristiques d'un régime de relaxation du laser à fibre DFB, et une structure rapide de période 0,28 μs correspondant au battement entre les fréquences maître et esclave. La compréhension fine de ces observations expérimentales nécessiterait une modélisation temporelle du milieu amplificateur et de la cavité laser sous injection optique qui n'a pas été conduite à ce jour, les simulations effectuées au cours du doctorat ayant été effectuées dans le domaine spectral. Nous verrons lors de la présentation du projet de recherche que l'étude par simulation numérique de certains phénomènes cyclo-stationnaires est au programme, la compréhension des phénomènes ici observés est ainsi prévue par une approche temporelle type Maxwell-Bloch.

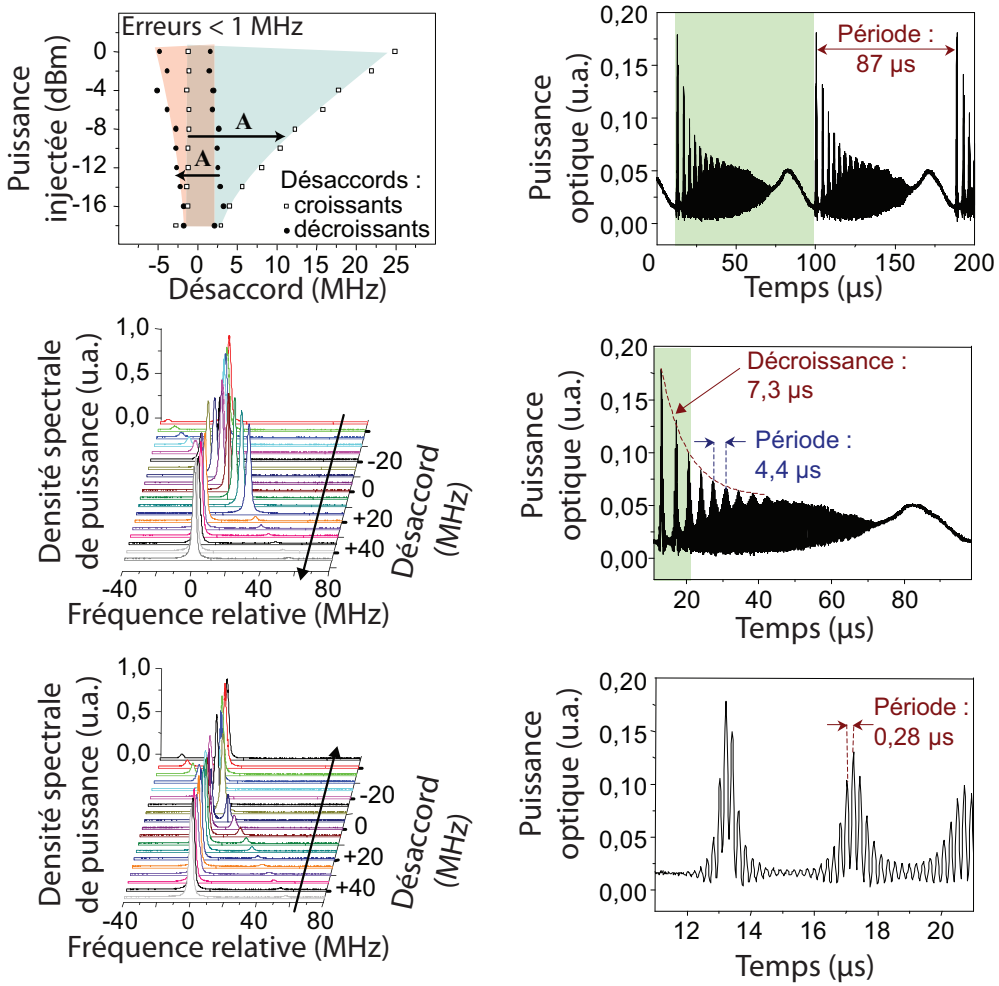

FIGURE 5.4 – Injection d'un laser DFB à fibre.
À gauche : *réponse spectrale d'un laser à fibre injecté : cartographie (en haut), et évolutions des spectres du laser injecté pour des désaccords croissants (milieu) et décroissants (bas).* ***À droite :*** *réponse temporelle du laser injecté observée à différentes échelles temporelles.*

5.3 Lasers ultra-cohérents

Les sources spectralement très étroites sont d'intérêt pour un grand nombre d'applications métrologiques, que ce soit pour des applications spectroscopique, pour le positionnement ou pour des interféromètres à grande échelle comme ici pour la synchronisation des antennes du projet ALMA (Attaccama Large Millimiter Array) au Chili. Une partie des recherches effectuées s'est ainsi portée sur l'étude du bruit de fréquence dans les sources lasers, tant du point de vue expérimental à DiCOS technologies (Qc, CA) — aujourd'hui fusionné avec Teraxion — que théorique (collaboration entre DiCOS et l'ENSSAT). Ces recherches ont été particulièrement menées lors du poste d'ATER, notamment avec l'encadrement expérimental d'un chercheur Vietnamien (T. Tam), et finalisées lors du stage de recherche post-doctoral effectué chez DicOS technologies. Nous nous sommes attachés à comprendre la structure spectrale d'un laser monomode (R:23), communément assimilée à un profil de Voigt, et avons identifié tant expérimentalement que théoriquement les origines physiques amenant à un tel profil spectral. Nous avons ainsi réalisé une source laser continue en bande C, accrochée sur une fréquence absolue, avec une largeur spectrale inférieure à 100 Hz (mesurée sur 1 ms). La stabilité d'un tel système requiert un excellent contrôle des deux boucles d'asservissement du laser, boucles contrôlant à la fois la fréquence absolue du laser (lent) et minimisant le bruit de fréquence du laser (rapide). Au cours de mes travaux, je me suis focalisé sur cette dernière ainsi que sa sensibilité à la température. Le système laser a servi de premier prototype pour la synchronisation des antennes du projet ALMA. Cette performance remarquable a amené à un dépôt de brevet (B-11).

5.4 Capteurs à fibre optique

Dans le cadre de contrats en tant que consultant pour iXFiber, j'ai pu réaliser une étude des lasers à fibre optique pour les réseaux de capteurs acoustiques sous-marins. J'ai ainsi développé un modèle numérique de ces lasers à fibre permettant, en partant des paramètres des fibres actives et des réseaux de Bragg, de déterminer la fréquence d'émission du laser et sa puissance optique. Ces travaux ne seront pas plus détaillés ici pour des raisons de confidentialité.

Les compétences acquises dans les domaines de la physique des lasers et des composants à fibre optique ont naturellement amené à l'étude de capteurs à fibre optique, au sein du laboratoire Edward L. Ginzton (Stanford University). Dans un premier temps, j'ai pu compléter l'étude d'un réseau de capteurs acoustiques à fibre optique basés sur l'effet Sagnac représenté Fig. 5.5, réseau étendu sur plusieurs km. De tels capteurs trouvent un intérêt dans de nombreux domaines, tels que la prospection pétro-

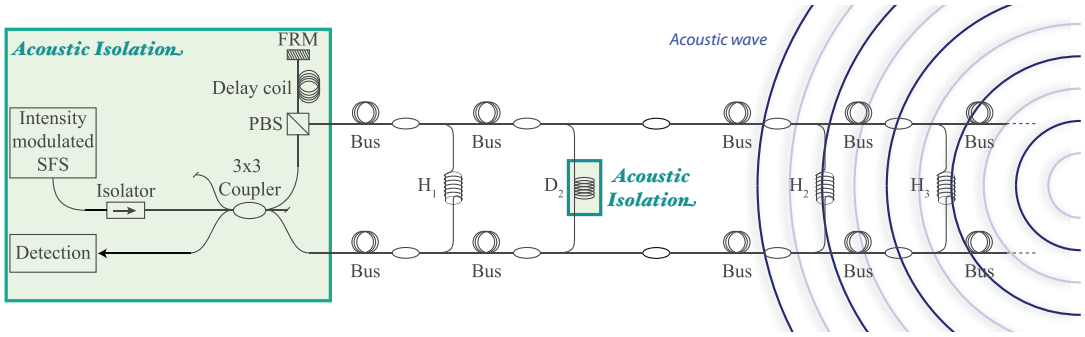

FIGURE 5.5 – Réseau de capteurs acoustiques.
Ce réseau est basé sur un interféromètre de Sagnac à plusieurs bras constitué d'hydrophones H *(fibres enroulées sur mandrins acoustiques) et de références D pour la suppression du bruit capté par le bus. Le cube séparateur de polarisation (PBS) et le miroir de Faraday (FRM) permettent l'insertion d'une ligne à retard sans dépendance en polarisation. La source est super-fluorescente (SFS).*

lière, la surveillance, le contrôle des structures civiles, etc. L'interféromètre de Sagnac présente de nombreux avantages sur les capteurs traditionnels, notamment une insensibilité au bruit de phase des sources, une plus grande dynamique en amplitude des signaux acoustiques détectés, etc. Pour une utilisation à grande échelle, par exemple pour de la prospection pétrolière, le signal acoustique détecté ne vient pas seulement exciter l'interféromètre aux niveau des hydrophones, mais aussi sur l'intégralité de la fibre, donc sur des centaines de mètres. Les signaux provenant des hydrophones sont ainsi noyés dans le bruit. Une technique simple de suppression du bruit a été démontrée expérimentalement, technique combinant le multiplexage temporel des signaux des différents capteurs et un traitement du signal adapté à la fonction non linéaire de transmission de l'interféromètre (R:21).

Le deuxième capteur à fibre étudié est un gyroscope à fibre optique à base de fibres à cœur creux, représentée Fig. 5.6. L'intérêt d'une telle fibre, à comparer aux fibres standard à maintien de polarisation utilisées dans les gyroscopes commerciaux et/ou militaires, est que la lumière se propage principalement dans l'air. De ce fait, nous pouvons limiter la sensibilité du dispositif aux principaux effets qui lui sont néfastes tel que nous l'avons montré avec V. Dangui (R:19), à savoir : l'effet Kerr optique (non-linéarités optiques), l'effet Shupe (sensibilité thermique), l'effet Faraday (sensibilité magnétique). Une caractérisation complète de ce gyroscope a été effectuée. Une stabilité accrue a été démontrée pour l'effet Shupe (R:21). L'étude du bruit du gyroscope a aussi permis d'identifier les limites de détection de ce système (R:20), limites imposées par le bruit de battement généré par la source optique large bande, l'utilisation d'une source cohérente étant proscrite afin de réduire l'impact des bruits interférométriques

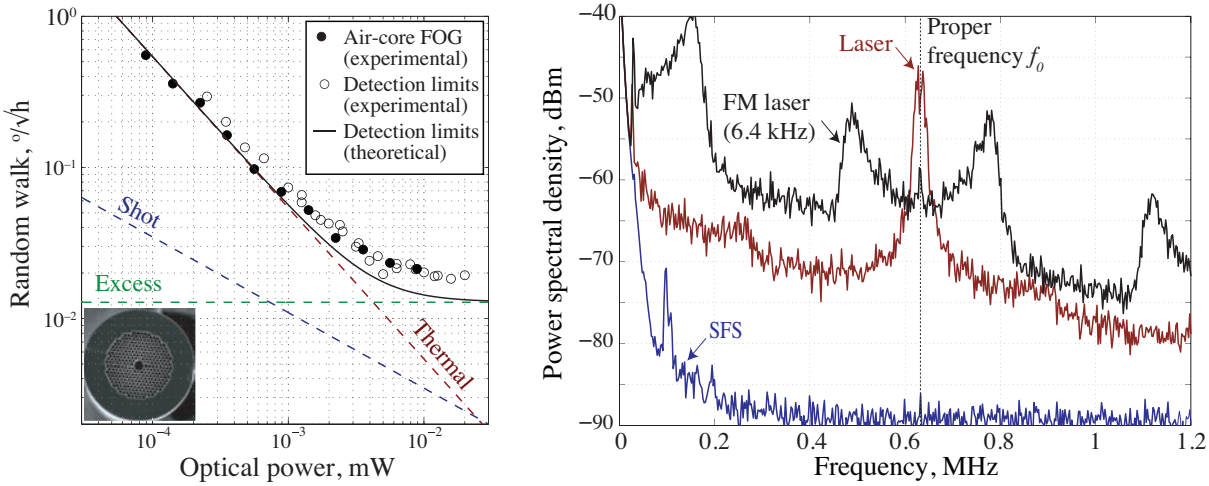

FIGURE 5.6 – Gyroscope à fibre optique à cœur creux à bande-passante photonique.
À gauche : *Marche aléatoire du gyroscope expérimental comparé aux limites fondamentales attendues en photo-détection (bruit thermique du détecteur, bruit de grenaille, bruit d'excès ou bruit de battement spontané-spontané). L'encart montre une coupe de la fibre photonique, le noir représentant l'air.*
À droite : *Spectre du signal détecté en sortie de gyroscope pour différentes sources optiques d'excitation : source super-fluorescente traditionnelle (SFS), source laser, source laser à modulation de fréquence.*

liés aux réflexions parasites ainsi qu'aux effets non linéaires (Kerr). Enfin, l'utilisation d'une source spectralement étroite mais à balayage de fréquence a été proposée pour le gyroscope dans une configuration originale qui permettrait de dépasser les limites fondamentales de détection actuelles de ce capteur, un brevet a été déposé (B-10) et le principe démontré expérimentalement (CI:35).

5.5 Lasers à fibre de puissance

Au cours de mes deux années en tant qu'ingénieur de recherche au laboratoire Foton, j'ai pu travailler sur la réalisation d'un laser à fibre de puissance pour des applications de marquage, dans le cadre d'un projet financé par la région Bretagne et faisant intervenir trois partenaires industriels (Quantel, iXFiber, Perfos). Les lasers de marquage sont typiquement des lasers déclenchés émettant des impulsions de durées allant de 10 à 100 ns, avec une puissance crête de l'ordre de plusieurs dizaines de kW. Le challenge scientifique est la minimisation des effets non linéaires par l'élaboration de fibres optiques innovantes. L'effet le plus délétère étant l'effet Raman, j'ai étudié numériquement quelles types de fibres optiques pourraient permettre une propagation

de ces impulsions sans déformation significative sur plusieurs mètres de fibre optique. De ces études, une fibre à bande-passante photonique a été réalisée par la plateforme Perfos (Lannion). La démonstration de ses capacités à limiter les effets non linéaires a été démontrée expérimentalement et numériquement (CI:34).

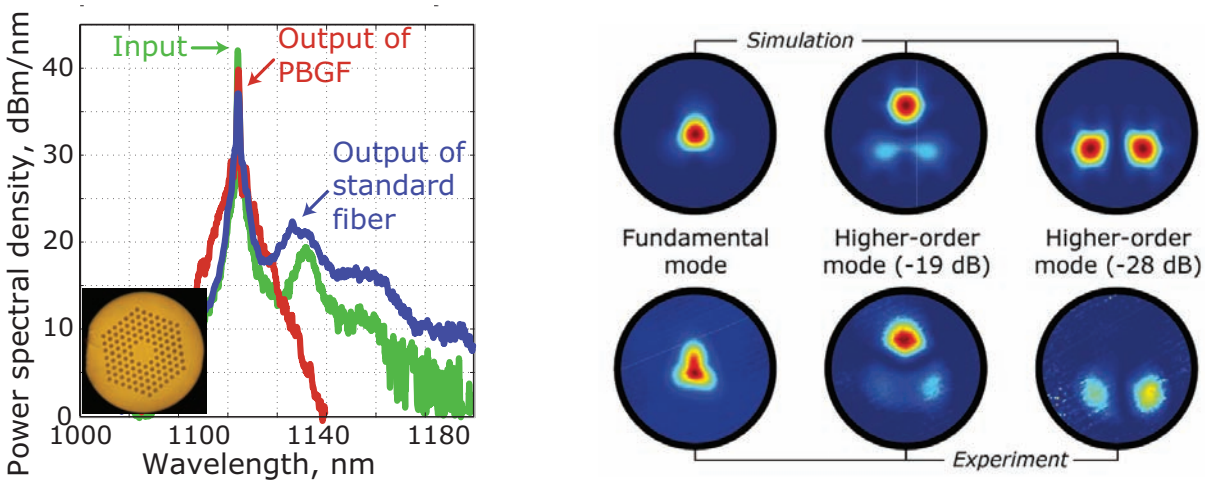

FIGURE 5.7 – Lasers à fibre de puissance à fibre quasi-monomode transverse. ***À gauche :*** *Déformation du spectre optique expérimental au cours de la propagation dans une fibre standard versus une fibre à bande-passante photonique (PBGF). Le spectre laser perd en cohérence longitudinale par amplification Raman stimulée sauf pour la PBGF. L'encart montre une photo de la fibre à bande-passante photonique réalisée par Perfos (Lannion).*
À droite : *Méthode de décomposition des modes transverses appliquée à une fibre à photonique à petit cœur. La figure du haut montre les modes transverses calculés pour la fibre, la figure du bas montre les modes extraits par la méthode de décomposition proposée, ainsi que les puissances optiques correspondantes.*

Afin d'étudier la déformation du spectre optique au cours de la propagation, j'ai développé un modèle original permettant de calculer numériquement et avec une grande efficacité l'évolution du spectre optique en présence d'effet Raman. En écrivant les équations d'évolution de l'intensité pour chaque fréquence du spectre incident, alors qu'habituellement nous ne considérons qu'une seule longueur d'onde dite de *pompe*, j'ai pu montrer qu'un spectre $I_{z+dz}(\nu)$ à une position $z+dz$ pouvait s'exprimer en fonction du spectre à la position z selon la formule :

$$I_{z+dz}(\nu) = I_z(\nu)\left\{1 + \frac{\delta z}{\nu_0}\left[g_{r_0} * P\right](\nu) - \frac{\delta z\,\nu^2}{\nu_0}\left[g_{r_0} \otimes Q\right](\nu) - \delta z\,\alpha(\nu)\right\}, \tag{5.1}$$

où ν_0 est la fréquence centrale de la pompe, g_{r_0} le spectre du coefficient de gain Raman, α le spectre du coefficient linéique de pertes, $*$ la fonction de convolution, $\otimes$ la fonction de corrélation, et P et Q deux fonctions mathématiques définies respectivement

par $P : x \mapsto x\, I(x)$ et $Q : x \mapsto I(x)/x$. Compte tenu de la grande efficacité du calcul numérique pour les opérations de convolution et de corrélation, il est ainsi facile de simuler la propagation d'un spectre optique le long d'une fibre optique. En introduisant un spectre de pertes $\alpha(\nu)$ lié au filtrage par la fibre à bande passante photonique, nous avons pu évaluer par simulation les bénéfices d'un tel filtrage, et ainsi guider le design de la fibre photonique.

Outre le filtrage spectral, l'effet Raman peut être réduit en réduisant l'intensité par élargissement du mode transverse. La fibre optique a donc été désignée de sorte que son mode transverse fondamental soit de grande aire effective (413 μm^2 pour la fibre réalisée). Avec une telle aire effective, la fibre peut cependant supporter plusieurs modes transverses, il a donc été nécessaire de mesurer expérimentalement le contenu modal de la fibre réalisée. J'ai ainsi développé une méthode expérimentale permettant d'imager les modes transverses injectés dans la fibre et de quantifier leur puissance optique. Le principe physique de cette méthode est celui proposé par Nicholson [8], j'ai cependant proposé une mise en œuvre alternative (R:13) permettant une mesure beaucoup plus rapide, plus simple, et non limitée aux fibres à grand cœur. Le principe de la mesure repose en l'analyse de l'état d'interférence local, dans le plan transverse, dû à la superposition des modes transverses. Cet état d'interférence dépend de la différence de chemin optique parcouru par les deux modes dans la fibre, donc de leur différence d'indice effectif. S'il y a plusieurs modes transverses, il est possible de les distinguer en faisant varier la fréquence du signal injecté dans la fibre, l'interférogramme observé sera alors la superposition des interférogrammes de chaque couple de mode, avec une période correspondante à la différence d'indice effectif entre les deux modes, et une amplitude associée au produit des amplitudes des deux modes associés. L'analyse spectrale de ces interférogrammes permet donc de distinguer les couples de modes existants, dans un premier temps par la méthode proposée par Nicholson [8], ou par une méthode plus précise tel que nous avons pu le démontrer au cours de la thèse de D. Minh Nguyen [9]. Nous observons Fig. 5.7 les résultats issus de cette méthode pour une fibre microstructurée à petit cœur développée dans le cadre de la thèse de N. Nguyen [10], montrant les modes propagés dans la fibre en accord avec les modes prédits par simulation, et quantifiant l'amplitude relative de ces modes par rapport au mode le plus fort (le fondamental ici).

5.6 Articulation entre thématiques de recherche

Les recherches menées sur cette thématique intitulée *Lasers et métrologie optique* se sont donc concentrées sur la réalisation et l'étude de **lasers cohérents temporellement**, sur des méthodes originales pour l'étude des **modes transverses** dans les fibres, sur des applications en **métrologie laser** (mesure de cohérence temporelle, mesure du facteur de Henry, perspective de mesure du taux d'émission spontané), et sur des **applications métrologiques** (réseaux de capteurs acoustiques, gyroscope) avec des **alternatives systèmes** permettant d'améliorer la sensibilité des capteurs étudiés. Au cours de ces études, j'ai pu bénéficier et maîtriser une **instrumentation optoélectronique** pointue. Nous verrons par la suite que nous retrouvons les mots-clefs mis en évidence en gras, dans un nouveau contexte thématique focalisé sur les *composants et systèmes THz*.

En terme d'encadrement, j'ai pu encadrer les stages de fin d'études d'O. Vaudel et de J. Poëtte, j'ai particulièrement encadré ce premier lors de sa première année de doctorat, mais aussi M. Nguyen sur l'analyse modale dans les fibres. J'ai enfin aussi participé à l'encadrement de V. Dangui et N. Nguyen.

Chapitre 6

Composants et systèmes THz

6.1 Contexte

Nous reprenons Fig. 6.1 le diagramme de Gant déjà présenté (Fig. 4.1) mais pour les travaux effectués autour de la thématique *Composants et systèmes THz*, menés dans le cadre des mes activités à l'Institut d'Électronique et des Systèmes (Université de Montpellier) en tant que Maître de Conférences depuis 2009.

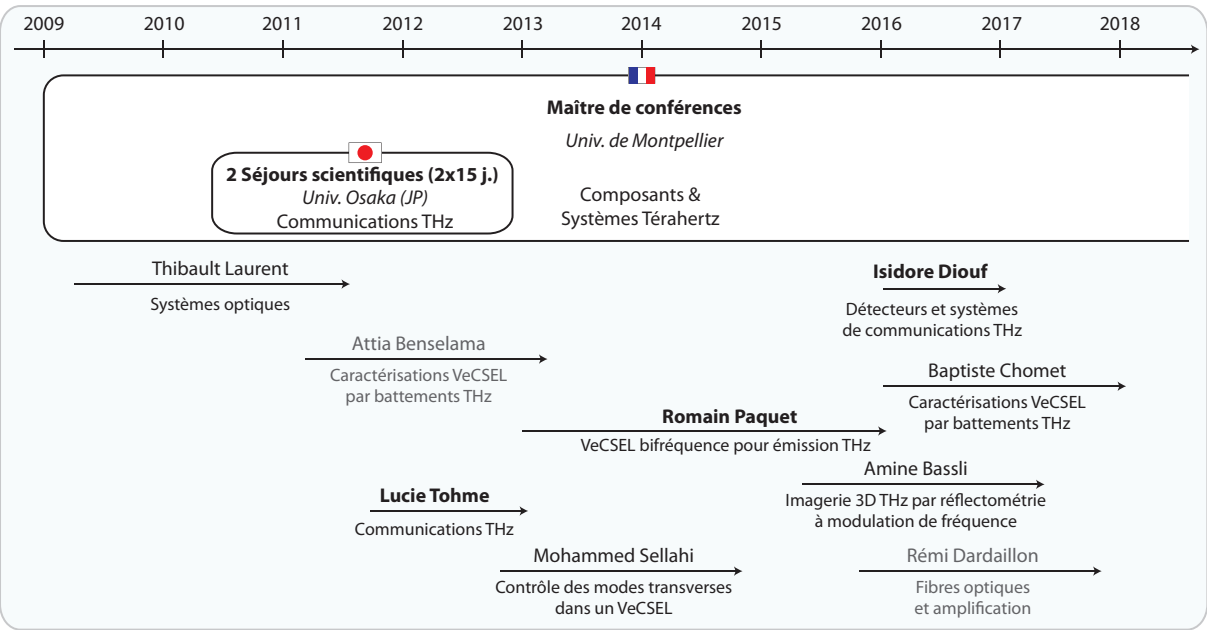

FIGURE 6.1 – Parcours de recherche et (co)encadrements de thèses.
Le nom des étudiants officiellement encadrés sont en caractères gras, ceux que j'ai encadrés de manière significative sont en caractères normaux, ceux pour lesquels l'interaction n'a été que ponctuelle sont en caractères grisés.

Nous relèverons dans ce document une interaction avec les doctorants suivants :
• **Lucie Tohme** (encadrement officiel) pour les premières démonstrations de communications sans fil à haut débit sur porteuse THz utilisant un transistor comme détecteur,
• **Isidore Diouf** (encadrement officiel) dans la continuité de cette thématique,
• **Romain Paquet** (encadrement officiel) pour l'étude des sources lasers bi-fréquences,
• **Amine Bassli** (encadrement très significatif) pour l'étude d'un réflectomètre THz à modulation de fréquence permettant une imagerie 3D à moindre coût,
• **Thibault Laurent** (encadrement significatif) sur les faisceaux THz pour la métrologie optique associée à ses études sur les composants GaN pour l'émission THz,
• **Mohammed Sellahi** (encadrement significatif) pour l'étude de la sélection de deux modes transverses avec des masques d'amplitude intégrés dans le laser VeCSEL, dans la continuité de son doctorat,
• **Baptiste Chomet** (encadrement significatif) pour l'étude de masques de phase pour l'émission bifréquence à grandes fréquences de battement, mais aussi pour des mesures de battements aux fréquences THz associés à des états lasers originaux,
• **Attia Benselama** (encadrement ponctuel) pour les premières mesures de stabilité des deux fréquences du laser bifréquence,
• **Rémi Dardaillon** (encadrement ponctuel) pour mon partage d'expertise expérimentale sur les fibres optiques et autres composants fibrés.
Nous noterons que j'ai encadré L. Tohme, R. Paquet et I. Diouf pour leurs stages de fin d'études.

6.2 Sources THz

6.2.1 État de l'art et positionnement

Les sources THz continues cohérentes, accordables et compactes sont essentielles pour nombre d'applications, que ce soit pour la sécurité (portiques d'aéroports, détection de drogues par spectroscopie), pour le contrôle industriel (imagerie THz), les communications avec multiplexage en fréquence, ou les applications biomédicales. Parmi les solutions existantes, les lasers à cascades quantiques [11] sont attractifs aux fréquences de quelques THz à quelques dizaines de THz, mais le fonctionnement est généralement impulsionnel et requiert un fonctionnement à basse température. À plus basses fréquences (centaines de GHz à quelques THz), l'approche électronique offre plusieurs solutions notamment basées sur les diodes Gunn, IMPATT [1], ou sur les diodes à effet tunnel résonant, mais avec une accordabilité limitée. Les sources à multiplication de fréquences offrent puissance, cohérence, et une accordabilité relativement

1. IMPATT: Impact ionization avalanche transit time

importante (limitée par la bande passante de fonctionnement monomode transverse des guides d'ondes creux), mais restent couteuses et encombrantes.

L'émission par photo-mélange reste ainsi une solution intéressante car elle permet d'offrir une accordabilité inégalable, un fonctionnement à température ambiante, un fort potentiel d'intégration, et repose sur une grande maturité technologique. Le principe consiste à exciter un photo-mélangeur par deux signaux optiques à deux fréquences différentes décalées de la fréquence à générer, fréquence dite de battement. La réponse non linéaire du photo-mélangeur permet de générer un signal à la fréquence de battement. Il existe plusieurs photo-mélangeurs pour l'émission THz : les antennes photo-conductrices telles que les antennes InGaAs inter-digitées fonctionnant à 1550 nm [12], les photodiodes UTC [13], les cristaux non linéaires [14]. En terme de cohérence temporelle, le photo-mélange impose a priori un bruit de fréquence à la fréquence de battement de l'ordre du double de celui aux fréquences optiques, soit une cohérence THz grandement dégradée de par le rapport d'échelle entre la fréquence des porteuses optiques et la fréquence de l'onde THz générée. La solution adoptée consiste alors à réaliser une seule source laser fonctionnement sur deux fréquences simultanément, avec une corrélation forte des contributions du bruit de fréquence, afin que la fréquence de battement soit affranchie des contributions corrélées, permettant ainsi l'émission d'un signal THz cohérent.

De nombreuses solutions ont été proposées dans la littérature pour la réalisation de sources lasers fonctionnant à deux fréquences, mais peu d'entre-elles offrent un fonctionnement stable, cohérent et accordable aux fréquences THz, de par la difficulté à contrôler la compétition de mode entre les deux fréquences de la cavité laser. En effet, afin d'assurer un fonctionnement bifréquences et d'éviter le fonctionnement sur deux paquets de modes, il est nécessaire de réaliser un laser à gain homogène. L'objectif, en terme de stabilité du laser, consiste alors à empêcher la compétition dans le milieu à gain entre les deux modes lasers. Il est ainsi possible de limiter l'interaction entre les modes de manière longitudinale par *spatial hole burning*[2] (SHB), tel que proposé par exemple dans des lasers à semi-conducteurs à émission par la tranche [15], mais avec des performances limitées en terme de stabilité et d'accordabilité. Il est aussi possible d'utiliser un filtrage spectral en cavité externe [16], mais au prix d'un montage complexe donc peu robuste, et ne permettant pas de s'affranchir d'interactions non linéaires dans le milieu à gain qui induisent un fonctionnement sur deux paquets de modes plutôt que sur deux modes. La solution la plus robuste proposée dans la littérature consiste à séparer les modes en polarisation [17] dans la cavité à l'aide d'un cristal biréfringent, permettant le fonctionnement de chaque mode sur un axe optique propre dans le milieu à gain, réduisant ainsi suffisamment la compétition entre les modes

2. Saturation du gain localisée (spatialement ou spectralement)

pour permettre un fonctionnement stable et simultané des deux fréquences. Cette architecture laser offre des performances exceptionnelles mais reste limitée en termes d'intégration de par les multiples éléments optiques intra-cavité mobiles, dégradant de ce fait la cohérence temporelle du battement. Nous allons proposer ici un fonctionnement bi-fréquence stable basé sur la coexistence de deux modes transverses dans un laser à cavité externe à émission par la surface (VeCSEL [3]), avec comme seul élément optique mobile le miroir externe, offrant ainsi plus de compacité, de robustesse, une plus grande cohérence temporelle, en plus des avantages intrinsèques aux solutions VeCSEL.

6.2.2 Laser à cavité externe verticale étendue bi-fréquence

Les VeCSELs sont en effet des solutions attractives [18] car ils peuvent fonctionner dans de nombreuses bandes spectrales, avec un gain large-bande pour des puits quantiques par exemple, ils peuvent aussi fonctionner à forte puissance et rester cohérents (spatialement, spectralement et en terme de polarisation), avec une dynamique de classe A. De ce fait, les VeCSELs ont déjà été étudiés pour un fonctionnement bifréquence, que ce soit basé sur deux modes longitudinaux [19] ou deux modes de polarisation [20], mais la première technique n'offre pas de fonctionnement stable des deux fréquences, la deuxième n'offrant pas de solution intéressante ici car la fréquence de battement est de l'ordre de la dizaine de GHz (pour des applications telles que la transmission optique de porteuses hyperfréquences), et restant limitée en terme de compacité compte tenu du grand nombre d'éléments optiques intra-cavité, tel que discuté précédemment.

Dans la continuité des activités de l'équipe VeCSEL de l'IES, j'ai ainsi pu encadrer la thèse de R. Paquet [21] pour la réalisation d'une source VeCSEL pour l'émission THz, basée sur la coexistence de deux modes transverses dans la cavité. Un tel effet a d'ailleurs été observé par A. Garnache dans une cavité VeCSEL avec une fréquence de battement de l'ordre de 300 GHz sans condition particulière quant à la stabilisation des modes transverses. Dans la continuité de la thèse de M. Sellahi dans laquelle l'étude de masques d'amplitude a été menée afin de sélectionner un mode transverse choisi dans le VeCSEL [22], nous avons exploré la stabilisation de deux modes transverses pour l'émission THz.

La structure proposée est présentée Fig. 6.2. Elle repose sur la stabilisation de deux modes transverses de Laguerre-Gauss (LG) dans la cavité plano-concave constituée du demi-VeCSEL avec un miroir de Bragg de haute réflectivité en face arrière, de multiples puits quantiques pour le milieu à gain, un filtre passe-bande constitué d'un miroir de Bragg peu réflectif pour un plus grand confinement au niveau des puits avec

3. Vertical-external-Cavity Surface-Emitting Lasers

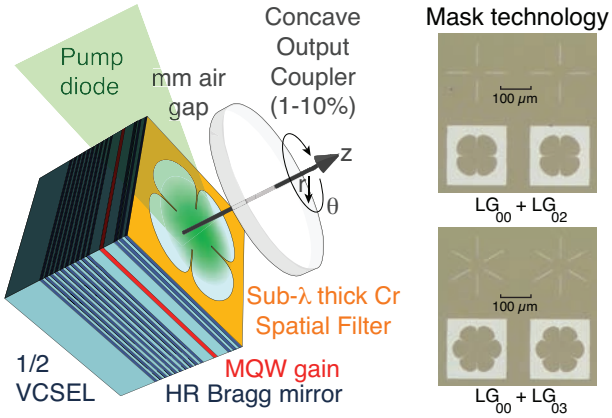

FIGURE 6.2 – Structure du VeCSEL bifréquences et technologie associée.
À gauche : *schéma de principe du VeCSEL bi-fréquence en cavité plano-concave.*
À droite : *photographie des masques métalliques absorbants pour la sélection des modes* LG_{00} *et* LG_{0m} *(*$m = 2$ *et 3 ici).*

de surcroît un filtrage spectral limitant les effets délétères associés aux interactions non linéaires telles que le mélange à quatre ondes, un masque d'amplitude en chrome (figure de droite) afin de sélectionner par les pertes les deux modes transverses choisis, un miroir sphérique externe pour fermer la cavité laser, et une pompe optique.

La figure 6.3 présente les modes de résonance possibles pour une cavité plano-concave, nous allons voir comment il est possible de ne sélectionner que deux modes parmi cet ensemble. Nous observons tout d'abord que le mode fondamental LG_{00} ne présente qu'un faible recouvrement spatial en intensité avec les modes d'ordres supérieurs LG_{mn} avec m & n non nuls. Ainsi, si nous supposons un couple de modes LG_{00} & LG_{mn} (avec m & n non nuls), leur coexistence est possible par *spatial hole burning* transverse, puisque en une position spatiale transverse donnée, le milieu à gain ne verra qu'un seul des deux modes, évitant ainsi toute compétition. La sélection de seulement deux modes parmi les bases de modes possibles s'effectuera à la fois par un filtrage par le gain et par les pertes. Les modes transverses d'ordres supérieurs étant moins confinés, avec un rayon évoluant proportionnellement à $2\,p + m$, il est possible d'éviter leur apparition en limitant le diamètre de la pompe optique, i.e. par une sélection par le gain. Quant aux autres modes transverses, il est possible de les sélectionner par les pertes grâces aux masques de pertes en chrome déposés sur la structure. La forme des masques est choisie de sorte que le mode fondamental ne soit pas affecté par les pertes (le masque est évidé en son centre), et de sorte qu'un seul mode transverse d'ordre supérieur ne soit pas affecté par les pertes, que ce soit avec des motifs en croix ou en négatif tel que présenté Fig. 6.2. Les masques en Cr sont d'une épaisseur inférieure à la longueur d'onde afin d'éviter toute perte par diffraction au cours de la propagation longitudinale, et sont placés sur un ventre du champ électromagné-

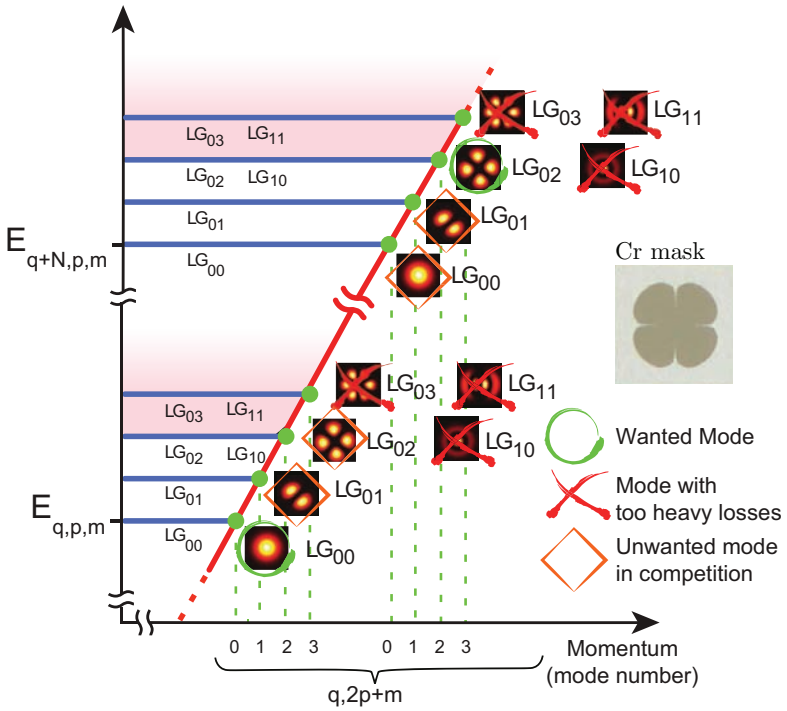

FIGURE 6.3 – Diagramme de dispersion des modes LG_{pm} de la cavité plano-concave pour les résonances longitudinales d'ordre q, avec sélection du couple de modes transverses LG_{00} & LG_{02} par un masque d'amplitude.

tique intra-cavité afin d'assurer un filtrage optimal. Quant à la sélection des modes longitudinaux et transverses, nous nous reposons sur la sélection inhérente au VeCSEL [23], qui offre une émission cohérente sur un seul mode longitudinal [23,24] avec une unique polarisation linéaire [18,23,25].

Au cours de la thèse de R. Paquet, nous avons pu réaliser un laser bi-fréquence pompé à 808 nm et émettant autour de 1 μm, dont le design et les performances optiques ont été publiées en référence (R:5). Nous pouvons observer Fig. 6.4 un seuil laser de l'ordre de 1,1 kW/cm^2 pour le mode fondamental, et de 1,4 kW/cm^2 pour le mode d'ordre supérieur, ces modes ayant été identifiés par l'observation du faisceau transverse en champ lointain (voir Fig. 6.5). Les deux modes apparaissant à des seuils proches et présentant des efficacités similaires, nous assurons ainsi un équilibre de puissance entre les modes, équilibre indispensable à la génération d'un battement THz de contraste maximum. L'équilibre en puissance de ces modes a été ajusté par design du masque de pertes comme a pu le montre R. Paquet au cours de sa thèse [21]. D'un point de vue spectral, nous observons un fonctionnement bi-fréquence stable à l'analyseur de spectre optique, avec une accordabilité de la différence de fréquence avec le taux de pompage, et un fonctionnement monomode pour chacun des deux modes, avec un taux de suppression modal (SMSR [4]) de 55 dB (limite quantique selon [18]).

4. Side-Mode Suppression Ratio.

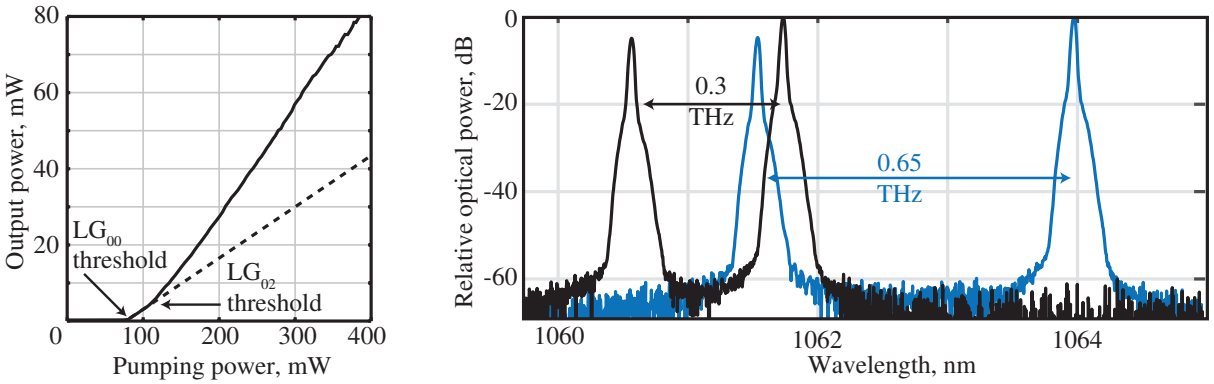

FIGURE 6.4 – Puissance et spectre du VeCSEL bi-fréquences.
À gauche : *puissance de sortie, montrant en pointillés la continuité de la puissance pour le mode LG_{00}.* ***À droite :*** *spectres optiques pour le couple de modes LG_{00} & LG_{02} at des taux de pompages de 2 (noir) et de 2.8 (bleu).*

La figure 6.5 représente la distribution d'intensité en champs lointain, avec une faible divergence ($1,3^{\circ}$ de demi-largeur à mi-hauteur) pour les modes de Laguerre-Gauss, en l'occurrence les modes LG_{00} & LG_{02}, proche donc de la limite de diffraction sans dégradation notable de la cohérence spatiale transverse, qui aurait pu être dégradée par la présence du masque de pertes. Le facteur M^2 mesuré est de 1,06 pour le mode fondamental ($1,06 \times (m+1)$ pour le mode d'ordre m).

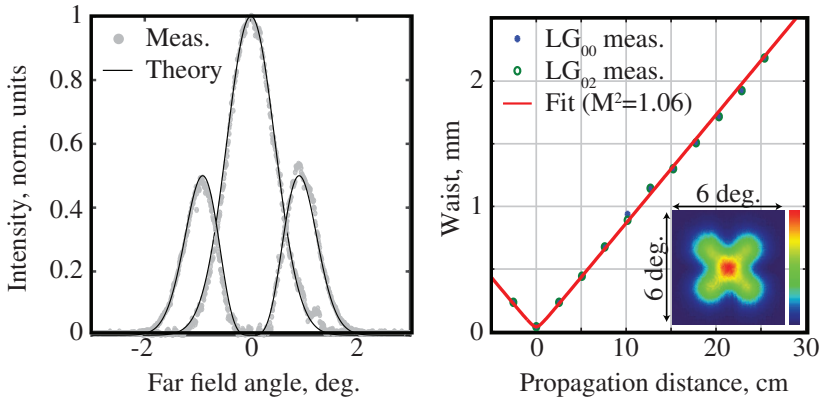

FIGURE 6.5 – Caractérisation du faisceau du laser bi-fréquence.
À gauche : *coupe transverse de l'intensité pour chacun des modes (théorie et expérience).* ***À droite :*** *mesure du facteur M^2 pour les deux modes, avec en encart le profil d'intensité bi-mode en champ lointain.*

En terme de polarisation, nous avons pu vérifier que les deux modes transverses étaient polarisés linéairement avec la même orientation, avec un taux d'extinction en polarisation de plus de 45 dB, taux déterminé à partir de la mesure de la puissance de battement RF (autour de 115 MHz) à l'analyseur de spectre électrique.

Si le spectre optique présenté Fig. 6.4 semble bi-fréquence, le temps de balayage de l'analyseur (typiquement plusieurs centaines de ms) pourrait être trop long pour permettre l'observation de bascules dynamiques d'un mode à l'autre — la dynamique temporelle du VeCSEL étant de l'ordre de la ns —- auquel cas le spectre observé ne serait que le spectre moyen. Afin de vérifier la simultanéité des deux modes, plusieurs expériences ont été menées avec plusieurs doctorants. Dans le cadre de la thèse d'A. Benselama, nous avons mesuré le spectre optique d'un VeCSEL bi-fréquence sans masque de pertes avec un analyseur de spectre rapide (Zoom Spectra) permettant l'acquisition des spectres optiques à un taux de 30 kHz, le principe de mesure n'étant pas basé sur l'observation du spectre par balayage d'un réseau de diffraction, mais sur l'observation de l'interférogramme d'un guide d'onde fermé à l'aide d'une ligne de capteurs CCD. Nous avons ainsi vérifié à ce taux plus rapide la stabilité du fonctionnement bi-fréquence comme le montre la Fig. 6.6. Plus récemment, dans le cadre de la thèse de R. Paquet et de B. Chomet, grâce à l'acquisition d'une *streak camera* (Hamamatsu C10910-02), nous avons pu mesurer le spectre bi-fréquence d'une structure avec masque avec une résolution temporelle de 5 ns tel que présenté Fig. 6.6, résolution suffisamment proche du temps de réponse du laser pour pouvoir s'assurer de la simultanéité du fonctionnement bi-fréquence. Enfin, toujours dans le cadre de la thèse de R. Paquet et avec l'aide précieuse de M. Myara, nous avons mesuré le bruit d'amplitude simultané de chaque mode transverse du laser, en séparant au préalable les modes transverses, opérant à différentes fréquences, à l'aide d'un monochromateur haute résolution (JY HR1000). Tel que le montre la Fig. 6.6, le bruit d'amplitude est proche de celui attendu pour un laser VeCSEL monofréquence [18], avec un écart type de 0,3% pour les variations de puissances intégrées sur toute la plage fréquentielle, assurant ainsi la stabilité du fonctionnement bi-fréquence.

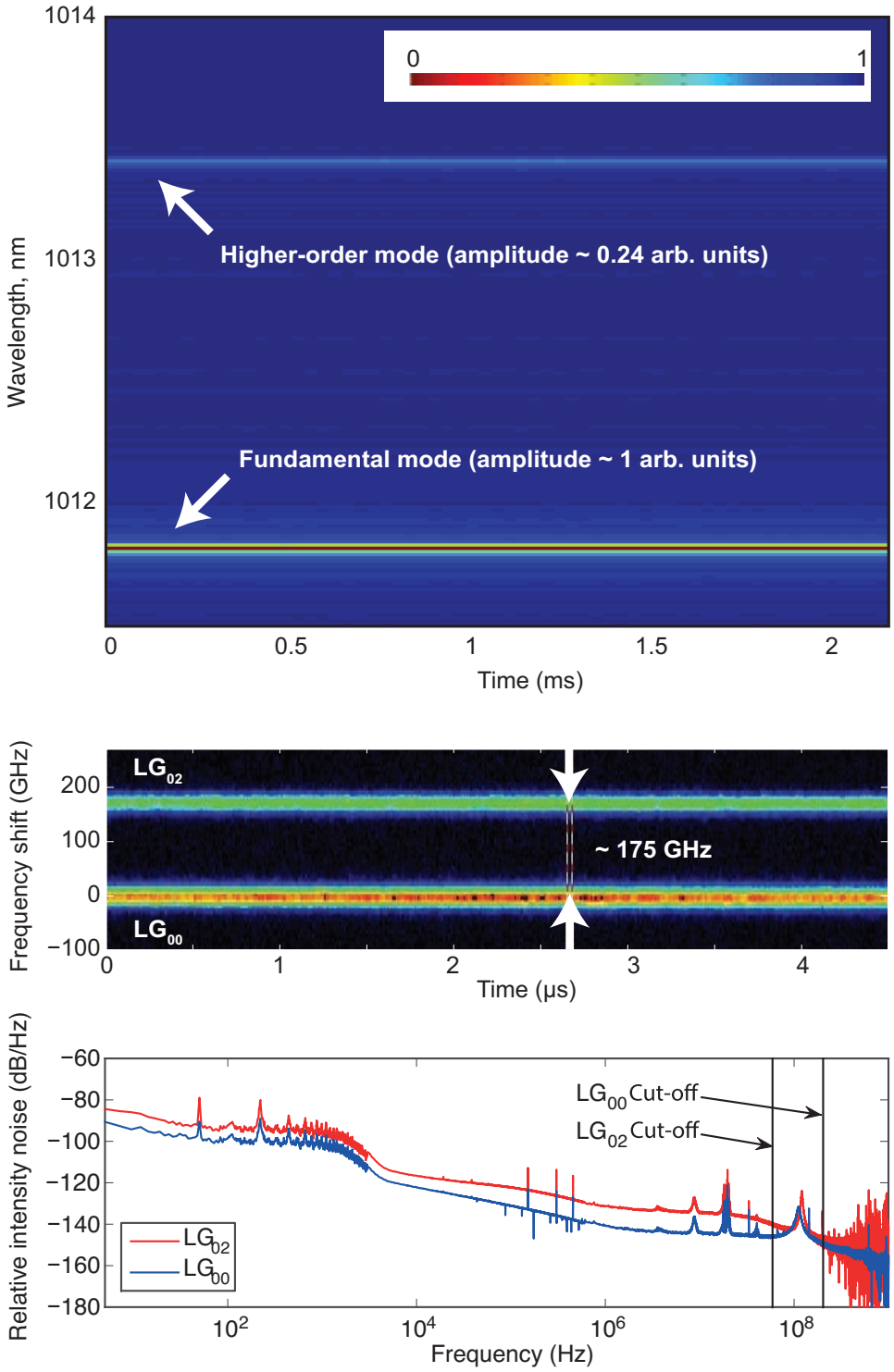

FIGURE 6.6 – Preuves de la simultanéité du laser bifréquence.
En haut : *évolution du spectre optique pour une structure sans masque, observée avec un Zoom Spectra avec une fréquence d'acquisition de 30 kHz.*
Au milieu : *évolution du spectre optique pour une structure avec masque, observée avec une streak caméra avec un spectre mesuré toutes les 5 ns.*
En bas : *bruit d'amplitude relatif de chaque mode transverse.*

Notons enfin que dans la continuité de la thèse de M. Sellahi, R. Paquet a aussi étudié la dynamique laser au démarrage, à l'aide des équations de Maxwell Bloch avec une description transverse des modes et des pertes, tel que publié avec ces deux doctorants en (R:2). Comme le montre la Fig. 6.7, nous observons le démarrage d'un grand nombre de modes, mais seulement les modes souhaités atteignent un état laser stationnaire, avec un fort taux d'extinction. L'intérêt de ces simulations est de guider le design des masques, tel que présenté dans la thèse de R. Paquet [21], notamment pour l'équilibrage des puissances des deux modes lasers.

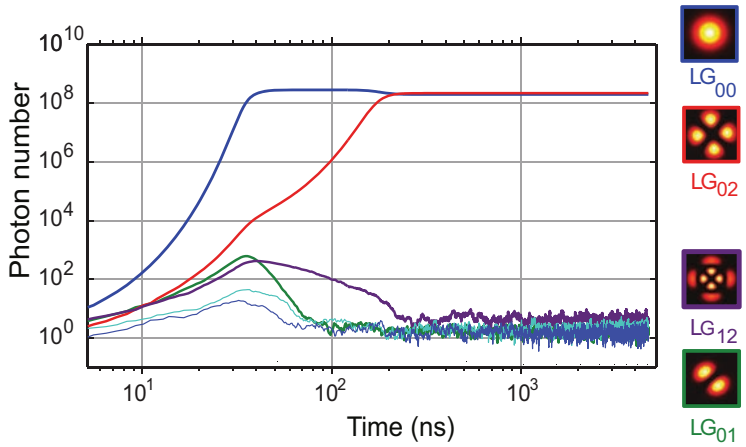

FIGURE 6.7 – Simulation du démarrage laser avec les équations de Maxwell-Bloch avec description transverse des champs électriques.

6.2.3 Émission THz continue accordable et cohérente

Le fonctionnement optique bi-fréquence du VeCSEL ayant été démontré, nous nous sommes attelés à l'émission THz et à la caractérisation du signal avec des méthodes métrologiques avancées que nous détaillerons ci-après. L'émission THz a été obtenue par l'excitation d'une photodiode UTC, la première démonstration ayant été effectuée avec R. Paquet lors d'une campagne expérimentale menée à l'IEMN avec Guillaume Ducournau, valorisée lors d'une conférence (CI:9). Les études exhaustives ont par la suite été effectuées avec une photodiode UTC commerciale fibrée à l'IES.

Couplage spatial et puissance de battement

Si le principe d'un laser bi-fréquence stable consiste en un découplage spatial des deux modes, l'objectif pour l'émission THz est cette fois de superposer ces modes afin de maximiser la puissance de battement THz. Si les modes transverses sont orthogonaux en champs sur l'intégralité du plan transverse, ce n'est pas le cas pour une aire restreinte de l'espace transverse. Il est ainsi possible, par exemple, de ne sélectionner

qu'un quadrant du faisceau bimode transverse LG_{00} & LG_{02} afin d'assurer une puissance de battement non nulle. Puisque nous allons utiliser un photo-mélangeur fibré pour l'émission THz, nous nous sommes intéressés au couplage du faisceau laser dans une fibre monomode transverse à maintien de polarisation. La Fig. 6.8 montre qu'il est possible d'atteindre une efficacité de battement de 21% (soit un lobe sur quatre environ) pour le couple de modes (LG_{00},LG_{02}) et de 11,6% (soit un lobe sur six environ) pour le couple (LG_{00},LG_{03}), une efficacité de 100% correspondant à une puissance de battement maximale pour deux modes colinéaires.

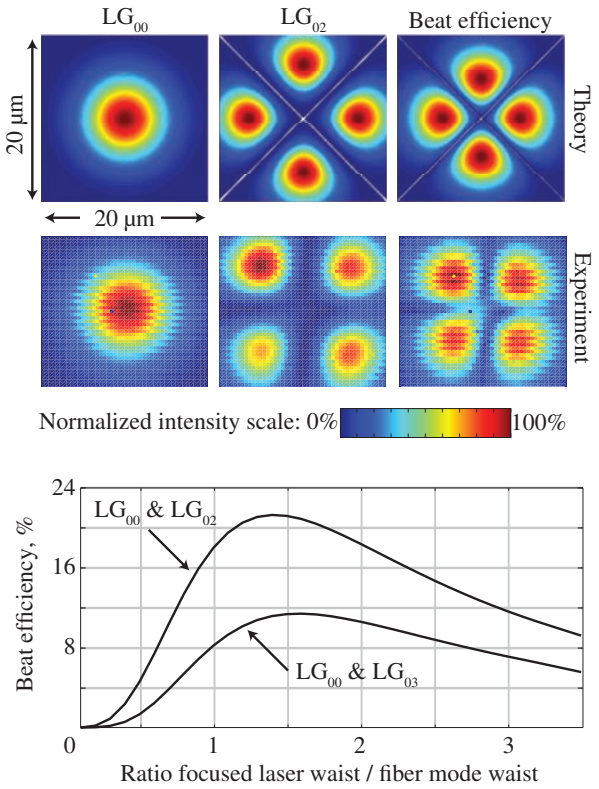

FIGURE 6.8 – Efficacité du battement THz par injection des modes de Laguerre-Gauss dans une fibre monomode hors-axe optique.
En haut : *coefficient de couplage (intensité) calculé par projection modale et représenté en fonction de la position relative de la fibre par rapport à l'axe optique (au centre) pour les modes LG_{00} & LG_{02} ; ainsi que l'efficacité de battement normalisée. L'expérience associée (stage M1 de Houda Belghiti) est aussi représentée.*
En bas : *efficacité du battement en fonction du rapport entre le rayon de mode minimum du faisceau laser sur le rayon de mode de la fibre pour ces couples (LG_{00},LG_{02}) et (LG_{00},LG_{03}).*

Comme le montre la figure 6.8, le battement est à la fois optimisé pour une position donnée de la fibre de couplage dans l'espace transverse, mais aussi pour un bon dimensionnement du modes laser en entrée de fibre. Enfin, nous avons pu montrer

dans le cadre de la thèse de R. Paquet et du stage M1 de Houda Belghiti [5], qu'un jeu de lentilles cylindriques permettait d'augmenter l'efficacité de battement à 38% pour le couple de modes LG_{00} & LG_{02}.

Émission THz et caractérisations primaires

Les modes ayant été projetés, il a été possible d'émettre le rayonnement THz à l'aide d'une photodiode commercial fibrée de chez NTT Electronics corp., avec lentille silicium haute-résistivité afin de permettre une émission large bande (aux dépens d'une puissance plus faible en comparaison à une solution avec guide d'onde). Notons que la photodiode est conçue pour une excitation à 1550 nm, mais fibrée par une fibre monomode transverse et à maintien de polarisation à 1 μm (fibre Panda pour 980 nm). Ainsi, l'efficacité de conversion entre puissances optique et THz est aussi diminuée de par l'absorption par le substrat, et surtout les pertes par phonons intra-bandes dues à une excitation à trop forte énergie de la jonction. Le montage réalisé pour l'émission THz et la caractérisation du faisceau est présenté Fig. 6.9. Nous observons à l'aide

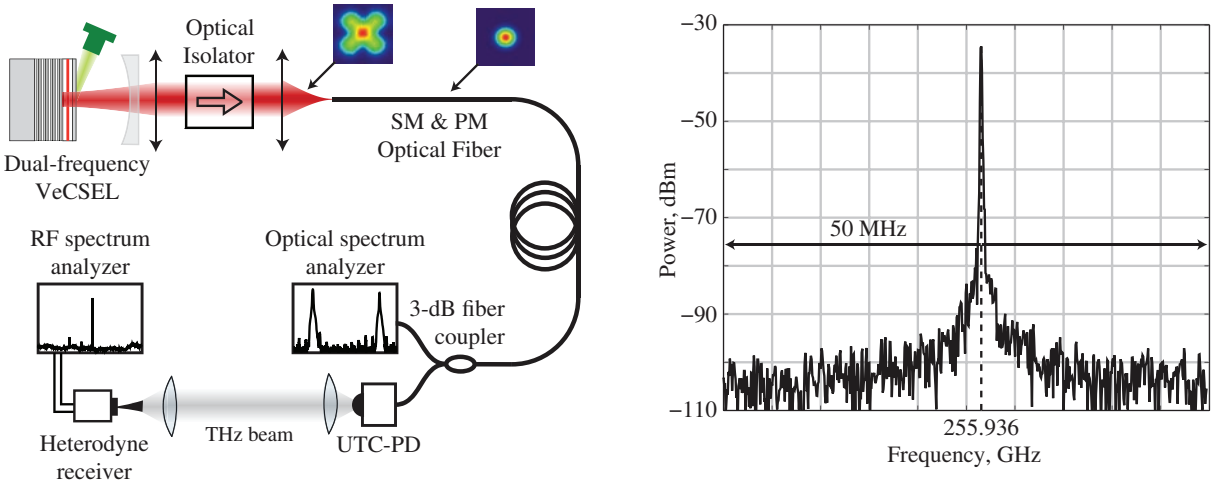

FIGURE 6.9 – Caractérisation du signal THz en puissance et spectralement. ***À gauche :*** *montage expérimental pour l'étude de l'émission THz issue de la photodiode UTC.* ***À droite :*** *spectre calibré cohérent avec une résolution de 100 kHz et un temps de mesure de 3 ms.*

d'une tête hétérodyne commerciale calibrée le spectre THz à l'analyseur de spectre électrique, après collimation et focalisation avec des lentilles Téflon de focales 10 cm. La puissance mesurée est donc diminuée d'environ 2 dB de par les pertes associées aux lentilles. Nous observons un spectre THz très stable sur la figure 6.9, avec une pleine largeur spectrale à mi-hauteur de 150 kHz, et une puissance proche du μW, puissance

5. Notons que je n'ai pas répertorié les (nombreux) stages M1 encadrés.

de saturation de l'UTC commerciale à cette fréquence. Nous remarquons aussi un excellent rapport signal-sur-bruit, supérieur à 60 dB, tel qu'attendu de par le rapport de suppression de mode important pour le VeCSEL bi-fréquence. Une telle cohérence est ainsi attractive pour des applications en spectroscopie.

Accordabilité

Nous avons pu observer une différence de fréquence notable entre les fréquences des deux modes transverses. L'étude des fréquences des modes transverses dans la cavité [26] montre que ces différents modes transverses n'oscillent pas sur le même ordre de résonance longitudinal. La figure 6.10(a) propose une origine physique quant à la sélection des ordres longitudinaux. De par le pompage optique, la structure est échauffée avec un gradient thermique radial autour de l'axe optique. Ainsi, compte tenu du recouvrement entre les modes transverses et le profil de température, le mode d'ordre supérieur observera une température inférieure à celle observée par le mode fondamental. Si la courbe de gain se décale avec la température, l'effet dominant quant à la sélection de l'ordre de résonance longitudinal est lié au décalage spectral du filtre de la micro-cavité (miroir de Bragg peu réflectif représenté Fig. 6.2), décalage plus important pour le mode fondamental que pour le mode d'ordre supérieur, et d'autant plus important à fort pompage d'où la possible accordabilité de l'émission THz. Dans le cadre de la thèse de R. Paquet et du stage d'Houda Belghiti, nous avons étudié l'échauffement de la structure à l'aide de simulations Comsol, et traduit cet échauffement en différence de fréquence.

Si nous observons les spectres optiques présenté Fig. 6.10, nous observons en effet une dérive des fréquences des deux modes (courbe (b) en haut) et de la différence de fréquence (courbe (b) en bas). Cependant, R. Paquet a pu observer un point d'inflexion fortement marqué quant à l'évolution de la fréquence de battement avec le taux de pompage (effet de *fourche* sur les cartographies). À faible pompage, la dérive de la fréquence de battement est celle attendue de par les simulations Comsol associées. À fort pompage, un phénomène physique supplémentaire accélère la dérive en fréquence de battement avec le pompage. L'origine physique de cet effet n'est pas déterminée à ce jour mais plusieurs pistes sont explorées par B. Chomet tel qu'indiqué en [21], notamment l'effet non linéaire tel l'effet Kerr se traduisant par exemple en un effet de lentille thermique. Cependant, ce phénomène est bienvenu car il permet d'offrir une plus grande plage d'accordabilité pour la fréquence de battement, avec une plage de 50 à 700 GHz pour le couple LG_{00} & LG_{03} notamment tel que reporté récemment en (R:2). Nous observons aussi sur cette figure la difficulté à obtenir un fonctionnement bi-fréquence stable à faibles fréquences de battement pour le couple LG_{00} & LG_{02}, du fait du plus fort recouvrement spatial entre ces modes, donc une plus grande compéti-

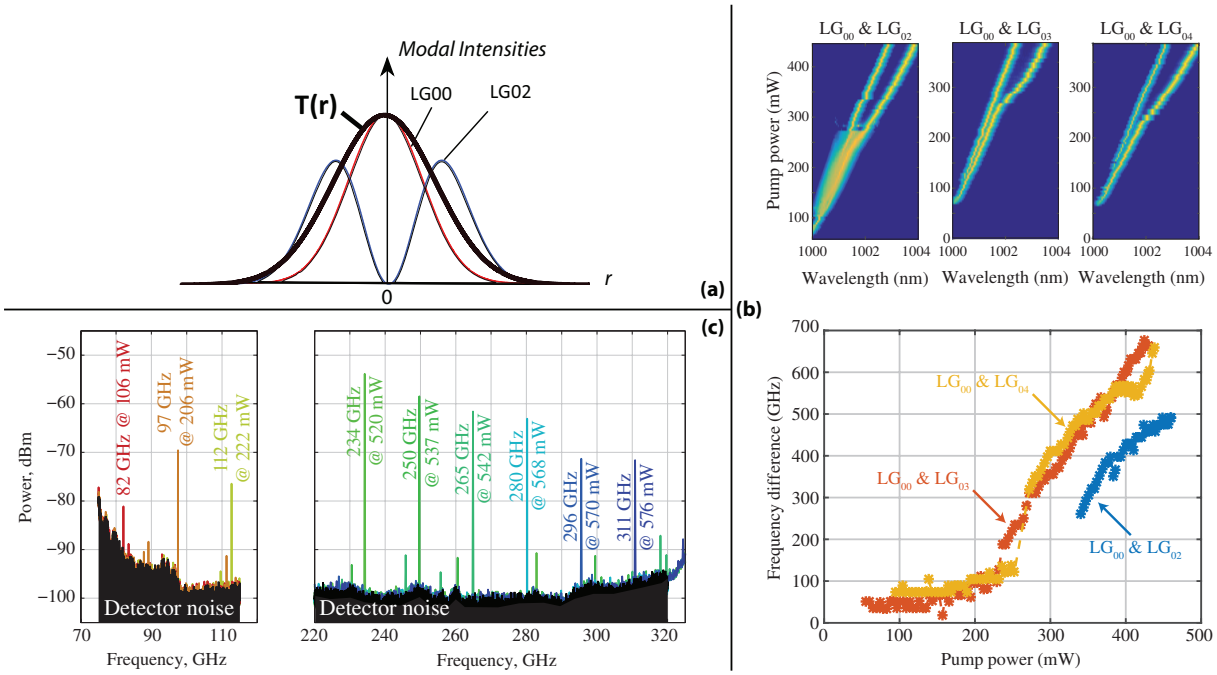

FIGURE 6.10 – Accordabilité du battement THz.
(a) : *principe de l'accordabilité thermique montrant la différence des recouvrements entre le profil radial de température $T(r)$ et les différents modes transverses.*
(b) : *évolution des spectres optiques (en haut) avec le pompage pour les couples de modes (LG_{00},LG_{02}), (LG_{00},LG_{03}) et (LG_{00},LG_{04}), l'évolution de la différence de fréquence étant représentée sur la courbe du bas.*
(c) : *spectres THz obtenus pour différents taux de pompage de la même structure laser fonctionnant sur les modes (LG_{00},LG_{03}). Les spectres sont observés avec les têtes de détection hétérodyne disponibles, à savoir une 75–110 GHz et une 220–325 GHz, avec une résolution spectrale de mesure de 300 kHz.*

tion, à comparer aux couples (LG_{00},LG_{03}) et (LG_{00},LG_{04}) pour lesquels le recouvrement spatial est suffisamment faible pour permettre un fonctionnement robuste sur toute la plage de pompage.

Enfin, nous pouvons observer Fig. 6.10 les spectres THz obtenus en fonction du pompage d'une seule et même structure VeCSEL, montrant l'accordabilité par saut de mode sur toute la gamme de mesure disponible, avec une puissance attendue pour la photodiode UTC utilisée, avec un effet de coupure aux basses fréquences dû à l'antenne bow-tie utilisée par NTT, et une coupure aux grandes fréquences associée à la bande-passante électronique de la photodiode.

Bruit de fréquence, largeur spectrale et temps de cohérence

La cohérence temporelle de l'émission THz a été menée avec l'aide de M. Myara grâce à son expertise incontournable [27]. Grâce aux avancées obtenues dans le cadre de la thèse de N. Von Bandel, nous avons caractérisé le bruit de fréquence optique de chaque mode transverse ainsi que le bruit de fréquences THz tel que représenté sur la Fig. 6.11. Pour le bruit de fréquence optique, R. Paquet a utilisé un Fabry-Perot comme

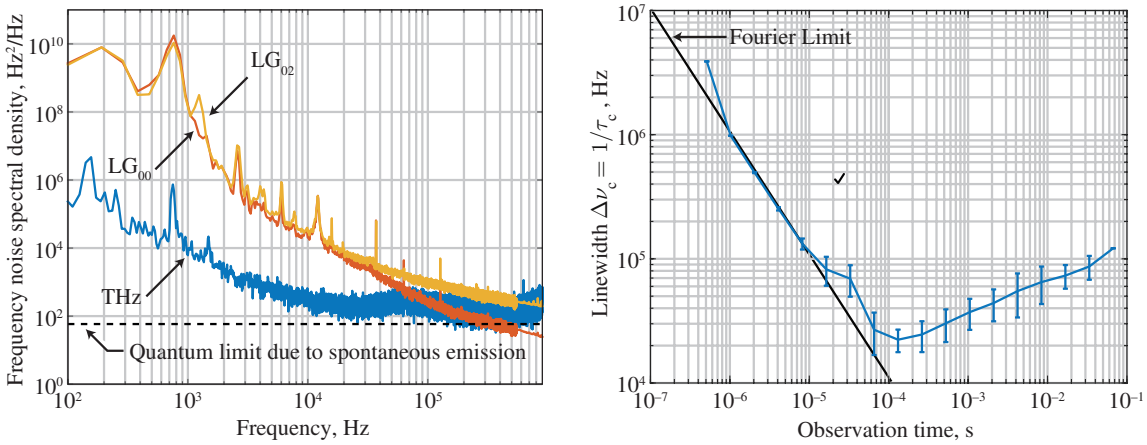

FIGURE 6.11 – Bruit de fréquence d'un laser bi-fréquence et du signal THz redressé pour le couple de modes (LG_{00},LG_{02}).
À gauche : *densité spectrale du bruit de fréquence pour les modes optique et THz.*
À droite : *calcul du temps de cohérence associé en fonction du temps d'observation.*

discriminateur de fréquence. La longueur du Fabry-Perot a été ajustée afin de positionner la fréquence de l'un ou l'autre des modes sur un flanc de la fonction d'Airy de l'interféromètre, afin de pouvoir mesurer indépendamment les spectres de bruit de fréquence représentés Fig.6.11. Nous observons l'allure typique du bruit de fréquence pour un VeCSEL [28], avec une forte contribution technique à basse fréquence (bruit de pompe, bruit mécanique), et une limite quantique atteinte autour du MHz [23]. Quant au bruit de fréquence THz, nous avons utilisé une tête hétérodyne en réception pour récupérer sur une porteuse de plus basse fréquence, inférieure à la fréquence de coupure de la chaîne d'acquisition utilisée, le bruit de fréquence du signal THz. Le signal a ainsi été ramené autour du GHz, et le bruit de fréquence extrait à l'aide d'une transformée de Hilbert grâce aux études amont menées en parallèle dans le cadre de la thèse de N. Von Bandel, et publiées ici [27]. Le résultat marquant de cette mesure est un bruit de fréquence THz de 4 ordres de grandeurs inférieur à celui du bruit de fréquence optique, justifiant ainsi le concept même de laser bi-fréquence, résultats valorisés en (R:2). À basse fréquence, les modes ne travaillant pas la même température, ils observent un bruit technique lié au bruit de pompe différent, ce qui justifie le résidu de bruit de fréquence. Le bruit mécanique peut quant à lui être diminué de manière

plus significative. À haute fréquence, le plancher de bruit reste inchangé car limité par l'émission spontanée, décorrélée pour les deux modes.

Afin de relier le bruit de fréquence à la largeur spectrale en fonction du temps d'observation, plusieurs méthodes existent, celle que j'ai pu étudier à partir de la fonction d'Airy généralisée (R:23), ou celle proposée par M. Myara [27]. Cette dernière méthode a été utilisée pour extraire, Fig. 6.11 (droite), la largeur spectrale du laser, soit l'inverse du temps de cohérence.

6.3 Détecteurs THz

Contrairement aux sources THz, les détecteurs ont connu un essor plus important, avec des performances, une compacité et un coût qui peuvent aujourd'hui répondre à nombre d'applications. Les détecteurs se révèlent extrêmement performants en terme de sensibilité, particulièrement les diodes Schottky intégrées dans des guide d'ondes [29], en terme de bande passante aussi avec des démonstrations de communication en laboratoire à très haut-débit [30], mais restent limitées en terme d'intégration électronique dans des circuits MIMIC [6]. Des matrices de détecteurs ont aussi été développés pour l'imagerie temps-réel, que ce soit à base de transistors ou de micro-bolomètres, avec des performances moindres en terme de sensibilité, de bande passante, mais offrant des solutions abouties pour l'imagerie. Les travaux présentés ici se focalisent sur l'étude des transistors comme détecteurs pour les communications sans fil très haut-débit, détecteurs attractifs notamment de par la maturité et le savoir-faire en micro-électronique pour ces composants commercialisés à grande échelle dans d'autres cadres applicatifs. Nous verrons que nous nous sommes intéressés à de nombreux types de transistors tel que représentés Fig. 6.12, avec ou sans antenne, avec ou sans amplificateur, de technologies différentes, commerciaux ou issus de collaborations de recherches.

6.3.1 Contexte et problématique télécoms

Dans un contexte de saturation des réseaux mobiles et de débits Wi-Fi faibles à comparer au débit disponible par fibre optique, le domaine des fréquences THz est attractif car il permet de lever plusieurs verrous majeurs. En terme de communications sans fils, le débit est aujourd'hui principalement limité par la porteuse aux fréquences micro-ondes, augmenter la fréquence porteuse des fréquences GHz aux fréquences THz permettrait donc d'augmenter de trois ordres de grandeur les débits disponibles. Une alternative aux fréquences THz serait l'utilisation de fréquences optiques, avec des

6. MMIC (Monolithic microwave integrated circuits) : Circuits hyperfréquences monolithiques intégrés.

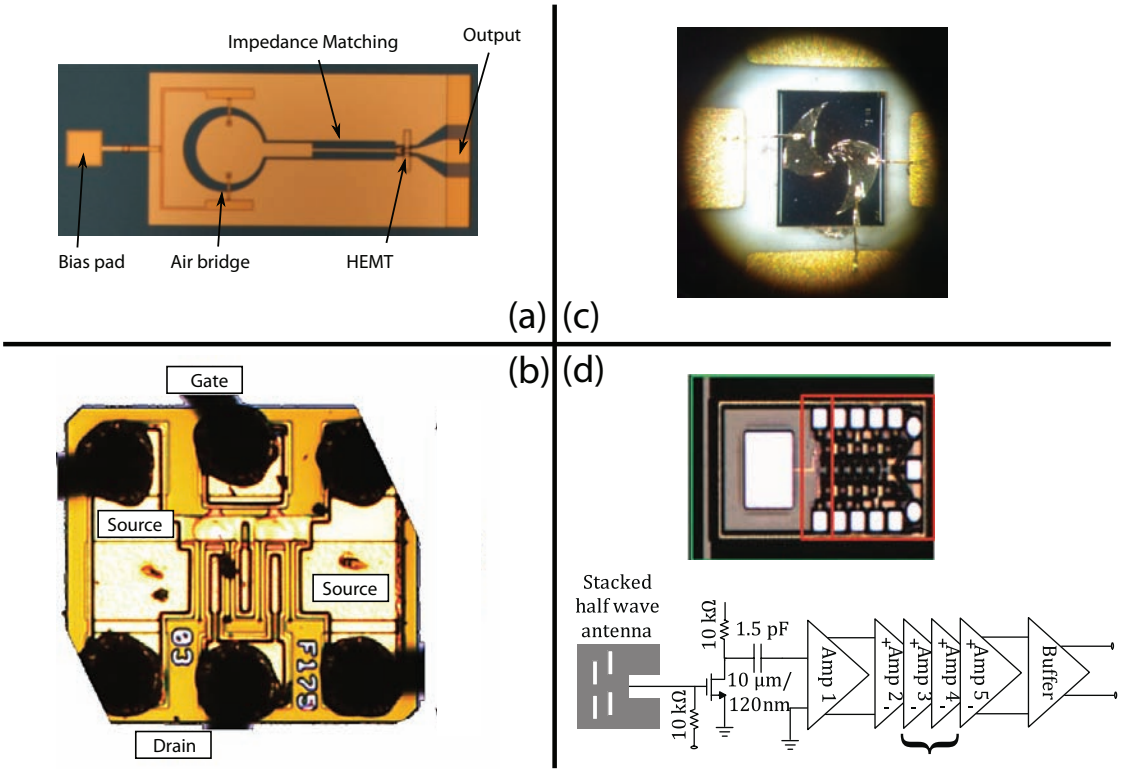

FIGURE 6.12 – Transistors évalués comme détecteurs pour les communications térahertz.
(a) *Nano-transistor InGaAs à effet de champs et antenne* slot-ring *réalisé à l'IEMN.* ***(b)*** *Transistor commercial à effet de champs GaAs.* ***(c)*** *Transistor bipolaire InP à double hétérojonction avec antenne log-spirale.* ***(d)*** *Transistor CMOS avec antenne imprimée.*

systèmes parfois dénommés Li-Fi [7]. Si de tels systèmes sont attractifs en terme de technologie de par la maturité des solutions photoniques issues des télécoms, les porteuses THz restent plus avantageuses dans un environnement réel de par la faible absorption des matériaux secs et non conducteurs, une diffraction naturelle plus importante limitant ainsi les zones d'ombres et augmentant intrinsèquement la couverture, mais aussi une fréquence finalement suffisante pour permettre une continuité, en termes de débit de communication, de la fibre optique vers le système sans fil. Les applications peuvent aller d'une communication sans contact très courte distance aux réseaux mobiles extérieurs en passant par le wifi intérieur. Si l'intégralité de ce panel applicatif est étudié, la faisabilité est fragilisée dans des milieux extérieurs et pour des propagations longues distances compte tenu de la forte absorption de l'eau aux fréquences THz. Ainsi, les fréquences clefs pour les applications télécoms THz sont de 300 GHz et 650 GHz car ces fréquences correspondent à deux fenêtres de transmission dans le spectre d'absorption de l'eau.

7. *Light Fidelity*, systèmes de communications sans fil par porteuse optique

Les travaux présentés ici concernent l'étude des transistors comme détecteurs télécoms, travaux effectués en partenariat avec le laboratoire Charles Coulomb de l'Université de Montpellier, dans la continuité de leurs études physiques sur les processus de détection THz d'un transistor HEMT [8], notamment selon la théorie de Diakonov et Shur [31], et en parallèle de leurs travaux sur l'imagerie THz. En comparaison à une application d'imagerie, l'application télécoms pour les détecteurs THz est plus contraignante. En effet, les performances exigées pour les télécoms sont similaires à celles exigées pour l'imagerie, mais sur des bandes passantes de plusieurs dizaines de GHz (au lieu de quelques dixièmes de Hertz pour une système d'imagerie utilisant une détection synchrone), que ce soit en termes de sensibilité en fonction de la fréquence porteuse, de bande-passante de modulation du signal redressé, de bruit, ou d'impédance de sortie (nécessairement 50 Ohms).

Tel que le montre la Fig. 6.13, la bande passante de communication dépend directement de la sensibilité du détecteur et de la puissance incidente. Ne considérant

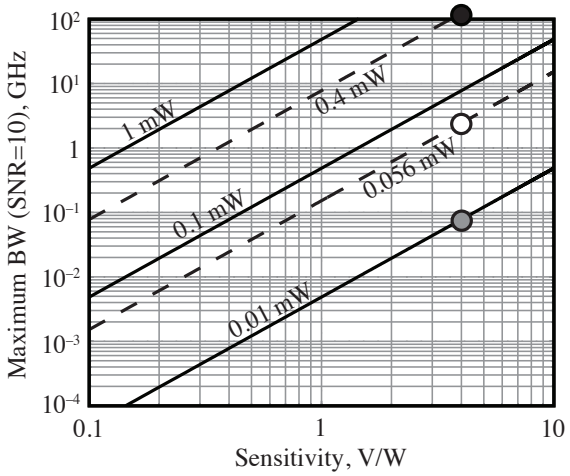

FIGURE 6.13 – Bande passante de communication théorique en fonction de la sensibilité du détecteur pour différentes puissances incidentes.
Le point noir correspond au débit potentiel pour les sensibilité et puissance reportées en (R:8), le point blanc à la communication hétérodyne réalisée (R:2), et le point gris à cette même communication sans l'apport de l'oscillateur local.

que le bruit thermique pour un détecteur d'impédance 50 Ohms, la bande passante de détection Δf maximale permettant d'assurer un rapport signal-sur-bruit SNR donné dépend directement de la puissance incidente P_{THz} et de la sensibilité du détecteur η selon la relation (R:2) :

$$\Delta f = \frac{(\eta\, P_{THz}/SNR)^2}{k_B\, T\, R}, \tag{6.1}$$

8. HEMT : *High-Electron-Mobility Transistor* pour transistor à haute mobilité électronique.

où k_B est la constante de Boltzmann et T la température. La Fig. 6.13 permet ainsi de prévoir le débit possible pour une communication selon la puissance disponible à l'entrée du détecteur et sa sensibilité, ce pour un rapport signal-sur-bruit de 10. La sensibilité typique d'un transistor en détection THz n'étant que de quelques V/W autour de 300 GHz, il est donc nécessaire de bénéficier de plusieurs centaines de μW de puissance incidente afin d'offrir des communications à des débits supérieurs au Gbits/s. Nous verrons par la suite, de par la simple balance entre gain et bande-passante, que seule une approche système permet de bénéficier à la fois d'une source THz haut-débit et (suffisamment) puissante. Nous verrons aussi qu'un point clef pour la réalisation d'une communication haut-débit réside dans la sensibilité du détecteur, puisque le bande passante de communication évolue quadratiquement avec la sensibilité. Nous verrons enfin l'importance de l'adaptation d'impédance pour le transistor, autre point clef indispensable pour une communication.

6.3.2 Caractérisations des détecteurs pour les télécommunications

Dans le cadre de l'encadrement de thèse de Lucie Tohme [32], nous avons pu mettre en place des méthodes et des bancs de caractérisation des détecteurs THz dédiés aux communications, méthodes par la suite complétées avec le stage de Steve Tehaamoana et la thèse en cours d'Isidore Diouf. Nous synthétiserons les résultats obtenus pour différents types de détecteurs tels que montré Fig. 6.12, des détecteurs issus de collaborations de recherches ou commerciaux, avec ou sans antenne, issus de technologies différentes (CMOS, InP, GaAs), et de fonctionnement physiques différents (transistors à effet de champs, ou transistors bipolaires).

Sensibilité et bande-passante quasi-statique

La première caractérisation des transistors consiste à déterminer leur capacité à détecter des signaux aux porteuses THz, pour ce faire nous évaluons leur sensibilité en fonction de la fréquence d'excitation de la porteuse, ce par plusieurs méthodes expérimentales tel que présenté Fig. 6.14. L'utilisation d'une source électronique à multiplication de fréquence est attractive pour les fortes puissances disponibles (quelques mW) mais reste restreinte en termes d'accordabilité, car limitée par la plage de fonctionnement monomode transverse des guides d'ondes creux utilisés. L'approche photonique, au contraire, offre une plage d'accordabilité extrêmement large, mais reste limitée en terme de puissance de sortie, typiquement quelques dizaines à centaines de μW. Compte tenu de la faible sensibilité des transistors et afin de gagner en rapport signal-sur-bruit pour la mesure de sensibilité, la source est modulée en amplitude. La tension en sortie du transistor peut ainsi être mesurée à l'aide d'une détection synchrone si nécessaire, ou à l'analyseur de spectre électrique. Nous définissons alors la

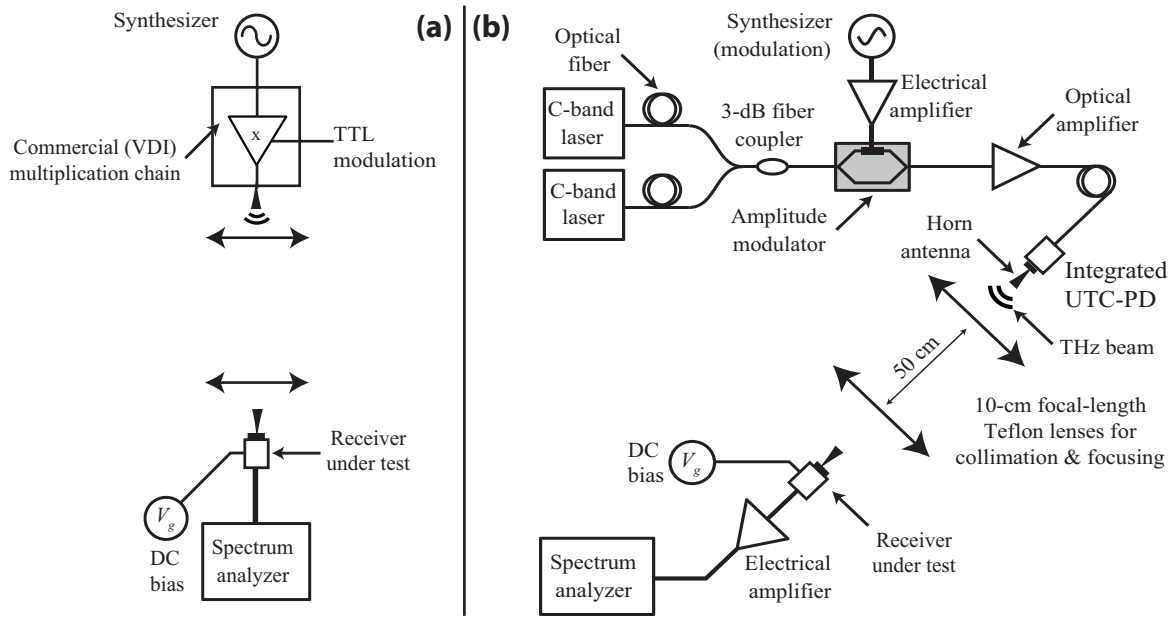

FIGURE 6.14 – Caractérisation de la sensibilité et de la bande-passante quasi-statique.
(a) *Caractérisation par une source électronique à multiplication de fréquence.*
(b) *Caractérisation par une source photo-mélangée.*

sensibilité comme le rapport de la tension efficace V_{rms} sur la puissance THz incidente P_{THz} :

$$\eta = \frac{V_{rms}}{P_{THz}}. \tag{6.2}$$

Pour ces mesures, la fréquence de modulation est généralement faible, typiquement de l'ordre du kHz car les sources à multiplication de fréquence continues ne peuvent être modulées plus rapidement.

Il est important de remarquer que certaines équipes n'utilisent pas la puissance THz incidente sur le détecteur, mais celle incidente sur la surface du détecteur, de dimensions inférieures à la longueur d'onde incidente. Une telle normalisation a un intérêt pour comparer l'efficacité d'un processus physique de détection indépendamment de la surface du détecteur par exemple. Cependant, compte tenu des limites fondamentales de diffraction, une telle normalisation de la sensibilité n'apporte pas d'information concrète quant au niveau de signal disponible en sortie de composant pour une puissance incidente donnée. Pour des applications concrètes, notamment pour les télécoms, nous préférons donc utiliser la formule indiquée Eq. (6.2) sans normalisation. Il est cependant possible de passer d'une définition à l'autre tel que discuté dans (R:8). Nous ne serons donc pas étonné des faibles sensibilité évoquées dans ce manuscrit, les facteurs de normalisation par la surface augmentant généralement les sensibilités d'un facteur de 2 à 3 ordres de grandeur.

Outre la sensibilité à une fréquence donnée, il est important d'évaluer la plage de fréquence sur laquelle le détecteur est sensible, i.e. la bande passante du spectre de détection, car un signal télécoms occupe un bande spectrale autour d'une porteuse de fréquence donnée d'autant plus grand que le débit est important. Nous présentons Fig. 6.15 la sensibilité du transistor commercial GaAs en fonction de la fréquence pour le montage photonique présenté Fig. 6.14, obtenu avec L. Tohme à l'Univ. d'Osaka. Nous observons une sensibilité de quelques V/W pour une plage de fréquence de

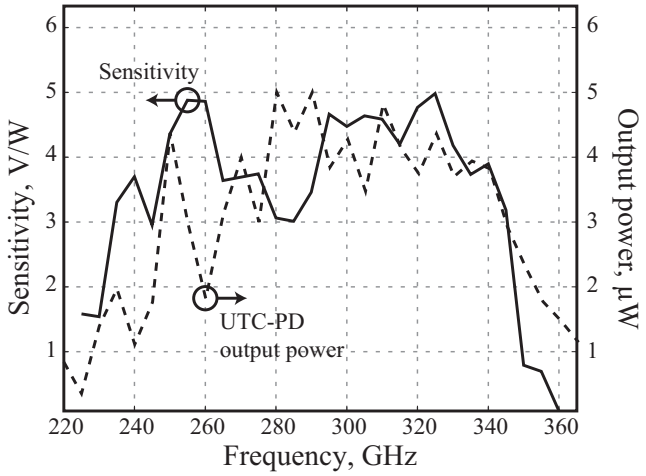

FIGURE 6.15 – Caractérisation quasi-statiques du HEMT commercial GaAs intégré pour la détection THz.

l'ordre de 90 GHz, offrant ainsi une bande de communication de 45 GHz de part et d'autre d'une porteuse de 290 GHz (R:11). Il est à noter que tous les transistors évalués présentent une sensibilité typique de 0,1 à 10 V/W sans antenne. Le transistor HEMT avec antenne slot-ring développé à l'IEMN a montré une sensibilité de l'ordre de 30–100 V/W autour de 300 GHz, une sensibilité de 10–40 V/W pour le circuit Si-CMOS (R:4), le transistor HBT [9] avec antenne log-spirale est en cours d'étude (R:3) mais ne montre pas à ce jour de sensibilité significativement augmentée.

Compte tenu de ces résultats, nous avons réalisé qu'il était difficile d'augmenter de manière très significative la sensibilité des transistors par l'ajout d'une antenne pour une opération large bande. L'utilisation des antennes est en effet délicate, car de par les forts indices des matériaux aux fréquences THz, le champ tend à se confiner dans le substrat, avec des effets parasites multiples tels qu'une réflexion avec filtrage Fabry-Perot longitudinale qui peut perturber l'antenne, mais aussi des modes de propagation transverse dans le substrat. De plus, il est essentiel d'accorder les impédances complexes de sortie de l'antenne et d'entrée du transistor, ce aux fréquences THz. D'autres études telles que l'évolution du diagramme de rayonnement de l'antenne et sa dispersion chromatique sont d'autres problématiques majeures qui restent à étudier scrupu-

9. HBT : *Heterojunction Bipolar Transistor* pour transistor bipolaire à hétéro-jonction.

leusement. Ces défis sont actuellement en cours d'étude avec l'encadrement de la thèse d'I. Diouf.

Bande passante dynamique

Si les méthodes de caractérisation de la sensibilité des transistors avaient été auparavant déjà mises en œuvre, nous avons pu développer des bancs de caractérisation originaux pour la mesure de la bande passante des transistors afin d'estimer leur possible utilisation pour des communications haut-débit. Ces caractérisations étant menées pour la première fois, nous avons mis en œuvre plusieurs montages expérimentaux avec L. Tohme, représentés Fig. 6.16, afin de valider ces premières mesures. Ces

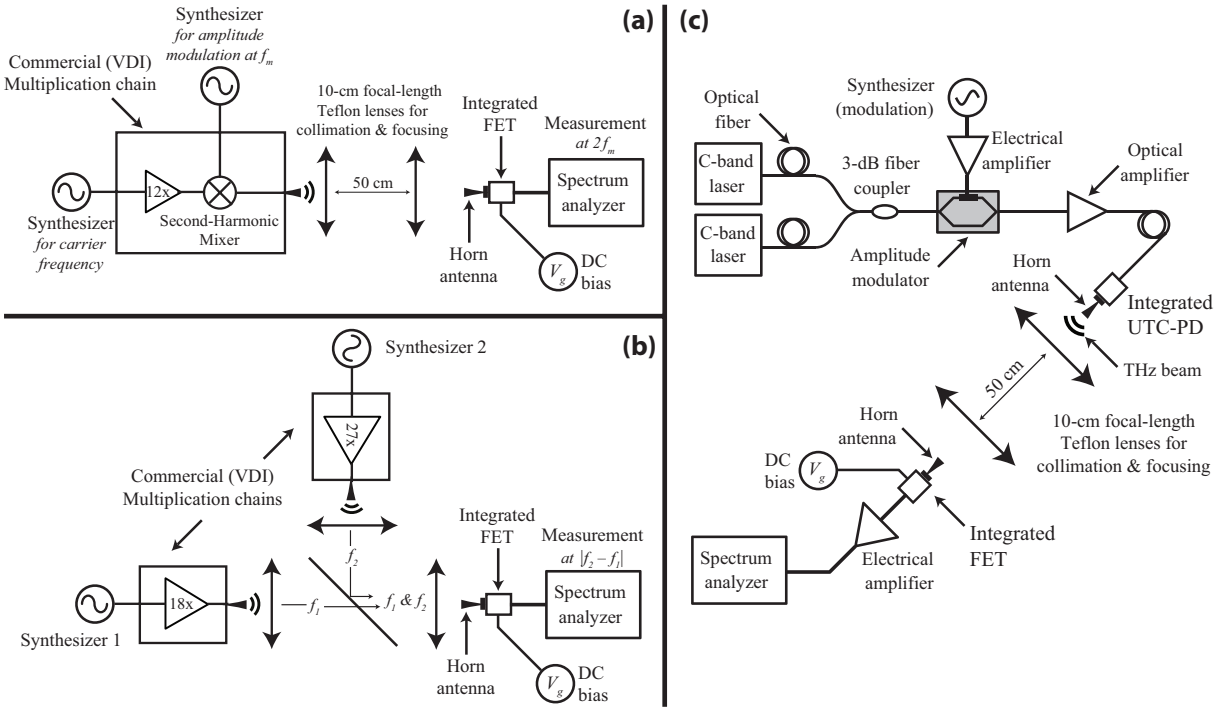

FIGURE 6.16 – Montages expérimentaux pour l'étude de la réponse dynamique des transistors comme récepteurs THz.
(a) *Modulation sans porteuse d'une source électronique,* ***(b)*** *montage hétérodyne CW,* ***(c)*** *modulation avec porteuse d'une source photonique (UTC).*

montages ont été mis particulièrement mis en œuvre à l'IES dans le cadre d'une collaboration industrielle avec Canon CRF (Fig. 6.16(a)), de l'ANR-I WITH (Fig. 6.16(b)) et dans ce même cadre à l'Univ. d'Osaka (Fig. 6.16(c))). Le premier montage est le plus utilisé actuellement, il consiste à utiliser une source à multiplication de fréquence dont le dernier étage est un mélangeur, excité par une modulation externe sinusoïdale, amenant ainsi à une modulation sans porteuse. De par la réponse non linéaire du transistor, nous retrouvons ainsi en sortie un battement à la différence de fréquence des deux raies de modulation, soit à la fréquence double de la fréquence de modulation.

Tel que représenté Fig. 6.17, en variant la fréquence de modulation de la source, il est possible de suivre la réponse du transistor en mesurant particulièrement l'amplitude du signal redressé, permettant ainsi de définir une bande passante de modulation tout comme nous le ferions pour un diagramme de Bode traditionnel. Comme

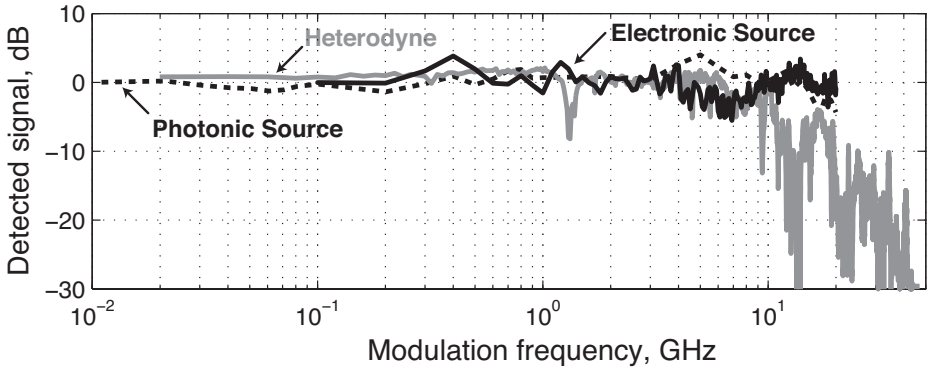

FIGURE 6.17 – Réponse de la bande passante de modulation du transistor HEMT GaAs commercial.
Différentes méthodes de caractérisation sont évaluées : modulation avec porteuse d'une source photonique (UTC), battement hétérodyne entre deux sources électroniques continues, modulation sans porteuse avec une source électronique.

nous pouvons le voir Fig. 6.17, ces mesures ont été confortées par d'autres mesures effectuées avec les montages alternatifs représentés Fig. 6.16. L'excitation hétérodyne du transistor par deux sources continues désaccordées permet aussi d'évaluer la dynamique de la réponse du transistor, avec moins de précision cependant car la précision de cette méthode est sensible aux alignements relatifs des deux sources, elle dépend aussi de la (non)-synchronisation des sources alimentées par deux synthétiseurs différents. Cette synchronisation étant aléatoire mais les variations relatives de phase et/ou de fréquence entre les deux synthétiseurs rapides devant le temps de mesure de l'analyseur de spectre électrique, nous observons malgré tout Fig. 6.17 un bon accord avec les résultats obtenus pour la source électronique modulée. Enfin, la dernière méthode est une méthode avec une approche photonique, initialement mise en œuvre au cours d'un séjour à l'Université d'Osaka (équipe de T. Nagatsuma) avec L. Tohme. Les signaux de deux lasers désaccordés sont modulés en amplitude avec porteuse grâce à un modulateur fibré de Mach-Zehnder, tel que représenté Fig. 6.16 (c). Le signal modulé est ensuite envoyé sur une photo-diode UTC pour l'émission du signal de modulation sur une porteuse de fréquence égale à la différence de fréquence des deux lasers. Les avantages de cette méthode sont indéniables en termes de flexibilité de la fréquence porteuse grâce à la facilité d'accorder les lasers, mais aussi en termes de fréquences maximales de modulation grâce aux technologies matures développées pour les communications à fibre optique. Un seul inconvénient pour cette méthode est la chute de

puissance avec l'augmentation des fréquences d'émission, associée au filtrage passe-bas de la photodiode UTC. Nous observons aussi Fig. 6.17 un bon accord quant à la fréquence de coupure de la réponse du transistor en bande de base.

Nous remarquerons que mon expérience en lasers et fibres optiques construite lors du doctorat et des années de post-doctorat, a été un précieux outil pour la maîtrise de systèmes de caractérisations aussi complexes que celui proposé par T. Nagatsuma.

Intégration hyperfréquence et mécanique

L'intégration des transistors pour les communications est un point clef à de multiples titres, ce malgré le peu de reconnaissance scientifique associé à ces travaux pourtant indispensables à une communication.

Nous avons démontré Fig. 6.13 que le débit dépend directement de la sensibilité, or la sensibilité du transistor est relativement faible, notamment de par sa petite taille devant la longueur d'onde. Ainsi, le transistor ne collecte qu'une infime partie de la puissance incidente (un centième à un millième typiquement). Afin d'optimiser la puissance couplée au transistor et de tendre facilement vers la limite de diffraction sans contrainte majeure sur les alignements optiques, il est possible d'intégrer le transistor derrière un guide d'onde creux associé à un cornet pour le couplage du faisceau incident. Tel que représenté Fig. 6.18, nous avons ainsi réalisé cette intégration grâce à l'équipement (machine-outil 5 axes), au savoir-faire, et à l'engagement de l'atelier de mécanique. Pour le premier prototype, le transistor a été positionné en sortie du guide d'onde, à quelques millimètres. Un tel positionnement n'est certes pas optimal tant d'un point de vue longitudinal, de par la cavité parasite associée à cet interstice, ou d'un point de vue transverse en termes de diffraction, mais les performances du composant se sont relevées malgré tout meilleures, notamment avec une sensibilité augmentée d'un facteur 10 environ, et un alignement grandement facilité, tel que nous l'avons montré dans la thèse de L. Tohme [32]. Nous travaillons actuellement sur de nouveaux designs pour une meilleure intégration, et une collaboration avec un fondeur pourrait aussi nous permettre d'intégrer le composant avec un plongeur résonant longitudinalement dans le guide d'onde fermé tout comme l'intégration effectuée pour les diodes Schottky.

L'intégration du composant s'est aussi revélée essentielle en terme de compatibilité électromagnétique. L'intégration du composant a en effet permis une isolation électromagnétique aux fréquences pouvant dégrader le rapport signal-à-bruit du signal de sortie du composant, i.e. en bande de base. Notons que les guides d'ondes creux ayant une fréquence de coupure minimale pour le mode fondamental de l'ordre de 200 GHz (valeur typique pour une fréquence de travail autour de 300 GHz), le cornet permet de ne coupler que le faisceau porteur et sa modulation. Enfin, nous remarquerons

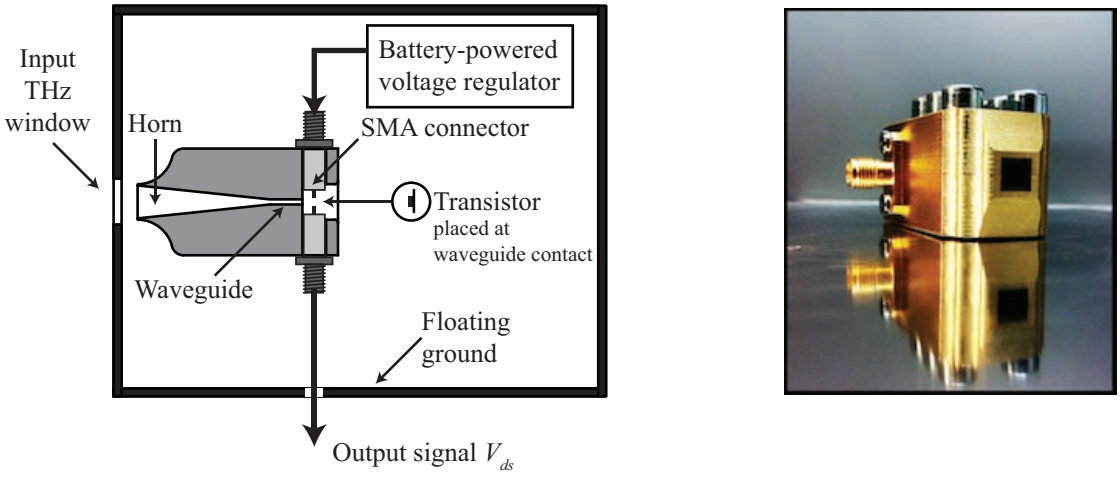

FIGURE 6.18 – Intégration du transistor commercial HEMT GaAs.
À gauche : *schéma de principe montrant l'intégration du composant derrière un guide d'onde avec (éventuellement) une masse flottante supplémentaire pour raisons de compatibilité électromagnétique.*
À droite : *photographie du composant intégré réalisé par l'atelier de mécanique à l'Institut d'Électronique et des Systèmes (IES).*

Fig. 6.18 qu'une isolation supplémentaire en masse flottante a été nécessaire dans certaines configurations expérimentales, car un couplage délétère par la masse s'est montré rédhibitoire pour certaines communications. Au cours des expériences réalisées, nous avons pu remarquer que les composants actifs — le transistor est polarisé tant pour augmenter sa sensibilité que pour l'adapter en impédance — pouvaient coupler les parasites externes, dont le signal de modulation, par leur polarisation électrique en particulier, que ce soit pour des sources électroniques tel que nous l'avons identifié lors d'expériences à l'IEMN, toujours avec L. Tohme (R:6), ou pour des sources photoniques (rayonnement du modulateur en particulier), tel nous l'avons reporté en (R:11).

Impédance de sortie

Grâce à l'étude des transistors bipolaires comme détecteurs THz, notamment dans le cadre de la thèse en cours d'I. Diouf, nous avons réalisé l'importance de l'étude de l'impédance de sortie du transistor. L'utilisation des transistors pour des communications requiert impérativement une impédance de sortie complexe proche de 50 ohms, afin de pouvoir connecter le transistor à une chaîne d'amplification ou de traitement du signal. Si une telle étude est évidente dans un contexte télécoms, elle n'est pas particulièrement reportée aux fréquences THz. À titre d'exemple, nous montrons Fig. 6.19 le spectre en sortie d'un HBT excité par une porteuse autour de 300 GHz avec une modulation sans porteuse de 700 MHz. Nous nous attendons à un signal redressé à

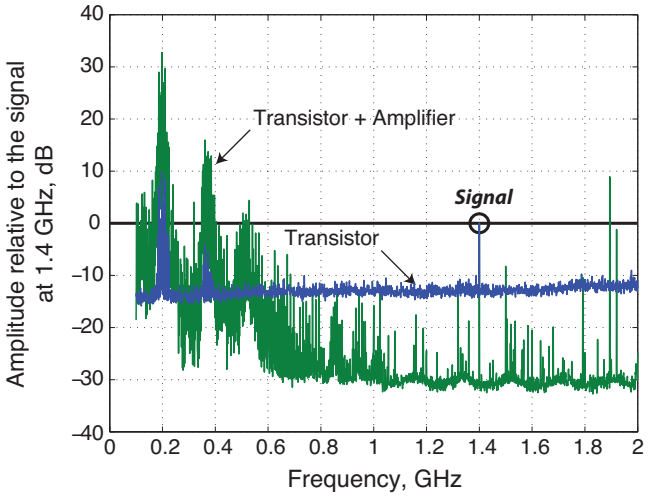

FIGURE 6.19 – Spectre électrique en sortie de transistor HBT.
Les spectres sont obtenus avec ou sans amplificateur en sortie de transistor, pour un signal redressé attendu à 1,4 GHz. Les spectres sont normalisés en puissance à la valeur du pic à 1,4 GHz.

1,4 GHz, que nous pouvons en effet observer sur le spectre à la valeur normalisée de 0 dB. Cependant, nous remarquons (courbe bleue) la présence d'oscillations parasites du composant à basses fréquences, avec une amplitude pouvant être d'un ordre de grandeur plus importante que le signal. Pour cette mesure, la plateau de bruit correspond au plancher de l'analyseur de spectre électrique. Si nous utilisons un amplificateur en sortie de transistor (courbe verte), nous gagnons en termes de dynamique de mesure, et pouvons observer des oscillations du composant à de multiples fréquences, particulièrement à basse fréquence. Nous observons une dégradation d'un ordre de grandeur du rapport entre la puissance du signal (normalisée à 0 dB) et la puissance des oscillations parasites (30 dB). Nous comprenons clairement avec une telle caractérisation que le rapport signal-sur-bruit en sortie du composant est ici rédhibitoire compte tenu de ces oscillations basses fréquences. Nous verrons par la suite que de telles oscillations sont dues à la forte désadaptation d'impédance du HBT en sortie, vis-à-vis de 50 ohms. Nous avons pu vérifier que ces oscillations n'étaient pas associées à des perturbations extérieures, notamment en polarisant sur batterie le composant et en effectuant des mesures dans une chambre anéchoïde, ce au cours du stage de fin d'étude de S. Tehaamoana.

L'étude de l'impédance de sortie a été effectuée en premier lieu par la simple méthode de la demi-tension sur le HEMT GaAs commercial dans le cadre de la thèse de L. Tohme, tel que présenté Fig. 6.20. Nous observons une impédance proche de 50 Ohms, ajustable par la polarisation du composant, et en bon accord entre la polarisation optimale en terme de sensibilité et l'impédance visée de 50 Ohms. Une telle impédance justifie notamment les succès obtenus en terme de communications avec ce

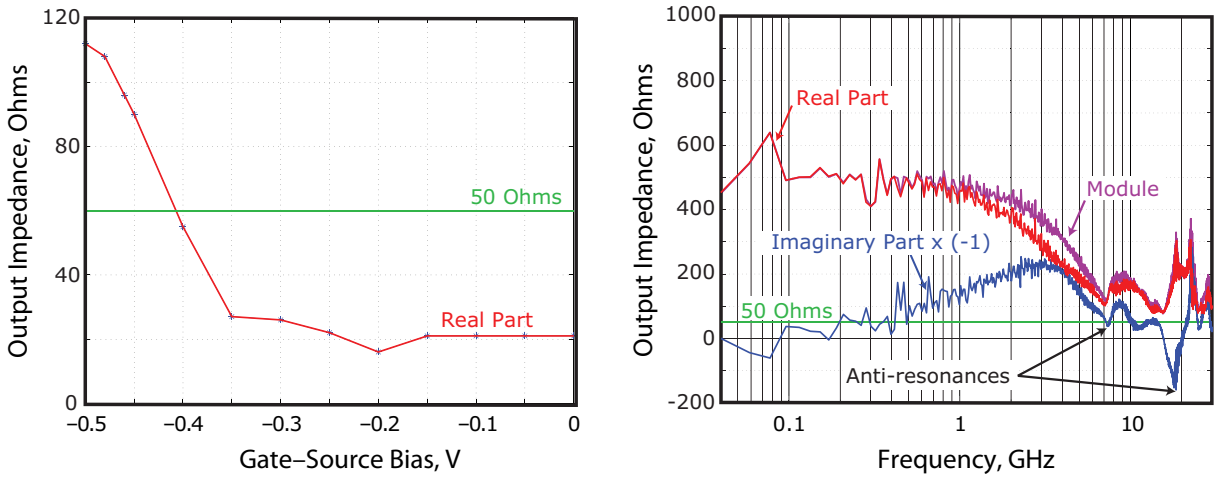

FIGURE 6.20 – Impédance de sortie de transistors pour la détection THz.
À gauche : *HEMT GaAs commercial à 100 MHz.* ***À droite :*** *HBT InP.*

composant, ainsi que la simplicité de cette étude. Pour les composants désadaptés tels que le HBT, il a été nécessaire d'effectuer des études plus complètes à l'analyseur de réseau. Nous observons clairement sur la Fig. 6.20 (droite) une impédance réelle forte à basse fréquence, justifiant les oscillations observées Fig. 6.19, mais aussi des anti-résonances à plus hautes fréquences que nous avons pu retrouver dans la réponse en modulation lors de la caractérisation du composant. L'étude fine de l'impédance initiée lors du stage de S. Tehaamoana est actuellement un axe fort de la thèse d'I. Diouf, afin notamment de déterminer s'il est possible à la fois d'adapter l'impédance par une polarisation adéquate du transistor, tout en conservant une sensibilité suffisante pour la détection THz.

6.3.3 Systèmes de communication

Les méthodes de caractérisations pour les applications télécoms ayant été présentées dans la section précédente, nous présenterons maintenant les systèmes de communication réalisés, avec différents types de modulation (avec ou sans porteuse) issues d'émetteurs photoniques (photodiode UTC), électroniques (chaîne de multiplication de fréquences) ou mixtes. Nous verrons dans un premier temps la réalisation d'une communication directe, nécessitant de ce fait une puissance significative, puis des communications hétérodynes permettant d'assurer la faisabilité de la communication même à faibles puissances.

Positionnement vis-à-vis de l'état de l'art des communications THz

Si nous repartons de l'état de l'art des communications THz dressé par G. Ducournau en 2015 [33] (cf. Fig. 6.21 à gauche) nous n'observons que peu de démonstrations

expérimentales autour de 300 GHz, fréquence d'intérêt pour les télécommunications de par la relativement faible absorption de l'eau. Sur la figure de droite, nous relevons

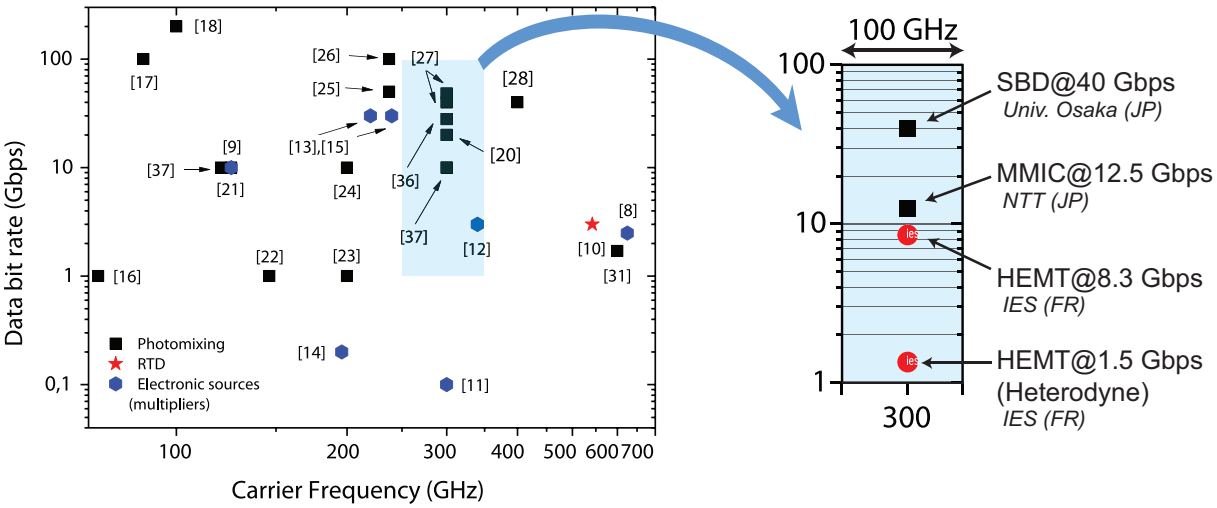

FIGURE 6.21 – État de l'art des communications THz.
À gauche : *état de l'art dressé issu de [33].*
À droite : *positionnement des performances obtenues avec des transistors.*

les transmissions mono-canal, afin de ne comparer que ce qui est comparable en terme de débit. Le record en terme de débit est ainsi réalisé par T. Nagatsuma à l'Université d'Osaka [30] utilisant des diodes Schottky comme récepteurs, nous trouvons aussi une communication à base de circuits MMIC réalisée par NTT [34]. Afin de positionner les travaux présentés dans ce document, j'ai ajouté les communications réalisées à l'aide d'un simple transistor GaAs comme détecteur THz.

L'excellente sensibilité (kV/W) des diodes Schottky est le point clef des débits obtenus par T. Nagatsuma, mais ces composants présentent plusieurs limitations pour une intégration industrielle, principalement leur haute impédance de sortie qui limite leur intégration avec des circuits rapides et des fonctionnalités électroniques intégrées (MMIC) ; mais aussi leur possible dégradation sous "forte" puissance térahertz, limitant ainsi leur souplesse d'utilisation. Quant aux performances obtenues par des circuits MMIC, ils offrent une séduisante intégration avec nombre de fonctionnalités, mais les performances obtenues sont basées sur un circuit complexe plutôt qu'un détecteur unique. Dans ce contexte, les performances obtenues avec un simple transistor sont ainsi prometteuses, car malgré leur faible sensibilité (1 V/W sans antenne), ils offrent une réelle capacité d'intégration tant mécanique qu'électronique grâce à leur faible impédance de sortie accordable, et résistent aux fortes puissances térahertz [35].

Communication directe

Tel que nous l'avons vu Fig. 6.13, une communication haut-débit avec les transistors n'est possible que pour des puissances incidentes suffisamment importantes. Dans le cadre d'un séjour à l'Université d'Osaka dans l'équipe de Tadao Nagatsuma, leader des communications THz, nous avons pu mettre en œuvre, avec L. Tohme, un système pour l'émission offrant une grande bande passante de modulation ainsi qu'une puissance atteignant quasiment 0,5 mW. De telles performances n'ont été possibles que par un système optoélectronique complexe présenté Fig. 6.22. La grande bande passante

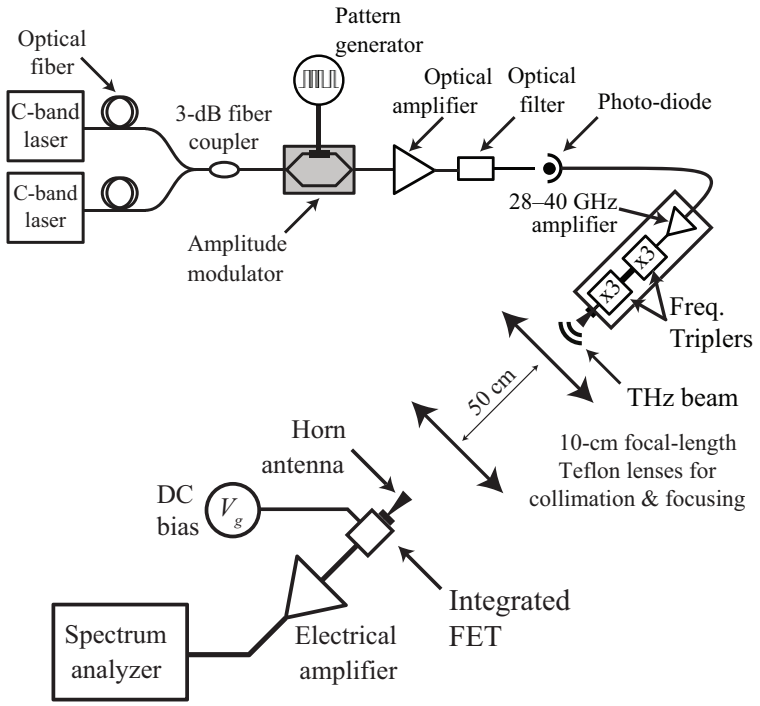

FIGURE 6.22 – Banc expérimental pour la réalisation d'une communication directe.

de modulation est possible par une modulation optique à l'aide d'un modulateur de Mach-Zehnder fibré modulant un battement optique issu de deux lasers en bande C. Après amplification et filtrage, ce battement optique modulé est converti en signal hyperfréquences autour de 33 GHz, grâce à une photo-diode rapide, ce signal passant ensuite dans une chaîne de multiplication de fréquence offrant une puissance de sortie importante sans avoir à être directement modulée (c'est l'entrée qui est modulée). Grâce à une telle puissance optique, un indéniable savoir faire de l'équipe Japonaise, et le détecteur intégré avec masse flottante présenté Fig. 6.18 et développé dans le cadre de la thèse de L. Tohme [32], nous avons pu réaliser une communication sans erreur sur une porteuse de 300 GHz jusqu'à 8,3 Gbps (R:8), ce qui reste à ma connaissance un record pour l'utilisation d'un unique transistor comme récepteur THz pour

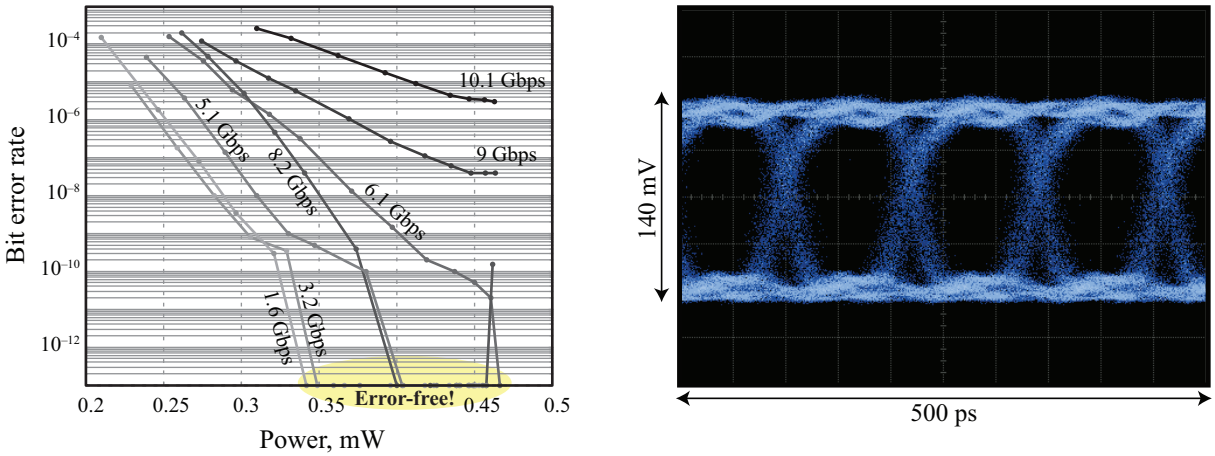

FIGURE 6.23 – Communication haut-débit avec un transistor à effet de champ commercial GaAs.
À gauche : *Taux d'erreur binaire pour différentes puissances incidentes à différents débits.* ***À droite :*** *Diagramme de l'œil pour une communication sans erreur à 8,3 Gbps.*

les communications, avec tous les avantages associés en terme de coût, de compacité et d'impédance. Afin de compenser la faible sensibilité du transistor, il est nécessaire de continuer les études du couplage d'antennes large-bande avec le transistor, ou de travailler sur un axe système comme nous allons le voir dans le cadre des communications hétérodynes.

Communication hétérodyne

La communication directe présentée précédemment (R:8) a été possible grâce à un montage expérimental certes ingénieux, mais complexe et couteux, afin d'offrir suffisamment de puissance au signal modulé pour démontrer une communication à haut-débit. Afin de contourner la problématique associée à la balance gain / bande passante, une alternative simple consiste à utiliser une source peu puissante mais rapide portant le signal à transmettre, ainsi qu'une source puissante et continue afin d'augmenter l'amplitude du signal détecté par hétérodynage, cela étant possible de par la réponse quadratique du transistor au signal THz incident.

Si nous considérons le transistor et la source continue comme un ensemble constituant un récepteur hétérodyne, une problématique usuelle est la synchronisation des deux sources, qui requiert habituellement un système d'asservissement de la fréquence et de la phase de la source continue. Afin de contourner cette problématique technique, j'ai utilisé deux sources électroniques de même facteur de multiplication, injectées par un même synthétiseur dont le signal a été séparé en deux signaux grâce à un coupleur

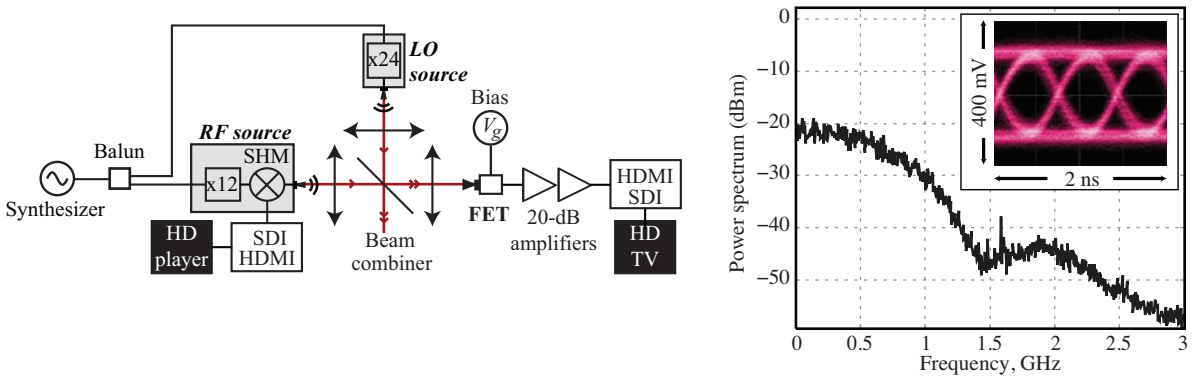

FIGURE 6.24 – Communication hétérodyne THz à 1,5 Gbps utilisant un transistor comme détecteur.
À gauche : *banc expérimental pour la réalisation d'une communication hétérodyne. Le signal transmis est une vidéo haute-définition (HD) dont le signal HDMI est adapté en signal série (SDI) avant de moduler directement le mixeur harmonique du second ordre (SHM) de la source hyperfréquences (RF). L'oscillateur local (LO) émet en continu.*
À droite : *spectre détecté avec son diagramme de l'œil associé.*

3 dB (*balun*), tel que représenté sur la Fig. 6.24, assurant ainsi une même fréquence porteuse pour les deux sources. Les deux sources n'étant pas à la même distance du récepteur, le déphasage entre les deux sources peut être ajusté en déplaçant légèrement une source (avec peu d'impact sur l'alignement grâce aux cornets) ou en ajustant légèrement la fréquence du synthétiseur. Nous avons ainsi montré (R:2) qu'une communication à 1,5 Gbps autour de 300 GHz était possible avec une puissance source de seulement 10 μW dans une configuration hétérodyne avec un oscillateur local de puissance supérieur à 100 μW. Cette communication a été prouvée par la transmission d'un signal vidéo HD en temps réel et non compressé dont le spectre en sortie de récepteur est présenté Fig. 6.24. Cette communication a été possible avec le détecteur commercial GaAs dans son cornet sans masse flottante, mais aussi avec le nano-transistor InGaAs avec antenne *slot-ring* réalisé à l'IEMN.

Nous noterons enfin l'expérience menée par G. Ducournau à l'IEMN avec un récepteur commercial hétérodyne à 600 GHz. L'hétérodynage assure ici aussi la faisabilité de la communication malgré la faible puissance incidente (10 nW à 600 GHz issus d'une photodiode UTC), avec cette fois la mise en œuvre d'une synchronisation indirecte simple mais ingénieuse basée sur un désaccord spectral imposé autour de 10 GHz entre les deux sources, et un détecteur d'enveloppe autour de 10 GHz en sortie de récepteur pour récupérer les données en bande de base (R:6).

Ces démonstrations montrent que les communications térahertz peuvent être réalisées à très faibles puissances dans des configurations hétérodynes, ouvrant des perspectives concrètes en termes de réalité applicative, notamment pour la téléphonie mobile. En terme d'intégration de détecteur, ces résultats orientent aussi les recherches vers des détecteurs avec oscillateur local intégré.

Chapitre 7

Projet de recherche

Dans la continuité des travaux effectués jusqu'à présent, je vais ici présenter comment s'articule mon projet de recherche pour les prochaines années, avec deux axes forts, principalement autour des **sources THz par photo-mélange** et des **détecteurs THz pour les communications**, ainsi que des projets plus exploratoires orientés vers le **THz pour l'agronomie**.

7.1 Sources THz

En termes d'applications THz, le verrou majeur reste la disponibilité de sources flexibles, à la fois bas-coût, compactes, accordables, éventuellement cohérentes et surtout puissantes. Comme nous l'avons détaillé dans la synthèse des travaux effectués, nous avons démontrer des performances inégalées dans la réalisation d'un laser bi-fréquences pour l'émission THz (R:1), avec un accordabilité par saut de 50 à 700 GHz avec une même structure, et des puissances limitées par la saturation de la photodiode UTC. Puisqu'il existe des sources électroniques plus compactes et plus puissantes à basse fréquences, par exemple des diodes Gunn émettant plusieurs dizaines de mW disponibles à 100 GHz, nous allons explorer comment décaler la plage d'accordabilité à plus hautes fréquences, mais aussi comment augmenter considérablement la puissance de sortie, afin d'offrir in fine des sources plus puissantes et accordables dans la gamme d'intérêt, soit 300 GHz – quelques THz.

7.1.1 Contexte de travail

Les travaux sur les sources THz s'intègrent dans la thématique VeCSEL de l'équipe TEHO, du département *Photonique & Ondes* du laboratoire. Ces travaux reposent sur l'expertise avérée d'Arnaud Garnache sur les structures VeCSEL, sur la maîtrise de la fabrication des structures semi-conductrices fabriquées dans le cadre de collabora-

tions avec le C2N (équipe d'Isabelle Sagnes), sur l'expertise indéniable de Mikhaël Myara en terme de métrologie optoélectronique, et sur les compétences et l'équipement THz que j'ai pu acquérir ces dernières années, avec une courbe d'apprentissage accélérée grâce aux compétences en hyperfréquences de Philippe Nouvel et Annick Pénarier qui ont complété celles que j'avais pu acquérir de l'autre côté du fossé (*gap*) THz, i.e. dans le domaine optique. À ce contexte déjà favorable au développement de sources THz par photo-mélange et à leur caractérisation fine, s'ajoutent des collaborations essentielles, que ce soit côté applicatif avec Innoptics, ou encore en termes de perspectives de recherche avec V. Roncin (LPL) pour l'asservissement de la source THz, V. Apostopoulos de l'Univ. de Southampton (UK) pour les sources impulsionnelles, ou avec M. Jarrahi de l'UCLA (CA, USA) pour l'émission forte puissance à base d'antennes photo-conductrices plasmoniques. Enfin, cette dernière collaboration sera catalysée par le récent recrutement de K. Maussang au sein du laboratoire, issu du LPA, compte tenu de son expertise sur les antennes photo-conductrices.

7.1.2 Accordabilité du battement THz

Origines physiques de l'accordabilité

À court terme, mon premier objectif de recherche consiste à identifier l'origine physique de la plage d'accordabilité étendue de la structure VeCSEL présentée précédemment. En effet, nous nous attendions, de par la dérive spectrale du filtre intra-cavité du VeCSEL avec le gradient de température radial induit par le pompage optique, à une accordabilité plus restreinte de la fréquence de battement. Si l'extension de cette plage d'accordabilité est la bienvenue, il reste nécessaire de déterminer son origine physique afin de mieux la maîtriser voire l'exploiter de manière plus étendue. Parmi les pistes attendues, je pense que l'effet Kerr a un rôle à jouer dans cet effet, sous une de ses multiples formes, que ce soit une augmentation isotrope transverse de l'indice optique amenant à une augmentation de l'intervalle spectral libre, que ce soit une augmentation anisotrope dans l'espace transverse amenant à un effet de lentille thermique, ou tout autres effets combinés qui restent à explorer.

Au cours de la thèse de R. Paquet, nous avons aussi identifié un design alternatif de la structure VeCSEL bi-fréquence qui offre des plages d'accordabilité plus importantes, et notamment des fréquences de battement allant jusqu'à plusieurs THz. Ce design s'affranchit de la micro-cavité par le dépôt d'une couche anti-reflet à la surface du demi-VeCSEL avant dépôt du masque d'amplitude. La fréquence de battement ne dépend alors plus du filtre passe-bande associé, et ouvre la plage d'accordabilité du battement sur l'intégralité de la courbe de gain. Nous avons pu montrer que l'ordre

de grandeur de la différence de fréquence dépend alors du remplissage de bande différentiel pour les puits quantiques vus par chacun des modes transverses. Les pertes imposées à chaque mode, de manière contrôlée par le design du masque d'amplitude, induisent un fonctionnement du puits quantique en régime laser à un niveau d'inversion différent. Compte tenu du décalage spectral de la courbe de gain associé au remplissage de bande, il apparaît une opération à des différences de fréquences importantes pour le laser, offrant ainsi la possibilité d'une émission THz à plus hautes fréquences, ce de manière contrôlée par le design du masque de pertes. Un inconvénient majeur réside cependant dans la plus grande difficulté à faire opérer le laser sur deux modes longitudinaux, au lieu de deux paquets de modes, car l'absence de filtrage spectral laisse libre cours au mélange à quatre ondes dans la structure. À court terme, une partie de mes recherches sera ainsi consacrée à l'étude de cette configuration laser, avec comme objectif le contrôle des fréquences d'oscillation des deux modes transverses, l'étude de l'accordabilité par ajustement de la longueur de cavité, et la recherche de solutions originales pour assurer une opération monomode longitudinale robuste de chaque mode transverse.

Translation spectrale de la fenêtre d'accordabilité

Un autre axe de recherche initié dans la cadre de la thèse de B. Chomet consiste en la réalisation de masques de phase micro-structurés à la surface du VeCSEL. Des premières observations montrent en effet que si nous déposons une couche de SiN à la surface du VeCSEL, couche micro-structurée dans sa périphérie (autour de l'axe optique) de sorte que l'indice effectif soit plus faible pour le mode d'ordre transverse plus élevé que le mode fondamental, il est alors possible d'imposer une différence de fréquence plus importante pour les deux modes transverses, et ainsi translater spectralement la plage d'accordabilité du laser bi-fréquence. Ces études feront aussi partie de mon programme de recherche à court terme, et seront couplées aux études sur l'origine physique de l'accordabilité.

7.1.3 Asservissement de la source THz

Nous avons montré une émission THz cohérente en sortie de photo-diode UTC, avec une caractérisation fine de la cohérence basée sur la mesure du spectre de bruit de fréquence THz. Si ces premiers résultats sont d'ores et déjà très satisfaisants, il restent environ de quatre ordres de grandeur supérieurs au bruit de fréquence d'une source commerciale par multiplication de fréquence, notamment dans la gamme de fréquence de la boucle à verrouillage de phase des synthétiseurs injectés en entrée de la chaîne de multiplication. Considérant, pour la source photonique étudiée, la fréquence de travail initiale (centaines de THz) et le fait que le laser soit en fonctionnement libre, la

cohérence est certes remarquable, mais devrait pouvoir être grandement améliorée par un asservissement adéquat, comme nous le proposons par la suite.

Asservissement des diodes de pompe

Pour le laser bi-fréquence, la cohérence est a priori principalement limitée par le bruit thermique, issu des instabilités en puissance du bruit de pompe, le bruit mécanique étant a priori grandement diminué de par le principe même d'une unique cavité optique pour les deux modes lasers. L'asservissement de l'intensité des diodes de pompe apparaît ainsi essentiel pour gagner en cohérence, et correspond pleinement aux travaux initiés par M. Myara et A. Garnache en collaboration avec Innoptics, dans le cadre du développement de sources VeCSELs mono-fréquence de haute pureté pour la spectroscopie. Les retombées de ces études seront ainsi bénéfiques pour mon axe de recherche centré sur le fonctionnement bi-fréquence du VeCSEL, et il sera évident à terme d'évaluer l'amélioration de la cohérence du signal THz avec asservissement de la diode de pompe.

Asservissement du battement THz

Dans le cadre d'une collaboration naissante avec le Laboratoire de Physique des Lasers (Univ. Paris 13), je souhaiterais asservir la différence de fréquence afin de gagner en cohérence et ainsi tendre vers les performances reportées avec le laser bi-fréquence asservi fonctionnant sur deux modes de polarisation [17]. Contrairement à cette dernière architecture laser, il est plus difficile pour le VeCSEL fonctionnant sur deux modes transverses d'asservir indépendamment les fréquences des deux modes, car la différence de fréquence est contrôlée par la puissance de pompe, commune aux deux modes transverses. Différentes solutions restent cependant envisageables avec un degré de complexité évoluant selon le degré de cohérence souhaité in fine, ces solutions sont basées sur des déclinaisons de la technique de Pound-Drever Hall [36] et sur la stabilisation sur la raie d'absorption spectroscopique d'une cellule de gaz, ou pourraient être basées sur une méthode précédemment proposée mais jamais démontrée expérimentalement (CI:30). L'étude de systèmes d'asservissement, en collaboration avec le LPL, est ainsi un axe de recherche à moyen terme important et naturel dans la continuité des travaux effectués sur l'émission THz basée sur le VeCSEL bifréquence.

7.1.4 Valorisation

Compte tenu de la grande robustesse du fonctionnement bi-fréquence du VeCSEL (avec filtre), de sa compacité, et dans la continuité de l'intégration du VeCSEL mono-fréquence en collaboration avec Innoptics, il apparaît judicieux de valoriser les travaux

effectués en engageant un projet de maturation industrielle. Un projet de maturation initiale a ainsi été financé par AxLR, et a permis de déterminer les verrous associés à la solution proposée pour l'émission THz. Afin de faciliter toute possible maturation, je souhaite développer deux axes de travail, technologique et applicatif.

Migration technologique vers la bande C

Afin notamment de répondre aux demandes industrielles, mais aussi d'offrir plus de puissance THz grâce à l'utilisation de photo-mélangeurs plus efficaces à 1550 nm qu'à 1064 nm, il me semble utile de tenter de reproduire le concept bi-fréquence basé sur le fonctionnement de deux modes transverses dans un VeCSEL sur une nouvelle technologie semi-conductrice. Quelques équipes ont montré qu'il était possible de réaliser des VeCSELs à 1550 nm en utilisant des puits quantiques en InP reportés sur GaAs par *water fusion* [37]. Si la puissance optique attendue est d'un ordre de grandeur inférieure, la puissance THz ne serait pas nécessairement impactée compte tenu des puissances de saturation des photo-mélangeurs, et l'intégration d'un amplificateur optique dans un système industriel permettrait sinon d'offrir une alternative intéressante aux sources THz actuelles, en terme de coût, de compacité et de fonctionnalités.

Démonstrations applicatives

D'un point de vue purement applicatif, il m'apparaît intéressant de réaliser des démonstrations expérimentales applicatives basées sur le VeCSEL bifréquences développé. Lors d'une collaboration avec T-WAVE, nous avons par exemple montré qu'une telle source offrait finalement assez de puissance pour réaliser du contrôle industriel non destructif, tel que démontré Fig. 7.1.

À court terme, je souhaite démontrer que cette source peut aussi être utilisée pour la spectroscopie, avec une accordabilité par saut de mode tel que nous l'avons démontré (R:1), mais aussi en utilisant une plage d'accordabilité plus limitée (un peu moins de 100 MHz) mais continue, en changeant puissance de pompe ou température de la structure, tel que démontré dans le cadre de la thèse de R. Paquet [21]. Une telle démonstration permettrait d'initier une collaboration avec l'équipe de Gaël Mouret au LPCA, Univ. du littoral (Dunkerque).

Enfin, compte tenu des expériences menées en communications THz, l'approche photonique offre de nombreuses perspectives systèmes pour des communications très haut-débit basées sur l'utilisation du VeCSEL THz, l'objectif étant une continuité du débit télécom du réseau optique jusqu'au THz. Combiné aux détecteurs THz développés pour les télécoms, je bénéficie ainsi des composants clefs pour engager des recherches autour de cette thématique.

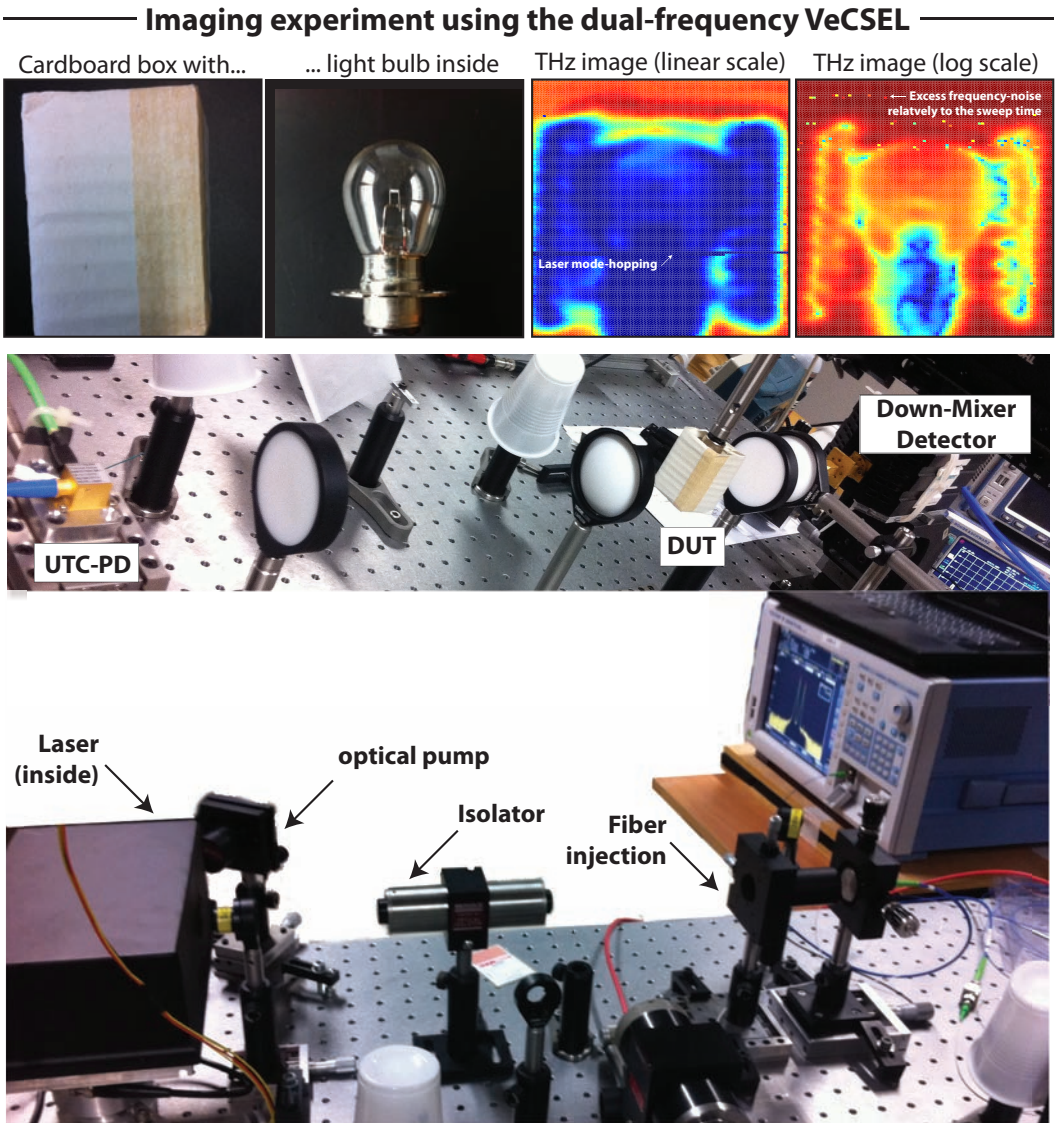

FIGURE 7.1 – Imagerie en transmission réalisée avec la source THz basée sur le VeCSEL bi-fréquence.
Nous montrons ici la faisabilité du contrôle industriel non destructif, réalisée en collaboration avec T-WAVE, par l'imagerie d'une ampoule sans la sortir de sa boîte en carton. Cet objet a été déplacé transversalement afin de mesurer la transmission avec une tête de réception commerciale hétérodyne.

7.1.5 Puissance THz

La limitation principale des sources THz photoniques étant la puissance délivrée, je souhaite engager un axe de recherche à long terme sur la réalisation de nouvelles antennes photo-conductrices, avec plusieurs axes originaux, notamment la réalisation d'antennes multi-polaires pour l'émission THz, l'intégration d'antennes photoconductrices dans la cavité laser, et la possibilité de réaliser des sources THz pulsées.

Antennes photo-conductrices plasmoniques

Afin d'augmenter la puissance THz émise pour l'émission THz continue, les antennes les plus efficaces sont celles développées par M. Jarrahi, avec des électrodes plasmoniques permettant un meilleur couplage entre la puissance optique incidente et l'antenne émettant le faisceau THz [38]. Dans le cadre d'une collaboration naissante avec l'UCLA, nous développons des antennes pour une excitation à 1064 nm, qui devraient permettre un gain de puissance THz de plusieurs ordres de grandeur à comparer à l'émission basée sur les photodiodes UTC. Outre les spécificités des antennes plasmoniques, un des challenges réside dans le choix du matériau photo-conducteur à 1064 nm. Cet axe de recherche est actuellement engagé.

Dans la continuité de cet axe de travail, nous souhaitons intégrer ces antennes dans la cavité laser, afin de bénéficier de la très grande puissance optique intra-cavité (de l'ordre du Watt pour notre VeCSEL), et ainsi offrir une source THz intégrée avec le VeCSEL, offrant encore plus de puissance. Les défis à relever pour une telle structure sont multiples, et ouvrent en même temps plusieurs perspectives. Le premier défi est de s'assurer que l'antenne induise suffisamment peu de pertes pour permettre de passer le seuil laser, tant d'un point de vue de l'absorption (souhaitable pour l'émission THz) que de la diffraction. D'autre part, de par la structure planaire des antennes photo-conductrices, il peut être nécessaire d'intégrer l'antenne sur un miroir plan, donc d'insérer intra-cavité une courbure du plan d'onde par dépôt d'une couche SiN microstructurée de manière transverse afin de réaliser un effet lentille, tel que démontré dans le cadre de la thèse de Mohammed Sellahi [39].

Enfin, l'insertion d'un élément absorbant dans la cavité peut amener à un fonctionnement pulsé à verrouillage de modes (*mode-locking*). Nous souhaitons ainsi investiguer le fonctionnement bi-fréquence pulsé du laser VeCSEL, en collaboration avec l'Univ. de Southampton, compte tenu de son expertise sur cette thématique. Nous pourrions ainsi ouvrir la voie vers de nouvelles sources THz pulsées fonctionnant à température ambiante, mais les défis à relever pour assurer un fonctionnement stable du VeCSEL sont nombreux, faisant de fait cet axe de recherche un axe à long terme.

Réseaux d'antennes photo-conductrices plasmoniques

Afin d'augmenter la puissance THz, une solution consiste aussi à multiplier les antennes, à l'image des réseaux de nano-antennes couplés à des lasers à cascade quantiques [40] ou des émetteurs multiplexés basés sur l'effet photo-Dember [41]. L'approche que je souhaite développer est l'intégration d'antennes photo-conductrices multipolaires telles que celles réalisées en hyperfréquences [42]. Une telle géométrie d'antenne semble judicieuse compte tenu du profil transverse du VeCSEL bi-fréquence constitué de multiples lobes, 4 pour le couple de modes LG_{00}/LG_{02}, 6 pour le couple

de modes LG_{00}/LG_{03} ou 8 pour le couple LG_{00}/LG_{04} (dont l'effet laser bi-fréquence a été démontré expérimentalement dans le cadre de la thèse de R. Paquet). De tels réseaux d'antennes permettraient de plus d'envisager la possibilité de contrôler la direction du faisceau si les phases relatives des différents pôles peuvent être ajustées. Ce dernier point est aussi essentiel compte tenu du profil de phase transverse des modes de Laguerre-Gauss, une excitation directe de ce faisceau sur une antenne multi-polaire amenant nécessairement à une émission présentant un minimum de puissance au centre du faisceau THz. Un tel réseau d'antennes couplées à des électrodes plasmoniques devrait ainsi permettre d'augmenter significativement la puissance THz issue du VeCSEL bi-fréquence. Une alternative à un tel réseau d'antennes multi-polaires consisterait à exciter un réseau de photo-mélangeurs indépendants, nous souhaitons notamment évaluer la puissance disponible en excitant un réseau de photo-diodes UTC, ce en collaboration avec l'IEMN.

7.2 Détecteurs THz

7.2.1 Contexte de travail

Lors de la synthèse des travaux de recherche, j'ai montré la possibilité de réaliser des communications THz à haut-débit à l'aide de transistors intégrés (R:8), mais surtout que le potentiel des ces composants attractifs n'était pas encore complètement exploité, notamment de par les difficultés à les coupler à des antennes larges bandes pour les communications. Dans la continuité de ces études et dans le cadre de la thèse d'Isidore Diouf (2016–), avec l'appui des compétences de la plateforme Hermes-Obi-@, impliquant particulièrement Philippe Nouvel et Annick Pénarier, mais aussi avec les compétences en modélisation des composants à semi-conducteurs de Christophe Palermo et Luca Varani, je souhaite continuer l'étude des communications THz haut-débit basées sur l'utilisation de transistors comme récepteurs. Ces recherches s'appuient sur des collaborations existantes avec le laboratoire L2C ou encore l'IEMN.

7.2.2 Antennes large-bande

Malgré quelques démonstrations ponctuelles, la réalisation d'antennes large-bande pour les communications associées à un transistor pour le redressement du signal THz ne sont pas encore pleinement maîtrisées, cela compte tenu de nombreux challenges propres à chaque transistor (transistor à effet de champ, transistor bipolaire). Les difficultés résident dans le couplage entre l'antenne et le transistor, en terme d'adaptation d'impédance complexe large-bande, mais aussi en terme d'excitation de l'antenne dipolaire, l'un des deux bras de ces antennes étant généralement connecté à la masse du

transistor, dégradant de fait le gain de l'antenne et sa directivité. Le design de l'antenne est aussi particulièrement délicat compte tenu du fort indice de réfraction des substrats utilisés aux fréquences THz, j'étudie notamment l'évolution de la direction du maximum de gain du diagramme de rayonnement de l'antenne avec la fréquence, dans le cadre de la thèse d'Isidore Diouf.

7.2.3 Intégration du détecteur

L'intégration du détecteur reste aussi largement inexploitée tant d'un point de vue électronique que d'un point de vue mécanique. Sur ce premier point, j'ai engagé une étude de l'impédance complexe en sortie de transistors dans le cadre de la thèse d'Isidore Diouf. L'objectif est de déterminer pour certains détecteurs tels les transistors bipolaires, s'il est possible d'assurer une adaptation d'impédance en sortie du composant, conjointement avec une sensibilité THz, par des conditions de polarisation adéquates. Ces études doivent se reposer sur des campagnes de mesures hyperfréquences à l'analyseur de réseau, sur des campagnes de mesures sous faisceau THz, et sur des études physiques du composant avec une approche intermédiaire entre physique du composant et circuit équivalent électronique, particulièrement pour les transistors bipolaires à double hétérojonction pour lesquels nous ne bénéficions d'aucun modèle numérique abouti.

En terme d'intégration mécanique, j'ai réalisé des guides d'ondes particulièrement désignés pour permettre une meilleure intégration mécanique du composant, et ainsi augmenter de manière significative la sensibilité d'un transistor intégré. Selon les perspectives collaboratives et financières, j'espère pouvoir évaluer la sensibilité d'un composant intégré à l'image des diodes Schottky, afin de déterminer l'ultime sensibilité de ces composants en détection THz, particulièrement pour les applications télécoms.

7.3 THz pour l'agronomie

Compte tenu de l'environnement scientifique local à l'Université de Montpellier, j'ai engagé un axe de recherche exploratoire en collaboration avec l'équipe de C. Romieu à l'INRA, sur la spectroscopie térahertz pour l'agronomie. L'objectif de ce projet initié est d'évaluer la faisabilité d'une analyse non destructive des plantes, afin d'aider à la compréhension des phénomènes physiologiques associés à la croissance d'une baie de raisin en particulier, l'analyse des spectres de transmission THz apportant des informations complémentaires aux techniques traditionnelles (e.g. spectroscopie infrarouge) tel que démontré par certaines équipes [43–45]. La collaboration avec l'INRA est particulièrement intéressante par leur expertise sur les micro-vignes, dont l'intérêt est de bénéficier 9 mois sur 12 de baies de raisin à des différents degrés de maturité

sur un même pied. Suite à un financement du Labex *Numev* obtenu en 2015, j'ai initié des mesures de transmission spectroscopique d'extraits de baies de raisins fournis par l'INRA, en collaboration avec l'Université de Bordeaux pour des mesures en spectroscopie temporelle (TDS). En termes de spectroscopie continue, ces études peuvent recouper celles sur la source THz, voire sur les détecteurs THz pour des études temporelles dynamiques. Ces recherches s'impliqueront naturellement dans une dynamique orientée vers l'agronomie et le vivant suite à l'obtention récente de la labellisation Initiatives - Science - Innovation - Territoires - Économie (iSITE) de l'Université de Montpellier (*MUSE*).

Troisième partie

Publications

Chapitre 8

Dépôts de brevets (11)

Nous remarquons dans la liste suivante que **11** brevets ont été déposés.

(B-1) A. Garnache, M. Myara, S. Blin, I. Sagnes, G. Beaudoin, M. Sellahi, and R. Paquet, "Dual-frequency Vertical External Cavity Surface Emitting Laser device for THz generation and method for generating THz", brevet FR3025948 publié le 18/03/2016

(B-2) L. Tohme, L. Varani, P. Nouvel, A. Song, C. Daher, S. Blin, J. Grahn, J. Torres, J. Mateos, and C. Gaquière, "Device and method for direct demodulation of signals with carrier frequencies up to the THz range", brevet EP2731264 A1 publié le 14/05/2014

(B-3) P. Le Bars, W. Sahyoun, W. Knap, D. Coquillat, F. Teppe, P. Nouvel, L. Tohme, A. Pénarier, and S. Blin, "FET terahertz detector with large bandwidth and large dynamic range", brevet GB2516884 publié le 11/02/2015

(B-4) P. Le Bars, W. Sahyoun, S. Blin, P. Nouvel, and A. Plagellat, "Automatic gain control in THz plasmonic detector AC loop", brevet GB1521476.0 déposé le 4 décembre 2015 (pending status)

(B-5) P. Le Bars, A. Pénarier, P. Nouvel, S. Blin, F. Cano, and T. Cohen, "Low complexity Terahertz detector", brevet GB1320291.6 déposé le 18 novembre 2013 (terminated before grant)

(B-6) W. Sahyoun, P. Le Bars, A. Pénarier, P. Nouvel, S. Blin, and L. Tohme, "Plasma FET-based clock recovery", brevet GB1322292.2, déposé le 17 décembre 2013 (terminated before grant)

(B-7) W. Sahyoun, P. Le Bars, A. Pénarier, P. Nouvel, S. Blin, and A. Hoffmann, " Electromagnetic wave detector", 2013, brevet GB1322784.8, déposé le 20 Décembre 2013 (terminated before grant)

(B-8) J.-F. Digonnet, H. K. Kim, S. Blin, V. Dangui, and G. Kino, "Optical sensor utilizing hollow-core photonic bandgap fiber with low phase thermal constant", US

Patent initial application 20080030741, now published under US Patent number 7,911,620

(B-9) S. Blin, M. Thual, T. N. Nguyen, D. M. Nguyen, P. Rochard, and T. Chartier, "Procédé et système d'observation de modes transverses d'un guide optique", Brevet numéro FR 2945637 publié le 19/11/2010.

(B-10) S. Blin, M. Digonnet, G. Kino, and S. Lloyd, "Low-noise fiber-optic sensor utilizing a laser source", US Patent 8,289,521

(B-11) J.-F. Cliche, M. Tetu, F. Baribeau, S. Blin, and N. Guy, "Narrow linewidth semiconductor laser device", US Patent 7,471,710

Chapitre 9

Liste des publications indexées

La liste des publications indexées présente :

— **26** articles de revues internationales à comité de lecture,

— **39** conférences internationales à comité de lecture dont 6 invitées,

— **13** conférences nationales à comité de lecture,

— **11** brevets,

— **15** conférences dans le cadre de groupement de recherches (GDR) ou de workshops.

En lecture électronique, il est possible de cliquer sur chaque article de revue et conférence internationale pour accéder au lien DOI [1] associé en ligne.

9.1 Articles de revues internationales à comité de lecture (RI:1–26)

(R:1) S. Blin, R. Paquet, M. Myara, B. Chomet, L. Le Gratiet, M. Sellahi, G. Beaudoin, I. Sagnes, G. Ducournau, P. Latzel, J.-F. Lampin, and A. Garnache, "Coherent and tunable THz emission driven by an integrated III–V semiconductor laser," *IEEE Journal of Selected Topics in Quantum Electronics*, vol. 23, no. 4, pp. 1–11, 2017.

(R:2) S. Blin, P. Nouvel, A. Pénarier, and J. Hesler, "Terahertz heterodyne communication using GaAs field-effect transistor receiver," *IEEE Electron Device Letters*, vol. 38, no. 1, pp. 20–23, 2017.

(R:3) D. Coquillat, V. Nodjiadjim, S. Blin, A. Konczykowska, N. Dyakonova, C. Consejo, P. Nouvel, A. Pénarier, J. Torres, D. But, S. Ruffenach, F. Teppe, M. Riet, A. Muraviev, A. Gutin, M. Shur, and W. Knap, "High-speed room temperature terahertz

1. DOI: *Digital Object Identifier*

detectors based on InP double heterojunction bipolar transistors," *International Journal of High Speed Electronics and Systems*, vol. 25, p. 1640011, 2016.

(R:4) S. Nahar, M. Shafee, S. Blin, A. Pénarier, P. Nouvel, D. Coquillat, A. M. Safwa, W. Knap, and M. M. Hella, "Wide modulation bandwidth terahertz detection in 130 nm CMOS technology," *The European Physical Journal Applied Physics*, vol. 76, no. 2, p. 20101, 2016.

(R:5) R. Paquet, S. Blin, M. Myara, L. Le Gratiet, M. Sellahi, B. Chomet, G. Beaudoin, I. Sagnes, and A. Garnache, "Coherent continuous-wave dual-frequency high-Q external-cavity semiconductor laser for GHz–THz applications," *Optics Letters*, vol. 41, no. 16, pp. 3751–3754, 2016.

(R:6) G. Ducournau, F. Pavanello, A. Beck, L. Tohme, S. Blin, P. Nouvel, E. Peytavit, M. Zaknoune, P. Szriftgiser, and J.-F. Lampin, "High-definition television transmission at 600 GHz combining THz photonics hotspot and high-sensitivity heterodyne receiver," *Electronics Letters*, vol. 50, no. 5, pp. 413–415, 2014.

(R:7) L. Tohmé, S. Blin, G. Ducournau, P. Nouvel, D. Coquillat, S. Hisatake, T. Nagatsuma, A. Pénarier, L. Varani, W. Knap, and J.-F. Lampin, "Terahertz wireless communication using GaAs transistors as detectors," *Electronics Letters*, vol. 50, no. 4, p. 323, 2014.

(R:8) S. Blin, L. Tohme, D. Coquillat, S. Horiguchi, Y. Minamikata, S. Hisatake, P. Nouvel, T. Cohen, A. Penarier, F. Cano, L. Varani, W. Knap, and T. Nagatsuma, "Wireless communication at 310 GHz using GaAs High-Electron-Mobility Transistors for detection," *Journal of Communications and Networks*, vol. 15, no. 6, pp. 559–568, 2013.

(R:9) W. Knap, S. Rumyantsev, M. Vitiello, D. Coquillat, S. Blin, N. Dyakonova, M. Shur, F. Teppe, A. Tredicucci, and T. Nagatsuma, "Nanometer size field effect transistors for terahertz detectors," *Nanotechnology*, vol. 24, no. 21, p. 214002, 2013.

(R:10) R. Sharma, T. Laurent, J. Torres, P. Nouvel, S. Blin, L. Varani, Y. Cordier, M. Chmielowska, J.-P. Faurie, and B. Beaumont, "Terahertz transmission and effective gain measurement of two-dimensional electron gas," *Physica Status Solidi (a)*, vol. 210, no. 7, pp. 1454–1458, 2013.

(R:11) S. Blin, F. Teppe, L. Tohme, S. Hisatake, K. Arakawa, P. Nouvel, D. Coquillat, A. Pénarier, J. Torres, L. Varani, W. Knap, and T. Nagatsuma, "Plasma-wave detectors for terahertz wireless communication," *IEEE Electron Device Letters*, vol. 33, no. 10, pp. 1354–1356, 2012.

(R:12) P. Nouvel, J. Torres, S. Blin, H. Marinchio, T. Laurent, C. Palermo, L. Varani, P. Shiktorov, E. Starikov, V. Gruzinskis, F. Teppe, Y. Roelens, A. Shchepetov, and

S. Bollaert, "Terahertz emission induced by optical beating in nanometer-length field-effect transistors," *Journal of Applied Physics*, vol. 111, no. 10, p. 103707, 2012.

(R:13) D. M. Nguyen, S. Blin, T. N. Nguyen, S. D. Le, L. Provino, M. Thual, and T. Chartier, "Modal decomposition technique for multimode fibers," *Applied Optics*, vol. 51, no. 4, pp. 450–456, 2012.

(R:14) T. Laurent, R. Sharma, J. Torres, P. Nouvel, S. Blin, L. Varani, Y. Cordier, M. Chmielowska, S. Chenot, J.-P. Faurie, B. Beaumont, P. Shiktorov, E. Starikov, V. Gruzinskis, V. V. Korotyeyev, and V. A. Kochelap, "Voltage-controlled sub-terahertz radiation transmission through GaN quantum well structure," *Applied Physics Letters*, vol. 99, no. 8, p. 082101, 2011.

(R:15) T. Laurent, R. Sharma, J. Torres, P. Nouvel, S. Blin, C. Palermo, L. Varani, Y. Cordier, M. Chmielowska, J.-P. Faurie, B. Beaumont, P. Shiktorov, E. Starikov, V. Gruzinskis, V. V. Korotyeyev, and V. A. Kochelap, "Measurement of pulsed current–voltage characteristics of AlGaN/GaN HEMTs from room temperature to 15 K," *Acta Physica Polonica A*, vol. 119, no. 2, pp. 196–198, 2011.

(R:16) T. Laurent, R. Sharma, J. Torres, P. Nouvel, S. Blin, L. Chusseau, C. Palermo, L. Varani, Y. Cordier, M. Chmielowska, S. Chenot, J.-P. Faurie, B. Beaumont, P. Shiktorov, E. Starikov, V. Gruzinskis, V. V. Korotyeyev, and V. A. Kochelap, "Voltage controlled terahertz transmission enhancement through GaN quantum wells," *Acta Phys. Polonica A*, vol. 119, no. 2, pp. 196–198, 2011.

(R:17) M. Thual, D. M. Nguyen, S. D. Le, T. Chartier, P. Rochard, C. Bastianelli, J. Troles, Q. Coulombier, D. Méchin, L. Brilland, T. N. Nguyen, and S. Blin, "Recent advances on low loss and highly nonlinear AsSe suspended core photonic crystal optical fibers," *Journal of Science and Technology*, vol. 1, no. 1, pp. 1–13, 2010.

(R:18) S. Blin, O. Vaudel, P. Besnard, and R. Gabet, "Power-or frequency-driven hysteresis for continuous-wave optically injected distributed-feedback semiconductor lasers," *Optics Express*, vol. 17, no. 11, pp. 9288–9299, 2009.

(R:19) M. Digonnet, S. Blin, H. K. Kim, V. Dangui, and G. Kino, "Sensitivity and stability of an air-core fibre-optic gyroscope," *Measurement Science and Technology*, vol. 18, no. 10, p. 3089, 2007.

(R:20) S. Blin, M. J. Digonnet, and G. S. Kino, "Noise analysis of an air-core fiber optic gyroscope," *IEEE Photonics Technology Letters*, vol. 19, no. 19, pp. 1520–1522, 2007.

(R:21) S. Blin, H. K. Kim, M. J. Digonnet, and G. S. Kino, "Reduced thermal sensitivity of a fiber-optic gyroscope using an air-core photonic-bandgap fiber," *Journal of Lightwave Technology*, vol. 25, no. 3, pp. 861–865, 2007.

(R:22) S. Blin, M. Bishop, K. Parameswaran, M. J. Digonnet, and G. S. Kino, "Pickup suppression in sagnac-based fiber-optic acoustic sensor array," *Journal of Lightwave Technology*, vol. 24, no. 7, p. 2889, 2006.

(R:23) G. Stéphan, T. Tam, S. Blin, P. Besnard, and M. Têtu, "Laser line shape and spectral density of frequency noise," *Physical Review A*, vol. 71, no. 4, p. 043809, 2005.

(R:24) J. Poette, S. Blin, G. Brochu, L. Bramerie, R. Slavik, J.-C. Simon, S. LaRochelle, and P. Besnard, "Relative intensity noise of multiwavelength fibre laser," *Electronics Letters*, vol. 40, no. 12, p. 1, 2004.

(R:25) S. Blin, C. Guignard, P. Besnard, R. Gabet, G. M. Stéphan, and M. Bondiou, "Phase and spectral properties of optically injected semiconductor lasers," *Comptes Rendus Physique*, vol. 4, no. 6, pp. 687–699, 2003.

(R:26) S. Blin, G. Stéphan, R. Gabet, P. Besnard, and D. Kilper, "Amplification process in a laser injected by a narrow band weak signal," *Europhysics Letters*, vol. 52, no. 1, p. 60, 2000.

9.2 Conférences internationales avec actes et comité de lecture (CI:1–41)

Conférences internationales invitées (5)

(CI:1) A. Garnache, M. Seghilani, M. Sellahi, R. Paquet, B. Chomet, M. Myara, S. Blin, L. Legratiet, G. Beaudoin, I. Sagnes, and P. Lalanne, "Generation of new coherent light states using III-V semiconductor laser technology: Vortex, continuum, dual frequency for THz and integration," *CLEO*, 2017.

(CI:2) A. Garnache, M. Seghilani, R. Paquet, M. Sellahi, B. Chomet, M. Myara, S. Blin, I. Sagnes, G. Beaudoin, and L. Legratiet, "Generation of new spatial and temporal coherent light states using III-V semiconductor laser technology: Vortex, continuum, dual frequency for THz," in *SPIE LASE*, pp. 97340F–97340F, International Society for Optics and Photonics, 2016.

(CI:3) M. J.-F. Digonnet, H. K. Kim, S. Blin, V. Dangui, and G. S. Kino, "Sensitivity and stability of an air-core fiber-optic gyroscope," *Optical Fiber Sensors (OFS)*, 2006.

(CI:4) P. Besnard, S. Blin, O. Vaudel, and S. LaRochelle, "Optical injection in semiconductor or fiber lasers: a comparison, the influence of coherence," *Photonics Europe*, 2004.

(CI:5) S. Blin, G. M. Stephan, R. Gabet, P. Féron, F. Lissillour, and P. Besnard, "Injected semiconductor laser," *Nonlinear Optical Phenomena and Nonlinear Dynamics of Optical Systems (ICONO)*, 2001.

Conférences internationales régulières (CI:1–36)

(CI:6) A. Bassli, A. Pénarier, S. Blin, P. Nouvel, A. Benbassou, and J. Belkadid, " Reflectometer THz for imaging 3D at 100 GHz," *International conference on Wireless technologies, embedded and intelligent system (WITS)*, 2017.

(CI:7) R. Paquet, B. Chomet, S. Blin, M. Myara, G. Beaudoin, I. Sagnes, L. Varani, and A. Garnache, "Coherent and tunable THz source," *International Conference on Noise and Fluctuations (ICNF)*, 2017.

(CI:8) L. Varani, N. Dyakonova, D. Coquillat, D. But, S. Blin, V. Nodjiadjim, A. Konczykowska, C. Consejo, F. Teppe, W. Knap, and M. Riet, "Reduction of Noise Equivalent Power in Terahertz Detector Based on InP Double Heterojunction Bipolar Transistors by Biasing the Collector," *International Conference on Noise and Fluctuations (ICNF)*, 2017.

(CI:9) R. Paquet, S. Blin, M. Myara, L. L. Gratiet, M. Sellahi, B. Chomet, F. Pavanello, P. Latzel, G. Ducournau, I. Sagnes, G. Beaudoin, and A. Garnache, "Coherent THz generation based on a novel dual-frequency III-V semiconductor laser," *International Conference on Infrared, Millimeter, and Terahertz waves (IRMMW-THz)*, 2016.

(CI:10) A. Mahi, C. Palermo, H. Marinchio, A. Belgachi, S. Blin, and L. Varani, "Analysis of THz detection saturation processes in InGaAs-based HEMTs," *International Conference on Infrared, Millimeter, and Terahertz waves (IRMMW-THz)*, 2016.

(CI:11) S. Nahar, S. Blin, A. Pénarier, D. Coquillat, W. Knap, and M. M. Hella, "Characterization of integrated antenna-coupled plasma-wave detectors with wide bandwidth amplification in 130nm CMOS," *IEEE MTT-S International Microwave Symposium (IMS)*, 2015.

(CI:12) S. Nahar, S. Blin, A. Pénarier, P. Nouvel, D. Coquillat, W. Knap, and M. M. Hella, "Plasmonic detection of wide band modulated THz radiations in GaAs technology," *International Conference on Infrared, Millimeter, and Terahertz waves (IRMMW-THz)*, 2015.

(CI:13) R. Paquet, M. Sellahi, S. Blin, M. Myara, I. Sagnes, G. Beaudoin, and A. Garnache, "Vertical-external-cavity surface-emitting laser for THz generation," *International Conference on Infrared, Millimeter, and Terahertz waves (IRMMW-THz)*, 2014.

(CI:14) G. Ducournau, F. Pavanello, A. Beck, L. Tohme, S. Blin, P. Nouvel, E. Peytavit, M. Zaknoune, P. Szriftgiser, and J. F. Lampin, "600 GHz HD-TV transmission combining UTC-PD and heterodyne receiver," *International Conference on Infrared, Millimeter, and Terahertz waves (IRMMW-THz)*, 2014.

(CI:15) W. Knap, D. B. But, N. Dyakonova, D. Coquillat, A. Gutin, O. Klimenko, S. Blin, F. Teppe, M. Shur, T. Nagatsuma, S. D. Ganichev, and T. Otsuji, "Recent results on

broadband nanotransistor based THz detectors," in *THz and Security Applications*, pp. 189–209, Springer Netherlands, 2014.

(CI:16) L. Tohme, G. Ducournau, S. Blin, D. Coquillat, P. Nouvel, A. Pénarier, W. Knap, and J. F. Lampin, "0.2 THz wireless communication using plasma-wave transistor detector," *International Conference on Infrared, Millimeter, and Terahertz Waves (IRMMW-THz)*, 2013.

(CI:17) L. Tohme and S. Blin and P. Nouvel and L. Varani and A. Penarier, "Room-temperature terahertz heterodyne mixing in GaAs commercial transistors," *International Conference on Infrared, Millimeter, and Terahertz Waves (IRMMW-THz)*, 2013.

(CI:18) D. Coquillat, Y. Kurita, K. Kobayashi, F. Teppe, N. Dyakonova, C. Consejo, D. But, L. Tohme, P. Nouvel, S. Blin, J. Torres, A. Pénarier, T. Otsuji, and W. Knap, "Contribution of the gate leakage current to terahertz detection by asymmetric dual-grating gate HEMT structures," *International Conference on Infrared, Millimeter, and Terahertz Waves (IRMMW-THz)*, 2013.

(CI:19) M. Sellahi, M. Myara, I. Sagnes, S. Ban, and A. Garnache, "Generation of single frequency highly coherent high-order laguerre gaussian modes with vertical-external-cavity-surface-emitting-laser," *Conference on Lasers Electro-Optics Europe International Quantum Electronics Conference (CLEO EUROPE/IQEC)*, 2013.

(CI:20) L. Tohmé, S. Blin, P. Nouvel, A. Pénarier, J. Torres, L. Varani, G. Ducournau, P. Artillan, S. Bollaert, Y. Roelens, D. Coquillat, D. But, W. Knap, and F. Teppe, "Signal-to-noise ratio in terahertz wireless communication using field-effect-transistors as detectors," *International Conference on Noise and Fluctuations (ICNF)*, pp. 1–3, June 2013.

(CI:21) W. Knap, D. But, N. Diakonova, D. Coquillat, M. Vitiello, S. Blin, A. El Fatimy, F. Teppe, A. Tredicucci, T. Nagatsuma, and S. Ganichev, "Nanotransistor based THz plasma detectors: low tempeatures, graphene, linearity, and circular polarization studies," in *SPIE Optical Engineering+ Applications*, pp. 88460M–88460M, International Society for Optics and Photonics, 2013.

(CI:22) A. Penot, J. Torres, T. Laurent, R. Sharma, P. Nouvel, S. Blin, L. Varani, W. Knap, Y. Codier, M. Chmielowska, S. Chenot, J.-P. Faurie, B. Beaumont, P. Shiktorov, E. Starikov, V. Gruzinskis, V. V. Korotyeyev, and V. A. Kochelap, "THz transmission modulated by a dc-bias through GaN quantum well structure," *Proc. SPIE*, vol. 8261, pp. 826111–826111–7, 2012.

(CI:23) F. Teppe, S. Blin, D. Coquillat, N. Dyakonova, L. Tohme, B. Chenaud, S. Hisatake, K. Arakawa, J. Torres, C. Consejo, P. Nouvel, P. Solignac, A. Pénarier, T. Nagatsuma, and W. Knap, "Plasma wave detectors for terahertz wireless communica-

tion and fast imaging applications," *International Conference on Infrared, Millimeter, and Terahertz Waves (IRMMW)*, 2012.

(CI:24) L. Tohme, S. Blin, P. Nouvel, J. Torres, J. Wang, K. Tse, K. Chu, Y. Chan, C. Palermo, and L. Varani, "Long-term memory effects in photo-excited InGaAs high-electron-mobility- transistors," *Proc. of the International Conference on Electron Dynamics In Semiconductors, Optoelectronics and Nanostructures (EDISON)*, pp. 7–12, 2011.

(CI:25) T. Laurent, R. Sharma, A. Penot, J. Torres, P. Nouvel, S. Blin, C. Palermo, L. Varani, Y. Cordier, M. Chmielowska, S. Chenot, J.-P. Faurie, B. Beaumont, E. Starikov, P. Shiktorov, V. Gružinskis, V. Korotyeyev, and V. A. Kochelap, "Voltage control of terahertz transmission through GaN quantum wells: Experiments and theory," *Proc. of the International Conference on Electron Dynamics In Semiconductors, Optoelectronics and Nanostructures (EDISON)*, pp. 5–12, 2011.

(CI:26) P. Nouvel, J. Torres, H. Marinchio, T. Laurent, S. Blin, L. Chusseau, C. Palermo, L. Varani, P. Shiktorov, E. Starikov, V. Gruzhinskis, F. Teppe, and D. Coquillat, "Measurements of THz emission from nanometric-size transistors," *International Conference on Infrared, Millimeter, and Terahertz Waves (IRMMW)*, 2010.

(CI:27) T. Laurent, R. Sharma, J. Torres, P. Nouvel, S. Blin, L. Chusseau, C. Palermo, L. Varani, Y. Cordier, M. Chmielowska, J. P. Faurie, B. Beaumont, E. Starikov, P. Shiktorov, and V. Gruzinskis, "Enhanced terahertz transmission of GaN quantum wells," *International Conference on Infrared, Millimeter, and Terahertz Waves (IRMMW)*, 2010.

(CI:28) H. Marinchio, C. Palermo, G. Sabatini, P. Ziadé, P. Shiktorov, E. Starikov, V. Gružinskis, T. Laurent, P. Nouvel, J. Torres, A. Pénarier, S. Blin, L. Chusseau, and L. Varani, "Hydrodynamic simulation of heterodyne terahertz detection in a field effect transistor," *International Conference on Infrared, Millimeter, and Terahertz Waves (IRMMW)*, 2010.

(CI:29) H. Marinchio, C. Palermo, G. Sabatini, P. Ziadé, T. Laurent, P. Shiktorov, E. Starikov, V. Gružinskis, P. Nouvel, J. Torres, A. Pénarier, S. Blin, L. Chusseau, and L. Varani, "Hydrodynamic study of electronic, optical and thermal excitation of plasma waves in HEMTs," *International Conference on Infrared, Millimeter, and Terahertz Waves (IRMMW)*, 2010.

(CI:30) T. Laurent, S. Ginestar, S. Blin, L. Chusseau, J. Torres, P. Nouvel, C. Palermo, and L. Varani, "Frequency stabilization of photo-mixing generated signal using a single michelson interferometer," *International Conference on Infrared, Millimeter, and Terahertz Waves (IRMMW)*, 2010.

(CI:31) D. M. Nguyen, T. N. Nguyen, S. Blin, M. Thual, and T. Chartier, "Scalar product technique in modal decomposition for multimode fibers," *Proc. SPIE*, vol. 7717, pp. 77170V–77170V–10, 2010.

(CI:32) S. Blin, T. N. Nguyen, D. M. Nguyen, P. Rochard, L. Provino, A. Monteville, T. Robin, A. Mugnier, B. Cadier, D. Pureur, M. Thual, and T. Chartier, "New methods for modal decomposition in multi-mode fibres," *Proc. SPIE*, vol. 7503, pp. 750346–750346–4, 2009.

(CI:33) S. Blin, D. M. Nguyen, T. N. Nguyen, L. Provino, M. Thual, and T. Chartier, "Simple modal analysis method for multi-mode fibers," *European Conference on Optical Communication*, 2009.

(CI:34) S. Blin, L. Provino, N. Traynor, A. Mugnier, D. Pureur, and T. Chartier, "Design of all-solid photonic-bandgap fibers for Raman-free propagation," *European Conference on Lasers and Electro-Optics and the European Quantum Electronics Conference (CLEO/Europe - EQEC 2009)*, 2009.

(CI:35) S. Blin, M. J. F. Digonnet, and G. S. Kino, "Fiber-optic gyroscope operated with a frequency-modulated laser," *Proc. SPIE*, vol. 7004, pp. 70044X–70044X–4, 2008.

(CI:36) S. Blin, M. Bishop, K. Parameswaran, M. J. Digonnet, and G. S. Kino, "Pickup suppression in Sagnac-based fiber-optic acoustic sensor array," *Proc. SPIE*, vol. 6004, pp. 600407–600407–11, 2005.

(CI:37) Y. G. Boucher, S. Blin, P. Besnard, and G. M. Stephan, "Generalized transfer function of a single-mode semiconductor laser across threshold: a self-consistent analysis," *Proc. SPIE*, vol. 5452, pp. 654–665, 2004.

(CI:38) S. Blin, O. Vaudel, G. M. Stéphan, P. Besnard, T. T. Tam, and S. LaRochelle, "Measuring spectral linewidth of highly-coherent laser using optical injection," *Conference on Lasers and Electro-Optics/International Quantum Electronics Conference and Photonic Applications Systems Technologies (CLEO)*, 2004.

(CI:39) C. Guignard, S. Blin, and P. Besnard, "New scheme for the synchronisation of low dimensional chaos," *European Quantum Electronics Conference (EQEC 2003)*, p. 138, 2003.

(CI:40) S. Blin, C. Palavicini, I. Castonguay, Y. Jaouen, P. Besnard, S. LaRochelle, and R. Gaber, "$\pi/2$ phase-shifted Er^{3+}-Yb^{3+} doped distributed feedback fibre laser characterisation using a phase-sensitive optical low-coherence reflectometer," *Conference on Lasers and Electro-Optics Europe (CLEO/Europe)*, p. 638, 2003.

(CI:41) S. Blin, G. Stephan, and P. Besnard, "Dependance of the frequency of an optically injected semiconductor laser," *International Quantum Electronics Conference (IQEC)*, 2002.

9.3 Conférences nationales (CN:1–13)

(CN:1) A. Pénarier, S. Blin, and P. Nouvel, "Caractérisation large bande de détecteurs THz," *Journées Nano, Micro et Optoelectronique (JNMO)*, 2016.

(CN:2) S. Blin, P. B. d'Augères, L. Provino, A. Monteville, A. Mugnier, D. Pureur, N. Traynor, T. Robin, B. Cadier, and T. Chartier, "Diffusion Raman stimulée restreinte dans une fibre optique toute-solide à bande interdite photonique," *Journées Nationales d'Optique Guidée (JNOG)*, 2009.

(CN:3) S. Blin, T. N. Nguyen, D. M. Nguyen, P. Rochard, L. Provino, A. Monteville, T. Robin, A. Mugnier, B. Cadier, D. Pureur, M. Thual, and T. Chartier, "Dispositif pour l'observation et l'analyse quantitative des modes transverses d'une fibre optique," Actes des Journées Nationales d'Optique Guidée (JNOG), pp. 327–329, 2009.

(CN:4) S. Blin, A. Mugnier, D. Pureur, and T. Chartier, "Méthode spectrale quasi-statique efficace pour la modélisation en intensité de la diffusion Raman stimulée," Actes des Journées Nationales d'Optique Guidée (JNOG), pp. 389–391, 2008.

(CN:5) blin2004mesure
S. Blin, O. Vaudel, P. Besnard, T. Tam, and S. La Rochelle, "Mesure de la largeur spectrale d'un laser cohérent par injection optique," Journées Nationales d'Optique Guidée (JNOG), 2004.

(CN:6) S. Blin et al., "Mesure de la largeur spectrale d'un laser cohérent par injection optique," *Journéees scientifiques du CNFRS*, 2004.

(CN:7) J. Poëtte, S. Blin, L. Bramerie, J.-C. Simon, P. Besnard, I. Castonguay, R. Slavík, and S. LaRochelle, "Etude du bruit relatif d'intensité d'un laser multifréquence," *Actes des Journées Nationales d'Optique Guidée (JNOG)*, pp. 427–429, 2003.

(CN:8) O. Vaudel, S. Blin, and P. Besnard, "Laser soumis à forte injection optique : régime de relaxation et larges zones de bistabilité," *Actes des Journées Nationales d'Optique Guidée (JNOG)*, pp. 555–557, 2003.

(CN:9) S. Blin, R. Gabet, G. Stéphan, and P. Besnard, "Intramodal and intermodal mapping of a semiconductor laser with optical injection," *Journal de physique IV, COLOQ7*, vol. 12, p. 313, 2002.

(CN:10) S. Blin, P. Besnard, J. Poëtte, I. Castonguay, S. La Rochelle, C. Palavicini, and Y. Jaouën, "Réalisation et caractérisation de lasers à fibre DFB : Importance de la valeur du saut de phase," Journées Nationales d'Optique Guidée (JNOG), 2002.

(CN:11) D. Trung, T. Vu, L. Minh, N. Loc, T. Tam, V. Cham, S. Blin, P. Besnard, and G. Stéphan, "Continously tunable erbium-doped fiber laser utilizing bragg reflectors," in *8th Biennial Vietnam National Conference on Radio and Electronics (REV'02)*, 2002.

(CN:12) T. Tam, D. Trung, T. Vu, L. Minh, V. Cham, N. Loc, S. Blin, P. Besnard, and G. Stéphan, "1.55 μm distributed feedback erbium-doped fiber laser," in *3rd National Conference on Optics and Spectroscopy*, Vietnam, 2002.

(CN:13) S. Blin, R. Gabet, G. Stéphan, and P. Besnard, "Mesure du gain d'un laser utilisé comme amplificateur," *OPTIX*, 2001.

9.4 Autres conférences, GDR, Workshops (A:1–14)

(A:1) R. Paquet, S. Blin, M. Myara, L. Legratiet, M. Sellahi, B. Chomet, P. Latzel, G. Ducournau, J.-F. Lampin, G. Beaudoin, I. Sagnes, and A. Garnache, "Coherent & tunable THz source," *GDR Nanoteramir*, 2016.

(A:2) garnacheRussianFrench2015
A. Garnache, M. Sellahi, M. Seghilani, R. Paquet, S. Blin, M. Myara, I. Sagnes, G. Beaudoin, X. Lafosse, L. Legratiet, and P. Lalanne, "Generation of new spatial and temporal coherent states using VeCSEL technology: Vortex, high order laguerre-gauss mode, continuum source," *8th Russian-French workshop on Nanosciences and Nanotechnologies*, **conférence invitée**, 2015.

(A:3) L. Tohme, S. Blin, P. Nouvel, A. Pénarier, G. Ducournau, S. Bollaert, J.-F. Lampin, D. Coquillat, W. Knap, J. Oden, J.-F. Roux, and J.-L. Coutaz, "THz wireless communications using plasma-wave detectors with integrated antenna," *THz days*, 2015.

(A:4) R. Paquet, M. Sellahi, S. Blin, M. Myara, A. Garnache, G. Beaudoin, L. Legratiet, I. Sagnes, G. Ducournau, F. Pavanello, P. Latzel, M. Zaknoune, and J.-F. Lampin, "Vertical-external-cavity surface-emitting laser for THz generation: optical to THz characterization," *THz days*, 2015.

(A:5) R. Paquet, M. Sellahi, B. Chomet, S. Blin, M. Myara, and A. Garnache, "Dual-frequency vertical-external-cavity surface-emitting laser for THz generation," *European Workshop on VeCSELs*, 2015.

(A:6) S. Blin and L. Tohme and P. Nouvel and A. Pénarier and D. Coquillat and W. Knap and G. Ducournau and J.-F. Lampin and S. Bollaert and S. Hisatake and T. Nagatsuma, "THz wireless communications at high data rate using plasma-wave field-effect transistors for détection: State of the art and perspectives," *Condensed Matter (CMD)*, **conférence invitée**, 2014.

(A:7) S. Blin, L. Tohme, P. Nouvel, A. Pénarier, D. Coquillat, W. Knap, G. Ducournau, J.-F. Lampin, S. Bollaert, S. Hisatake, and T. Nagatsuma, "THz wireless communications at high data rate using plasma-wave field-effect transistors for detection:

state of the art and perspectives," *GDR-I Semiconductor sources and detectors of THz radiation*, 2013.

(A:8) R. Paquet, M. Sellahi, I. Sagnes, G. Beaudoin, M. Myara, S. Blin, and A. Garnache, "Dual-frequency vertical-external-cavity surface-emitting laser for terahertz generation," *European Workshop on VeCSELs*, 2013.

(A:9) D. Coquillat, K. Kurita, K. Kobayashi, F. Teppe, N. Diakonova, D. But, L. Tohme, P. Nouvel, S. Blin, J. Torres, *et al.*, "Sub-threshold attenuation of terahertz detection by asymmetric dual-grating gate HEMT structures," in *International Workshop on Optical Terahertz Science and Technology*, p. 217, 2013.

(A:10) S. Blin, M. Seghilani, D. Ghezzaz, P. Besnard, M. Myara, and A. Garnache, "Spectral properties of an homogeneous laser under feedback simulated with the generalized Airy's function: application to a vecsel," *European Workshop on VeCSELs*, 2012.

(A:11) G. Ducournau, S. Blin, D. Coquillat, A. Beck, T. Akalin, E. Peytavit, F. Schuster, W. Knap, J. Torres, F. Teppe, *et al.*, "UTC-PD emitters and FET based receivers for sub-THz wireless communication system," International TeraNano & GDRI Workshop, 2011.

(A:12) R. Paquet, D. Lapeine, S. Blin, J.-P. Guillet, P. Nouvel, J. Torres, A. Penarier, L. Varani, P. Solignac, D. Coquillat, *et al.*, "First communication link using a 300-GHz source and a si plasma-wave detector," International TeraNano & GDRI Workshop, 2011.

(A:13) S. Blin, T. N. Nguyen, D. M. Nguyen, M. Thual, L. Provino, and T. Chartier, "Simple modal analysis method for slightly mutli-mode optical fibers," in *8th meeting of COST 299 FIDES*, 2009.

(A:14) blinIWPA2004
S. Blin, O. Vaudel, T. T. Tam, P. Besnard, S. LaRochelle, R. Gabet, and G. Stéphan, "Spectral and time phenomena in optical injection using distributed feedback semiconductor or fibre lasers," *International Workshop on Photonics Applications (IWPA)*, **conférence invitée**, 2004.

Bibliographie

[1] C. Huygens, "Oeuvres completes de Christiaan Huygens," *M. Nijhoff (Ed.)*, vol. 17, no. 156–189, 1660.

[2] I. Joindot and M. Joindot, "Les télécommunications optiques," *Ed. Dunod*, 1996.

[3] W. Loh and R. Laming, "1.55 μm phase-shifted distributed feedback fibre laser," *Electronics Letters*, vol. 31, no. 17, pp. 1440–1442, 1995.

[4] O. Vaudel, "Étude de synchronisation de chaos par simple injection optique," *Doctorat de l'Université de Rennes I - Laboratoire Foton*, 2007.

[5] S. Blin, "Réalisation de lasersa fibre à contre-réaction répartie pour l'étude de l'injection optique : comparaison à l'injection avec des lasers à semi-conducteurs," *Doctorat de l'Université de Rennes I - Laboratoire Foton*, 2003.

[6] R. Adler, "A study of locking phenomena in oscillators," *Proceedings of the IRE*, vol. 34, pp. 351–357, June 1946.

[7] G. M. Stéphan, "Spectral properties of an injected laser," *Phys. Rev. A*, vol. 58, pp. 2467–2471, Sep 1998.

[8] J. Nicholson, A. D. Yablon, S. Ramachandran, and S. Ghalmi, "Spatially and spectrally resolved imaging of modal content in large-mode-area fibers," *Optics Express*, vol. 16, no. 10, pp. 7233–7243, 2008.

[9] D. M. Nguyen, "Investigations et caractérisations de fibres et guides optiques très fortement non-linéaires," *Doctorat de l'Université de Rennes I - Laboratoire Foton*, 2011.

[10] T. N. Nguyen, "Étude de composants optiques à base de fibres optiques non-linéaires," *Doctorat de l'Université de Rennes I - Laboratoire Foton*, 2008.

[11] G. Scalari, C. Walther, J. Faist, H. Beere, and D. Ritchie, "Electrically switchable, two-color quantum cascade laser emitting at 1.39 and 2.3 THz," *App. Phys. Lett.*, vol. 88, no. 14, pp. 141102–141102, 2006.

[12] J. Mangeney, A. Merigault, N. Zerounian, P. Crozat, K. Blary, and J. Lampin, "Continuous wave terahertz generation up to 2 THz by photomixing on ion-irradiated $In_{0.53}Ga_{0.47}As$ at 1.55 μm wavelengths," *Appl. Phys. Lett.*, vol. 91, no. 24, pp. 241102–241102, 2007.

[13] H. Ito, T. Furuta, F. Nakajima, K. Yoshino, and T. Ishibashi, "Photonic generation of continuous THz wave using uni-traveling-carrier photodiode," *J. of Lightwave Technol.*, vol. 23, no. 12, pp. 4016–4021, 2005.

[14] M. Scheller, J. R. Paul, A. Laurain, A. Young, S. W. Koch, and J. V. Moloney, "Terahertz generation by difference frequency conversion of two single-frequency VECSELs in an external resonance cavity," in *SPIE LASE*, pp. 89660E–89660E, International Society for Optics and Photonics, 2014.

[15] A. Klehr, J. Fricke, A. Knauer, G. Erbert, M. Walther, R. Wilk, M. Mikulics, and M. Koch, "High-power monolithic two-mode DFB laser diodes for the generation of THz radiation," *IEEE J. of Select. Top. in Quant. Electron.*, vol. 14, no. 2, pp. 289–294, 2008.

[16] C. Friedrich, C. Brenner, S. Hoffmann, A. Schmitz, I. C. Mayorga, A. Klehr, G. Erbert, and M. R. Hofmann, "New two-color laser concepts for THz generation," *IEEE J. of Select. Top. in Quant. Electron.*, vol. 14, no. 2, p. 270, 2008.

[17] A. Rolland, G. Loas, M. Brunel, L. Frein, M. Vallet, and M. Alouini, "Non-linear optoelectronic phase-locked loop for stabilization of opto-millimeter waves: towards a narrow linewidth tunable THz source," *Opt. Exp.*, vol. 19, no. 19, pp. 17944–17950, 2011.

[18] A. Laurain, M. Myara, G. Beaudoin, I. Sagnes, and A. Garnache, "Multiwatt–power highly–coherent compact single–frequency tunable vertical–external–cavity–surface–emitting–semiconductor–laser," *Optics Express*, vol. 18, no. 14, pp. 14627–14636, 2010.

[19] M. Wichmann, M. Shakfa, M. Scheller, A. Rahimi-Iman, B. Heinen, J. Moloney, S. Koch, and M. Koch, "Systematic investigation of single-and multimode operation in vertical-external-cavity surface-emitting lasers," in *SPIE LASE*, pp. 89660N–89660N, International Society for Optics and Photonics, 2014.

[20] S. De, G. Baili, M. Alouini, J.-C. Harmand, S. Bouchoule, and F. Bretenaker, "Class-A dual-frequency VECSEL at telecom wavelength," *Opt. Lett.*, vol. 39, pp. 5586–5589, Oct 2014.

[21] R. Paquet, "Nouvelles sources lasers pour génération THz," *Thèse de doctorat, Université de Montpellier*, 2016.

[22] M. Sellahi, M. S. Seghilani, I. Sagnes, G. Beaudoin, X. Lafosse, L. Legratiet, P. Lalanne, M. Myara, and A. Garnache, "Generation of new spatial and temporal coherent states using VECSELtechnology: VORTEX, high order laguerre-gauss mode, continuum source," in *SPIE LASE*, pp. 89660U–89660U, International Society for Optics and Photonics, 2014.

[23] A. Garnache, A. Ouvrard, and D. Romanini, "Single–frequency operation of external–cavity VCSELs: non-linear multimode temporal dynamics and quantum limit," *Optics Express*, vol. 15, no. 15, pp. 9403–9417, 2007.

[24] S. E. Hodges, M. Munroe, J. Cooper, and M. G. Raymer, "Multimode laser model with coupled cavities and quantum noise," *J. of the Opt. Soc. of Am. B*, vol. 14, no. 1, pp. 191–199, 1997.

[25] S. Cortez, O. Krebs, and P. Voisin, "In-plane optical anisotropy of quantum well structures: from fundamental considerations to interface characterization and optoelectronic engineering," *J. of Vac. Sci. & Technol. B*, vol. 18, no. 4, pp. 2232–2241, 2000.

[26] A. E. Siegman, *Lasers*. University Science Books, 1986.

[27] N. Von Bandel, M. Myara, M. Sellahi, T. Souici, R. Dardaillon, and P. Signoret, "Time dependant linewidth: beat-note digital acquisition and numerical analysis," *Opt. Exp.*, vol. 24, no. 24, pp. 27961–27978, 2016.

[28] M. Myara, M. Sellahi, A. Laurain, A. Michon, I. Sagnes, and A. Garnache, "Noise properties of NIR and MIR VECSELS," in *Proc. SPIE*, vol. 8606, 2013.

[29] J. L. Hesler, L. Liu, H. Xu, Y. Duan, and R. M. Weikle, "The development of quasi-optical THz detectors," *Infrared, Millimeter and Terahertz Waves (IRMMW-THz)*, 2008.

[30] T. Nagatsuma, S. Horiguchi, Y. Minamikata, Y. Yoshimizu, S. Hisatake, S. Kuwano, N. Yoshimoto, J. Terada, and H. Takahashi, "Terahertz wireless communications based on photonics technologies," *Optics Express*, vol. 21, no. 20, pp. 23736–23747, 2013.

[31] M. I. Dyakonov and M. S. Shur, "Plasma wave electronics: novel terahertz devices using two dimensional electron fluid," *IEEE Transactions on Electron Devices*, vol. 43, no. 10, pp. 1640–1645, 1996.

[32] L. Tohme, "Communication térahertz sans fil à haut débit avec un transisor à haute mobilité électronique comme détecteur," *Thèse de doctorat, Université de Montpellier*, 2014.

[33] G. Ducournau, P. Szriftgiser, F. Pavanello, E. Peytavit, M. Zaknoune, D. Bacquet, A. Beck, T. Akalin, J.-F. Lampin, and J.-F. Lampin, "THz communications using photonics and electronic devices: the race to data-rate," *Journal of Infrared, Millimeter, and Terahertz Waves*, vol. 36, no. 2, pp. 198–220, 2015.

[34] H.-J. Song, J.-Y. Kim, K. Ajito, M. Yaita, and N. Kukutsu, "Fully integrated ASK receiver MMIC for terahertz communications at 300 GHz," *IEEE Transactions on Terahertz Science and Technology*, vol. 3, no. 4, pp. 445–452, 2013.

[35] D. B. But, C. Drexler, M. V. Sakhno, N. Dyakonova, O. Drachenko, F. F. Sizov, A. Gutin, S. D. Ganichev, and W. Knap, "Nonlinear photoresponse of field effect transistors terahertz detectors at high irradiation intensities," *Journal of Applied Physics*, vol. 115, no. 16, 2014.

[36] R. Drever, J. Hall, F. Kowalski, J. Hugh, and G. Ford, "Laser phase and frequency stabilization using an optical resonator," *Applied Physics B*, vol. 31, pp. 97–105, 1983.

[37] Y. Ohiso, C. Amano, Y. Itoh, K. Tateno, T. Tadokoro, H. Takenouchi, and T. Kurokawa, "1.55-μm vertical-cavity surface-emitting lasers with wafer-fused InGaAsP/lnP-GaAs/AlAs DBRs," *Electronics Letters*, vol. 32, no. 16, pp. 1483–1484, 1996.

[38] C. W. Berry, N. Wang, M. R. Hashemi, M. Unlu, and M. Jarrahi, "Significant performance enhancement in photoconductive terahertz optoelectronics by incorporating plasmonic contact electrodes," *Nature Communications*, vol. 4, 2013.

[39] M. Seghilani, "Coherent III-V-semiconductor laser emitting phase-, amplitude- and polarization-structured light for advanced sensing applications," *Thèse de doctorat, Université de Montpellier*, 2015.

[40] J. Wu and H. Mosallaei, "Engineered dielectric pattern nanoantenna: a quantum cascade laser (qcl) device application," *IEEE Transactions on Antennas and Propagation*, vol. 59, no. 1, pp. 32–38, 2011.

[41] D. McBryde et al., "Multiple double-metal bias-free terahertz emitters," *Applied Physics Letters*, no. 201108, 2014.

[42] P. Meyer and D. Prinsloo, "Generalized multimode scattering parameter and antenna far-field conversions," *IEEE Transactions on Antennas and Propagation*, vol. 63, no. 11, pp. 4848–4826, 2015.

[43] E. Castro-Camus et al., "Leaf water dynamics of arabidopsis thaliana monitored in-vivo using terahertz time-domain spectroscopy," *Scientific Report*, 2013.

[44] U. Jepsen et al., "Investigation of aqueous alcohol and sugar solutions with reflection terahertz time-domain spectroscopy," *Optics Express*, vol. 15, no. 22, pp. 14717–14737, 2007.

[45] N. Born et al., "Monitoring plant drought stress response using terahertz time-domain spectroscopy," *Plant Physiol.*, vol. 164, no. 4, pp. 1571–1577, 2014.

Annexe : Tirés à part

Les 7 tirés à part choisis reflètent les thématiques scientifiques principalement étudiés, et notamment l'aboutissement de l'encadrement de R. Paquet (tiré à part #1), de L. Tohme (#3), de D. Nguyen (#4) et d'O. Vaudel (#5). Nous précisons les articles originaux (A) et les lettres (L).

1. **(A)** S. Blin et al., "Coherent and tunable THz emission driven by an integrated III–V semiconductor laser," *J. of Select. Topics in Quant. Electron.*, 23(4), 2017.
2. **(L)** S. Blin et al., "Terahertz heterodyne communication using GaAs field-effect transistor receiver," *Electron Device Lett.*, 38(1), 2017.
3. **(A)** S. Blin et al., "Wireless communication at 310 GHz using GaAs High-Electron-Mobility Transistors for detection," *J. of Comm. and Networks*, 15(6), 2013.
4. **(A)** D. M. Nguyen et al., "Modal decomposition technique for multimode fibers," *Applied Optics*, 51(4), 2012.
5. **(A)** S. Blin et al., "Power-or frequency-driven hysteresis for continuous-wave optically injected distributed-feedback semiconductor lasers," *Optics Express*, 17(11), 2009.
6. **(A)** S. Blin et al., "Reduced thermal sensitivity of a fiber-optic gyroscope using an air-core photonic-bandgap fiber," *J. of Lightwave Technology*, 25(3), 2007.
7. **(A)** G. Stéphan et al., "Laser line shape and spectral density of frequency noise," *Physical Review A*, 71(4), 2005.

Coherent and Tunable THz Emission Driven by an Integrated III–V Semiconductor Laser

Stéphane Blin, Romain Paquet, Mikhaël Myara, Baptiste Chomet, Luc Le Gratiet, Mohamed Sellahi, Grégoire Beaudoin, Isabelle Sagnes, Guillaume Ducournau, Philipp Latzel, Jean-François Lampin, and Arnaud Garnache

***Abstract*—We demonstrate coherent and tunable THz emission by excitation of a unitraveling-carrier photodiode by a dual-frequency III–V semiconductor laser emitting up to 80 mW of optical power around 1 μm. The laser is an optically-pumped vertical-external-cavity surface-emitting laser that operates simultaneously on two transverse Laguerre–Gauss modes. Modes frequency difference is driven by thermal effects, band-filling effects and/or phase masks, allowing THz emission from 50 GHz to few THz. To reach THz emission from a pigtailed photodiode, we detail quantitatively how orthogonal transverse modes can be coupled within a single-mode fiber, leading to more than 20% beat efficiency. Coherent THz emission spectrum is presented with a linewidth of about 150 kHz for 3-ms acquisition time, and an output power limited by the photodiode (typically 1 μW at 300 GHz). Frequency noise is measured for the optical transverse modes along with the THz signal. The latter presents a frequency noise that is about 20-dB lower than the optical ones, thus proving that the dual-frequency concept allows frequency noise reduction by correlating part of the technical noise of the two modes.**

***Index Terms*—Submillimeter wave generation, semiconductor lasers.**

I. Introduction

COHERENT, tunable and compact continuous-wave Terahertz (THz) sources are required for many applications, such as bio-medical sensing and imaging, communications, or security. A large variety of solutions exists for THz emission, from optics to electronics, but existing solutions are often cumbersome or limited in terms of output power, tunability and/or modulation bandwidth. At the upper band of the THz spectrum (far-infrared side), sources are usually pulsed and/or require low-temperature operation, e.g. for quantum-cascade lasers [1] or P-germanium laser [2]. At the lower band of the THz spectrum, electronic-based sources usually operate easily at room temperature in a continuous-wave operation, but at a fixed frequency of emission, e.g. for Gunn, impact ionization avalanche transit time or resonant-tunnelling diodes. Frequency-multiplied sources, driven by a microwave synthesizer, offer enhanced tunability, but do not provide simultaneously sufficient output power and high modulation bandwidth, compactness, or affordability. Photo-mixing techniques offer precious advantages such as wideband tunability and high-modulation bandwidth at room temperature. A straightforward solution consists in exciting a photo-mixer with two lasers emitting at different frequencies to generate a THz beat note. Different kinds of efficient photo-mixers have been developed (some even commercialized) in the last decade, such as ErAs:GaAs inter-digitated photo-mixer [3], uni-traveling-carrier photo-diode (UTC-PD) [4], ion-irradiated InGaAs inter-digitated photo-mixers [5], or using difference-frequency generation (DFG) [6]. However, coherent and tunable THz emission is usually based on either complex and/or expensive systems for optical-beating generation. We propose a breakthrough solution to generate dual-frequency high-power coherent and tunable laser emission, in a robust and integrated device exploiting III-V semiconductor nanotechnologies, for THz generation.

Photo-mixing based on two uncorrelated lasers have been demonstrated, e.g. using UTC-PDs [7], [8] or DFG [6]. Unfortunately, using such uncorrelated sources leads to a deteriorated coherence of the terahertz radiation, therefore a stable dual-frequency laser is required in order to cancel-out technical perturbations. Many attempts to reach compact, stable, continuously-tunable, coherent and powerful dual-frequency lasers have been already proposed for terahertz generation, but none of them meets fully the requirements for applications such as terahertz generation. Well-known multimode operation can be observed in monolithic semiconductor edge-emitting diodes that rely on complex non-linear processes, like spatial hole burning (SHB) and four-wave-mixing (FWM). Mode competition becomes sufficiently small to allow for multimode operation, but usually in a quite unstable coupled state with complex dynamics (partition fluctuations), i.e. with no robustness, without tunability and with limited coherence (highly-divergent

Manuscript received October 6, 2016; revised January 10, 2017; accepted January 11, 2017. This work was supported in part by the AxLR.

S. Blin, R. Paquet, M. Myara, M. Sellahi, and A. Garnache are with the IES, CNRS UMR 5214 – Université de Montpellier, Montpellier 34095, France (e-mail: stephane.blin@umontpellier.fr; paquet@ies.univ-montp2.fr; MYARA@ies.univ-montp2.fr; sellahi@ies.univ-montp2.fr; agarnache@univ-montp2.fr).

B. Chomet is with the IES, CNRS UMR 5214 – Université de Montpellier, Montpellier 34095, France, and also with the Innoptics, Institut d'Optique d'Aquitaine, Talence 33400, France (e-mail: chomet@ies.univ-montp2.fr).

L. Le Gratiet, G. Beaudoin, and I. Sagnes are with the C2N, CNRS UMR 9001, Université Paris Sud/Saclay, Marcoussis 91460, France (e-mail: luc.legratiet@lpn.cnrs.fr; Gregoire.Beaudoin@lpn.cnrs.fr; isabelle.sagnes@lpn.cnrs.fr).

G. Ducournau, P. Latzel, and J.-F. Lampin are with the IEMN, CNRS UMR 8520, Université de Lille, Lille 59650, France (e-mail: guillaume.ducournau@iemn.univ-lille1.fr; philipp.latzel@etudiant.univ-lille1.fr; jean-francois.lampin@isen.iemn.univ-lille1.fr).

Color versions of one or more of the figures in this paper are available online at http://ieeexplore.ieee.org.

Digital Object Identifier 10.1109/JSTQE.2017.2654060

elliptical beam, linewidth of tens of MHz, parasitic frequencies) [9]. External-cavities diode laser using spectral filter(s) can allow bi-frequency stability, but to the detriment of output power, cavity complexity, alignment sensitivity/robustness, beam quality, and coherence as the laser tends to operate two sets of longitudinal modes rather than two modes [10]. Another technique used to reduce mode coupling consists in a separation of laser beams within the cavity. Such a two-axis cavity can be obtained for example by polarization separation [11] and shows interesting results in terms of tunability and coherence. However, tunability occurs by steps, output power is limited to few milliwatts, cavity is complex with intra-cavity movable elements, almost impossible to integrate on a single device, and coherence is degraded. More recently, a Brillouin-based dual-frequency laser was demonstrated [12] but continuous-tunability and compactness remain insufficient. Finally, one can control the power of the two laser lines of a crystal by tilting one of the cavity mirrors [13], allowing high output power but no tunability.

Among these possible laser designs, Vertical-external-Cavity Surface-Emitting Lasers (VeCSEL) are very promising solutions for dual-frequency lasers as they are inherently compact, wavelength flexible, widely tunable, powerful and highly coherent (spectrally, spatially and in terms of polarization) along with a class-A dynamics regime [14]. Dual-frequency operation has been already demonstrated using a VeCSEL by stabilization of two polarization modes [15] with the advantage of a 1550-nm emission wavelength, but the beat frequency was limited to few GHz, and most importantly the laser was operated on two different optical axis for the two polarization modes, along with moveable intra-cavity elements such as an etalon filter, thus reducing the possible laser integration, robustness and stability. Dual-frequency laser operation based on the coexistence of two longitudinal modes has been demonstrated for THz generation in a VeCSEL [16], but such a design does not allow for simultaneous operation of both laser lines. None of the state-of-the-art methods offering an inherently robust, compact/integrated and flexible solution for cw, coherent and tunable beat signals in the GHz–THz range, we recently proposed a novel dual-frequency highly-coherent laser based on the stabilization of two transverse modes in a single-axis cavity VeCSEL [17], and proved the simultaneous operation of the two modes. This laser configuration operates on a single optical axis and is free of moveable intra-cavity element, thus assuring a very robust operation, but is also free of etalon spectral filter that is limiting for tunability. Here, we will present for the first time the properties of the THz emitted signal that is obtained by exciting a UTC photodiode with the dual-frequency VeCSEL, along with a detailed study of the beat signal tunability and temporal coherence. We also present an original laser configuration based on the introduction of an integrated meta-material phase-mask to shift the beat frequency in the THz range even for the cold cavity.

II. Dual-Frequency VeCSEL Principle, Design and Fabrication

A. Dual-Mode Laser Principle

The dual-frequency VeCSEL is based on the stabilization of two Laguerre-Gauss (LG) transverse eigenmodes, of minimum waist $w_0 \gg \lambda$, in a high-Q single-axis short laser cavity. As LG modes diffract naturally in a free-space concave-type cavity, they offer feeble mutual intensity spatial overlap to ensure stability, but enough field overlap (locally) to allow for beating. Modes can be selected by using transverse spatial filtering and SHB dynamics in the gain medium. Here we developed a dual-frequency cw laser that exploits a GaAs-based Quantum-Well (QW) VeCSEL technology integrating an intracavity sub-λ thick spatial filter on the end gain mirror, that consists of a metallic mask and eventually a metamaterial-based phase mask. Fig. 1 (from Ref. [17]) reminds the dual-frequency optically-pumped QW VeCSEL design. We developed two distinct designs, called here *broadband laser-*♯1 and *filtered laser-*♯2a, for respectively 100's GHz and 1000's GHz beat frequency range. The laser parameters of these two configurations are given in Table I. The laser cavity is formed by a wavelength-thick GaAs-based gain mirror and a concave dielectric output coupler with a radius of curvature R_c and a transmission T. The cavity length L_c is set by a 1 to 10 mm-long air gap leading to a Free Spectral Range ($FSR = c/(2\,L_c)$) in the 15–150 GHz range. It defines a stable short linear cold cavity of high axial symmetry, supporting a degenerate petals-like $\mathrm{LG_{pm}}$ eigenmode orthogonal basis as shown in Fig. 2(a) and (b), where $p(m)$ represents the radial (azimutal) number ($\in \mathbb{N}$) [18]. The discrete set of possible eigenmodes and frequencies for the intra-cavity electric field $\vec{\mathcal{E}}(t, \vec{r})$

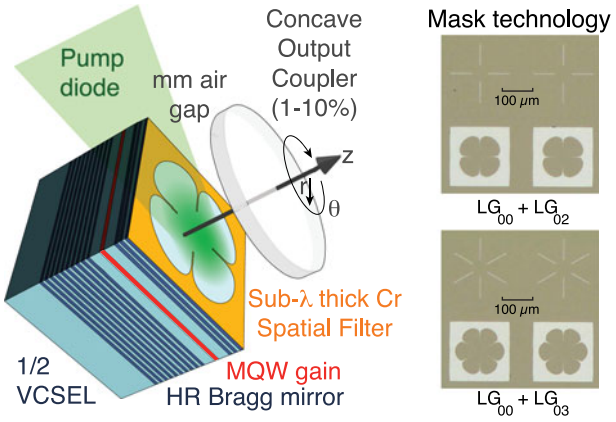

Fig. 1. (a) Two-frequency short plano-concave cavity VeCSEL design and technology. b) Metallic masks for $\mathrm{LG_{00}}$ plus $\mathrm{LG_{0}}_m$ ($m = 2, 3$ here) modes oscillation (optical microscope).

TABLE I
Laser Parameters for both Designs

Parameter	Laser-♯1	Laser-♯2a	Units
1/2-VCSEL design	AR coating	μ-cavity filter	
1/2-VCSEL bandwidth Γ_g	6	0.3	THz
Γ	1	11	
Tuning $\delta\nu$	600/% of gain	-30/K	GHz/
R_{th}	80	80	K/W
FSR	150	16	GHz
$\delta\nu_G$	36	11	GHz
T	1	10	%
R_{cc}	4	10	mm
w_0	25	25	μm

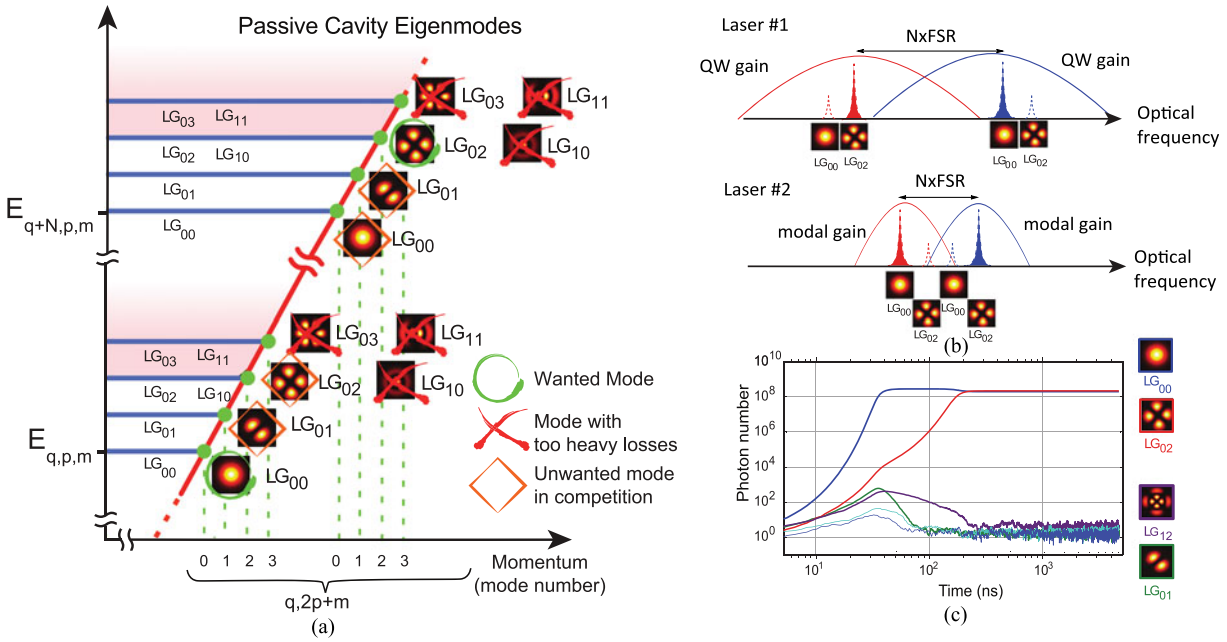

Fig. 2. (a) Photon energy-momentum dispersion diagram of confined LG_{pm} modes in a stable concave-type cavity (longitudinal mode q), integrating a loss mask. (b) Spectrum of the dual-frequency VeCSEL. (c) Multi-transverse mode laser buildup for a VeCSEL emitting on LG_{00} and LG_{02} modes at steady state (pump rate is twice the threshold).

are defined by p, m and the longitudinal eigenmode number q, and normalized LG wave-functions $\Phi_{\rm pm}(r,\theta)$ $(\in R)$ [18]:

$$\Phi_{\rm pm}(r,\theta) = \sqrt{\frac{2p!}{\pi w^2 (p+|m|)!}} \left(\frac{\sqrt{2}r}{w}\right)^{|m|} L_p^{|m|}\left(\frac{2r^2}{w(z)^2}\right) \times \exp\left(-\frac{r^2}{w(z)^2} - \frac{ikr^2}{2R(z)} + im\theta\right). \quad (1)$$

In the rotating-wave-approximation, the complex electric field $\vec{\mathcal{E}}$ can be written as an expansion in a set of normal eigenmodes and polarization eigenvectors of the cavity, as:

$$\vec{\mathcal{E}}(\vec{r},t) = \sum_{\rm qpm,x} E_{\rm qpm}(t)\Phi_{\rm pm}(r,\theta)\frac{\cos(kz)}{\sqrt{2L_c}} e^{i\omega_{\rm qpm}t}\,\vec{x}\,, \quad (2)$$

where $E_{\rm qpm}(t)$ are slowly time-varying envelopes; $L_p^{|l|}$ is the generalized Laguerre polynomial; $R(z)$ is the wavefront radius of curvature; $w(z) \gg \lambda$ is the Gaussian beam waist, $z_R = \pi\, w_0^2/\lambda$ is the Rayleigh length; $\omega_{\rm qpm}/2\pi$ are cold cavity eigen frequencies for q, p, m quantum numbers given by the photon energy-momentum dispersion relation, assuming a unique polarization state [18], $\omega_{\rm qpm} = 2\,\pi\, FSR\,[q + (1 + 2\,p + |m|)\,\varphi/\pi]$, where $\varphi = \cos^{-1}(\sqrt{1 - L_c/R_c})$ is the Gouy phase shift.

This design takes advantage of VeCSEL concept, offering weak thermally-induced wavefront distortion/astigmatism, exhibiting inherent powerful coherent emission in a single mode q, p, m, and single linear polarization eigenvector $\vec{x}$, with high Side-Mode Suppression Ratio (SMSR) at quantum limit [14], [19]. Indeed short-cavity (sub-cm) LG_{00} VeCSEL exhibits regular and stable dynamics thanks to QW homogeneous-broadening-induced mode competition and to inefficient non-linear mode coupling (no longitudinal SHB; weak FWM) [19], [20]. Polarization state of optically-pumped VeCSEL is commonly linear along [110] crystal axis $(\vec{x})$ due to strong coupling in QW between non-degenerate linear eigenvectors, as explained by the spin-flip model [21], and thanks to in-plane crystal optical anisotropy (linear gain dichroism, structure birefringence) [14], [19], [22]. Moreover, due to low cavity loss rate $\gamma_0 = T.FSR$, VeCSELs exhibit low-noise class-A dynamics for >mm-long cavity [14], [19]. To reach our goal, we exploit a remaining degree of freedom, which is to "engineer" the laser dynamics of LG modes: in contrast to monolithic VCSELs supporting LP confined modes with complex class-B dynamics [21], a VeCSEL stabilizes LG modes of radius $r_{\rm pm} = w_0\sqrt{2\,p+m} \gg \lambda$ [18], thus offering weak transverse eigenmode coupling in QW and efficient SHB, as $w_0 \sim 25\,\mu$m here, much larger than QW carrier diffusion length.

B. III-V VeCSEL Designs and Fabrication

Here we present two laser designs in order to reach stable dual frequency operation and to tune the resulting beating frequency in the 0.03–3 THz frequency range. These laser designs (#1 and #2a/b) are represented in Fig. 3.

1) Gain Structure Designs Integrating Sub-λ Masks for Transverse mode Control: Two 1/2-VCSEL gain mirror structures were grown on a [001] GaAs doped substrate in a low-pressure metal-organic chemical vapor deposition D-180-Veeco TurboDisc reactor using TMGa, TMAI, TMIn, and AsH3 at 60 mTorr at a temperature of 700°C. They contain a high reflectivity (99.9 %) $Al_{0.85}Ga_{0.15}As$/GaAs 27-pairs Distributed Bragg Reflector (DBR), and a $13\,\lambda/2$-thick active layer. It contains 6 strain-balanced InGaAs/GaAsP QWs emitting at $\lambda \simeq 1\,\mu$m and GaAs pump absorbing barriers. Strain compensa-

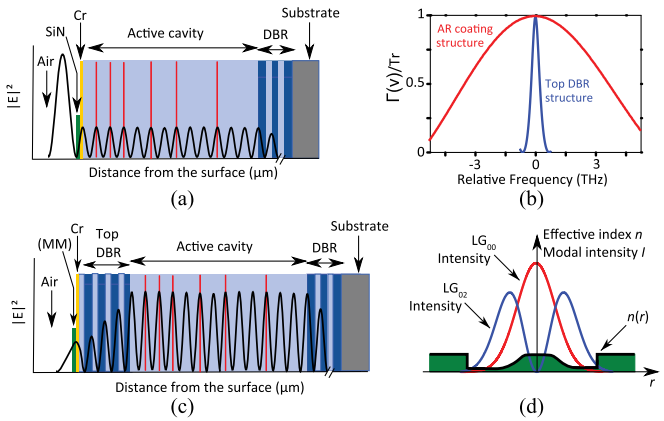

Fig. 3. (a) Structure design #1. (b) Structure design #2a (without meta-material (MM)) and #2b (with MM). (c) Spectrum of the laser field enhancement factor over the coupler transmission for the structure-♯1, -♯2a and -♯2b. (d) Effective refractive index spatial distribution and mode intensity distribution.

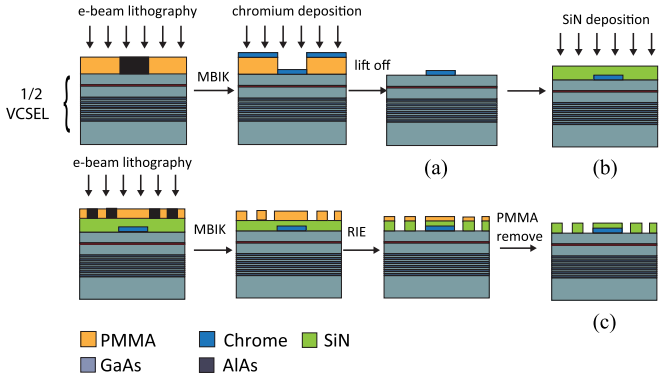

Fig. 4. Technological process for the fabrication of metallic mask and meta-materials: 1) A polymethyl methacrylate (PMMA) resist layer is spin-coated on the wafer and patterned by electron beam lithography with a resolution of 1.25nm. 2) PMMA is developed in a methylisobutylketone (MBIK) solution. 3) After deposition of a thin layer (5–20 nm) of chromium using physical vapor deposition (PVD), a lift-off is realized. 4) A sub-wavelength-thick SiN is deposited by ion-beam-assisted electron beam vacuum evaporation. 5) On the top of the SiN layer, a PMMA resist layer is spin-coated and patterned by e-beam lithography. 6) PMMA is then developed in a MBIK solution. 7) The SiN layer is then etched by Reactive Ion Etching (RIE). 8) PMMA is removed by an oxygen plasma. (a) Structure ♯1, (b) Structure ♯2a, (c) Structure ♯2b.

tion layers of GaAsP are included to avoid plastic relaxation of the active region structure. The two surrounding 280-nm-thick barriers are in GaAsP with 5% of phosphore to compensate the QW strain ($\Delta a/a \simeq 1.3\%$). The GaAsP barriers band-gap energy is of 1.48 eV (6 meV band offset). A low phosphore concentration is chosen to minimize the barrier height between GaAs and GaAsP at 300 K, for efficient capture of excited carriers in the QWs. These QWs are located on optical standing-wave antinodes, with a 111010100100 distribution function from surface to Bragg such as the excited carrier density is almost equal in all QWs to ensure a low laser threshold and a homogeneous gain. The active region is designed for efficient optical pumping in the thick GaAs barriers with a GaAs commercial diode laser emitting in the 780–830 nm range. The total pump absorption in the barriers is $\sim 87\%$ (absorption coefficient $\sim$1.2 μm^{-1}). For QWs excited carrier population $n \sim 2\,n_{\rm tr}$, where $n_{\rm tr}$ is the transparency carrier population, the 6 QWs provide enough gain to compensate 1% of optical losses (for a structure with an AR coating). The measured spectral shift of the maximum gain with optical losses is found to be $\delta\nu/\delta g = 600$ GHz/%. QW gain (dichroism) along the [110] crystal axis is measured to be 10% superior to the one along the [1-10] axis.

a) Structure design ♯1 for broadband operation: On the top of the $13\,\lambda/2$-thick active layer, a 30-nm-thick AlAs confinement layer and then, to avoid oxydation, a 15(35)-nm-thick GaAs(InGaP) cap layer are grown. A spatially-distributed absorbing filter (mask) is deposited on top surface at an antinode of the longitudinal intra-cavity E-field, followed by a $\lambda/4$ SiN thick anti-reflection coating to reduce micro-cavity resonance filtering effect. The transverse filter consists in a 10-nm-thick Cr mask, induces $\sim 90\,\%$ optical losses for a filling factor of 1. Its transverse shape is computed and processed by e-beam lithography and reactive ion etching, as shown in Fig. 4, to dramatically increase losses for unwanted LG modes ($> 10\,\%$), while ensuring low losses for at least the two targeted LG modes.

The shape of the mask can be a simple set of 2–3-μm-wide line segments or a more sophisticated *flower* increasing high-order modes losses $\gamma_{\rm pm} = \iint_S \gamma(r,\theta,t)\,\Phi_{\rm pm}\,ds$ (see Fig. 1). The Cr mask spatial distribution is stopped at $\sim 0.1\,\%$ of the LG_{0m} E-field maximum intensity and the central disk is completely empty. Due to its strong overlap with the Gaussian pump beam, we involved the LG_{00} mode. The second one is a LG_{0m} mode with $m \geq 2$ for weak overlap. This design leads to a cold cavity selecting only few transverse modes in the LG basis (Fig. 2(a)).

b) Structure design ♯2a with spectral filter: On the top of the $13\,\lambda/2$-thick active layer we added a 3-pairs $\mathrm{Al}_{0.18}\mathrm{Ga}_{0.82}\mathrm{As}$/AlAs DBR (transparent at pump energy) before the cap to create a low-finesse micro-cavity filter, the Cr mask being deposited on the top surface. This micro-cavity resonance increases the gain of the structure by a factor $\Gamma = 11$ where Γ represents the ratio between the laser intensity in the micro-cavity to the one in the air.

c) Structure design ♯2b with spectral filter and meta-material phase mask: To increase the beat frequency, we shift the cold cavity filter wavelength of each LG mode, by implementing a meta-material (MM) [23] on the top surface of structure-♯2a (Fig. 4(c)). The SiN layer is patterned with holes (diameter of 50–280 nm) to create an effective refractive index with spatial dependance ($n(r)$ of 1.2–2) as shown in Fig. 3(d). The spectral shift between the two LG modes increases as $\Delta\lambda/\lambda \sim 0.01\,(\overline{n}_{00} - \overline{n}_{02})\,e/\lambda$ where e is the thickness of the SiN layer, $\overline{n}_{00}$ the effective index seen by the LG_{00} mode, $\overline{n}_{02}$ the effective index seen by the LG_{0m}. Performing simulations based on the Fox-Li method we found that a 70-nm-thick SiN layer with a 4$^{\rm th}$-order super-gauss-shaped-index spatial distribution, will keep diffraction losses below 1% for the LG_{00} mode and below 0.1% for the LG_{0m} mode. This gives a redshift of the LG_{00} mode frequency that exceeds -150 GHz.

2) Laser Dynamics for Improved Design: In order to assure strong dual-mode operation at steady state and to optimize the mask design, laser dynamics were studied. Indeed, whereas most

unwanted LG modes experience so heavy losses $\gamma_{\rm pm}$ that they can not reach the threshold, some can still build up. Their overlap with the two wanted modes leads to transverse SHB (Fig. 2(b)). The short cavity approximation allows at 1^{st} order to neglect FWM in the dynamics [20], as any eigenmode frequency beating $\omega_{\rm qpm} - \omega_{q'p'm'}/2\pi$ is larger than carrier relaxation rate $\gamma_e \geq \gamma_0$ here. Thus the laser will operate on a single longitudinal mode q and polarization eigenvector $\vec{x}$ for each mode $\mathrm{LG_{pm}}$: only the multi-transverse mode laser non-linear dynamics has to be studied. For this purpose we used the spatio-temporal Maxwell-Bloch equations of motion [19], [20] for the E-Field complex amplitude $E_i(t)$ (slowly varying envelope) of each LG mode, and the electronic population inversion $\Delta n(r,\theta,t) = n - n_{\rm tr}$. No longitudinal SHB has to be considered here as QWs have a delta-like z-distribution (compared to λ). We use a single subscript i to describe all the possible $\mathrm{LG_{pm}}$ modes. The transverse distribution of the population inversion $\Delta n(r,\theta,t)$ was approximated at 1^{st} order as $\Delta n \approx \sum_i n_i \Phi_i$ where $n_i = \iint_S \Delta n\, \Phi_i \, \mathrm{d}s$ are the population inversion spatial harmonics. This assumption for the gain saturation spatial profile is in principle physically valid at low pump rate above threshold. The equation set for photon numbers $|E_i(t)|^2$ and inversion numbers n_i reads as:

$$\begin{aligned} \frac{dE_i}{dt} &= \left[(1 - i\,\alpha_H)\, B_i \sum_k n_k\, C_{\rm ik} - \gamma_i \right] \frac{E_i}{2} + F_i \\ \frac{dn_i}{dt} &= P_i - \gamma_e\, n_i - \sum_l \sum_k B_l\, |E_l|^2\, n_k\, D_{\rm lki} \end{aligned} \tag{3}$$

where $B_i = B_0\,[1 - (i\,FSR/\Gamma_g)^2]$ is the Einstein stimulated emission coefficient, with Γ_g the modal gain bandwidth (HWHM). $B_0 = [4\,c\,\Gamma/(\pi\, w_0^2\, L_c)] \times \mathrm{d}g/\mathrm{d}n$ where $\mathrm{d}g/\mathrm{d}n$ is the QW differential gain. $F_i(t)$ is the random Langevin forces for photons, with $\langle F_i(t)\rangle = 0$ and $\langle F_i(t)\, F_k^*(t')\rangle = \xi\, \gamma_i\, \delta(t-t')\, \delta_{i-k}$ to modelize spontaneous emission quantum noise. Here ξ is the ratio of spontaneous emission to stimulated emission rate reduced to one photon. Here we neglected Langevin force for electronic carriers, as such quantum noise is clamped by saturation in a class-A laser. α_H is the linewidth enhancement factor. $P_i = \iint_S \rho_p(r,\theta,t)\, \Phi_i \, \mathrm{d}s$ are the pump distribution harmonics in the LG basis; ρ_p is the pump density distribution. $C_{\rm ik} = \iint_S |\Phi_i|^2\, \Phi_k \, \mathrm{d}s$ and $D_{\rm lki} = \iint_S |\Phi_l|^2\, \Phi_k\, \Phi_i \, \mathrm{d}s$ are normalized spatial gain coupling coefficients due to SHB, leading to spatial self- and cross-saturation effects and non-linear mode coupling: the goal of this laser design is to obtain weak mode-coupling coefficients between the two wanted modes. We numerically solved (3), using the fixed-step 4th-order Runge-Kutta method, for various mask designs and $i < 10$, for $\gamma_e = \gamma_0 = 10^9\ s^{-1}$, $B_0 = 1\ s^{-1}$, $\xi = 1.5$ and $\alpha_H = 3$. $|E_i(t)|^2$ build-ups for a $\mathrm{LG_{00}/LG_{02}}$ design are shown in Fig. 2(c). The steady state is reached after $\sim 1\,\mu s$, with high extinction ratio of unwanted modes, at quantum limit. Similar behaviour with stable dual-mode operation are obtained for higher $m > 2$ design and low/high pump rates. It is a theoretical proof of stable simultaneous two-mode operation in cw.

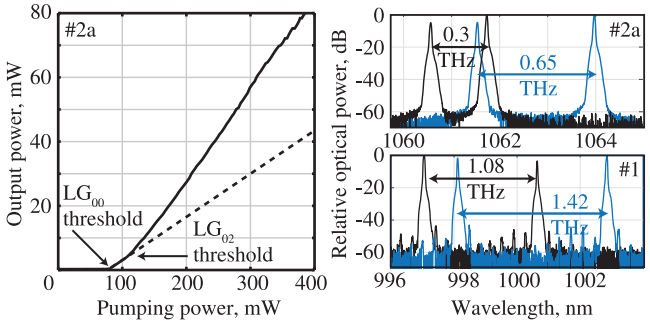

Fig. 5. Power and spectral characterization of the laser. Left: Output power for design ♯2a, the dashed line shows the continuity of the output power for $\mathrm{LG_{00}}$ mode. Right: Optical spectra for $\mathrm{LG_{00}/LG_{02}}$ simultaneous operation for design ♯2 (top) at pumping rates of 2 (black) and 2.8 (blue); and for design ♯1 (bottom) at rates of 1.7 (black) and 2.7 (blue).

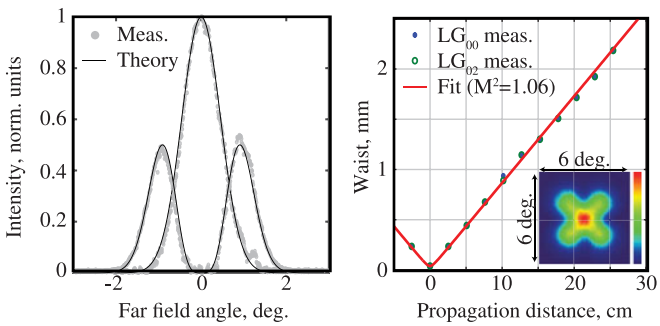

Fig. 6. Dual-frequency beam characterization. Left: cross section measurement of the beam intensity for each of the two modes. Right: M^2 measurement for the two modes with, in inset, the beam far-field intensity profile.

III. Laser Implementation and Characterizations

For the two possible designs, the GaAs substrate back-sides of the chips were polished with an angle ($\sim 2°$), and a 200-nm chromium layer was evaporated to avoid parasitic Fabry-Perot fringes and backscattering ($\sim 300\ \mu$m thick). The gain-mirror temperature is stabilized at 293 K thanks to a Peltier thermoelectric cooler, and optically pumped by a 808-nm 400-mW low-noise single-mode laser diode, focused on a 50-μm-radius circular spot (at $\sim 70\,°$ Brewster angle). This pumping scheme allows to minimize thermally-induced wavefront distortion, thus preserving the LG basis. The radius of the $\mathrm{LG_{0m}}$ mode matches with the pump radius. The laser elements are glued on a breadboard, and the whole laser is placed in a metallic box for acoustic isolation purpose. The laser beam is collimated using a 75-mm-focal achromatic lens, followed by an optical isolator to prevent from parasitic feedback.

The laser is operating in a stable cw dual-frequency state at room temperature at a wavelength of $\sim 1\ \mu$m. We observe in Fig. 5 the threshold density for the $\mathrm{LG_{00}}$ mode around 1.1 kW/cm^2, and the threshold density for the $\mathrm{LG_{02}}$ mode and the dual-frequency operation around 1.4 kW/cm^2, as confirmed by a simultaneous observation of the far-field intensity map (see Fig. 6). This shows an increase of the threshold density with higher-order transverse-mode operation, due to a lower overlap between pump and laser mode. We observe dual-frequency laser

operation over a wide range of beating frequency from 0.03 to 3 THz, using laser-♯1 and -♯2a. Fig. 5 shows the optical spectra, with a SMSR of longitudinal modes as high as 55 dB (at quantum limit) [14]. Fig. 6 shows the far-field transverse distribution that exhibits two low-divergence (1.3° half-width at half maximum) LG modes, namely the LG_{00} and LG_{02} modes, close to diffraction limit without any degradation of spatial coherence by diffraction on the metallic mask. The beam quality factor M^2 has been measured. The far-field image is acquired along propagation, and fitted by the Laguerre-Gauss mode wave-functions. A LG_{0m} quality factor of $M^2 = 1.06 \times (m+1)$ is measured for this dual-frequency laser. Changing the mask design allows simultaneous operation of LG_{00} and higher LG_{0m} mode with $m = 3, 4$ with larger spectral difference. The laser operates on the same linear polarization state for both modes. It follows the [110] crystal axis as expected [14], with an orthogonal polarization extinction ratio > 45 dB, as measured from the beating note power at a RF frequency of ~ 115 MHz (degeneracy lift fixed by birefringence) on the noise spectrum. This peaks arise due to a slight rotation of the isolator axis compared to [110]. Finally, short-term simultaneous dual-frequency operation was checked by recording the cw optical spectrum at the output of a high-resolution grating monochromator (JY HR1000), using a streak camera (Hamamatsu C10910-02) with a time resolution of 5 ns (see Ref. [17]).

IV. Coherent and Tunable THz Emission

A. Spatial Coupling & Beat Power

The stability of the dual-frequency laser relies on the low overlap between the two transverse modes in intensity. However, the electrical fields of these transverse modes being the eigenvectors of an orthonormal basis, their crossed projection is perfectly zero, thus prohibiting any signal generation at the beat frequency in a non linear element (non linear cristal, photodiode, etc.). To overcome this major limitation, one should ideally transform the beam in a way that maximizes the scalar product between the two modes of interest. One straightforward solution consists in restraining the transverse space, since the scalar product is zero over the all transverse plane but differs from zero locally. For example, in the case of the dual-frequency operation based on the coexistence of the LG_{00} and LG_{02} modes, one could use a simple mask that would select only one lobe of the LG_{02} mode, thus one-quarter of the LG_{00} mode.

Since we are using a fibered UTC photodiode for THz emission, we propose to restrain the transverse plane by coupling the laser beam within a polarization-maintaining single-mode optical fiber. The two modes being linearly-polarized along the same axis, they are injected along the axis of a polarization eigenmode of the optical fiber. To allow some coupling of the asymmetrical modes (LG_{02}, LG_{03}, LG_{04}, etc.) with the fundamental mode of the optical fiber, that is symmetrical, we offset the fiber position in the transverse plane relatively to the optical axis. Modal calculations show in Fig. 7(top) the two-dimensional mapping of the coupling of the LG_{00} and LG_{02} modes with the fiber mode, as a function of the fiber position relatively to the optical axis (at center). As expected, the best coupling is obtained for

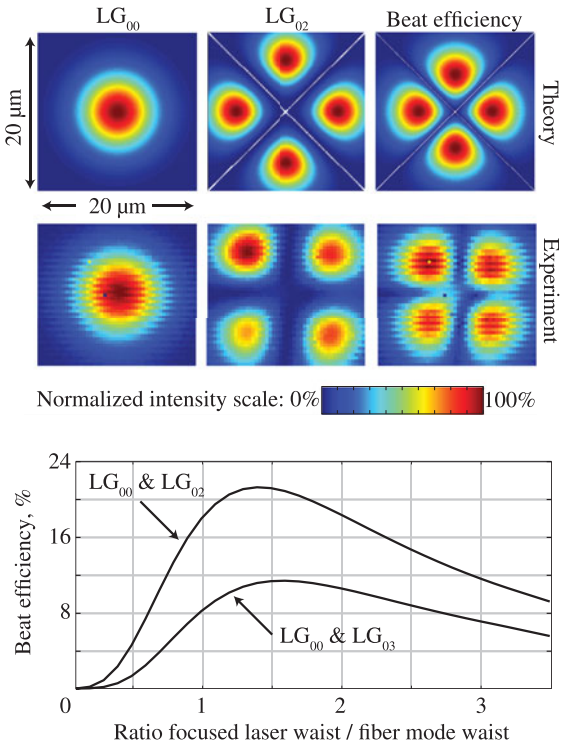

Fig. 7. Beat efficiency by Laguerre-Gauss modes injection within a single-mode fiber. Top: The normalized coupling coefficient (intensity) is calculated using modal simulation and mapped as a function of the fiber position relatively to the optical axis (at center) for the LG_{00} and LG_{02} modes; along with the normalized beat efficiency map. Associated experimental mapping are also represented. Bottom: Beat efficiency dependence on the ratio between the injected laser beam waist and the fiber mode waist, for the (LG_{00}, LG_{02}) and (LG_{00}, LG_{03}) combinations.

the symmetrical mode (LG_{00}) at center position, while it is at the center of the lobes of the LG_{02} mode for this asymmetrical mode. From these simulations, we plotted the beat efficiency, defined as the ratio of the beat power over the beat power that would be emitted if the two modes were perfectly collinear. The experimental validation of these calculations was conducted by moving a panda-type polarization-maintaining optical fiber in the transverse plane with two-dimensional nano-positionners, and measuring at the optical spectrum analyzer the injected power of each mode, which is trivial since the two transverse modes have different frequencies. As shown in Fig. 7(top), there is a very good agreement with the modal simulation, for the coupling maps of the LG_{00} and LG_{02} modes, but also for the beat efficiency map. Finally, Fig. 7(bottom) shows how the beat efficiency scales as a function of the ratio of the laser waist at the fiber input over the fiber mode waist. If the laser waist is 1.4 times larger than the fiber mode waist, a maximum beat efficiency of 21% can be reached for the LG_{00} and LG_{02} combination. Similar calculations could be conducted for higher-order modes. For the LG_{00} and LG_{03} mode, a maximum beat efficiency of 11.6% could be reached as shown in Fig. 7(bottom). As the order of the mode increases, the beat efficiency decreases, since the mode is less confined thus the overlap reduces with the LG_{00} mode, but also because the number of lobes increases. If the beat

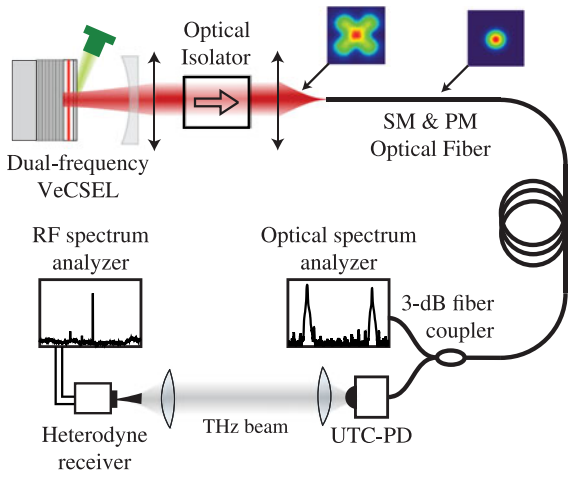

Fig. 8. Experimental setup for simultaneous study of optical and THz spectra using a commercial UTC-PD emitter.

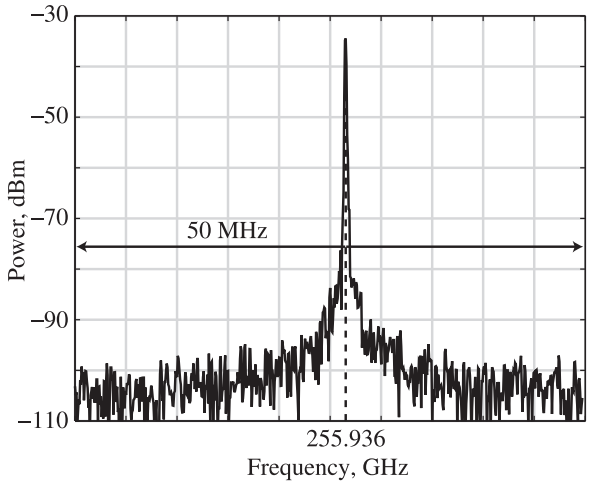

Fig. 9. Coherent THz spectrum at the UTC-PD output for a 100-kHz resolution bandwidth and a 3-ms sweep time, for laser design ♯2a.

efficiency was to low to drive the photo-mixer, one straightforward solution would consist in using an optical amplifier.

B. THz Coherent Emission

THz emission was successfully achieved by exciting a commercial UTC-PD (from NTT Electronics corp.) that integrates a high-resistivity Si lens for broadband emission. As shown in Fig. 8, this emitter is pigtailed with a single-mode (SM) polarization-maintaining (PM) fiber (panda-type). The laser beam is collimated with a 75-mm focal lens, optically isolated, then focused in an offsetted fiber using a 15-mm focal lens. We use a fiber coupler to control the fiber injection by monitoring the optical spectrum of the injected signal, while injecting this signal in the UTC-PD. The THz beam that comes from the UTC-PD is collimated using a 10-cm focal-length Teflon lens, then focused using an identical lens into a calibrated heterodyne head receiver that allows to observe the THz spectrum on a RF analyzer. As shown in Fig. 9, we observe a very coherent

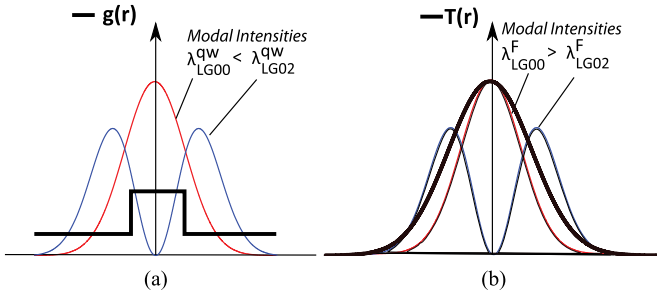

Fig. 10. (a) Tuning principle with design-♯1: difference of losses between the two LG modes. (b) Tuning principle with design-♯2a : difference of temperature between the two LG modes.

signal around 256 GHz with a full-width at half-maximum of 150 kHz for a 3-ms measuring time, that tends to be limited by the 100-kHz resolution bandwidth of the RF analyzer. The output power of −35 dBm is limited by the maximum output power of the UTC-PD, after taking account of the 2-dB losses due to the Teflon lenses. We also observe a very large signal-to-noise ratio, that exceeds 60 dB, thanks to the active heterodyne receiver head. The impact of measuring time on coherence will be discussed in the following section relative to frequency noise. The combination of such a coherence and a signal-to-noise ratio is attractive for applications such as spectroscopy.

C. THz Tunability

The frequency difference between the two LG modes ($\gg \gamma_e/2\pi$) is a multiple N of FSR plus/minus the Gouy phase-shift-induced frequency offset $\delta\nu_G$ [18] (Fig. 2). For design ♯2a the beat frequency, so N, is ruled by pump power: gain mirror heating induces a temperature radial gradient across the modes [14], leading to a red shift, at a rate $\delta\nu/\delta T$, of the micro-cavity filter wavelength between LG_{0m} and LG_{00}, as represented in Fig. 10. The beat frequency falls in the range $\delta\nu = 0.03$–0.7 THz. Alternatively, with design ♯1, we exploit QW band-filling process by electronic carriers (different losses/excitation between the modes), leading to blue shift, at a rate $\delta\nu/\delta g$ with QW gain change, to increase the possible beat frequency range above the THz level.

As shown in Fig. 11(top) for the laser design ♯2a, the frequency difference between the two modes increases with pump power. For the (LG_{00}, LG_{02}) modes pair, we observe a chaotic regime at low pump power ($<$ 260 mW), likely because spectral *and* spatial overlaps between the two modes are too strong. As we increase the pump power, the spectral overlap decreases (beat frequency increases) and a coherent dual-frequency operation is reached. For the (LG_{00}, LG_{03}) and (LG_{00}, LG_{04}) modes pairs, the spatial overlap is small enough to maintain a coherent dual-frequency operation from threshold (at pump power of 50 mW) to the maximum available pump power (450 mW). The frequency difference between the two modes is represented in Fig. 11(bottom), and shows a non linear evolution of the beat frequency as a function of the pump power, due to a change in the chirp of the fundamental mode (higher wavelength), as observed on the top figure, mainly for the (LG_{00}, LG_{03}) and

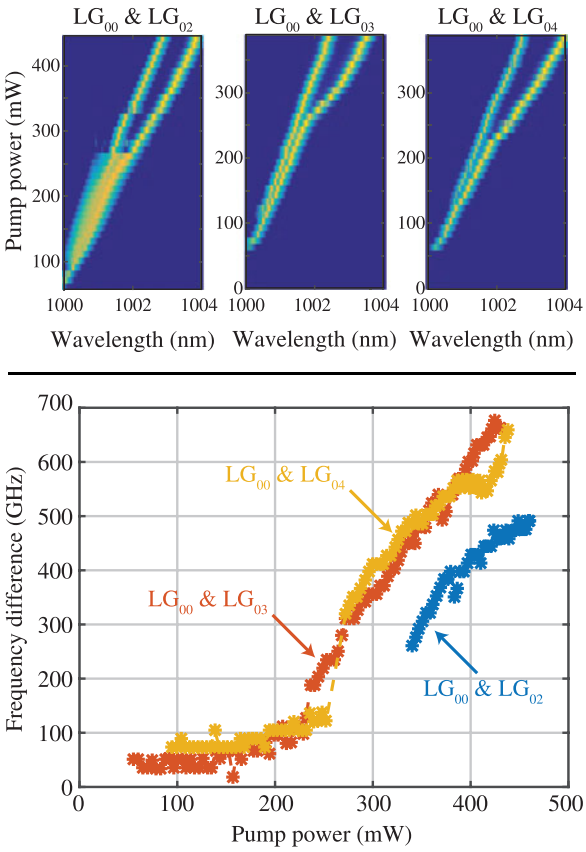

Fig. 11. Beat frequency tunability controlled by the pump power for laser design ♯2a. The top part presents the evolution of the optical spectrum with pump power for the (LG_{00}, LG_{02}), (LG_{00}, LG_{03}) and (LG_{00}, LG_{04}) modes. The lower part shows the beat frequency dependence on pump power for these same modes pairs.

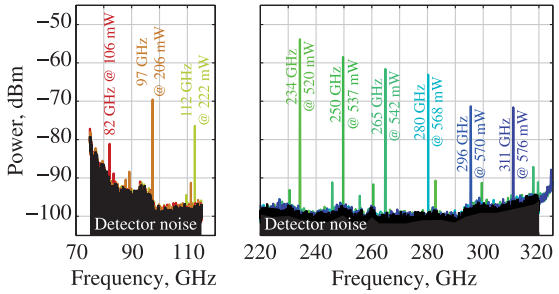

Fig. 12. THz spectra for the (LG_{00}, LG_{03}) modes using the thermally-driven structure. Spectra are measured using a calibrated heterodyne head receiver operating in the 75–110 GHz range (left) or 220–325 GHz range (right), both for a 300-kHz resolution bandwidth.

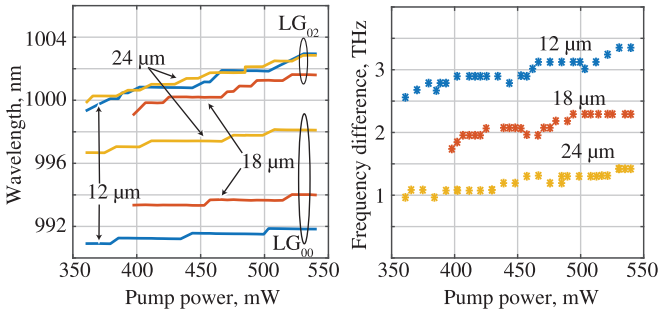

Fig. 13. Tunability for laser ♯1 with pump power for different absorbing mask inner dimensions. Left: Modes wavelengths; Right: beat frequency.

(LG_{00}, LG_{04}) modes pairs. Up to 250 mW of pump power, the chirp can be estimated quite accurately by evaluating the mode temperature. However, the change in the chirp of the fundamental mode is not fully explained yet, and could be due to non linear intra-cavity effects for example. Nevertheless, this physical effect opens up the tunability window, since the beat frequency can be tuned from 50 GHz up to 700 GHz using a same structure, e.g. for the (LG_{00}, LG_{03}) modes pair. Additionally, we have shown that laser design ♯2b allows to offset this tunability window, with a beat frequency starting in the range 100–600 GHz, depending on the meta-material spatial distribution, and thus allows to reach higher beat frequencies.

By looking closer at the beat frequency tuning, one could observe 15-GHz steps that correspond to the free spectral range of the laser cavity. Such a step-tunability can be observed easily by looking at the THz spectra at different pump power, as shown in Fig. 12 for the (LG_{00}, LG_{03}) modes pair. On this figure, the THz spectra measured at different pump powers were superimposed, that clearly shows the 15-GHz-steps tunability of the THz source. Low THz power is observed at low frequencies, i.e. at lower pumping rates, since the optical power is lower and the UTC-PD presents a cut-off frequency due to its bow-tie antenna dimensions. At high frequencies, we also observe low THz power due to the cut-off of the UTC-PD emitter. Finally, the THz power is not as high as the one shown in Fig. 9 since the beat efficiency is lower for the (LG_{00}, LG_{03}) modes pair than the (LG_{00}, LG_{02}) modes pair, as calculated in Fig. 11. Note that adding a saturated optical fiber amplifier before the UTC-PD would be a straightforward solution to maximize and stabilize the output THz power from the UTC-PD, while keeping THz tunability.

For the structure ♯1 that is dominated by bandfilling effects, Fig. 13(top) shows an increase of the wavelength of the LG_{00} and LG_{02} modes with pump power, due to thermal effects as previously described. However, as shown in the bottom figure, we observe a much larger frequency difference ($>$ 1 THz) if compared to the thermally-driven structure ($<$ 700 GHz). One striking effect is the influence of the absorbing mask dimension on modes wavelengths, particularly for the fundamental mode. As the mask inner dimension increases, the fundamental mode observes lower losses, and thus operates at a lower gain, i.e. for a reduced conduction band-filling, leading to an increased wavelength of operation. Since the higher-order mode presents a much reduced overlap with the inner part of the mask, it is much less sensitive to the add of these extra losses. For the 24 μm, 18 μm and 12 μm inner dimensions of the mask, losses were calculated to be respectively of 1.6%, 0.71% and 0.27% for the fundamental mode.

D. Frequency Noise, Linewidth and Coherence Time

Among all characteristics, the main interest of a two-frequency laser is the correlation in time that may exist between

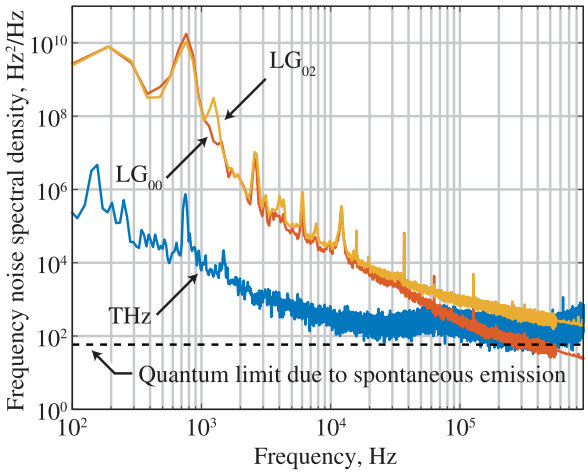

Fig. 14. Frequency noise spectrum of each optical mode compared to the frequency noise of the THz beating for laser ♯2a.

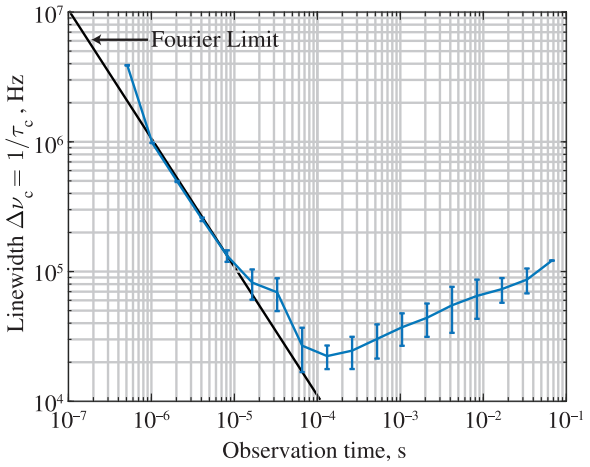

Fig. 15. Temporal coherence of the THz signal for the (LG_{00}, LG_{02}) pair.

the frequency fluctuations of the two emitted modes: this correlation gives rise to a low frequency noise THz beat-note. In a single-frequency VeCSEL, the strongest part of the frequency fluctuations is due to both the mechanical and to the thermally induced index fluctuations that occur in the gain chip due to the intensity noise of the pump power [24]. At high frequency, the linewidth is limited by the spontaneous emission quantum noise (given by Langevin forces in (3)). This contribution of course depends on the specific VeCSEL configuration under study, but it is as low as 100 Hz^2/Hz [19].

The frequency noise of each optical mode was measured thanks to a traditional Fabry-Perot discriminator set-up. Because the laser emits two optical modes, we have to ensure that only one mode fluctuations are observed at a time. For that reason, the frequency comb of the frequency discriminator was carefully designed to permit the frequency-to-intensity conversion of one VeCSEL mode only, while the power of the second one is rejected by the cavity. This operation was performed for each of the two optical modes. In a second step, the heterodyne receiver described in Fig. 8 was coupled to a GHz wide-memory data acquisition card, in order to sample in time the THz beat-note. This beat note was downshifted below 1 GHz by using the spectrum analyzer in a zero-span mode and by adjusting manually the local oscillator frequency. The intermediate-frequency signal at the heterodyne head output was amplified using a 20-dB-gain 0.1–1-GHz-bandwidth low-noise amplifier. The beat-note time sample was then analyzed thanks to a numerical Hilbert transform, in order to extract the frequency noise fluctuations, as described in Ref. [25].

The results of these experiments, shown in Fig. 14, demonstrate the efficiency of this two-frequency laser concept. We indeed obtain a THz beating exhibiting low frequency noise compared to the optical frequency noise of the two laser modes (up to four decades). This is due to the fact that the same fluctuations feed simultaneously the two optical modes. Because the two modes are mostly uncorrelated, the frequency noise fundamental limit is simply due to the spontaneous emission quantum noise of the two optical fields. This white noise limit is almost reached at a frequency as low as 10 kHz.

From the THz beating signal sampled in time domain and used to evaluate the frequency noise spectrum presented in Fig. 14, we also extracted the value of the coherence time. For this purpose, we used the numerical computation proposed in Ref. [25], that leads to the spectral width $\Delta\nu_c$ defined by Mandel and Wolf [26], [27] as a function of the observation time. This definition of the spectral width is, to our knowledge, a far better estimation than the traditional FWHM as it is consistent whatever the spectral shape. Moreover, it is easily related to the coherence time thanks to the simple relation (time-frequency uncertainty criteria) $\tau_c = 1/\Delta\nu_c$. The results coming from this process are displayed in Fig. 15.

The important result is that the THz oscillator is close to the Fourier limit up to times as long as 0.1 ms, exhibiting a linewidth below 30 kHz, without care of mechanical stability in this experiment. The technical low-frequency noise of the laser increases the spectral width before reaching the quantum limit, due to the residual decorrelation that exists between the two optical modes.

V. Summary and Perspectives

We demonstrated THz emission by seeding a uni-travelling-carrier photodiode by an optically-pumped dual-frequency vertical-external-cavity surface-emitting laser that operates around 1 μm with an output power of 80 mW for a 400-mW pump power. Thanks to integrated amplitude and phase masks based on III-V mature technologies, a compact and quasi-monolithic laser was realized, offering robust dual-frequency operation along with high-coherence optical properties from a temporal, spatial and polarization point of view. This robust two-wavelengths operation within a homogeneous-gain medium was obtained by the coexistence of two selected Laguerre-Gauss transverse modes within the free space plano-concave type optical cavity, this selection being possible thanks to adequate amplitude mask design driven by simulations based on spatio-temporal Maxwell-Bloch equations. Two kinds of structures

where realized and characterized, one including an integrated intra-cavity filter that allows thermal tuning of the beat frequency by adjusting the pump power, another with an anti-reflection coating that shifts the beat frequency towards high beat frequencies due to band-filling effects. The former showed beat-frequency tunability from 50 GHz to 750 GHz by 15-GHz steps (free spectral range steps), while the latter showed similar frequency extension but starting at few THz, depending on the mask losses applied to the fundamental mode. Calculations of the transverse modes coupling by injection within a single-mode fiber showed more than 20% of beat efficiency, thus offering a simple and reasonable solution to couple these modes towards THz emission using a fibered photo-mixer. Thanks to the outstanding performances of the laser, we demonstrated THz emission from the uni-travelling-carrier photodiode with high temporal coherence, and measured THz spectra with heterodyne-head receivers with 10–40+ dB of dynamic range within a 300-kHz resolution bandwidth, that could be attractive to many applications, e.g. for spectroscopy or imaging. The temporal coherence was specifically studied and the proof of concept of the dual-frequency operation was validated, since the THz frequency noise is about 40-dB lower than the optical frequency noise, thus proving that deleterious technical noises are partially correlated for the two optical modes and therefore disappear partially from the beat signal. Further work on pump power stabilization by using more adequate electronics should allow to reduce even more the THz frequency noise and thus compete with electronic-multiplied source, despite the decades between the seeding oscillators frequencies, i.e. either a phase-locked 10's of GHz signal for the electronic source or two 300-THz free-running signals for the optical source.

One drawback of this work being the limited output THz power, due to the uni-travelling-carrier photodiode limitation, alternative solutions should be investigated. One could use next-generation photodiodes and use arrays of them, or use intra-cavity plasmonic photo-conductive antennas or non-linear crystal rectification to generate much higher THz output power by taking advantage of the high intracavity intensity. Also, the main concepts that have been exposed in this article could be transposed to 1,55 μm for higher-efficiency photo-mixers and commercial applications.

REFERENCES

[1] G. Scalari, C. Walther, J. Faist, H. Beere, and D. Ritchie, "Electrically switchable, two-color quantum cascade laser emitting at 1.39 and 2.3 THz," *Appl. Phys. Lett.*, vol. 88, no. 14, 2006, Art. no. 141102.

[2] H. Hübers, S. Pavlov, and V. Shastin, "Terahertz lasers based on germanium and silicon," *Semicond. Sci. Technol.*, vol. 20, no. 7, pp. S211–S221, 2005.

[3] J. Bjarnason *et al.*, "ErAs: GaAs photomixer with two-decade tunability and 12 μW peak output power," *Appl. Phys. Lett.*, vol. 85, no. 18, pp. 3983–3985, 2004.

[4] H. Ito, T. Furuta, F. Nakajima, K. Yoshino, and T. Ishibashi, "Photonic generation of continuous THz wave using uni-traveling-carrier photodiode," *J. Lightw. Technol.*, vol. 23, no. 12, pp. 4016–4021, Dec. 2005.

[5] J. Mangeney *et al.*, "Continuous wave terahertz generation up to 2 THz by photomixing on ion-irradiated $In_{0.53}Ga_{0.47}As$ at 1.55 μm wavelengths," *Appl. Phys. Lett.*, vol. 91, no. 24, 2007, Art. no. 241102.

[6] M. Scheller *et al.*, "Terahertz generation by difference frequency conversion of two single-frequency VECSELs in an external resonance cavity," *SPIE Int. Soc. Opt. Photon.*, vol. 8966, 2014, Art. no. 89660E.

[7] H. Ito *et al.*, "High-power photonic millimetre wave generation at 100 GHz using matching-circuit-integrated uni-travelling-carrier photodiodes," *Inst. Electr. Eng. Proc. Optoelectron.*, vol. 150, no. 2, pp. 138–142, Apr. 2003.

[8] C. Renaud *et al.*, "A high responsivity, broadband waveguide uni-travelling carrier photodiode," *Photon. Eur*. Int. *Soc. Opt. Photon.*, vol. 6194, 2006, Art. no. 61940C.

[9] A. Klehr *et al.*, "High-power monolithic two-mode DFB laser diodes for the generation of THz radiation," *IEEE J. Sel. Topics Quantum Electron.*, vol. 14, no. 2, pp. 289–294, Mar./Apr. 2008.

[10] C. Friedrich *et al.*, "New two-color laser concepts for THz generation," *IEEE J. Sel. Topics Quantum Electron.*, vol. 14, no. 2, pp. 270–276, Mar./Apr. 2008.

[11] A. Rolland *et al.*, "Non-linear optoelectronic phase-locked loop for stabilization of opto-millimeter waves: Towards a narrow linewidth tunable THz source," *Opt. Express*, vol. 19, no. 19, pp. 17944–17950, 2011.

[12] G. Ducournau *et al.*, "Highly coherent terahertz wave generation with a dual-frequency Brillouin fiber laser and a 1.55 μm photomixer," *Opt. Lett.*, vol. 36, no. 11, pp. 2044–2046, 2011.

[13] F. Pallas, E. Herault, J. Zhou, J.-F. Roux, and G. Vitrant, "Stable dual-wavelength microlaser controlled by the output mirror tilt angle," *Appl. Phys. Lett.*, vol. 99, no. 24, 2011, Art. no. 241113.

[14] A. Laurain, M. Myara, G. Beaudoin, I. Sagnes, and A. Garnache, "Multiwatt–power highly–coherent compact single–frequency tunable vertical–external–cavity–surface–emitting–semiconductor–laser," *Opt. Express*, vol. 18, no. 14, pp. 14627–14636, 2010.

[15] S. De *et al.*, "Class-A dual-frequency VECSEL at telecom wavelength," *Opt. Lett.*, vol. 39, no. 19, pp. 5586–5589, Oct. 2014.

[16] M. Wichmann *et al.*, "Systematic investigation of single-and multi-mode operation in vertical-external-cavity surface-emitting lasers," *SPIE Int. Soc. Opt. Photon.*, vol. 8966, 2014, Art. no. 89660N.

[17] R. Paquet *et al.*, "Coherent continuous-wave dual-frequency high-Q external-cavity semiconductor laser for GHz-THz applications," *Opt. Lett.*, vol. 41, no. 16, pp. 3751–3754, Aug. 2016.

[18] A. E. Siegman, *Lasers*. Mill Valley, CA, USA: University Science, 1986.

[19] A. Garnache, A. Ouvrard, and D. Romanini, "Single–frequency operation of external–cavity VCSELs: Non-linear multimode temporal dynamics and quantum limit," *Opt. Express*, vol. 15, no. 15, pp. 9403–9417, 2007.

[20] S. E. Hodges, M. Munroe, J. Cooper, and M. G. Raymer, "Multimode laser model with coupled cavities and quantum noise," *J. Opt. Soc. Amer. B*, vol. 14, no. 1, pp. 191–199, 1997.

[21] A. Gahl, S. Balle, and M. S. Miguel, "Polarization dynamics of optically pumped VCSEL's," *IEEE J. Quantum Electron.*, vol. 35, no. 3, pp. 342–351, Mar. 1999.

[22] S. Cortez, O. Krebs, and P. Voisin, "In-plane optical anisotropy of quantum well structures: From fundamental considerations to interface characterization and optoelectronic engineering," *J. Vacuum Sci. Technol. B*, vol. 18, no. 4, pp. 2232–2241, 2000.

[23] M. S. Seghilani *et al.*, "Photonic crystal-based flat lens integrated on a Bragg mirror for high-Q external cavity low noise laser," *Opt. Express*, vol. 22, pp. 5962–5976, 2014.

[24] M. Myara *et al.*, "Noise properties of NIR and MIR vecsels (invited paper)," *Proc. SPIE*, vol. 8606, Feb. 2013, Art. no. 86060Q.

[25] N. Von Bandel *et al.*, "Time dependant linewidth: Beat-note digital acquisition and numerical analysis," *Opt. Express*, vol. 24, no. 24, pp. 27961–27978, 2016.

[26] L. Mandel and E. Wolf, *Optical Coherence and Quantum Optics*. Cambridge, U.K.: Cambridge Univ. Press, 1995.

[27] B. Saleh and M. C. Teich, *Fundamentals of photonics*. Hoboken, NJ, USA: Wiley, 1991.

Stéphane Blin was born in St Nazaire, France, on January 6, 1977. He received the Ph.D. degrees in physics from Enssat, Lannion, France, and in electrical engineering from Université Laval, Québec, Canada, in 2003. From 2000 to 2004, he led original optical injection experiments at very low injection levels which led to original metrological methods, and studied frequency noise of highly-coherent lasers with DiCOS Technol. From 2004 to 2007, his research interests include on acoustic fiber-sensor arrays and air-core photonic-bandgap fiber-optic gyroscope at Ginzton Laboratory, Stanford University, CA, USA. From 2007 to 2009, he worked at Foton laboratory (Enssat) on high-peak-power fiber lasers for material processing applications. Since 2009, he has been with the Institut d'Électronique et des Systèmes, University of Montpellier, France, as an Associate Professor. His current research interests include THz-waves generation, detection, and systems.

Romain Paquet was born in 1990. He received the Master's degree in optoelectronics and microwave engineering from the University of Montpellier, Montpellier, France, in 2013. He is currently working toward the Ph.D. degree on dual frequency lasers for THz generation from the Institut d'Électronique et des Systèmes, Montpellier, France.

Mikhaël Myara was born in Montreuil-sous-Bois, France, on November 2, 1975. He received the Engineer degree in applied computer science and optoelectronics in 1998, and the Ph.D. degree in optoelectronics, from the University of Montpellier, Montpellier, France, in 2003. He is currently with the Institut d'Électronique et des Systèmes, University of Montpellier, where he is mainly involved in research on the study of photonic sources coherence by means of noise metrology.

Baptiste Chomet was born in Paris, France, on February 11, 1990. He received the M.S. degree in physics from Enssat, Lannion, in 2013. Since then, he has been with the Institut d'Électronique et des Systèmes, University of Montpellier as an Engineer and working toward the Ph.D. degree. He is currently working on the development of highly sensitive optical sensors for near- and mid-IR applications.

Luc Le Gratiet joined the CNRS in 2001. He has more than 20 years experience in the field of micro- and nanotechnology. He is currently working on the fabrication of nanostructures for photonics. He is a specialist of electron beam writing, atomic deposition technique, polishing of semiconductors. Since 2012, he has been a member of Comité National de la Recherche Scientifique which is the evaluation authority of the CNRS.

Mohamed Sellahi was born in Algeria, in 1984. He received the Engineer Diploma in electrical engineering and electronics from the University of Boumerds, Boumerdès, Algeria, in 2008, the Masters degree in optoelectronics and microwave engineering in 2011, and the Ph.D. degree in optoelectronics from the University of Montpellier, Montpellier, France, in 2014. His research interests include on semiconductor lasers, laser beam shaping, laser dynamics, and optical noise.

Grégoire Beaudoin received the M.Sc. degree in physics from the University of Strasbourg, Strasbourg, France. He is an Engineer at the Centre National de la Recherche Scientifique. He is Technical Responsible of the MOCVD epitaxy at the Center for Nanoscience and Nanotechnology (C2N Marcoussis), France.

Isabelle Sagnes was born in Tunisia, in 1967. She received the Ph.D. degree in physics for her work on the electrooptical properties of epitaxial heterostructures on Silicon from the University Joseph Fourier, Saint-Martin-d'Hères, France, in 1994. From 1994 to 1997, she was with France Telecom/CNET-CNS, Grenoble, as a Process Engineer in silicon microelectronics technology, with a special interest in CVD growth of epitaxial Si/SiGe heterostructures, rapid thermal processing (oxidation, nitridation, implant annealing), and bipolar and CMOS technologies. She joined the CNET Laboratory, Bagneux, France, in 1998 as a Research Engineer in semiconductor III–V compounds and in 1999 the CNRS in the FT/CNRS joint laboratory named LPN: Laboratoire de Photonique et Nanostructures, Marcoussis, France. Since June 2016, LPN has merged with IEF (Institut d'Electronique Fondamentale) to form the Center for Nanosciences and Nanotechnologies (C2N) of Paris-Saclay University. She is an author or coauthor of about 300 papers in international journals. Her research interests include MOCVD growth of vertical cavity systems on GaAs and InP substrates, MOCVD growth of quantum dots on InP substrates, heteroepitaxy of GaAs on Ge/Si virtual substrate, Ge growth in a III–V reactor, and III–V device technology as the processing of photonic crystals and GaAs/AlAs micropilars.

Guillaume Ducournau received the Diplome d'ingénieur from ESIGELEC, Rouen, France, in 2002 and the Ph.D. degree in fiber optic communication systems using DPSK modulation schemes from the Université de Rouen, Mont-Saint-Aignan, France, in 2005. In 2002, he worked in Canada on optical fiber Bragg gratings. Since 2007, he has been an Assistant Professor at the IEMN/University of Lille 1 and Polytech'Lille Graduate School. He is mainly involved in THz communications research using optoelectronic THz photomixers, THz instrumentation, and imaging. He has 13 years of experience in the domain of optical fibers technology and THz instrumentation. In order to carry out his research, he developed several experimental setups dedicated to the characterization of optoelectronics and THz devices. He is author or coauthor of more than 100 publications in peer-reviewed international journals or peer reviewed conferences proceedings. His current research focuses on THz communications in the 300-GHz band based on photonic devices.

Philipp Latzel studied physics at the TU Dresden in Germany, received the diploma in 2009, and received the Ph.D. degree in high efficiency THz photomixers from IEMN, University of Lille 1, Lille, France, in 2014. In 2010, he worked as a Research Assistant on organic solar cells at the IAPP, TU Dresden. . His research interests include UTC photodiodes and photoconductors in the THz frequency range and their application in THz communication systems.

Jean-François Lampin received the Engineering degree from the Institut Supérieur d'Electronique du Nord, Lille, France, in 1994 and the Ph.D. degree from the University of Lille, Lille, France, in 1997. He was a Postdoctoral Researcher in the Laboratoire d'Optique Appliquée, Palaiseau, France, where he was involved in the study of electron relaxation with pump-probe experiments based on femtosecond lasers. Since 1998, he has been a Research Scientist at the Institute of Electronics, Microelectronics and Nanotechnology, Centre National de la Recherche Scientifique, Villeneuve d'Ascq, France. His research interests include terahertz (THz) generation and detection, subpicosecond lifetime semiconductors, THz optoelectronic generation using photoconductors and photodiodes, THz antennas, and THz communications.

Arnaud Garnache born in France, in 1972. He received the Ph.D. degree in physics from the University J. Fourier Grenoble, France, in 1999. He is a Senior Scientist CNRS, Ph.D., HDR. He is the leader of the VeCSEL team at IES. He was a Postdoctoral Fellow at University of Southampton, Southampton, U.K., working on ultra-short pulses high-power VECSEL. Since 2001, he has been at IES, where his research interests include on technological development and physical properties of highly-coherent III–V semiconductor laser sources for photonic applications in the NIR and MIR, and nonconventional photon states. He directed about 10 Ph.D.'s and is author/coauthor of about 120 publications and 6 patents. He was the conference chair of the European WORKSHOP VECSEL 2012, 2013, 2015. In 2000, he was awarded the Young Researcher Prize by the French Physical Society; in 2011 the Award of Scientific Excellence CNRS; in 2013 the innovation award "photon de bronze," French Optical Society with INNOPTICS.

Terahertz Heterodyne Communication Using GaAs Field-Effect Transistor Receiver

Stéphane Blin, Philippe Nouvel, Annick Pénarier, and Jeffrey Hesler

***Abstract*— We report the first successful terahertz heterodyne communication using a field-effect transistor for detection. The communication is a real-time transmission of an uncompressed high-definition TV signal at a data rate of 1.5 Gbps with a 307-GHz carrier frequency. The emitter is a frequency-multiplied amplifier chain whose last stage is a second harmonic mixer that multiplies the carrier signal by the data. The receiver only consists of a GaAs high-electron-mobility transistor that acts as a quadratic receiver, and two 20-dB-gain amplifiers, no limiting amplifier or forward error correction were used. A direct communication would be impossible with such a combination of modulation scheme at emission and quadratic detection at reception, while it is possible in a heterodyne configuration. In addition, for the same source power, the heterodyne scheme allows to increase the communication bandwidth from 80 MHz to more than 2 GHz for a local oscillator power of –8 dBm.**

***Index Terms*— Terahertz radiation, communication systems, millimeter wave FETs.**

I. Introduction

NEXT-GENERATION wireless communication systems require higher carrier frequencies in order to increase the possible data rate that is supported. In this letter, we are interested in wireless high-data-rate transmission in the terahertz (THz) domain, since the use of a THz carrier frequency possibly enables data transmission up to 100 Gbps [1]. Schottky barrier diodes (SBD) are widely used as detectors for high-data-rate communication experiments up to tens of Gbps [2]. Due to their high sensitivity (a few kV/W), zero-biased SBD are presently the best available detectors for THz communication but their high output impedance (about 1 kΩ) limits integration with low-impedance high-bandwidth amplifiers for monolithic microwave integrated circuits (MMIC), and they are not robust to high input THz powers. Biased SBD would offer a lower output impedance but with a reduced sensitivity.

In order to overcome these drawbacks, we propose the use of a pseudomorphic High-Electron-Mobility Transistor (pHEMT) for THz detection. Interest in using nanometer field-effect transistors for THz applications was initiated in the early 1990s by Dyakonov and Shur [3] and paved the way to successful applications, particularly for imaging systems [4].

Manuscript received October 12, 2016; accepted October 29, 2016. Date of publication November 3, 2016; date of current version December 27, 2016. The review of this letter was arranged by Editor S. J. Koester.

S. Blin, P. Nouvel, and A. Pénarier are with IES, UMR 5214 CNRS, Université de Montpellier, 34095 Montpellier, France (e-mail: stephane.blin@umontpellier.fr).

J. Hesler is with VDI Inc., Charlottesville, VA 22902 USA.

Color versions of one or more of the figures in this letter are available online at http://ieeexplore.ieee.org.

Digital Object Identifier 10.1109/LED.2016.2624782

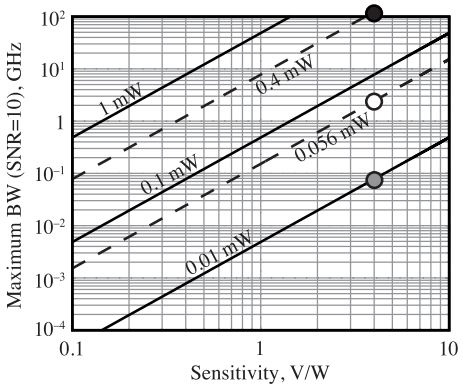

Fig. 1. Possible communication bandwidth for a signal-to-noise ratio of ten, as a function of receiver sensitivity for various incoming THz powers. The black dot corresponds to a direct communication using a THz power of 400 μW as reported in [7], the grey dot to a direct communication with a source power of 10 μW, the white dot to the heterodyne communication demonstrated herein for a source power of 10 μW but with an effective power of 56 μW, improving by more than 25x the possible bandwidth.

Transistors are suitable detectors in many ways, because their output impedance is low and tunable (from tens of Ω to kΩ) by adjusting the gate voltage, thus allowing for on-chip integration with MMIC, they are robust to high input power [5], and low cost. Very recently, their capability to detect amplitude-modulated signals was demonstrated for modulation frequencies up to a few GHz [6], and error-free communications were demonstrated up to 8.3 Gbps [7], both for a carrier frequency around 300 GHz (frequency that largely exceeds the transistor bandwidth). As the transistor true sensitivity is about a V/W, i.e. about three decades lower than the Schottky diode, this reported 8.3-Gbps communication was only possible with the use of a quite complex source in order to reach sufficiently high output power (up to 0.5 mW).

In this letter, we use the same pHEMT detector than the one used for the reported high-data rate communication [7]. The transistor is a commercial GaAs transistor (ATF-36077 from Avago Technologies) with a nominal gate length of 0.2 μm, and a total gate periphery (width) of 200 μm, with gold-based metalizations and nitride passivation that ensure high reliability. The transistor is packaged in a low parasitic, surface-mountable ceramic package (077 type), the upper part of the ceramic being removed in order to increase the incoming THz power on the transistor.

A straightforward calculation of signal to noise ratio (SNR) emphasises how the communication bandwidth is limited by fundamental thermal noise as represented in Fig. 1. By taking account of Johnson-Nyquist noise only and assuming an impedance-matched load circuit, the available bandwidth Δf can be expressed as $(\eta\, P_{THz}/SNR)^2/(k_B\, T\, R)$, where k_B is the Boltzman constant, T the temperature, R the resistance,

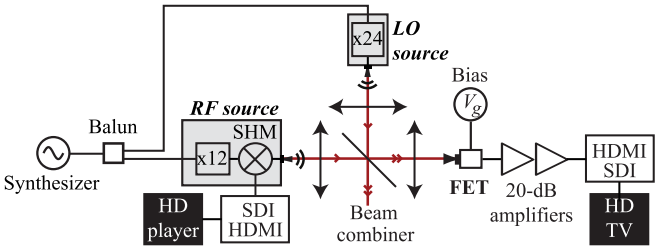

Fig. 2. Experimental setup for heterodyne communication at 0.3 THz using a GaAs pHEMT detector.

η the receiver sensitivity and P_{THz} the incoming THz power. The sensitivity is defined as the ratio of the root-mean-square (rms) value of the detected voltage at the transistor output, by the incoming THz power. As shown in Fig. 1, bandwidth increases quadratically with sensitivity and incoming power. For a given sensitivity of 4 V/W for the transistor, Fig. 1 shows that thermal noise limits the possible communication bandwidth to 100 GHz for a power of 0.4 mW (black dot) which is attractive for high data rate wireless communication, but such a bandwidth is reduced to only 80 MHz for an output power of 10 μW (grey dot).

In this article, we propose a strategy to obtain a significant improvement of the communication system performances, to compensate for the low sensitivity of the transistor. Successful heterodyne detection was demonstrated using GaAs [8] or silicon [9] transistors at room temperature, respectively at 300 GHz and 650 GHz. Therefore, we propose and demonstrate in this letter, for the first time, a THz heterodyne communication using a field-effect transistors transistor for detection. Fig. 1 shows that in an heterodyne scheme with a $-$8dBm THz power for the local oscillator, one should expect an effective incoming power of 56 μW, that increases the possible bandwidth from 80 MHz to more than 2 GHz (white dot in Fig. 1), thus offering an attractive bandwidth for communications thanks to an improvement factor of more than 25 times.

II. Terahertz Heterodyne Communication

The experimental setup is presented in Fig. 2 and consists of two sources, one being the radio frequency source (RF) used to carry the signal, the other being a continuous-wave source used as a local oscillator (LO). In our final demonstration, the signal is an uncompressed real-time high-definition video whose high-definition (HD) multimedia interface (HDMI) is converted into a 8B10B serial digital interface (SDI) in order to modulate the amplitude of the RF source. The RF source is a commercial multiplication chain from VDI (Virginia Diodes Inc.) and consists of a 12-times multiplication chain driven by a synthesiser, followed by a second-harmonic mixer (SHM) that multiplies the input carrier-frequency signal by the data. These data are the intermediate-frequency (IF) signal to be retrieved at the transistor output. As a consequence, the signal at the output of the RF source presents a double-side-band amplitude-modulation with a suppressed carrier (DSB-AM-SC). It is important to notice that such a modulation scheme at emission (DSB-AM-SC for the RF source) would not permit any digital communication using a quadratic receiver at detection, therefore the heterodyne scheme (addition of the LO signal) is at the same time necessary to the communication, and interesting as it improves the possible communication bandwidth by improving the effective incoming power. The RF signal is collimated using a Teflon lens (focal length of 10 cm), transmitted through a 3-dB beam combiner (high-resistivity Si substrate) then focused on the transistor using an identical lens. At the detection side, the LO source consists of a 24-times multiplication chain driven by the same synthesiser than the RF source in order to avoid synchronisation instabilities. Note that driving the two sources using the same synthesiser is possible as both sources present overall the same frequency multiplication factor (x24). To this end, we used an amplitude- and phase-matched balun (HL9402 from Hyperlabs Inc.). The LO signal is also collimated thanks to a Teflon lens with a focal lens of 10 cm, then superimposed to the RF signal thanks to the beam combiner. The IF signal is retrieved at the output of the transistor by measuring the drain–source voltage. The sources and the transistor have horn antennas (see [7] for details concerning the transistor integration). The transistor output signal is amplified with two identical amplifiers whose gain is 20 dB, bandwidth is 100 kHz – 1 GHz, and noise figure is 2.9 dB. The SDI signal is then converted to a HDMI signal that is observed successfully on a HD TV. The transmission length is about 50 cm but might be easily increased in this configuration, at least up to the Rayleigh length.

At the detector side, i.e. after passing though the lenses and the beam splitter, the power of the RF source is about $-$20 dBm ($-$23 dBm on each side of the suppressed-carrier frequency) while that of the LO source is about $-$8 dBm. As mentioned previously, both multiplication chains are driven by the same synthesizer, thus assuring a very robust synchronisation between the two sources. Note that synchronisation of two synthesizers using the 10-MHz reference was not sufficient to realise a successful communication. The phase shift (at the carrier frequency) between these two sources can be adjusted either by moving the position of one source relatively to the other (using a micrometer translation stage) without any significative impact on alignements thanks to the horn antennas, or by adjusting the synthesiser frequency. In order to verify the robustness of the synchronisation, the SHM was driven by a 500-MHz sinusoidal signal, and the stability of the beat frequency was observed at the transistor output by using an oscilloscope and a spectrum analyzer. The former showed a stable sinusoidal signal, while the latter showed a resolution-limited (10 Hz) peak for a sweep time as long as 100 s, thus confirming that the frequency noise added by the multiplication chain does not degrades significantly the synchronisation performances of the heterodyne scheme.

As detailed in [7], the transistor is packaged within a home-made horn with a rectangular waveguide (WR-3.4) to increase the gathered THz power, thus improving the pHEMT effective sensitivity up to a few V/W around 300 GHz. The rectangular waveguide was designed to assure a small incoming beam waist at the transistor, and to reduce detection of undesired noise. This screening is important because the undesired coupled signals might be amplified by the transistor, thus reducing the signal-to-noise at the transistor output. Transistors are also biased with a gate–source voltage (typically $-$0.45 V) in order to increase their sensitivity.

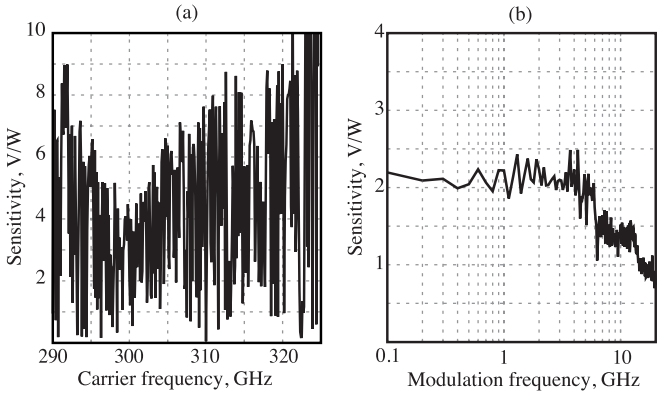

Fig. 3. (a) Calibrated sensitivity for a 1-GHz sinusoidal amplitude modulation. The voltage corresponds to the rms amplitude as it is measured at the spectrum analyzer. (b) Sensitivity of the transistor to modulation frequency for a 307-GHz carrier frequency. The voltage corresponds to rms amplitude.

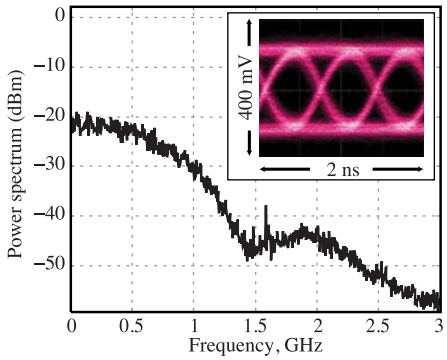

Fig. 4. Spectrum of the video signal at the transistor output after amplification for input RF and IF power of –8 dBm and –20 dBm at the detector, respectively. The inset shows the corresponding eye diagram.

The dependence of the transistor sensitivity on carrier frequency was characterized, as shown in Fig. 3(a). The RF mixer has been driven by a 1-GHz sinusoidal signal, and the synthesiser frequency varied in order to measure the transistor response (drain–source voltage) from 290 to 325 GHz, this bandwidth being limited by the overlap of the frequency operation of the two sources. A calibrated mixer head has been used in place of the transistor in order to measure the incoming power spectrum for each carrier frequencies, thus allowing the calibration of the measurement in order to measure the sensitivity of the transistor (V/W). As the transistor is a quadratic receiver, it is sensitive to the beat power between the LO peak and the RF side peaks. Assuming a LO power P_{LO}, and sidebands powers P_{RF-} and P_{RF+}, the effective beat power used for calibration is then $\sqrt{P_{LO}\,(P_{RF-}+P_{RF+})}$. As shown in Fig. 3(a), the sensitivity of the transistor is about 4 V/W over a wide bandwidth, which is in very good agreement with previously-reported measurements using alternative setups (see [7] for example), thus validating this method of calibration, and proving that the amplitude of the demodulated signal amplitude is proportional to $\sqrt{P_{LO}}$. The oscillations that are observed in Fig. 3(a) are due to the synchronization dependence on carrier frequency. Indeed, for a sinusoidal modulation, one can show that the demodulated signal presents an over-modulation $\cos(2\,\pi\,d\,\nu/c)$, where d is the optical & electrical path difference between LO and RF signals at reception, ν the carrier frequency, and c the speed of light. Here, the path difference comes mainly from the optical path difference between LO and RF sources, relatively to the detector. At a given LO frequency, the signal can be maximized by adjusting d, for example by translating the LO source closer or further away from the detector.

The dependence of the transistor sensitivity on modulation frequency has been also characterized as shown in Fig. 3(b), using the same calibration technique. The carrier frequency is fixed to 307 GHz to provide a high sensitivity along with a possible broadband modulation, and the modulation frequency is increased from 0.1 to 20 GHz. The rigorous 3-dB bandwidth is about 6 GHz, but overall we could evaluate a nice cutoff frequency close to 20 GHz, thus offering a high-bandwidth detector for communications. Note the slight discrepancy (about a factor of two) between Fig. 3(a) at 307 GHz and Fig. 3(b) at 1 GHz likely due to changes in optical alignements.

To verify the ability of this heterodyne scheme to transmit real data, we demonstrated the transmission of a real-time uncompressed high-definition video signal at a rate of 1.5 Gbps. The transmission was successful and very robust, as the video could be observed on the HD TV without any interruption. Figure 4 shows the spectrum of the video signal at the transistor output (after amplification). One can verify that it is in good agreement with the 8B10B video encoding. The inset of Fig. 4 shows the eye diagram of the signals, showing a very open eye and a peak-to-peak amplitude of about 350 mV.

III. Conclusion

High data-rate heterodyne transmission was demonstrated using a field-effect transistor as a detector. We demonstrated the successful transmission of a real 1.5 Gbps signal. Based on the cut-off frequency of the detector, we believe that successful communications can be demonstrated up to 10 Gbps, and that heterodyne communication is very suitable for wireless THz communications systems that use transistors as detectors, because successful communications would be possible using a lower source power. Combined to an increased sensitivity of the transistors (e.g. using an integrated antenna), an integrated and powerful oscillator, along with silicon-based technology, we believe that transistors are a very attractive solution for future wireless communications receivers.

Acknowledgment

Thanks to ANR (WITH) and Region of Languedoc-Roussillon (HERMES Platform) for supporting this work, and to J.-F. Roux (Univ. of Savoie, France) for the beam splitter.

References

[1] H.-J. Song and T. Nagatsuma, "Present and future of terahertz communications," *IEEE Trans. THz Sci. Technol.*, vol. 1, no. 1, pp. 256–263, Sep. 2011.

[2] T. Nagatsuma, S. Horiguchi, Y. Minamikata, Y. Yoshimizu, S. Hisatake, S. Kuwano, N. Yoshimoto, J. Terada, and H. Takahashi, "Terahertz wireless communications based on photonics technologies," *Opt. Exp.*, vol. 21, no. 20, pp. 23736–23747, 2013, doi: 10.1364/OE.21.023736.

[3] M. I. Dyakonov and M. S. Shur, "Plasma wave electronics: Novel terahertz devices using two dimensional electron fluid," *IEEE Trans. Electron Devices*, vol. 43, no. 10, pp. 1640–1645, Oct. 1996.

[4] W. Knap, S. Rumyantsev, M. S. Vitiello, D. Coquillat, S. Blin, N. Dyakonova, M. Shur, F. Teppe, A. Tredicucci, and T. Nagatsuma, "Nanometer size field effect transistors for terahertz detectors," *Nanotechnology*, vol. 24, no. 21, p. 214002, 2013, doi: 10.1088/0957-4484/24/21/214002.

[5] D. B. But, C. Drexler, M. V. Sakhno, N. Dyakonova, O. Drachenko, F. F. Sizov, A. Gutin, S. D. Ganichev, and W. Knap, "Nonlinear photoresponse of field effect transistors terahertz detectors at high irradiation intensities," *J. Appl. Phys.*, vol. 115, no. 16, p. 164514, 2014, doi: 10.1063/1.4872031.

[6] S. Blin, F. Teppe, L. Tohme, S. Hisatake, K. Arakawa, P. Nouvel, D. Coquillat, A. Pénarier, J. Torres, L. Varani, W. Knap, and T. Nagatsuma, "Plasma-wave detectors for terahertz wireless communication," *IEEE Electron Device Lett.*, vol. 33, no. 10, pp. 1354–1356, Oct. 2012, doi: 10.1109/LED.2012.2210022.

[7] S. Blin, L. Tohme, D. Coquillat, S. Horiguchi, Y. Minamikata, S. Hisatake, P. Nouvel, T. Cohen, A. Pénarier, F. Cano, L. Varani, W. Knap, and T. Nagatsuma, "Wireless communication at 310 GHz using GaAs high-electron-mobility transistors for detection," *J. Commun. Netw.*, vol. 15, no. 6, pp. 559–568, Dec. 2013, doi: 10.1109/JCN.2013.000104.

[8] L. Tohme, S. Blin, P. Nouvel, L. Varani, and A. Pénarier, "Room-temperature terahertz heterodyne mixing in GaAs commercial transistors," in *Proc. 38th Int. Conf. Infr. Millim. Terahertz Waves (IRMMW-THz)*, Sep. 2013, pp. 1–2, doi: 10.1109/IRMMW-THz.2013.6665895.

[9] D. Glaab, S. Boppel, A. Lisauskas, U. Pfeiffer, E. Öjefors, and H. G. Roskos, "Terahertz heterodyne detection with silicon field-effect transistors," *Appl. Phys. Lett.*, vol. 96, no. 4, p. 042106, 2010, doi: 10.1063/1.3292016.

Wireless Communication at 310 GHz using GaAs High-Electron-Mobility Transistors for Detection

Stéphane Blin, Lucie Tohme, Dominique Coquillat, Shogo Horiguchi, Yusuke Minamikata, Shintaro Hisatake, Philippe Nouvel, Thomas Cohen, Annick Pénarier, Fabrice Cano, Luca Varani, Wojciech Knap, and Tadao Nagatsuma

Abstract: **We report on the first error-free terahertz (THz) wireless communication at 0.310 THz for data rates up to 8.2 Gbps using a 18-GHz-bandwidth GaAs/AlGaAs field-effect transistor as a detector. This result demonstrates that low-cost commercially-available plasma-wave transistors whose cut-off frequency is far below THz frequencies can be employed in THz communication. Wireless communication over 50 cm is presented at 1.4 Gbps using a uni-travelling-carrier photodiode as a source. Transistor integration is detailed, as it is essential to avoid any deleterious signals that would prevent successful communication. We observed an improvement of the bit error rate with increasing input THz power, followed by a degradation at high input power. Such a degradation appears at lower powers if the photodiode bias is smaller. Higher-data-rate communication is demonstrated using a frequency-multiplied source thanks to higher output power. Bit-error-rate measurements at data rates up to 10 Gbps are performed for different input THz powers. As expected, bit error rates degrade as data rate increases. However, degraded communication is observed at some specific data rates. This effect is probably due to deleterious cavity effects and/or impedance mismatches. Using such a system, real-time uncompressed high-definition video signal is successfully and robustly transmitted.**

Index Terms: **Communications technology, FET, HEMT, plasma waves, receivers, THz.**

I. INTRODUCTION

Wireless communication systems at data-rates exceeding tens of Gbps require carrier signals at frequencies higher than those presently used in widespread systems based on microwave-frequency carriers (mobile phones, Wi-Fi, etc.). A terahertz-based communication link is therefore a promising breakthrough solution to achieve data-rates up to 100 Gbps as described [1]–[3]. If compared to existing wireless optical communications that are based on higher-frequency carrier signals, terahertz solutions present two significant advantages for indoor communications. First, THz beams spread more easily thanks to diffraction [4], [5], as the Rayleigh length of THz beams is smaller than that of infrared beams due to its larger wavelength. Secondly, THz beams present smaller attenuation than infrared beams in a typical indoor environment, as dry and non-metallic materials are mostly transparent to THz waves. However, THz communication systems suffer from the lack of suitable sources and detectors as mentioned in [6]. Consequently, a significant effort must be devoted to the study and development of THz solid-state sources and detectors at frequencies corresponding to atmosphere absorption minima, such as 300 GHz and 650 GHz. In this paper, we investigate the use of plasma-wave detector at 310 GHz for high-data-rate wireless communication.

Presently, the most widespread detector for THz communications is the Schottky barrier diode (SBD) [1], [7]–[9], mainly due to its high sensitivity (typically few kV/W). Plasma-wave transistors are alternative solutions for THz detection with specific attractive features for high-speed communications such as (i) lower output impedance favorable to impedance matching with high-bandwidth amplifiers, (ii) easy on-chip integration with demodulation circuit, and (iii) robustness to high input THz power. High-electron-mobility transistors (HEMT) operate as envelope detectors thanks to the non-resonant plasma rectification (self-mixing effect) as detailed in [10]–[12]. Consequently, such detectors can operate in direct detection systems. Other solutions such as heterodyne detection present attractive performances in terms of minimum detection level [13]–[15]. However, they require stringent synchronization between the local oscillators of the source and detector, or specific techniques at detection to correct for synchronization mismatch. The use of a commercial HEMT for heterodyne detection has been already investigated in [16] but our paper focuses on direct detection.

In Table 1, we present a rough overview of the room-temperature performances at 300 GHz of SBD (as reported by Virginia Diode Inc. and in [17]), Si MOSFET (reported in [18]) and GaAs HEMT (reported in [19]). In terms of sensitivity, it is important to notice that such numbers only give a rough comparison between these detectors as both measurements and metrics are different. For instance, the typical SBD sensitivity is measured using a 25-dB-gain horn antenna, thus improving the collected THz power, while no horn antenna was used to evaluate transistor sensitivities. On the other hand, transistor sensitivities were calculated using the THz power which effectively illuminates the transistor surface (as proposed in [20]), while all the THz power was used to calculate the sensitivity of the SBD. However, if one calculates the transistor sensitivity as if it

Manuscript received July 1, 2013.

This work was supported by the "WITH" JST-ANR project, by CNRS and GDR-I project "Semiconductor sources and detectors of THz frequencies" in the framework of the "GIS Teralab". We acknowledge the Region of Languedoc-Roussillon through the "HERMES Platform".

S. Blin, L. Tohme, P. Nouvel, T. Cohen, A. Pénarier, F. Cano and L. Varani are with IES, UMR 5214 CNRS, Université Montpellier 2, GIS Teralab, 34095 Montpellier, France. D. Coquillat and W. Knap are with L2C, UMR 5221 CNRS, Université Montpellier 2, GIS Teralab, 34095 Montpellier, France. email: {Stephane.Blin, knap}@univ-montp2.fr.

S. Horiguchi, Y. Minamikata, S. Hisatake and T. Nagatsuma are with Graduate School of Engineering Science, Osaka University, Toyonaka, Osaka, Japan. email: nagatuma@ee.es.osaka-u.ac.jp.

Digital object identifier 10.1109/JCN.2013.000104

Table 1. Reported sensitivity, noise-equivalent power (NEP) and modulation bandwidth (BW) for SBD and transistor detectors at room temperature for a 300-GHz-frequency signal.

Detector	Sensitivity	NEP (W/$\sqrt{\text{Hz}}$)	BW
SBD	few kV/W	10^{-12}	$\approx$ 20 GHz
Si MOSFET	5 kV/W	10^{-12}	n/a
GaAs HEMT	10 V/W	$< 13\times10^{-9}$	few GHz

was measured behind an identical horn antenna and using the total THz power, we would obtain sensitivities of 3.9 kV/W and 27 V/W for the Si MOSFET and the GaAs HEMT, respectively. Therefore, Table 1 remains useful because even by correcting the sensitivities their values remain of the same order of magnitude than those reported in the table. Finally, note that the reported GaAs HEMT sensitivity and NEP are worst than those of Si MOSFET, because the latter presents an integrated bow-tie antenna. However, the GaAs HEMT was mounted on microstrip lines, thus offering possible detection of amplitude-modulated signal at modulation frequencies up to 8 GHz. Therefore, the transistor can compete with SBD as a detector for THz communications in terms of sensitivity and bandwidth.

As already mentioned, detection of amplitude-modulated THz signals was recently demonstrated at 300 GHz using plasma-wave transistors for a sine-wave modulation at frequencies up to a few GHz [19]. The first data communication was demonstrated very recently using a 200-GHz carrier frequency for data rates ranging up to hundreds of Mbps [21]. In this paper, we present for the first time a 310-GHz error-free (bit error rate lower than 10^{-11}) transmission at data rates up to 8.2 Gbps using plasma-wave transistors as detectors. Such an improvement, if compared to previously reported results [19], [21], is due to an increased effective sensitivity of the transistor associated with the use of a horn antenna, along with careful electromagnetic isolation thanks to a floating-ground isolation.

II. THZ DETECTION BASED ON PLASMA WAVES

A. Plasma-Wave Detector

The interest in using nanometer field-effect transistors (FETs) for THz applications was initiated in the early 1990s by the theoretical work of Dyakonov and Shur, who predicted that the channel of a FET could act as a resonator for plasma waves [22]. It was also shown that the nonlinear properties of the 2D plasma in the transistor channel could be used for resonant detection and mixing of THz radiation [23]. Rectification and detection of THz radiation is also possible in the non-resonant case (low electron mobility) when plasma waves decay at a distance smaller than the channel length. Fig. 1 shows the principle of THz detection of transistors.When the THz radiation is collected by the transistor through the metallic gate electrode, the THz AC voltage produced between gate and source simultaneously modulates the carrier density and drift velocity in the channel. This leads to nonlinearity and, as a result, a photoresponse appears in the form of a DC voltage between source and drain. For high-carrier-mobility devices (e.g., GaAs- and GaN- based FETs at cryogenic temperatures) the THz field can create plasma waves

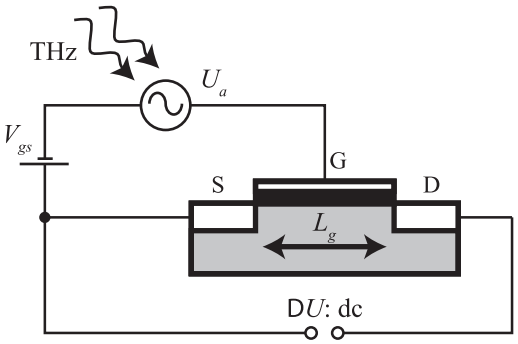

Fig. 1. Principle of THz detection based on high-electron-mobility transistor. The THz signal induces an alternating voltage U_a. The transistor sensitivity is enhanced by applying a DC voltage between gate and source. A DC voltage proportional to the input THz amplitude is measured between the source and drain pads.

that propagate in the channel, and resonant plasma modes can be excited, leading to a resonant narrowband and gate-bias-tunable detection [23]–[26]. At room temperature, plasma waves are usually overdamped and the THz radiation causes only a carrier density perturbation that decays exponentially on a distance of the order of a few tens of nanometers. A more detailed description of the physical mechanism of THz detection by FETs can be found in [27]. Currently, the most promising application appears to be room-temperature broadband THz detection in the non-resonant regime for imaging and wireless communication applications.

Different kinds of FETs, like GaAs HEMTs [24], [28], GaN HEMTs [29], InGaAs HEMTs [24], [28], [30], silicon metal-oxide-semiconductor FETs [18], [31], [32], or nanowire and graphene-based FETs [33], [34] with a gate length of the order of hundreds of nanometers exhibit good broadband THz sensitivities and can reach a NEP that is competitive with the best conventional room-temperature THz detectors. Further progress in FETs THz detection should address the improvement of the THz coupling and improvement of the transistor design. Recently, double-grating-gate field-effect transistor structures with asymmetry between source and drain to enhance the photoresponse have been designed and used for ultra-high sensitive detection and imaging at frequencies up to 2 THz [35], [36].

Moreover, FET-based THz detectors can be used to detect low-power continuous-wave THz signals due to their very good NEP, but also high-power THz pulses delivered by a free-electron laser. Therefore, their estimated damage threshold is of a few hundreds of Watts [37], that is much higher than that of SBD. Moreover, FET detectors exhibit a linear response up to an input intensity of about 1 kW/cm^2, followed by a sub-linear detection up to several MW/cm^2 [37], [38]. The saturation limit shifts to higher intensities when the frequency increases. The possibility to obtain ultrafast linear detection over a large range of powers is an important advantage for robust wireless communications.

B. Integration

Integration of transistors for successful use in communication systems is absolutely necessary for two main reasons. First, as

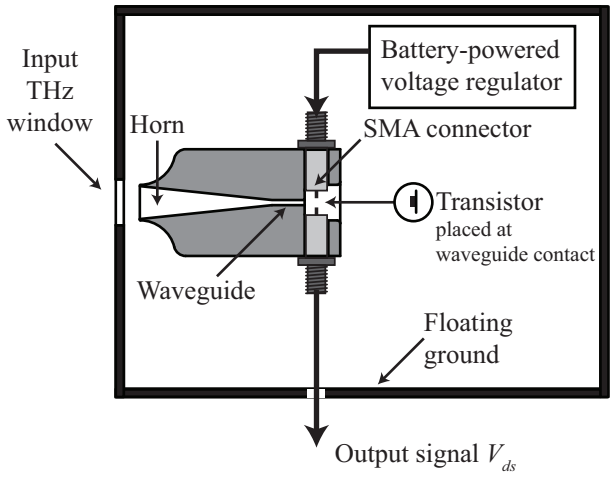

Fig. 2. Plasma-wave detector integration. A floating-ground metallic case is used for electromagnetic shielding. The transistor is placed at the waveguide output. A diagonal horn is used to collect larger THz power. The transistor is biased using a battery-powered voltage regulator placed within the shielding case.

the transistor detects the incoming THz signal coupled to the gate, this electrode should be isolated from any other spurious electromagnetic signals to assure reasonable signal-to-noise ratio. Otherwise, HEMTs may amplify deleterious signals, especially within their typical operation bandwidths (up to few GHz or tens of GHz), which significantly degrades the signal-to-noise ratio for high-data-rate communications. Secondly, the transistor dimensions are much smaller than the diffraction-limited upcoming beam waist. Therefore, it is necessary to assure the smallest possible incoming beam waist to collect as much power as possible through the transistor surface.

In order to achieve both electromagnetic isolation and small beam waist, the HEMT is packaged as shown in Fig. 2. Improved collected THz power is assured thanks to a standard input horn. The horn was designed to have a full 3-dB beamwidth of 12° and a gain of 20 dB. The length of the horn is 26 mm with an aperture at front side of 5 mm $\times$ 5 mm. The angle of the pyramid construction is 6°. The THz signal is then concentrated on a small beam waist within a rectangular hollow waveguide (transverse dimensions equal to 432 μm $\times$ 864 μm), so that a single linear polarization is coupled to the waveguide. Integration was designed and machined thanks to digital micromachining. In order to evaluate its performances, the horn was mounted on a commercial frequency-multiplied source emitting at 290 GHz and the far-field imaging of the emitted beam was measured using a HEMT transistor as a detector. In order to improve the spatial resolution, this detector was not integrated, i.e., no input horn was used. We conducted imaging experiments in a plane orthogonal to the optical axis using 2D motorized linear stages. As shown in Fig. 3, the horn presents the expected performances, namely a symmetric Gaussian-like beam with a divergence comparable to that of Gaussian-beam simulations and a commercial horn with similar design.

Having confirmed the horn and waveguide quality, the THz detector was implemented by placing the transistor as close as possible to the waveguide output (about 500 μm). The transistor was connected to subminiature version A (SMA) connectors for biasing (gate–source voltage), and also for extracting the detected signal (drain–source voltage) produced by the incoming THz signal. In this paper, we used an ultra-low-noise GaAs pseudomorphic HEMT for detection. The transistor is packaged in a low-parasitic surface-mountable ceramic package. The top side of the cap was removed to improve detection (by suppressing the ceramic absorption) and reduce the distance between the waveguide and the transistor itself. Therefore, the top surface of the transistor (where pads are visible) was directly exposed to the incoming beam. Finally, the HEMT was shielded within a conductive enclosing to avoid electromagnetic coupling. Despite such efforts, we observed significant ground coupling issues. As a consequence, we used an external floating-ground enclosure inside which we placed both the integrated transistor and its battery-powered biasing supply.

III. WIRELESS COMMUNICATION USING UTC-PD EMITTER AND HEMT DETECTOR

A. Experimental Setup

A communication link based on a uni-travelling-carrier photo-diode (UTC-PD) emitter is presented in Fig. 4. The UTC-PD emitter is excited by an optical beating generated by two continuous-wave fiber-coupled external-cavity lasers. The laser signals are coupled using a 3-dB fiber coupler then amplified using an erbium-doped fiber optical amplifier. The amplitude modulation of the optical beating is achieved using a Mach-Zehnder modulator. Precautions were taken in order to avoid any spurious radiation, especially at the modulation frequency. The critical components such as the amplitude modulator, its amplifier, and the UTC-PD are carefully packaged, thus assuring efficient shielding. The THz signal at the UTC-PD output is collimated using a 10-cm focal-length teflon lens, then focused to the HEMT using an identical lens after propagation over 50 cm. The HEMT is biased with a DC voltage between the gate and the source, and the drain-source signal produced by the incident THz beam is amplified using different kinds of amplifiers depending on the specific application such as system characterization, uncompressed high-definition (HD) video real-time transmission, or high-data-rate communications.

B. Plasma-Wave Detector Spectral Sensitivity

In order to determine the most favorable frequency of the communication link, the sensitivity of the HEMT has been measured from 220 GHz to 365 GHz. The THz signal is modulated using a sine wave at 11 MHz (minimum emitting frequency of the available synthesizer), and the detected signal is enhanced using a 40-dB-gain amplifier with an input impedance of 1 MΩ and a bandwidth of 10 MHz. The signal is observed by the electrical spectrum analyzer at 11 MHz by using a resolution bandwidth of 3 Hz. The amplitude modulation offers better accuracy than direct DC measurements. As shown in Fig. 5, the detected signal is above 0 dBmV from 250 GHz to 340 GHz, thus offering a 90-GHz bandwidth which is suitable for communications. The noise level is measured by blocking the THz beam in front of the UTC-PD emitter. Using a resolution bandwidth of 3 Hz, we measured a large signal-to-noise ratio of about 60 dB

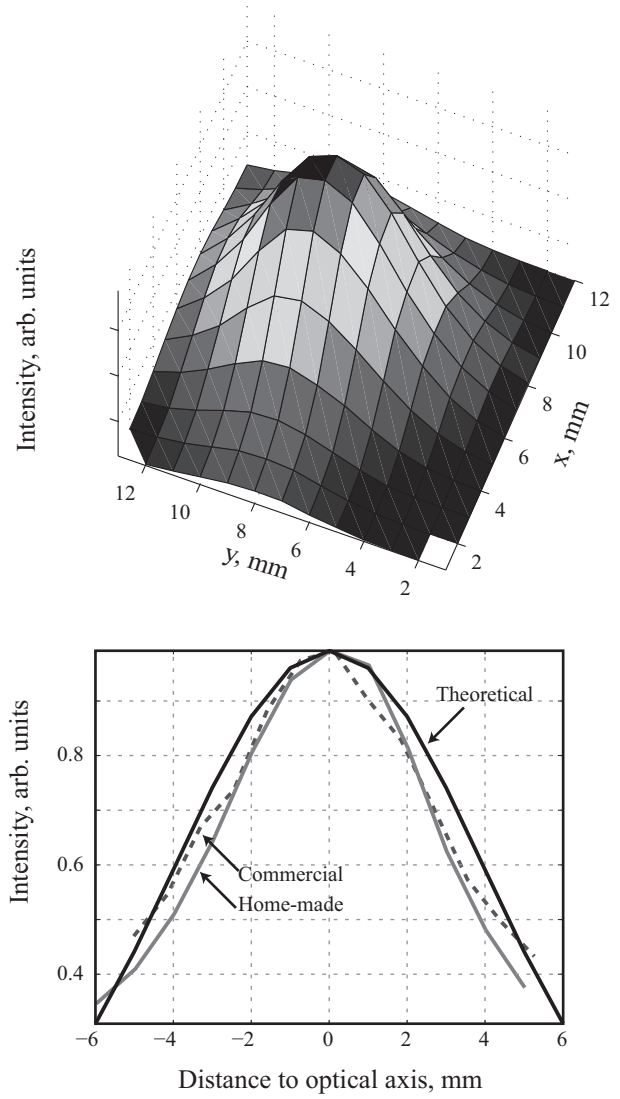

Fig. 3. Horn characterization at 290 GHz. The top graph represents the far-field intensity measured in a plane orthogonal to the optical axis for the home-made horn. The bottom graph presents a cut of the intensity along the x direction for the home-made horn and the commercial horn. The theoretical intensity is calculated using a Gaussian-beam propagation simulation.

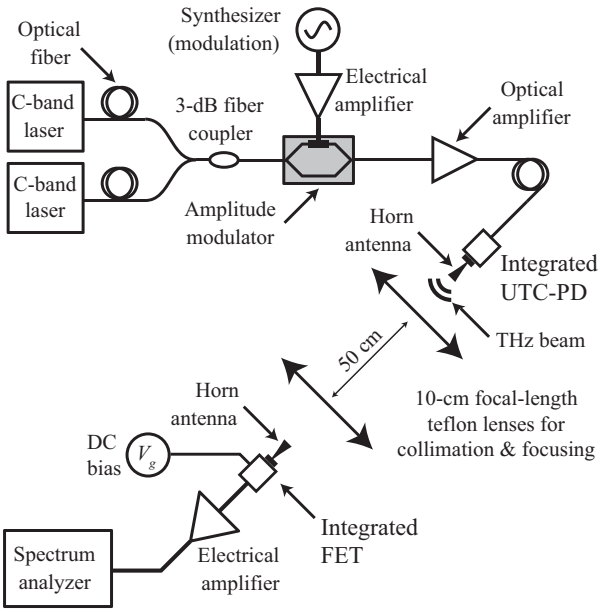

Fig. 4. Experimental setup for THz communication using the UTC-PD emitter and the plasma-wave receiver.

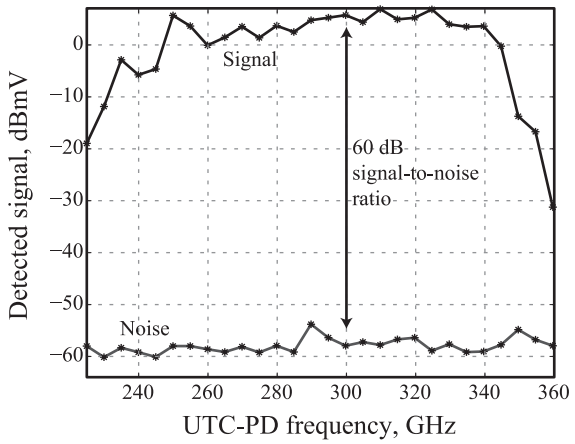

Fig. 5. Sensitivity dependence of the experimental setup. The UTC-PD emitting frequency is tuned and the detected signal at the transistor output is measured using the electrical spectrum analyzer. Noise is measured by blocking the THz signal at the transistor input window.

from 250 GHz to 340 GHz.

In order to evaluate the sensitivity of the transistor, the UTC-PD output power was measured using a calibrated THz power-meter based on a pyroelectric sensor. For this experiment, the sensor was directly connected to the output waveguide of the UTC-PD (after horn removal) and the optical beating was not modulated. As shown in Fig. 6, the sensitivity of the transistor is about a few volts per watt. Note that such a sensitivity is underestimated as it does not take into account the free space loss (about 4–6 dB due to absorption and reflection at teflon lenses). The sensitivity of the HEMT detector was increased thanks to the input horn, but could be further improved by 1–2 orders of magnitude using a 300-GHz antenna coupled to the gate and source terminals of the transistor, as previously reported for example on Silicon technology [18].

C. *Characterization of the Baseband Modulation Bandwidth of the Plasma-Wave Detector*

As shown in Fig. 5, broadband detection should allow for high-bandwidth communication. In order to evaluate such a bandwidth, the baseband modulation bandwidth of the system has been measured as shown in Fig. 7. A sine modulation of the THz amplitude is applied at increasing frequencies, and the baseband signal amplitude is measured at the transistor output using an electrical spectrum analyzer. We measure the amplitude of the signal at the frequency of amplitude modulation. For these experiments, we used a 30-dB 50-Ω 18-GHz amplifier. Fig. 7(a) shows a bandwidth of about 20 GHz, in agreement with a transistor bandwidth of 18 GHz as given in the datasheet. In order to assure that such a bandwidth is not related to the amplifier at detection side, the modulation setup and the detection scheme

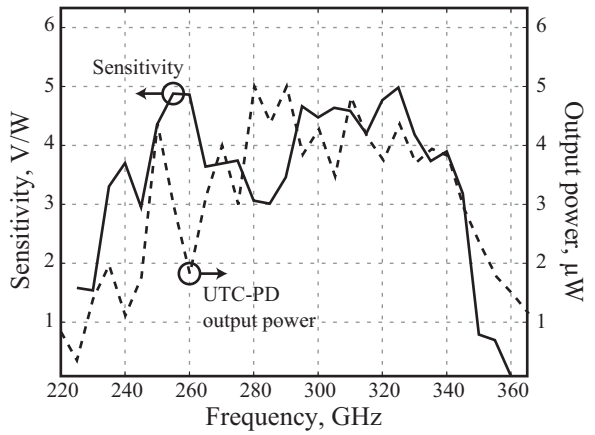

Fig. 6. HEMT sensitivity measurement. The UTC-PD output power is measured at a bias voltage of 1 V and for a photocurrent of 3 mA.

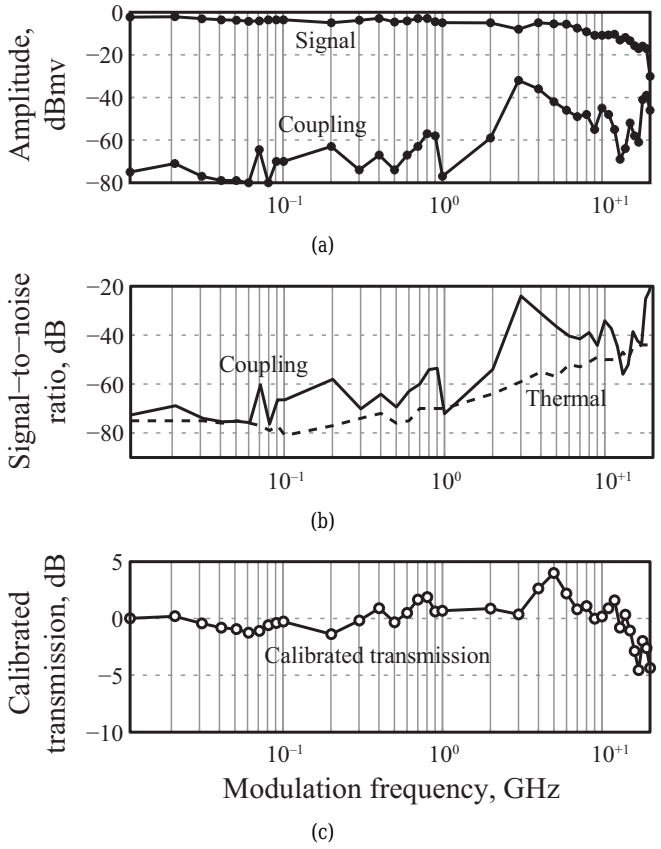

Fig. 7. Characterization of the baseband bandwidth of the plasma-wave detector: (a) presents the detected signal and remaining coupling amplitudes, the latter being measured by blocking the input THz beam, as a function of the frequency of the sine-wave amplitude modulation of the THz beam, (b) shows the signal-to-coupling and signal-to-thermal-noise ratios, the thermal noise being the white noise floor (amplifier thermal noise), and (c) shows the calibrated characterization of the plasma-wave detector after careful calibration of both modulation setup and amplifier.

were calibrated. The calibration measurement was conducted by sending the modulated optical signal on a high-bandwidth photodiode and amplifying the photodiode signal using the same amplifier. The calibrated characterization of the detector is represented in Fig. 7(c). We observe a detector bandwidth of about 20 GHz if measured relatively to the low-frequency plateau. The resonance observed at about 5 GHz is not clearly understood yet, but it could correspond to either an impedance mismatch and/or the presence of deleterious optical cavities.

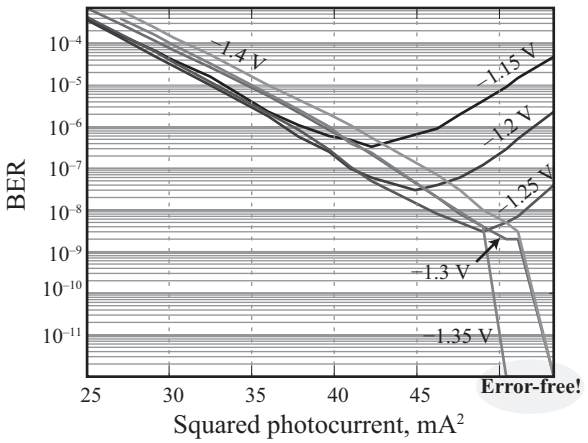

Fig. 8. BER measurement at 1.4 Gbps as a function of squared photocurrent (proportional to input THz power) at different biases of the UTC-PD. The emission frequency is 310 GHz. Error-free operation was fixed at a level of 10^{-12}.

Fig. 7(b) also shows the signal-to-noise ratio, and the signal-to-coupling ratio, where the noise is the white noise (mainly the amplifier thermal noise) and the coupling is the direct detection of the modulation signal by the transistor (without THz carrier). Even if we observe an increase of the coupling at higher modulation frequencies, the signal-to-coupling ratio exceeds 20 dB thanks to the previously-described integration, thus overpassing the direct-coupling limitation due to insufficient shielding of the experimental setup on source side and detector side [19].

D. Data Transmission

As the HEMT detector presents sufficient bandwidth and signal-to-noise ratio, data transmission experiments have been conducted. Even if the baseband characterization shows a good signal-to-noise ratio, this value is measured within a small bandwidth. High-data-rate communications require a large bandwidth, therefore successful communications are more challenging than detecting a sinusoidal modulation.

For communication experiments, a pseudo-random bit sequence has been used for binary on/off amplitude modulation. The bit-length sequence was limited to $2^7 - 1$ because unidentified deleterious low-frequency noise was observed at higher bit lengths. The HEMT signal was amplified using a 50-dB 50-Ω 1-GHz amplifier followed by a limiting amplifier. Error-free transmission up to 1.8 Gbps has been achieved, and the dependence on THz power and UTC-PD biasing has been evaluated as detailed in the following at a data rate of 1.38 Gbps.

THz power dependence on bit error rate (BER) was conducted by varying the input optical power at the UTC-PD emitter, and monitoring the photocurrent at the UTC-PD. As THz power is expected to be proportional to the square of the photocurrent,

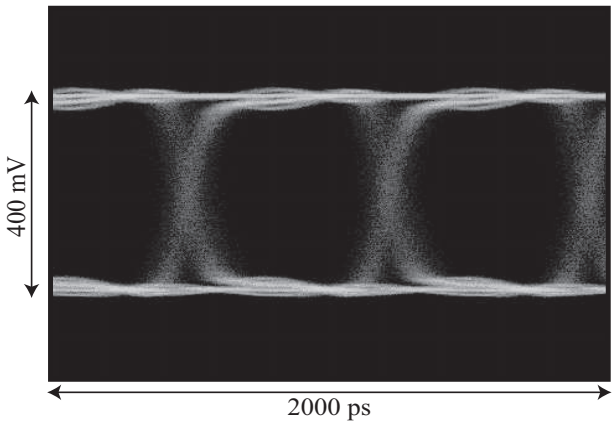

Fig. 9. Eye diagram at 1.4 Gbps using the UTC-PD source and the plasma-wave detector at 310 GHz, during an error-free (BER $< 10^{-10}$) transmission.

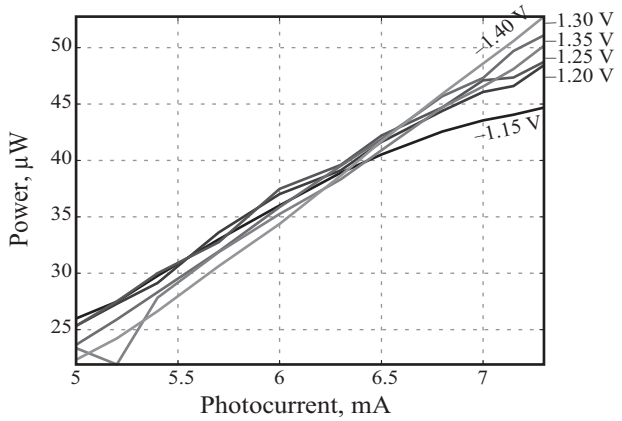

Fig. 10. Calibration of the UTC-PD emitted power for BER measurements. The output power is measured as a function of the photocurrent at different UTC-PD biases.

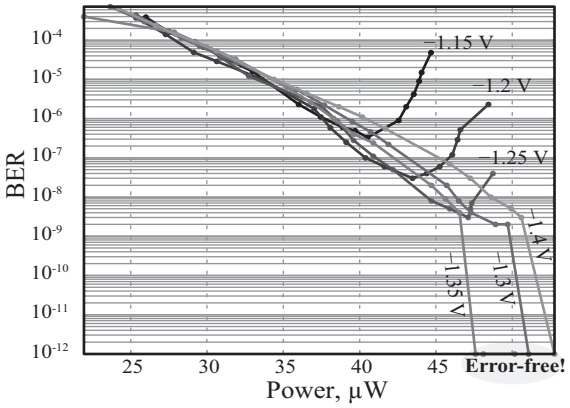

Fig. 11. BER at 310 GHz as a function of input THz power at different UTC-PD biases. The data rate is 1.4 Gbps.

BER is plotted in Fig. 8 as a function of the squared photocurrent. As can been seen in this experiment, the BER decreases as the photocurrent increases, and error-free communication is achieved at sufficiently high photocurrent, i.e. for sufficiently high THz power. Error-free operation is indicated on the figure by arbitrary choosing a value of the BER of 10^{-12} on the graph, such a value being 1–2 orders of magnitude below the minimum measurable BER. An opened eye diagram of successful error-free communication is presented in Fig. 9. At high photocurrent and low biasing of the UTC-PD, we observe in Fig. 8 a degradation of the BER. Further investigations showed that such a degradation is not correlated to a power drop but to a noise increase as will be discussed in the following.

Although an error-free communication was possible at sufficiently high source power, we observed a significant timing jitter in Fig. 9, which is much larger than that of the system (1 ps or less). This jitter contributes to the degradation of the BER. As shown in Fig. 7, the frequency response of the detector is not flat from 3 GHz to 10 GHz. Therefore, the detected eye pattern is distorted at the transistor output, and the amplitude noise is converted into jitter through the limiting amplifier. If we increase the source power and the gain of the amplifier at the transistor output, the jitter is reduced at the limiting amplifier output, as detailed in the following (see Fig. 18).

The calibration of the UTC-PD output power was carefully conducted in order to understand the origin of the BER degradation at low biasing and high photocurrents. A calibrated power-meter was used to measure the average power for various biasings at the data-rate of the experiment. Fig. 10 shows that the average output power increases with photocurrent but saturation appears at high photocurrents. Such a saturation is more evident if the bias is low, as previously shown in the case of large pulsed signals [39] or continuous-wave operation [40].

Using the previously-presented calibration, the BER can be plotted as a function of the output power as shown in Fig. 11. From this calibration, we conclude that at low power, the BER does not depend on the UTC-PD biasing. As the incident power increases, the BER reduces until a given limit where it starts degrading. This limit appears at lower powers for lower biases. Calibrated experiments allowed to identify that such a BER degradation is not related to a power drop. Further investigations were conducted by monitoring the emission spectrum of the UTC-PD using a spectrum analyzer mixer. We observed a degradation of the emission spectrum at high photocurrents, characterized by a significant increase of the white noise level. Therefore, at high photocurrents, the increase of the measured THz power with photocurrent probably corresponds to an increase of the white noise rather than to an increase of the THz carrier power.

Higher-data-rate communication should be investigated with the UTC-PD emitter and the plasma-wave receiver, but this would require a larger-bandwidth amplifier with identical gain (50 dB) in order to compensate for the limited output power of the UTC-PD and the limited sensitivity of the transistor.

IV. WIRELESS COMMUNICATION USING FREQUENCY-MULTIPLIED SOURCE AND HEMT DETECTOR

A. Communication Link

As shown in the previous section, error-free transmission at 310 GHz was demonstrated for the first time using a HEMT de-

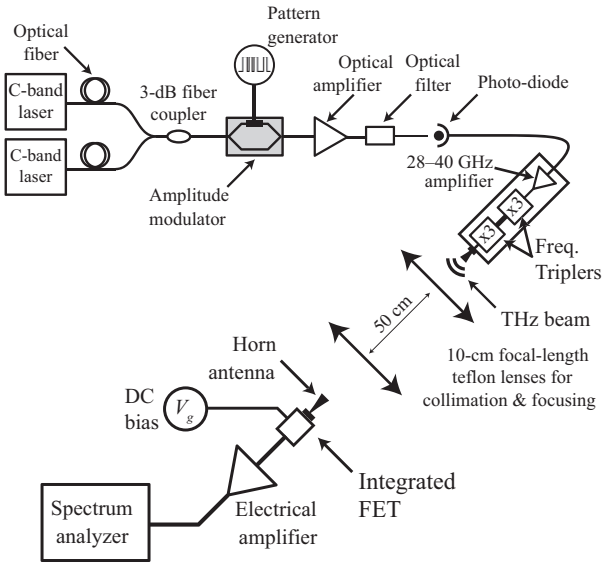

Fig. 12. Communication link using a frequency-multiplied source as emitter and a plasma-wave transistor as detector.

tector, but the data rate was limited to 1.8 Gbps due to the relatively low output power of the UTC-PD emitter (about 50 μW at a photocurrent of 7.25 mA) and the limited detector sensitivity (about 4 V/W). In order to investigate communications at higher data rates, a communication link using a frequency-multiplied source has been implemented as described in Fig. 12, similarly to the one reported in [41]. The frequency-multiplication chain consists of a 28–40-GHz input amplifier, followed by two frequency triplers. This chain is driven at its input by an electrical signal which is generated by exciting a high-bandwidth photodiode with an amplitude-modulated optical beating. The optical beating generation is similar to the one previously used with the UTC-PD emitter but in this case, the optical beating frequency is of tens of GHz only as THz generation is then provided thanks to the frequency-multiplied chain. Having a frequency multiplication factor of 9, driving the chain by an optical beating within the 28–40 GHz range allows to generate a THz signal at frequencies between 250 and 360 GHz. In our experiments, we used a 34.3-GHz optical beating, thus leading to a frequency of the THz output signal of 308.7 GHz. In order to increase the signal-to-noise ratio, a 4-nm optical bandpass filter was used to reduce the amplified spontaneous emission at the amplifier output. The HEMT was biased with a DC voltage and its signal amplified using a 50-Ω 30-dB 18-GHz amplifier followed by a limiting amplifier whose output is either observed using the spectrum analyzer, a digital sampling oscilloscope or a BER measurer.

B. Calibration and BER Measurements

As discussed in the previous section, a careful calibration is delicate thus this part needs to be described in detail. As shown in Fig. 13, the output power calibration is conducted using a calibrated pyro-electric sensor both for continuous-wave emission (DC) and modulated emission. As shown in this figure, the output power is calibrated as a function of the photocurrent monitored at the photodiode. Since the calibration changes significantly as optical signal are modulated or not, we used the power

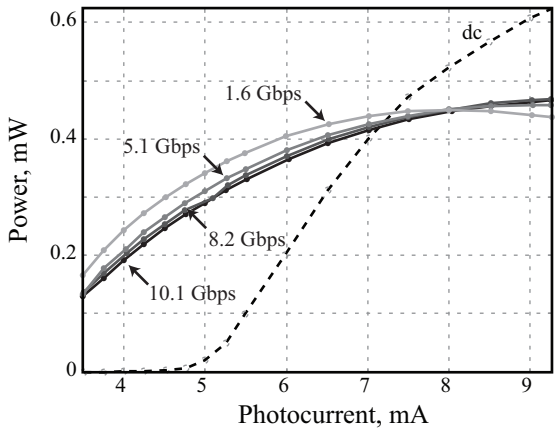

Fig. 13. Calibration of the frequency-multiplied source output THz power as a function of the driving-photodiode photocurrent at different data rates.

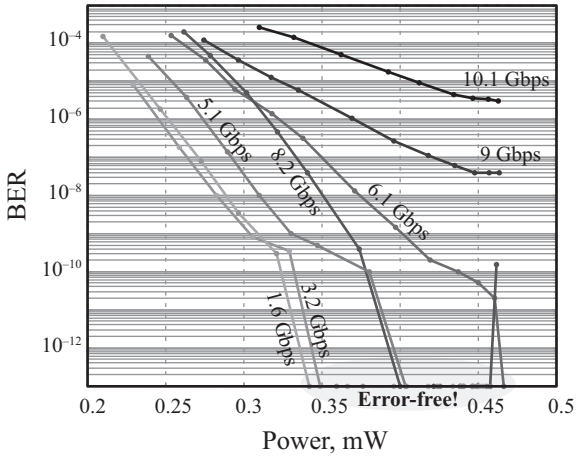

Fig. 14. Bit error rate measurements at 308.7 GHz as a function of THz power at different data rates. Error-free transmission is fixed at a level of 10^{-13}.

calibrated using binary on/off modulated data in the following BER measurements.

Fig. 14 shows the evolution of the BER with THz power at different data rates. It exhibits the expected degradation when the THz power reduces and the data rate increases. For the first time, an error-free communication is demonstrated using a plasma-wave receiver at data rates up to 8.2 Gbps. In this experiment, error-free transmission corresponds to a BER lower than 10^{-11} and is arbitrary fixed in the figure at a level of 10^{-13}. Error-free regime is obtained for a THz power of about 350 μW at a data rate of 1 Gbps, and for 450 μW at 8.2 Gbps. One might note that a lower THz power was required when using the UTC-PD source to achieve error-free propagation (see Fig.11), as a higher-gain (20-dB more) preamplifier was used. Open eyed diagrams for error-free communication are presented in Figs. 15 and 16 at 5.3 Gbps and 8.3 Gbps, respectively.

At higher data rates (9 Gbps and 10.1 Gbps), the BER seems to reach a plateau for high THz input powers. Separate experiments were conducted in order to determine the maximum bit rate of the source and they showed a limitation at about

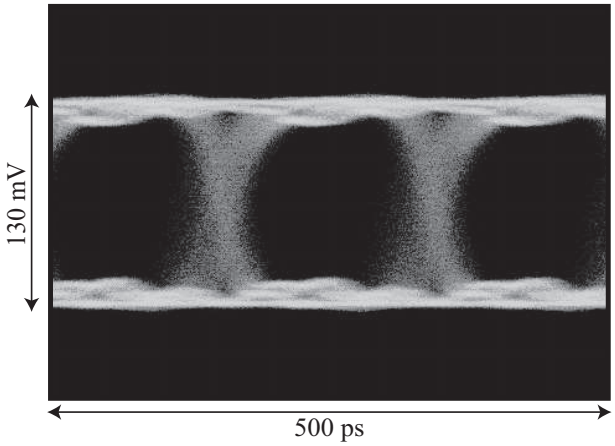

Fig. 15. Error-free (BER $< 10^{-11}$) eye diagram at 5.3 Gbps using the frequency-multiplied source and the plasma-wave receiver.

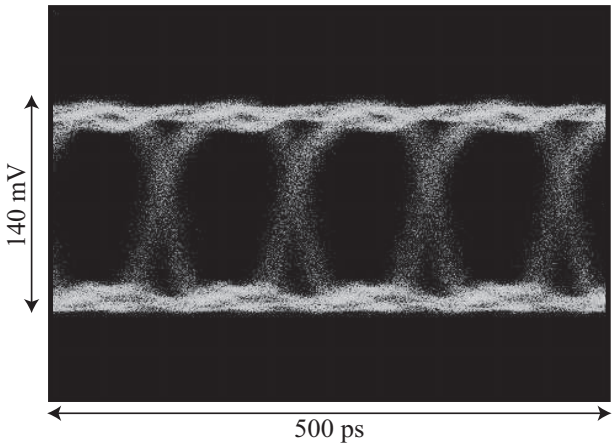

Fig. 16. Error-free (BER $< 10^{-11}$) eye diagram at 8.3 Gbps using the frequency-multiplied source and the plasma-wave receiver.

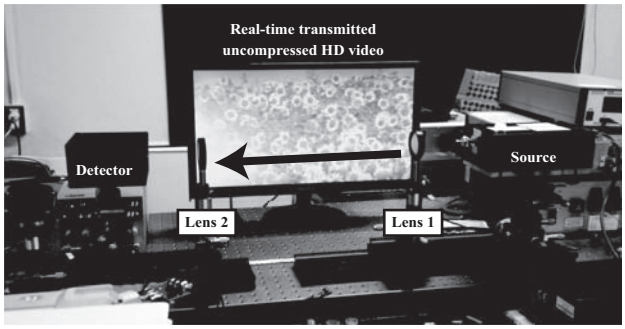

Fig. 17. Photograph of the video transmission showing the frequency-multiplied source on the right, the plasma-wave receiver on the left (inside its electromagnetic shielding box), and two teflon lenses in-between for collimation and focusing. The source amplitude is modulated by a real-time high-definition and uncompressed video signal. Transmitted signal is observed on the TV screen at the background.

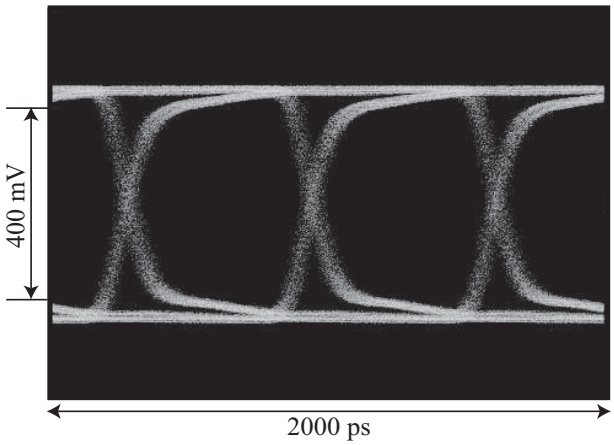

Fig. 18. Eye-diagram measured at a data rate identical to that of the high-definition uncompressed real-time video.

10 Gbps [41], mainly due to the limited bandwidth of the first stage power amplifier which drives the multiplier diodes used to generate higher harmonics (3×3) in the frequency-multiplied chain. Therefore, we believe that the plateau observed at high THz input powers (see Fig. 14) and high data rate is due to a limited bandwidth of the transistor, which likely corresponds to the presence of the 5-GHz resonance that has been observed while measuring the baseband modulation bandwidth (see Fig. 7(c)).

Although error-free transmission could be obtained at high data rates, the BER was significantly degraded at some erratic data-rates. We believe that such unexpected behaviour is related to cavity effects, either between source and detector, within lenses, or within the transistor integration. Another cause could be an impedance mismatch at the transistor output. Any of these reasons or any combination of them would lead to a degradation of the BER. Further work consists in a more careful optical design in order to reduce such potentially deleterious cavity effects along with impedance matching circuit design.

C. Real-Time Uncompressed HD Video-Transmission

Since error-free communication was demonstrated at data rates of few Gbps, real-time uncompressed HD video signal should be easily transmitted as its clock frequency is around 1.5 GHz. In order to demonstrate such a transmission, the pattern generator was replaced by a DVD player whose high-definition multimedia interface (HDMI) signal was converted in a serial signal thanks to a HDMI-to-SDI converter (SDI stands for serial data interface). At the transistor output, a 50-dB 50-Ω 1-GHz pre-amplifier was used, followed by a limiting amplifier whose output was connected to a SDI-to-HDMI converter in order to observe the video on a HD TV. Successful and very robust real-time HD uncompressed video communication was observed as shown in Fig. 17. Eye-diagram at a data rate of 1.5 Gbps, i.e. at the same data rate than that of the high-definition uncompressed video signal, is shown in Fig. 18.

V. SUMMARY AND PERSPECTIVES

For the first time, high-data-rate transmission has been demonstrated using a plasma-wave transistor as a THz detector. Error-free transmission has been obtained up to 8.2 Gbps using a frequency-multiplied source and up to 1.8 Gbps using a UTC-PD source, at 310 GHz and 309 GHz, respectively, and over a distance of 50 cm. The UTC-PD-emitter output

power being about an order of magnitude lower than that of the frequency-multiplied source, achievable data rates are reduced using the former source but could be improved if the plasma-wave receiver sensitivity is increased.

Since the main drawback of using a transistor for broadband THz detection is due to its limited sensitivity and its susceptibility to deleterious electromagnetic couplings, a careful integration has been conducted in order to collect as much power as possible. The integration consists of an input diagonal horn antenna followed by a hollow waveguide, and a floating-ground shielding to reduce the detection of spurious signals.

Further work consists in improving the detector sensitivity by using a broadband antenna connected to the transistor gate and source contacts. Having an increased sensitivity is important as similar communication performances would be possible with no teflon lens or horn antenna, thus offering an integrated solution which could be used in mobile devices, computers, etc. In order to offer more robust communications using plasma-wave transistors, further work also requires (i) a careful optical design including anti-reflection coating to reduce deleterious cavity effects, (ii) an impedance-matching design between the transistor output and the amplifier, and (iii) an improvement in the electromagnetic isolation of the transistor. Additionally, more advanced modulation schemes, such as multi-level amplitude modulation, should allow to significantly increase the possible communication data rate using HEMT as THz detectors. We believe that such improvements should make plasma-wave transistors the most competitive detectors for high data-rate communications.

ACKNOWLEDGMENTS

We acknowledge Guillaume Ducournau and Jean-François Lampin from IEMN (Univ. Lille 1, France), along with Jean-François Roux (IMEP-LAHC, Univ. of Savoie, France) for preliminary experiments within the ANR-JST WITH project which helped converging towards higher electromagnetic compatibility detector.

REFERENCES

[1] H. Song and T. Nagatsuma, "Present and future of terahertz communications," *IEEE Trans. Terahertz Sci. Technol.*, vol. 1, no. 1, pp. 256–263, 2011.

[2] J. Federici and L. Moeller, "Review of terahertz and subterahertz wireless communications," *J. Appl. Physics*, vol. 107, no. 11, p. 111101, 2010.

[3] T. Kleine-Ostmann and T. Nagatsuma, "A review on terahertz communications research," *J. Infrared Milimeter Terahertz Waves*, vol. 32, no. 2, pp. 143–171, 2011.

[4] C. Jansen, S. Priebe, C. Moller, M. Jacob, H. Dierke, M. Koch, and T. Kurner, "Diffuse scattering from rough surfaces in THz communication channels," *IEEE Trans. Terahertz Sci. Technol.*, vol. 1, no. 2, pp. 462–472, 2011.

[5] T. Kürner, "Towards future THz communications systems," *Int. J. Terahertz Sci. Technol.*, vol. 1, no. 2, pp. 462–472, 2011.

[6] D. Dragoman and M. Dragoman, "Terahertz fields and applications," *Progress in Quantum Electronics*, vol. 28, no. 1, pp. 1–6, 2004.

[7] C. Jastrow *et al.*, "300 GHz transmission system," *Electron. Lett.*, vol. 44, no. 3, pp. 213–214, 2008.

[8] L. Moeller *et al.*, "2.5 Gb/s error-free transmission at 625 GHz using a narrow-bandwidth 1 mWTHz source," in *Proc. Tech. Dig. URSI General Assembly and Scientific Symposium*, 2001.

[9] K. Ishigaki *et al*, "Direct intensity modulation and wireless data transmission characteristics of terahertz-oscillating resonant tunnelling diodes," *Electron. Lett.*, vol. 48, no. 10, pp. 582–583, 2012.

[10] M. Dyakonov and M. Shur, "Detection, mixing, and frequency multiplication of terahertz radiation by two-dimensional electronic fluid," *IEEE Trans. Electron Devices*, vol. 43, no. 3, pp. 380–387, 1996.

[11] W. Knap and M. I. Dyakonov, "Field-effect transistor for terahertz applications," *Handbook of terahertz technology for imaging, sensing and communications, Woodhead Publishing Series in Electronic and Optical Materials*, no. 34, 2013.

[12] W. Knap *et al.*, "Field effect transistors for terahertz detection: Physics and first imaging applications," *J. Infrared Millimeter Terahertz Waves*, vol. 30, pp. 1319–1337, 2009.

[13] J. Antes, S. Konig, A. Leuther, H. Massler, J. Leuthold, O. Ambacher, and I. Kallfass, "220 GHz wireless data transmission experiments up to 30 Gbit/s," in *Proc. IEEE MTT-S International Microwave Symposium Digest (MTT)*, pp. 1–3, 2012.

[14] G. Ducournau, A. Beck, F. Pavanello, P. Latzel, T. Akalin, E. Peytavit, M. Zaknoune, and J. Lampin, "22 Gbit/s wireless link at 400 GHz using photonic transmitter and heterodyne electronic detection," in *Proc. 7th Terahertz Days*, 2013.

[15] T. J. Chung and W.-H. Lee, "10-Gbit/s wireless communication system at 300 GHz," *ETRI J.*, vol. 35, no. 3, 2013.

[16] L. Tohme, S. Blin, P. Nouvel, L. Varani, and A. Pénarier, "Room-temperature terahertz heterodyne mixing in GaAs commercial transistors," in *Proc. IRMMW-THz (Mainz, Germany)*, 2013.

[17] H.-J. Song, K. Ajito, A. Wakatsuki, Y. Muramoto, N. Kukutsu, Y. Kado, and T. Nagatsuma, "Terahertz wireless communication link at 300 GHz," in *Proc. Int. Topical Meeting Microw. Photon. (MWP)*, 2010, pp. 42–45.

[18] F. Schuster, D. Coquillat, H. Videlier, M. Sakowicz, F. Teppe, L. Dussopt, B. Giffard, T. Skotnicki, and W. Knap, "Broadband terahertz imaging with highly sensitive silicon CMOS detectors," *Optics Express*, vol. 19, no. 8, pp. 7827–7832, 2011.

[19] S. Blin, F. Teppe, L. Tohme, S. Hisatake, K. Arakawa, P. Nouvel, D. Coquillat, A. Pénarier, J. Torres, L. Varani, W. Knap, and T. Nagatsuma, "Plasma-wave detectors for terahertz wireless communication," *IEEE Electron Device Lett.*, vol. 33, no. 10, pp. 1354–1356, 2012.

[20] A. Lisauskas *et al.*, "Terahertz imaging with Si MOSFET focal-plane arrays," in *Proc. SPIE*, 2009, vol. 7215, no. 6.

[21] L. Tohme, G. Ducournau, S. Blin, D. Coquillat, P. Nouvel, A. Pénarier, W. Knap, and J. F. Lampin, "0.2 THz wireless communication using plasma-wave transistor detector," in *Proc. IRMMW-THz*, 2013.

[22] M. Dyakonov and M. Shur, "Shallow water analogy for a ballistic field effect transistor: New mechanism of plasma wave generation by dc current," *Phys. Rev. Lett.*, vol. 71, pp. 2465–2468, Oct. 1993.

[23] M. I. Dyakonov and M. S. Shur, "Plasma wave electronics: Novel terahertz devices using two dimensional electron fluid," *IEEE Trans. Electron Devices*, vol. 43, no. 10, pp. 1640–1645, 1996.

[24] J.-Q. Lu and M. S. Shur, "Terahertz detection by high-electron-mobility transistor: Enhancement by drain bias," *Appl. Physics Lett.*, vol. 78, no. 17, pp. 2587–2588, 2001.

[25] W. Knap, Y. Deng, S. Rumyantsev, and M. Shur, "Resonant detection of subterahertz and terahertz radiation by plasma waves in submicron field-effect transistors," *Appl. Physics Lett.*, vol. 81, no. 24, pp. 4637–4639, 2002.

[26] A. El Fatimy, F. Teppe, N. Dyakonova, W. Knap, D. Seliuta, G. Valusis, A. Shchepetov, Y. Roelens, S. Bollaert, A. Cappy, *et al.*, "Resonant and voltage-tunable terahertz detection in InGaAs InP nanometer transistors," *Appl. Physics Lett.*, vol. 89, no. 13, p.131926, 2006.

[27] M. Dyakonov, "Generation and detection of Terahertz radiation by field effect transistors," *Comptes Rendus Physique*, vol. 11, no. 7, pp. 413–420, 2010.

[28] S. Boubanga-Tombet, F. Teppe, D. Coquillat, S. Nadar, N. Dyakonova, H. Videlier, W. Knap, A. Shchepetov, C. Gardés, Y. Roelens, *et al.*, "Current driven resonant plasma wave detection of terahertz radiation: Toward the Dyakonov-Shur instability," *Appl. Physics Lett.*, vol. 92, no. 21, p. 212101, 2008.

[29] A. Muravjov, D. Veksler, X. Hu, R. Gaska, N. Pala, H. Saxena, R. Peale, and M. Shur, "Resonant terahertz absorption by plasmons in gratinggate GaN HEMT structures," in *Proc. SPIE DSS*, 2009, p. 73110D.

[30] P. Nouvel, H. Marinchio, J. Torres, C. Palermo, D. Gasquet, L. Chusseau, L. Varani, P. Shiktorov, E. Starikov, and V. Gruzinskis, "Terahertz spectroscopy of plasma waves in high electron mobility transistors," *J. Appl. Physics*, vol. 106, no. 1, p. 013717, 2009.

[31] R. Tauk, F. Teppe, S. Boubanga, D. Coquillat, W. Knap, Y. Meziani, C. Gallon, F. Boeuf, T. Skotnicki, C. Fenouillet-Beranger, *et al.*, "Plasma wave detection of terahertz radiation by silicon field effects transistors: Responsivity and noise equivalent power," *Appl. Physics Lett.*, vol. 89, no. 25, p. 253511, 2006.

[32] E. Ojefors, U. R. Pfeiffer, A. Lisauskas, and H. G. Roskos, "A 0.65 THz focal-plane array in a quarter-micron CMOS process technology," *IEEE J. Solid-State Circuits*, vol. 44, no. 7, pp. 1968–1976, 2009.

[33] L. Romeo, D. Coquillat, M. Pea, D. Ercolani, F. Beltram, L. Sorba, W. Knap, A. Tredicucci, and M. Vitiello, "Nanowire-based field effect transistors for terahertz detection and imaging systems," *Nanotechnol.*, vol. 24, no. 21, p. 214005, 2013.
[34] L. Vicarelli, M. Vitiello, D. Coquillat, A. Lombardo, A. Ferrari, W. Knap, M. Polini, V. Pellegrini, and A. Tredicucci, "Graphene field-effect transistors as room-temperature terahertz detectors," *Nature Materials*, 2012.
[35] T. Watanabe, S. B. Tombet, Y. Tanimoto, Y. Wang, H. Minamide, H. Ito, D. Fateev, V. Popov, D. Coquillat, W. Knap, *et al*, "Ultrahigh sensitive plasmonic terahertz detector based on an asymmetric dual-grating gate HEMT structure," *Solid-State Electron.*, 2012.
[36] V. Popov, D. Fateev, T. Otsuji, Y. Meziani, D. Coquillat, and W. Knap, "Plasmonic terahertz detection by a double-grating-gate field-effect transistor structure with an asymmetric unit cell," *Appl. Physics Lett.*, vol. 99, no. 24, p. 243504, 2011.
[37] D. But, C. Drexler, N. Dyakonova, O. Drachenko, S. Ganichev, and W. Knap, "Nonlinear photoresponse of FET THz broadband detectors at high power irradiation," in *Proc. IRMMW-THz (Mainz, Germany)*, 2013.
[38] W. Knap, S. Rumyantsev, M. S. Vitiello, D. Coquillat, S. Blin, N. Dyakonova, M. Shur, F. Teppe, A. Tredicucci, and T. Nagatsuma, "Nanometer size field effect transistors for terahertz detectors," *Nanotechnology*, vol. 24, no. 21, p. 214002, 2013.
[39] T. Ishibashi, T. Furuta, H. Fushimi, S. Kodama, T. Nagatsuma, N. Shimizu, and Y. Miyamoto, "InP/InGaAs uni-traveling-carrier photodiodes," *IEICE Trans. Electron.*, vol. 83, no. 6, pp. 938–949, 2000.
[40] A. Hirata, H. Ishii, and T. Nagatsuma, "Design and characterization of a 120-GHz millimeter-wave antenna for integrated photonic transmitters," *IEEE Trans. Microw. Theory Tech.*, vol. 49, no. 11, pp. 2157–2162, 2001.
[41] T. Nagatsuma, S. Horiguchi, Y. Minamikata, Y. Yoshimizu, S. Hisatake, S. Kuwano, N. Yoshimoto, J. Terada, and H. Takahashi, "Terahertz wireless communications based on photonics technologies," *Opt. Express*, vol. 21, pp. 23736–23747, Oct. 2013.

Stéphane Blin was born in St Nazaire, France on January 6, 1977. He received the Ph.D. degree in Physics from Enssat, Lannion, France and the Ph.D. degree in Electrical Engineering from Université Laval, Québec, Canada in 2003. From 2000 to 2004, he led original optical injection experiments at very low injection levels which led to original metrological methods, and studied frequency noise of highly-coherent lasers with DiCOS Technol. From 2004 to 2007, he was engaged in research on acoustic fiber-sensor arrays and air-core photonic-bandgap fiber-optic gyroscope at Ginzton Laboratory, Stanford University, CA. From 2007 to 2009, he worked at Foton laboratory (Enssat) on high-peak-power fiber lasers for material processing applications. Since 2009, he joined the Institut d'électronique du sud, University of Montpellier 2, France as an associate professor. His current research interests are THz-waves generation, detection, waveguides and systems.

Tadao Nagatsuma received B.S., M.S., and Ph.D. degrees in electronic engineering from Kyushu University, Fukuoka, Japan, in 1981, 1983, and 1986, respectively. From 1986 to 2007, he was with Nippon Telegraph and Telephone Corporation (NTT), Atsugi, Kanagawa, Japan. Since 2007, he has been a Professor at Graduate School of Engineering Science, Osaka University. His research interests include millimeter-wave and terahertz photonics and their application to sensors and wireless communications. Prof. Nagatsuma is a Fellow of the Institute of Electronics, Information and Communication Engineers (IEICE), Japan, a Senior Member of the IEEE, and Members of the Technical Committee on Microwave Photonics of the IEEE Microwave Theory and Techniques Society, and the Microwave Photonics Steering Committee, and serves as an Associate Editor of the IEEE Photonics Technology Letters. He is the Recipient of numerous awards including the 1992 IEEE Andrew R. Chi Best Paper Award, the 1997 Okochi Memorial Award, the 1998 Japan Microwave Prize, the 2000 Minister's Award of the Science and Technology Agency, the 2002 Asia-Pacific Microwave Conference Prize, the 2004 Yokosuka Research Park Award, the 2006 Asia-Pacific Microwave-Photonics Conference Award, the 2006 European Microwave Conference Prize, the 2007 Achievement Award presented by the IEICE, the 2008 Maejima Award presented by the Post and Telecom Association of Japan, the 2011 Commendation for Science and Technology by the Minister of Education, Culture, Sports, Science and Technology, the 2011 Recognition from Kinki Bureau of Telecommunications, Ministry of Internal Affairs and Communications, the 2011 Asia-Pacific Microwave Conference Prize, the 2012 Osaka University Presidential Awards for Achievement, and the 2013 Nikkei Electronics Japan Wireless Technology Award.

Wojciech Knap obtained his M.S. and Ph.D. degrees from Faculty of Physics – Warsaw University Poland. His Ph.D. concerned the Terahertz (Far infrared) properties of narrow gap semiconductors HgTe and InSb. After his M.S. degree he obtained a Permanent Assistant Professor position at University of Warsaw Solid State Physics Department. In 1987 he left to France and worked at University of Montpellier, Grenoble High Magnetic Field Laboratory, Toulouse Pulsed High Magnetic Field Laboratory. In 1992 he obtained a permanent position at French National Center for Scientific Research - CNRS – Montpellier. Between 1999 and 2001 he worked (sabbatical) at USA – Rensellear Polytechnic Institute – at group of Prof. M. Shur. He obtained also a long term grant from Japan Society of Promotion of Science and spent a year in Prof. T. Otsuji group - Tohoku University 2007–2008. His main scientific interests and activities are: i) Fair Infrared-FIR (Terahertz - THz) properties of semiconductors: Investigation of absorption, detection and emission of Far Infrared (THz) radiation by free and shallow impurity bound carriers, ii) Quantum phenomena in transport: Weak localisation and anti-localisation and ballistic behaviour in low dimensional systems, and iii) Terahertz Plasma excitations in nanotransistors.

Modal decomposition technique for multimode fibers

Duc Minh Nguyen,[1,*] Stéphane Blin,[2] Thanh Nam Nguyen,[1] Sy Dat Le,[1] Laurent Provino,[3] Monique Thual,[1] and Thierry Chartier[1]

[1]Université Européenne de Bretagne, France/CNRS (UMR6082) Foton, 6 rue de Kerampont 22300 Lannion, France

[2]Institut d'Electronique du Sud, UMR 5214 CNRS, Université Montpellier 2, 34095 Montpellier, Cedex 5, France

[3]Perfos, 11 rue Louis de Broglie, 22300 Lannion, France

*Corresponding author: dnguyen@enssat.fr

Received 19 July 2011; revised 21 November 2011; accepted 23 November 2011; posted 23 November 2011 (Doc. ID 151385); published 26 January 2012

We propose a new solution for modal decomposition in multimode fibers, based on a spectral and spatial imaging technique. The appearance of spurious modes in the spectral and spatial processing of the images at the output of the fiber under test when it has more than two modes is demonstrated theoretically. The new method, which allows us to identify spurious modes, is more accurate, simpler, and faster than previously reported methods. For demonstration, measurements in a standard step-index multimode fiber and a small-core microstructured fiber are carried out successfully. © 2012 Optical Society of America

OCIS codes: 060.2270, 060.2320.

1. Introduction

In the last decade, the advent of highly nonlinear microstructured fibers [1,2] offers all-new possibilities in all-optical signal processing, such as data regeneration, time-division demultiplexing, or wavelength conversion. These applications are often based on the third-order nonlinear optical effects, which are limited by multimode propagation. However, single-mode propagation is not guaranteed in some microstructured fibers, either due to fiber design or imperfections in the fabrication process. On the other hand, multimode fibers are used in many applications, such as high powered lasers, to reduce optical nonlinear effects due to their large mode-areas or in sensing applications for utilizing modal interferences. Therefore, modal analysis of multimode fibers is necessary in order to identify the existing modes and to determine the power distribution within this set of modes. Several methods for a full modal decomposition have been proposed. With these methods, the transverse modes propagating in the fiber are identified, as well as relative optical power, spatially resolved transverse amplitude, and phase of the electrical field [3–6]. The method proposed by Shapira *et al.* [3] determines experimentally the mode profiles using an algorithm based on the observation of near-field and far-field images at the waveguide output. The disadvantages, however, are the complexity of the algorithm and the need to acquire two images of near-field and far-field. A more direct measurement of the higher-order modes (HOMs) was made by using a bulk-optic Fabry–Perot resonator, but careful alignment of the bulk optics and a relatively large fraction of power ($>3\%$) in the HOMs are necessary [4]. Finally, methods described in [5,6] using differential delay measurements effectively discriminate transverse modes and measure relative optical power of each mode, but transverse mode amplitude profiles are not extracted. More recently, a new method has been introduced by Nicholson *et al.* [7,8], namely the S^2 imaging, for spatially and spectrally resolved imaging of mode content in fibers. The technique is sensitive to HOMs and allows determination of accurate values of their relative optical power. However, the spatial solution is limited by diffraction limits, and only large-mode-area fibers can

1559-128X/12/040450-07$15.00/0

be characterized. The measurement is also time consuming due to the two-dimensional scanning of the mode at every position (x,y) of the output surface of the large-core fiber, and it is limited to the case when the power of HOMs is small enough, in comparison to the fundamental mode, to be able to ignore interferences between two HOMs. In this paper, we demonstrate theoretically that spurious modes always appear in the S^2 imaging technique when the fiber under test has more than two modes. A new technique for modal decomposition whose algorithm is developed to the general case in which interferences between HOMs are taken into account is proposed. The measurement setup is improved as the two-dimensional spatial scanning in the S^2 imaging technique is replaced by a unidimensional scanning of the wavelength. The characterization process is thus much faster, the method is not limited to large-mode-area fibers, optical alignments are straightforward, and there is no moving part, since only near-field images are observed. The paper is organized as follows. Section 2 discusses spurious modes in the S^2 imaging method. Section 3 describes the principle of the new method. Experimental demonstration with a standard step-index multimode fiber and a small-core microstructured fiber is presented in Section 4.

2. Spurious Modes in S^2 Imaging Method

Measurement based on interference effects is well known in optical systems, either due to its sensitivity or its accuracy. The S^2 imaging technique [7,8], which is based on the processing of the spectrally and spatially resolved interference images at the output of the fiber under test, is therefore a useful method for full modal decomposition. Spectral interference observed in the near-field images is caused by the group-delay difference between the HOMs and the fundamental mode propagating in the fiber. Figure 1(a) presents an example of a typical optical spectrum measured at an arbitrary point (x,y), where interferences between several transverse modes are locally observed. These interferences lead to several different mode beats at different time delays in the Fourier transform of the spectrum, as shown in Fig. 1(b). If the fiber supports two transverse modes, there is only one spectral interference between the fundamental mode and the HOM. A peak in the Fourier transform of the optical spectrum obtained from each spatial point in the near-field image is then observed. In a more general case when the fiber has more than two modes, the S^2 imaging technique assumes that the power of HOMs is weak compared to the power of the primary LP_{01} mode, and thus interference between two different HOMs is considered negligible. This means that if the fiber supports n HOMs, there will be n different beat frequencies visible, corresponding to interferences between the primary LP_{01} mode and different HOMs. However, the condition that the HOMs are weak compared to the fundamental mode is ambiguous. We will demonstrate in this section that even when the relative power between the HOMs and the LP_{01} is low, the interference between the HOMs cannot be ignored. Let us suppose that the fiber has n HOMs and that their amplitudes E_i are related to the amplitude E_0 of the fundamental mode LP_{01} by a constant α_i such that

$$E_i(x,y,w) = \alpha_i(x,y,w)E_0(x,y,w)\exp(iw\tau_i), \quad (1)$$

where τ_i is the period of the beat frequency between the corresponding HOM and the LP_{01} caused by their relative group-delay difference. The spectral intensity caused by interference between all modes propagating in the fiber can be written as

$$\begin{aligned} I(x,y,w) &= I_0(x,y,w)\left[1+\sum_{j=1}^{n}\alpha_j(x,y,w)e^{iw\tau_j}\right] \\ &\quad\times\left[1+\sum_{k=1}^{n}\alpha_k(x,y,x)e^{-iw\tau_k}\right] \\ &= I_0\Bigg(1+\sum_{j=1}^{n}\alpha_j^2+\sum_{j=1}^{n}\alpha_j(e^{iw\tau_j}+e^{-iw\tau_j}) \\ &\quad+\sum_{j>k}^{n}\alpha_j\alpha_k(e^{iw(\tau_j-\tau_k)}+e^{-iw(\tau_j-\tau_k)})\Bigg), \end{aligned} \quad (2)$$

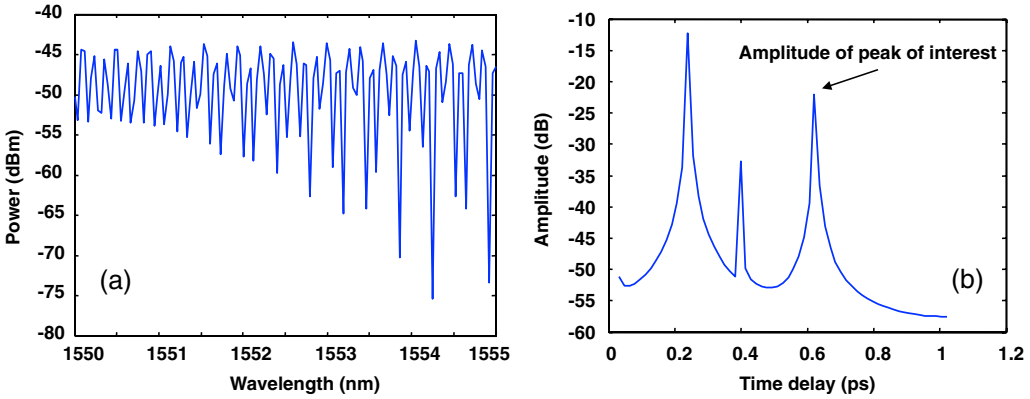

Fig. 1. (Color online) (a) Typical spectrum measured at an arbitrary (x,y) point and (b) its Fourier transform showing multiple beat frequencies.

with $I_i = |E_i|^2$. The Fourier transform of the spectral intensity is then

$$B(x,y,\tau) = \left[1 + \sum_{j=1}^{n} \alpha_j^2(x,y)\right] B_0(x,y,\tau) + \sum_{j=1}^{n} \alpha_j(x,y)[B_0(x,y,\tau-\tau_i) + B_0(x,y,\tau+\tau_i)] + \sum_{j>k}^{n} \alpha_j(x,y)\alpha_k(x,y)[B_0(x,y,\tau-\tau_i+\tau_k) + B_0(x,y,\tau+\tau_i-\tau_k)], \quad (3)$$

where $B_0(x,y,\tau) = F\{I_0(x,y,w)\}$ is the Fourier transform of the optical spectrum of the fundamental mode. The second term in the right hand side of Eq. (3) is caused by the interference between the HOMs and the LP_{01} mode. It is also responsible for the appearance of n peaks at time delay τ_j in the spatial-dependent Fourier transform of the optical spectrum. The ratio $f_j(x,y)$ of these peaks, which is defined as the amplitude of the Fourier transform of the spectral intensity at the corresponding group-delay difference divided by the amplitude at group-delay zero, can be then written as

$$f_j(x,y) = \frac{B(x,y,\tau=\tau_j)}{B(x,y,\tau=0)} = \frac{\alpha_j(x,y)}{1+\sum_{j=1}^{n}\alpha_j^2(x,y)}. \quad (4)$$

The last term in the right hand side of Eq. (3) comes from interferences between two HOMs. This term leads to additional $n!/(2(n-2)!) = C_n^2$ peaks at time delay $|\tau_j - \tau_k|$ in the Fourier transform, in which their ratio f_{jk} can be calculated from

$$f_{jk}(x,y) = \frac{B(x,y,\tau=\tau_j-\tau_k)}{B(x,y,\tau=0)} = \frac{\alpha_j(x,y)\alpha_k(x,y)}{1+\sum_{j=1}^{n}\alpha_j^2(x,y)}. \quad (5)$$

For simplicity, we call the peaks corresponding to interferences between the LP_{01} and the HOMs peaks P_j and the peaks corresponding to interference between two HOMs peaks P_{jk}. When the fiber has only one HOM or the relative power of the HOMs to the LP_{01} is very low, we return to the case explained in the S^2 imaging method [7], in which Eqs. (4) and (5) become

$$f_j(x,y) = \frac{\alpha_j(x,y)}{1+\alpha_j^2(x,y)}, \quad (6)$$

$$f_{jk}(x,y) \approx 0. \quad (7)$$

This means that peaks P_{jk} vanish and only n peaks P_j are observed in the Fourier transform. Mode image and relative power of each HOM, as in the principle of the S^2 imaging method, are then extracted separately and independently from each peak P_j from Eq. (6). In a general case when interferences between two HOMs are taken into account, n peaks P_j and C_n^2 peaks P_{jk} are observed. Only modes extracted from n peaks P_j are real HOMs and modes extracted from the peaks P_{jk} are spurious modes. It is also impossible to determine spatial intensity profile and relative power of HOMs independently from Eq. (6) instead of using Eq. (4). Moreover, the condition that the relative power of HOMs is low to ignore interferences between two HOMs is ambiguous. Interference between two HOMs LP_{11} and LP_{02} is discovered in the Fourier transform as shown in Fig. 2(a) even when their relative power to the primary mode LP_{01} is low, −20 dB and −30 dB, respectively. As shown on this spectra, peaks are easily identified and accuracy of mode retrieval relies directly on the ratio between these peaks and the fast Fourier transform (FFT) background. In this figure, in addition to two real peaks P_1, P_2 at time delay τ_1, τ_2 corresponding to two HOMs LP_{11} and LP_{02}, the spurious peak P_{12} corresponding to interference between the LP_{11} and the LP_{02} at time delay $\tau_2 - \tau_1$ is found. Figure 2(b) is another example of the Fourier transform in the case of

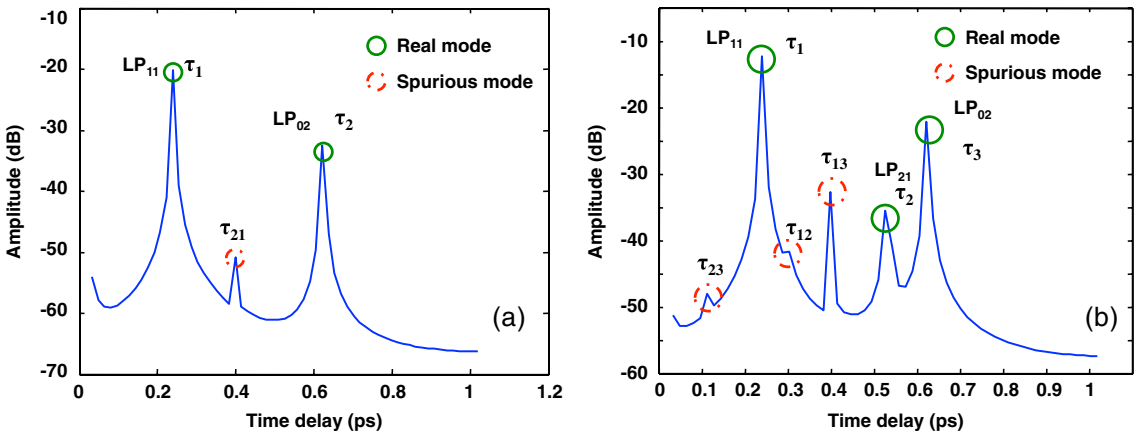

Fig. 2. (Color online) The Fourier transform when (a) the fiber supports two HOMs LP_{11} and LP_{02} and (b) when three HOMs are supported: LP_{11}, LP_{21}, and LP_{02}.

a fiber that supports three transverse HOMs LP_{11}, LP_{02}, and LP_{21} at relative powers of −12 dB, −21 dB, and −33 dB, respectively. Three spurious peaks corresponding to mutual interferences between these HOMs are observed. Modes extracted from spurious peaks P_{jk} are spurious modes that result from intrinsic properties of the wave propagation in the fiber. Besides, there is another kind of spurious mode that comes from extrinsic elements such as the instability of the measurement or the laser source. Since the Fourier transform reflects all phenomena causing interference at the output spectra, any oscillation in the measurement will lead to a spurious peak in the Fourier transform. In summary, the problem of spurious modes is really a challenge in the S^2 imaging method that can reduce the accuracy of the measurement, not only in the number of HOMs but also in their relative optical power. A full solution in the general case is therefore necessary.

3. Modal Decomposition Technique

In this section, we propose a new technique for full modal decomposition that is an alternative of the S^2 imaging method but with much improvement both in the calculated algorithms and the measurement setup. The algorithm used to retrieve modes in the S^2 imaging technique is based on the hypothesis that one mode (usually the fundamental one) is much more powerful than the others, and thus neglects the possible interferences between other modes. These interferences are misinterpreted by the algorithm, which leads to the apparition of spurious modes at the algorithm output. We present an alternative to this algorithm that is not limited to the case of a dominant mode, and provide a solution to identify and then eliminate these spurious modes, thus offering artifact-free analysis of the measurement. Moreover, replacement of a broadband laser source with a tunable laser source helps the new technique to have only one-dimensional scanning, instead of two-dimensional scanning in the previous method. The measure is therefore faster, simpler, and more stable.

The experimental setup is presented in Fig. 3. The implementation is simple, although it is the first time, to the best of our knowledge, that such a setup is used both to discriminate transverse modes and to determine their spatial profiles. Light from a tunable source is coupled to the fiber under test. Drawbacks of the S^2 imaging method due to a two-spatial dimensional scanning, which is necessary to measure the magnified image of the fiber end with a single-mode

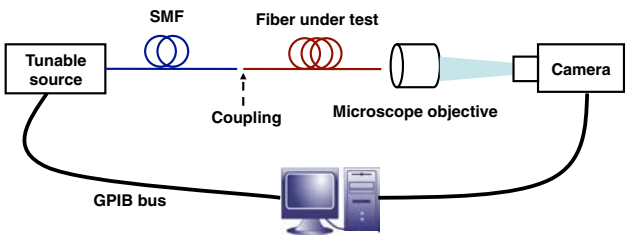

Fig. 3. (Color online) Experimental setup for the new technique.

fiber, are alleviated by simply scanning the wavelength of the tunable source and observing the magnified near-field image of the fiber end using a camera, as presented in Fig. 3. As transverse modes do not propagate at the same speed in the fiber, we observe an interference pattern at the fiber output (as previously described in Eq. (2)). At every position (x,y) of this pattern, the interference state depends on modes amplitudes, but also on relative propagation phases (which thus depend on wavelength). As explained in the previous section, the interference states at every position evolve periodically as the wavelength is increased. The magnified near-field image of the fiber output is recorded every time the wavelength of the source is changed. Transmission spectra at each position (x,y) as shown in Fig. 1(a) are then extracted from the set of images, acquired at each wavelength of the source. The integrated Fourier transform of these optical spectra (cf. Figure 1(b)) is then calculated. Maximum peaks in the Fourier transform will be used to retrieve all the existing modes. However, spurious peaks that correspond to interferences between two HOMs or an oscillating instability of the measurement must be excluded first. An exclusion technique consisting of two steps is implemented to solve this problem.

The first step is to remove spurious peaks that are not caused by intrinsic properties of the wave propagation in the fiber. Since time delays of the peaks related to interferences between different modes propagating in the fiber are always proportional to the fiber length, while this does not occur for the spurious peaks that do not come from intrinsic properties of the fiber, we can eliminate spurious peaks by measuring the fiber with two different lengths. The peak whose time delay remains when the fiber length changes is a spurious peak and will be eliminated.

The last step is to remove spurious peaks resulting from interferences between two HOMs. Since the power of HOMs is normally much smaller than that of the fundamental mode, the coefficient α_j in Eqs. (4) and (5) is smaller than 1. We can also see from these two equations that the ratio f_{jk} of the peak P_{jk} corresponding to the interference between the mode P_j and the mode P_k is always smaller than the ratio f_j and f_k of the peaks P_j and P_k. The two highest peaks P_1 and P_2 at time delays τ_1 and τ_2 in the Fourier transform are then real peaks due to this property. The first spurious peak P_{12} is then determined at the position $|\tau_2 - \tau_1|$. Amplitude of this spurious peak is also larger than other spurious peaks because it corresponds to the interference of the two largest HOMs. All other peaks whose amplitudes are higher than the one of this peak are therefore real peaks. Spurious peaks that come from interferences between these real peaks can be then determined according to their differences in time delays. We call these spurious peaks the P_{12-s}. The highest peak P_3 that is lower than the peak P_{12} and is not one of the peaks P_{12-s} is also a real peak. All remaining peaks that are higher than P_3 are real

peaks, and spurious modes corresponding to interferences between these real peaks can be then calculated. The same procedure is implemented until all peaks are classified.

In summary, using the exclusion technique, we can determine all real peaks P_j and eliminate other spurious peaks. All the existing modes are retrieved using the ratio $f(x,y)$ of these peaks. From Eq. (4), the coefficient is related to $f_j(x,y)$ by

$$\alpha_j(x,y) = \frac{f_j(1 - \sqrt{1 - 4\sum_1^n f_k^2})}{2\sum_1^n f_k^2}. \tag{8}$$

The intensities of HOMs are then given by

$$I_j(x,y) = I_T(x,y)\frac{\alpha_j^2(x,y)}{1 + \sum_{k=1}^n \alpha_k^2}, \tag{9}$$

where $I_T(x,y)$ is the integrated optical spectrum at a given (x,y) point. Relative optical power and spatially resolved transverse amplitude can be calculated from Eq. (9).

Moreover, with the new measurement setup, only one-dimensional scanning required on the wavelength is done. In the S^2 technique, the two-spatial dimensional scanning requires careful optical alignments at the fiber under test output, which is time consuming and can require multiple hours of scanning to achieve a sufficient solution. These alignments are much simpler in our technique, as transverse/angular alignments can be approximate. The new technique is therefore simpler and not time consuming. It takes several minutes for a measurement.

Accuracies in reproducing modal images or relative modal powers are improved due to the faster nature of the experiment and new algorithms in which interferences between two HOMs are taken into account.

As the previously published technique is slow, modal content could change during the scanning, thus conducting to erroneous mode images (and thus erroneous relative modal power). Note that the more modes are propagating in the fiber, the faster the interference figure at the fiber output changes. Therefore, the faster technique we propose allows for more accurate imaging of a multimode fiber supporting few modes, or allows characterizing a fiber supporting more modes.

The accuracy of the measurement is also improved by using the new algorithms of the new technique in which the interferences between two HOMs are taken into account. In the case of a multimode fiber supporting three HOMs, which is expressed in Section 2 and in Fig. 2(b), relative powers between HOMs and the fundamental mode calculated by the S^2 technique, in which interferences between two HOMs are ignored, and the values calculated by the new algorithms are compared in Table 1. A better accuracy is obtained with the new technique compared to the S^2 technique.

Table 1. Relative Power Calculated by the Previously Published Algorithms and the New Algorithms

	LP_11	LP_02	LP_12
Given values	−12 dB	−21 dB	−33 dB
S^2 technique	−12.1 dB	−22.2 dB	−34.3 dB
New technique	−12.08 dB	−21.7 dB	−33.16 dB

4. Experimental Results

For the experimental demonstration of this technique, we used the experimental setup presented in Fig. 3 with a commercial C-band external-cavity laser. The laser wavelength is swept from 1540 nm to 1550.24 nm with 1024 steps. Light propagates in a standard single-mode fiber whose mode field diameter is about 10.4 μm. This fiber is butt-coupled to the fiber under test. A microscope objective with a magnification of 80 is used to image the near-field at the fiber output. Images are captured using a camera, which returns an 8 bit 200 × 200 points image. The experimental data acquisition was done in a few minutes, thus offering great environment stability. Data processing also requires a few minutes and returns mode intensity profiles, along with their relative optical power. Two fibers are tested, a standard step-index multimode fiber and a small-core microstructured fiber, respectively.

A. Standard Step-Index Multimode Fiber

We mesure 0.5 m-long and 1 m-long standard multimode fibers using the new technique. The core diameter of the fiber is 12 μm, and the core/cladding index difference is 9.8 10^{-1}. This fiber should therefore support four LP modes: LP_{01}, LP_{11}, LP_{21}, and LP_{02}. The new technique takes several minutes for measurement. Figure 4(a) presents the Fourier transform measured for the 0.5 m-long fiber. Three peaks are found. However, the time delay of 4.18 ps of the last peak remains unchanged when the fiber length is changed to 1 m. As explained in the principle of the technique, the last peak is a spurious peak. Expected mode profiles and their relative optical powers are then retrieved using the algorithm (8) and (9), as shown in Fig. 4(b). The fact that the LP_{21} was not observed in the measurement is not due to the principle technique. The technique allows us to characterize the modal content at the fiber output for a given configuration (optical injection, bending, etc.). However, the number of modes excited in our case is only three (LP_{01}, LP_{11}, and LP_{02}) due to the optical injection. It is then evident that the technique discovers only three modes. All four modes are extracted in another measurement for the same fiber but with another configuration of optical injection, as presented in Fig. 5(b). A good agreement with the theoretical modes in Fig. 5(a) confirms the method. To give more proof of the method, an effort to find the origin of the extrinsic spurious mode is

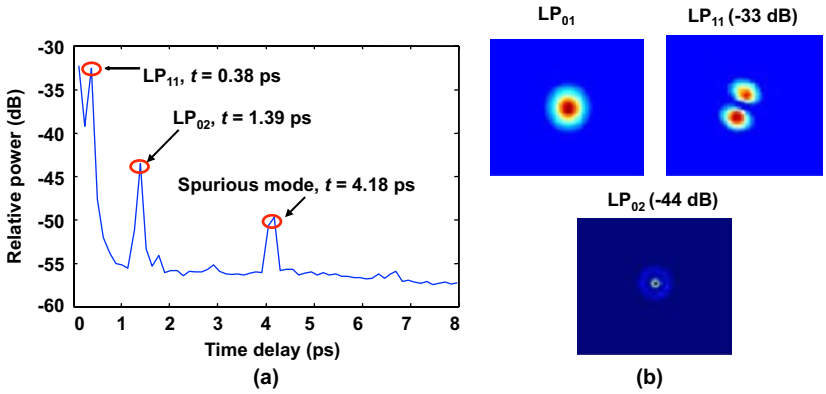

Fig. 4. (Color online) (a) The Fourier transform measured by the new technique for the standard multimode fiber and (b) the HOM profiles and their relative powers.

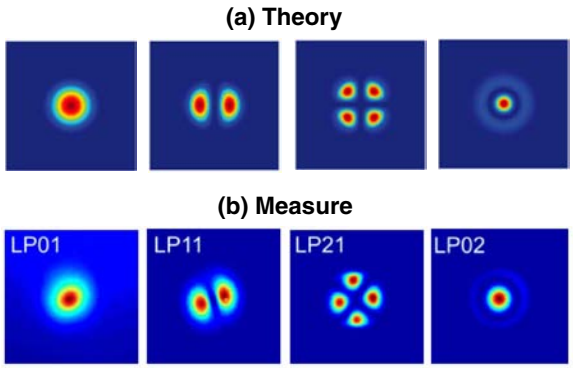

Fig. 5. (Color online) (a) Theoretical modes and (b) modes extracted by the technique in the new measurement for the same standard step-index fiber but with the new condition of the optical injection.

performed. In the principle, the power of the source must be fixed, while the laser wavelength is varied. However, by investigating the power of the laser source as a function of the wavelength, a small modulation of the source power as a function of the wavelength with a period $\Delta\lambda$ of 3.8 nm is found. This modulation leads to a peak in the Fourier transform with the corresponding time delay calculated from $\tau = 2\lambda^2/(c\Delta\lambda) = 4.18$ ps. This value is the same as the time delay of the spurious peak. Consequently, we can conclude that the spurious mode in the experiment results from the power instability of the source, and once again, the spurious mode, as well as the principle of the new technique, is verified.

B. Microstructured Fiber

The second fiber under test is a 1.5-m-long commercially available solid-core microstructured fiber whose fundamental mode has a 2.8-μm-average-diameter triangular shape. The structure of the fiber is sketched in Fig. 6. The triangular core region comprises a germanium-doped center element (red) surrounded by three fluorine-doped rods (blue) embedded in a standard triangular air/silica cladding structure with lower mean refractive index. The diameter of the doped elements equals the pitch. Experimental results are shown in Fig. 7. The fundamental mode and two HOMs are observed. Theoretical modes of the fiber were also calculated, and a good agreement was found with experimental results only if a transverse index inhomogeneity was included in the fiber structure. HOMs 1 and 2 would both have the same intensity profiles for a perfectly homogenous fiber. The main limitation of this experiment

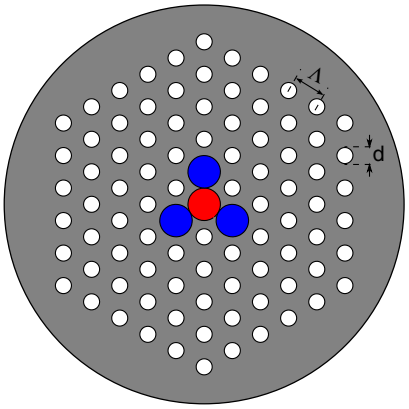

Fig. 6. (Color online) Transverse section of the photonic-crystal fiber. $\Lambda = 1.5$ μm, $d = 0.75$ μm.

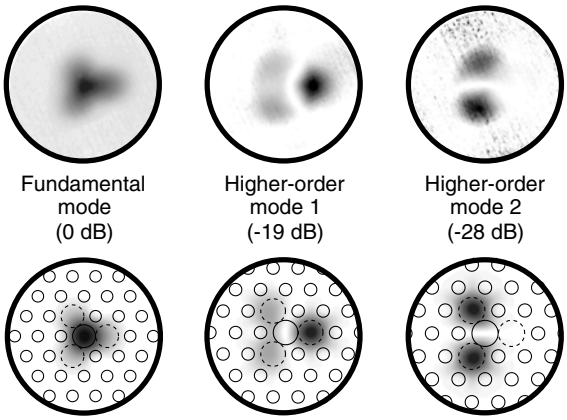

Fig. 7. Experimental (top) and numerical (bottom) intensity profiles of transverse modes for a small-core photonic-crystal optical fiber.

is the need for a tunable laser source, which is not available around some wavelengths. Therefore, we replaced the tunable laser source with the combination of a superfluorescent source and a tunable optical fiber with a 0.27 μm spectral width. Similar results were obtained, thus indicating that optical fibers can be characterized at some exotic wavelengths. Additionally, the cost of the experimental setup can be reduced.

5. Conclusion

A new method for modal analysis of optical fibers was proposed and demonstrated. This method alleviates most of the drawbacks of existing techniques. The algorithm of the method is developed to be able to take into account interferences between two HOMs. The method can thus eliminate spurious modes and offer a more accurate measurement. The characterization process is improved by replacing a two-dimensional scanning in the S^2 imaging technique with unidimensional scanning. This setup is simple and suitable to any optical-fiber core size and not only limited to large-mode-area fibers. A standard step-index multimode fiber and a small-core microstructured fiber have been used to demonstrate the method.

Authors are thankful to Thierry Robin and Benoit Cadier (iXfiber, Lannion, France) for providing the step-index fiber.

References

1. D. M. Nguyen, S. D. Le, K. Lengle, D. Mechin, M. Thual, T. Chartier, Q. Coulombier, J. Troles, L. Bramerie, and L. Brilland, "Visual system-response functions and estimating reflectance," IEEE Photon. Technol. Lett. **22**, 1844–1846 (2010).
2. B. J. Eggleton, B. Luther-Davies, and K. Richardson, "Chalcogenide photonics," Nat. Photon. **5**, 141–148 (2011).
3. O. Shapira, A. F. Abouraddy, J. D. Joannopoulos, and Y. Fink, "Complete modal decomposition for optical waveguides," Phys. Rev. Lett. **94**, 143902–143905 (2005).
4. N. Andermahr, T. Theeg, and C. Fallnich, "Novel approach for polarization-sensitive characterization of transversal modes in few-mode optical fibers," Appl. Phys. B **91**, 353–357 (2008).
5. T.-J. Ahn and D. Y. Kim, "High-resolution differential mode delay measurement for a multimode optics fiber using a modified optical frequency domain reflectometer," Opt. Express **13**, 8256–8262 (2005).
6. S. Ring, D. Menashe, U. Levy, S. Steinblatt, Y. Danziger, and M. Tur, "Characterization in mode coupling in few-mode fibers using optical low-coherence reflectometry," in *Optical Fiber Communication Conference* (2008), paper OWO5.
7. J. W. Nicholson, A. D. Yablon, S. Ramachandran, and S. Ghalmi, "Spatially and spectrally resolved imaging of modal content in large-mode area fibers," Opt. Express **16**, 7233–7243 (2008).
8. J. W. Nicholson, A. D. Yablon, J. M. Fini, and M. D. Mermelstein, "Measuring the modal content of large-mode-area fibers," IEEE J. Sel. Top. Quantum Electron. **15**, 61–70 (2009).

Power- or frequency-driven hysteresis for continuous-wave optically injected distributed-feedback semiconductor lasers

Stéphane Blin[1], Olivier Vaudel[1], Pascal Besnard[1,*] and Renaud Gabet[2]

[1] *Foton-Enssat, CNRS UMR 6082*
6 rue Kerampont, BP 80518, 22305 Lannion cedex, France
[2] *Télécom ParisTech, CNRS/LTCI UMR5141*
46 rue Barrault 75634 Paris, France
[*] *Corresponding author:*
pascal.besnard@enssat.fr

Abstract: Bistabilities between a steady (or pulsating, chaotic) and different pulsating regimes are investigated for an optically injected semiconductor laser. Both numerical and experimental studies are reported for continuous-wave single-mode semiconductor distributed-feedback lasers emitting at 1.55 μm. Hysteresis are driven by either changing the optically injected power or the frequency difference between both lasers. The effect of the injected laser pumping rate is also examined. Systematic mappings of the possible laser outputs (injection locking, bimodal, wave mixing, chaos or relaxation oscillations) are carried out. At small pumping rates (1.2 times threshold), only locking and bimodal regimes are observed. The extent of the bistable area is either 11 dB or 35 GHz, depending on the varying parameters. At high pumping rates (4 times threshold), numerous injection regimes are observed. Injection locking and its bistabilities are also reported for secondary longitudinal modes.

OCIS codes: (140.1540) Chaos ; (140.2020) Diode lasers ; (140.3070) Infrared and far-infrared lasers ; (140.3490) Lasers, distributed-feedback ; (140.3520) Lasers, injection-locked ; (140.3570) Lasers, single-mode ; (140.5960) Semiconductor lasers

References and links

1. H. L. Stover and W. H. Steier, "Locking of laser Oscillators by light injection," Appl. Phys. Lett. **8**, 91–93 (1966).
2. L. E. Erikson and A. Szabo, "Spectral Narrowing of dye Laser Output by injection of Monochromatic Radiation into the Laser Cavity," Appl. Phys. Lett. **18**, 433–435 (1971).
3. G. Stéphan, "Spectral properties of an injected laser," Phys. Rev. A **58**, 2467–2471 (1998).
4. M. Bondiou, "Étude des propriétés spectrales d'un laser semi-conducteur soumis à injection optique," PhD thesis, Rennes I University (1999). (in French).
5. R. Gabet, "Étude expérimentale et théorique de l'injection optique dans un laser à semi-conducteurs : application à la détection de faibles signaux cohérents à 1.55 μm," PhD thesis, ENSSAT, Rennes I University (2000). (in French).
6. J. Troger, "Novel measurement scheme for injection-locking experiments," IEEE J. Quantum Electron. **35**, 32–38 (1999).
7. G.H.M. van Tartwijk, H. de Waardt, B.H. Verbeek, and D. Lenstra, "Resonant Optical Amplification in a Laser Diode: Theory and Experiment," IEEE J. Quantum Electron. **30**, 1763–1768 (1994).
8. A. Hohl, H.J.C. van der Linde, R. Roy, G. Goldstein, F. Broner, and S.H. Strogatz, "Scaling Laws for Dynamical Hysteresis in a Multidimensional Laser System," Phys. Rev. Lett. **74**, 2220–2223 (1995).

#108455 - $15.00 USD Received 10 Mar 2009; revised 25 Apr 2009; accepted 10 May 2009; published 19 May 2009

9. T. Erneux, A. Gavrielides, V. Kovanis, "Low pump stability of an optically injected diode laser," Quantum Semiclassic. Opt. **9**, 811–818 (1997).
10. S. Kobayashi and T. Kimura, "Injection locking in AlGaAs semiconductor laser," IEEE J. Quantum Electron. **17**, 681–689 (1981).
11. H. Kawaguchi, K. Inoue, T. Matsuoka, and K. Otsuka, "Bistable output characteristics in semiconductor laser injection locking," IEEE J. Quantum Electron. **21**, 1314–1317 (1985).
12. H. M. Gibbs, S. L. McCall, T. N. C. Venkatesan, A. C. Gossard, A. Passner, and W. Wiegmann, "Optical bistability in semiconductors," Appl. Phys. Lett. **35**, 451–453 (1979).
13. K. Otsuka and H. Iwamura, "Analysis of a Multistable Semiconductor Light Amplifier," IEEE J. Quantum Electron. **QE-19**, 1184–1186 (1983).
14. K. Otsuka and S. Kobayashi, "Optical Bistability and Nonlinear Resonance in a Resonant-Type Semiconductor Laser Amplifier," Electron. Lett. **19**, 262–263 (1983).
15. T. Nakai, J. Ogasawara, and R. Ito, "Optical Bistability in a Semiconductor Laser Amplifier," Jpn. J. Appl. Phys. **22**, L310–L312 (1983).
16. D. L. Boiko, G. M. Stéphan and P. Besnard, "Fast polarization switching with memory effect in a vertical cavity surface emitting laser subject to modulated optical injection," J. Appl. Phys. **86**, 4096–4099 (1999).
17. R. Hui, A. D'Ottavi, A. Mecozzi and P. Spano, "Injection locking in distributed feedback semiconductor lasers," IEEE J. Quantum Electron. **27**, 1688–1695 (1991).
18. S.K. Hwang and J.M. Liu, "Attractors and basins of the locking-unlocking bistability in a semiconductor laser subject to strong optical injection," Opt. Commun. **169**, 167–176 (1999).
19. V. Kovanis, T. Erneux and A. Gavrielides, "Largely detuned injection-locked semiconductor lasers," Opt. Commun. **159**, 177–183 (1999).
20. S. Wieczorek, B. Krauskopf, T. Simpson, and D. Lenstra, "The dynamical complexity of optically injected semiconductor lasers," Phys. Rep. **416**, 1–128 (2005).
21. S. Blin, C. Guignard, P. Besnard, R. Gabet, G. Stéphan, M. Bondiou, "Phase and spectral properties of optically injected semiconductor lasers," Comptes Rendus Physique **4**, 687–699 (2003).
22. S. Blin, G. Stéphan, R. Gabet, and P. Besnard, "Amplification process in a laser injected by a narrow-band weak signal," Europhys. Lett. **52**, 60–65 (2000).
23. P. C. De Jagher, W. A. van der Graaf, and D. Lenstra, "Relaxation-oscillation phenomena in an injection-locked semiconductor laser," Quantum Semiclassic. Opt. **8**, 805–822 (1996).
24. S. Wieczorek, B. Krauskopf, and D. Lenstra, "A unifying view of bifurcations in a semiconductor laser subject to optical injection," Opt. Commun. **172**, 279–295 (1999).
25. S. L. Chuang, *Physics of Photonic Devices*, Wiley Series in Pure and Applied Optics, 2nd ed. (Wiley, 2009).
26. S. Blin, "Compléments à l'étude expérimentale et théorique de l'injection optique dans des lasers à semiconducteurs et des lasers à fibre à 1550 nm," PhD thesis, ENSSAT (Rennes I University, FRANCE) and Faculté des Sciences et de Génie (Laval University, QUÉBEC - CANADA) (2003). (in French).
27. T. B. Simpson, J. M. Liu, K. F. Huang, and K. Tai, "Nonlinear Dynamics Induced by External Optical Injection in Semiconductors Lasers," Quantum Semiclassic. Opt. **9**, 765–784 (1997).
28. A. Gavrielides, V. Kovanis, P. Varangis, T. Erneux, and T. B. Simpson, "Subharmonic Resonances in an Optically Injected Semiconductor Laser," Proc. SPIE **2693**, 654–665 (1996).
29. G. Iooss and D. Joseph, *Elementary stability and bifurcation theory*, 2nd ed. (Undergraduate texts in Mathematics, 1980).
30. J. Guckenheimer and P. Holmes, *Nonlinear oscillations, Dynamical systems, and Bifurcations of vector fields* in Applied Mathematical Sciences, vol. 42 (1991).
31. S. Blin, O. Vaudel, T. Tam, P. Besnard, S. LaRochelle, R. Gabet, and G. Stéphan, "Spectral and Time Phenomena in Optical Injection Using Distributed Feedback Semiconductor or Fibre Lasers," in *International Workshop on Photonics and Applications (IWPA)* (Hanoï (Vietnam), 2004).
32. O. Vaudel, C. Guignard, and P. Besnard, "Synchronization map of two uni-directionally coupled chaotic semiconductor lasers," in *EUROMECH Nonlinear Dynamics Conference (ENOC)* (Eindhoven (The Netherlands), 2005). Paper 18-427.
33. O. Vaudel, "Étude de synchronisation de chaos par simple injection optique," PhD thesis, ENSSAT, Rennes I University (2007). (in French).
34. I. Petitbon, P. Gallion, G. Debarge, and C. Chabran, "Locking bandwidth and relaxation oscillations of an injected-locked semiconducteur laser," IEEE J. Quantum Electron. **24**, 148–154 (1988).
35. O. Vaudel, J.-F. Hayau, and P. Besnard, "Synchronization between optically injected semiconductor lasers on undamped relaxation oscillations," Opt. Quantum Electron. **40**, 109–118 (2008). Special issue on Nonlinear Photonics - Contributions from the PHASE and IPSSO 2007 International Workshops.
36. A. Gavrielides, V. Kovanis, P.M. Varangis, T. Erneux and G. Lythe, "Coexisting periodic attractors in injection locked diode lasers," Quantum Semiclassic. Opt. **9**, 785–796 (1997).
37. S. Wieczorek, T. Simpson, B. Krauskopf, and D. Lenstra, "Global Quantitative Predictions of Complex Laser Dynamics," Phys. Rev. E **65**, 045,207(R) (2002).

#108455 - $15.00 USD Received 10 Mar 2009; revised 25 Apr 2009; accepted 10 May 2009; published 19 May 2009

1. Introduction

A few years after the first experimental demonstration of a laser by Maiman, Stover [1] presented an optical injection experiment with gas lasers. The signal of a laser, called the *master* laser (ML), was seeded into a second laser called the *slave* laser (SL). Several studies on optical injection then showed that when the frequencies of both lasers are close together and for an appropriate injected power, the slave laser gets the spectral properties of the master one in terms of frequency and linewidth [2–5]. Afterwards, optical injection has been widely used by scientists to obtain tunable, powerful and narrow linewidth lasers for various applications [6] such as telecommunication, spectroscopy or metrology.

In optics, optical bistability usually refers to optical devices where two resonant transmission states are possible and stable, dependent on the input. Such possibility may be provided by resonant optical amplifiers [7] or by optically injected semiconductor lasers if the pumping rate of the injected laser is very close to threshold [8,9]. The first optical bistabilities observed by the way of optical injection were obtained using semiconductor Fabry-Perot lasers by Kobayashi [10] in 1981, and then using distributed feedback (DFB) semiconductor lasers by Kawaguchi [11] in 1985. Such bistable behaviors are based on a saturation-induced refractive-index change due to the injected light, as firstly observed in a semiconductor étalon in 1979 [12] and later predicted [13] and demonstrated [14,15] in a resonant-type semiconductor laser amplifier. Beyond the physics, these bistable behaviors offer potential optical memories applications [16] for ultra-fast processing.

It has been pointed out that the bistability could be associated to a continuous wave output and a periodic orbit (called wave-mixing) [17–19]. This last bistability leads to a hysteresis loop that has been largely analyzed when the injected power or the optical frequency difference between the two lasers (detuning) is swept back and forth.

Wieczorek [20] pointed out the theoretical existence of multistability and of generalized form of bistability, which means the coexistence of two attractors as for example a chaotic attractor and a periodic orbit in a same region of parameters. But from the experimental point of view, it has been only noted by an uncommented mention of an abrupt change in the RIN spectra [20].

In this paper, we concentrate on this generalized form of bistability. To this end, we carry out systematic mapping of the possible long time regimes at both low and high pumping rates of the injected laser. We propose a general view of the bistable properties of an injected laser by carrying out systematic mapping of the injection regimes at different bias currents of the SL when the detuning is increased or decreased. We show a clear hysteresis in these diagrams: the regime at a given operating point (injected power, detuning) is path dependent on the control parameter (for example detuning). Moreover maps are established for larger power (respectively -detuning) extent than previously reported values (~ 5 dB above the reported measurements; respectively 200 GHz-range and more instead of the usual 20 GHz-range for the detuning) [17,18] (resp. [19,20]). While in [17,18], only the wave-mixing–locking bistability is described, our study concerns the coexistence of different regimes (or of different type of attractors). Therefore, we present a broader review of the bistable properties of optically injected lasers than previously reported.

The paper is organized as followed: Section 2 details experimental results obtained with a 1.55-μm single-mode semiconductor DFB laser injected by an external continuous-wave signal, section 3 describes a numerical study, which confirms the experimental observations, and section 4 draws a conclusion.

#108455 - $15.00 USD Received 10 Mar 2009; revised 25 Apr 2009; accepted 10 May 2009; published 19 May 2009

2. Experimental observation of optical bistabilities

2.1. Experimental setup

The experiment consists of a unidirectional coupling from the master laser to the slave laser, imposed by the presence of a double-stage optical isolator (70 dB isolation). Figure 1 displays the sketch of the proposed experiment. The ML is a free-mode-hopping external-cavity single-mode tunable semiconductor laser with a good repeatability and a good stability (frequency jitter of 1 MHz, power fluctuations of 0.01 dB).

The SL is a massive InP/InGaAsP buried-double-heterostructure DFB chip. All components are either pigtailed or fiber-based components. Lasers are properly isolated from external perturbations inside an acoustic box, and all optical components located between the ML and the SL are polarization-maintaining (PM) ones, thus allowing perfect reproducibility of the experiments. The master laser signal is amplified to 18 dBm using an erbium-doped fiber optical amplifier (EDFA). The injected power is then tuned using a variable optical attenuator, thus offering a constant signal to noise ratio of the injected signal.

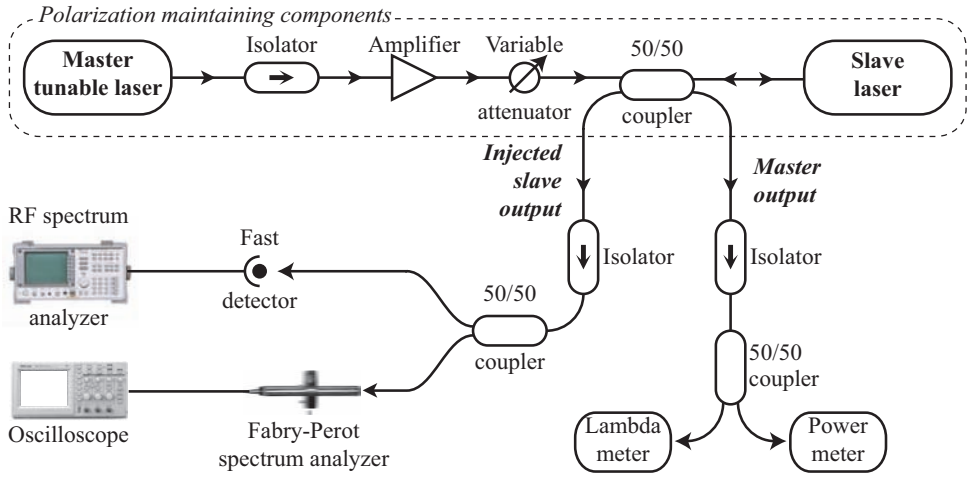

Fig. 1. Experimental setup.

The control parameters of interest in an optical injection experiment are the injected power P_{inj} and the detuning $\Delta\nu = \nu_m - \nu_s$, which is the difference between the master frequency (ν_m) and the slave one (ν_s). The pumping rate r of the slave is fixed during experiments. This metric is defined as $r = I/I_{th}$ where I is the bias current and I_{th} the bias current at threshold. These control parameters are monitored using a power-meter and a lambda-meter as shown in Fig. 1. The optical and electrical spectra of the injected slave are observed using respectively a Fabry-Perot (FP) analyzer and a fast detector coupled to a radio-frequency (RF) spectrum analyzer. The FP is a pigtailed but free-space interferometer with a 135-GHz free spectral range and a finesse of 100, providing a 1.35-GHz resolution. Thus, it is not possible to describe the narrow line of the master laser (whose full width at half maximum is 125 kHz), linewidth transfer and phase locking phenomena have been documented in other publications [2–5,21,22]. The bandwidth of the fast detector allows to observe RF spectra of the injected laser from 0 to 15 GHz.

In this article, experimental results are obtained either by fixing the detuning and varying the injected power, or by fixing the injected power and varying the detuning. These experiments are carried out at two different pumping rates of the slave laser, close to threshold ($r = 1.2$) and far from threshold ($r = 4$).

#108455 - $15.00 USD Received 10 Mar 2009; revised 25 Apr 2009; accepted 10 May 2009; published 19 May 2009

2.2. *Experimental results close to threshold*

The slave is operated at $r = 1.2$. Fig. 2 gives different FP spectra of the injected slave for a fixed detuning of -20 GHz and for increasing (a) or decreasing (b) values of injected powers between -20 and 0 dBm. The injected power is mainly limited by coupling losses between the fiber pigtail and the laser chip. In this figure, the frequency scale is relative to the free slave frequency. Three regimes can be observed as described in the following.

1. Free slave regime: For weak injected powers, the seeded master-light has no effect and the injected slave laser acts as an injection-free laser, as shown in Figs. 2(a)-2(b) for $P_{inj} = -20$ dBm.
2. Bimodal regime (limit cycle): For intermediate injected powers, the injected laser is bimodal, i.e., both natural and injected lines coexist, as shown in Fig. 2(a) for $P_{inj} = -15$ dBm.
3. Injection locking: For stronger injected powers, injection locking occurs and the injected slave signal gets the spectral properties of the master signal, as shown in Figs. 2(a)-2(b) for $P_{inj} = 0$ dBm.

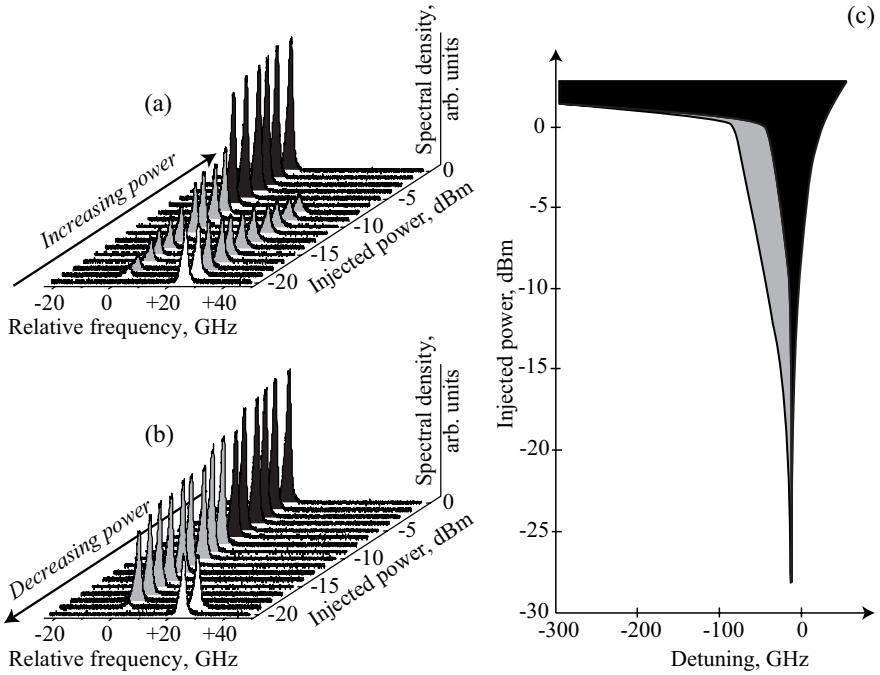

Fig. 2. Experimental observation of optical bistability for an injected slave laser pumped at 1.2 times the threshold. Experimental spectra of the injected slave laser are observed for an increasing (a) or a decreasing (b) injected power. An experimental mapping of the injection regimes is represented in (c). In (a–c), the black color corresponds to the locking regime, the white corresponds to the bimodal regime or the free slave laser. The grey color corresponds to the bistable area. If the detuning or injected power is decreasing, this color corresponds to the locking regime; otherwise it corresponds to a bimodal regime.

Figures 2(a)-2(b) clearly shows the bistability between locking and bimodal regimes. Specifically, we observe that the locking area appears for an increasing injected power of -7.5 dBm,

#108455 - $15.00 USD Received 10 Mar 2009; revised 25 Apr 2009; accepted 10 May 2009; published 19 May 2009

but disappears for the decreasing injected powers of -17.5 dBm, thus describing a 10-dB-extended bistable area. Figure 2(c) displays a map of the locking area (in black) when the injected signal is varying between -30 and $+2$ dBm and when the detuning is varying between -300 and $+100$ GHz. The grey-filled area corresponds to the injection locking regime only for decreasing detuning or injected power. The log scale permits to stress the progressive adiabatic decrease of the grey area along with the decrease of the injected power. The irregularity and lack of symmetries of this map are striking features. A bistable area only exists at negative detuning. This asymmetry has already been mentioned in the literature and it has been reported [23,24] that this behavior is related to the non-zero linewidth-enhancement factor α_H of the slave laser. The larger α_H is, the more asymmetric the map is. Note that the slave laser used in these experiments has an α_H-parameter value of nearly 6.

The locking region of the bistable area can be obtained either by a decrease of the detuning or a decrease of the injected power. Once the laser is locked, it maintains locked for a larger interval of detuning. The larger extent of the bistable area described here is 11 dB, for detuning varying between -44 and -7 GHz; or 35 GHz for an injected power of 0 dBm. In Fig. 2(a), we can observe that for injected powers varying from -20 to -7.5 dBm, the master peak is progressively amplified at the expense of the slave peak, until the slave peak suddenly disappears while entering the locking regime. For decreasing detuning as shown in Fig. 2(b), the abrupt transition occurs for an injected power of -17.5 dBm, i.e., when the injected laser leaves the locking regime for a bimodal regime.

Figure 3 shows another map with the same experimental conditions but for a larger detuning, varying from $-1{,}000$ to $+1{,}000$ GHz. We observe that the master can excite the longitudinal side modes of the slave, as shown by the correlation between the locking area and the free SL spectrum. This spectrum is clearly asymmetric, which is typical of a distributed feedback laser without phase-shift [25]. The side-mode suppression ratio of the free slave laser is greater than 30 dB; therefore, a higher injected power is necessary to obtain injection locking of these secondary modes. In Fig. 3, lines with percentages inside the bimodal regime indicates about the ratio of the total optical power inside the amplified master line. The bistability area decreases as the side mode is further away from the lasing mode. Note that for high injected powers (≥ 3 dBm), a permanent locking regime is reached whatever is the excited mode. This broader view shows clearly that the bistable (or grey) area stops at finite injection power and that it exists for other longitudinal modes.

It is worth mentioning that we have carried out similar experiments in [26] using the same master laser but a distributed feedback *fiber* laser as a slave laser. DFB fiber lasers are characterized by a linewidth, which is typically an order of magnitude lower than DFB semiconductor lasers. As a consequence, we observed a reduction of the locking area by the same factor [26]. However, a notable feature of the DFB fiber laser that differs from the semiconductor laser is the fact that the bistable area appears for positive detuning.

2.3. Experimental results far from threshold

The existence of non-locking injection regimes, such as chaos or wave mixing, led Simpson [27] to draw a map of the regimes of an optically-injected laser in 1997, for a laser biased at 1.6 times its threshold. In our experiment, injected slave laser maps are quite similar at 1.6 and 4 times the threshold $(4I_{th})$, so we only present the $4I_{th}$-map in this article.

Figure 4 displays a map of the different phenomena which can be observed when the injected signal is varying between -50 and $+8$ dBm, the detuning is varying between -70 and $+30$ GHz. Compared to the laser close to threshold, many other injection regimes due to nonlinear effects appear when the slave is far from threshold. The injection regimes are: Locking area (L), wave mixing (1, 2, 4), Chaos (C), and undamped Relaxation oscillation regime (R).

#108455 - $15.00 USD Received 10 Mar 2009; revised 25 Apr 2009; accepted 10 May 2009; published 19 May 2009

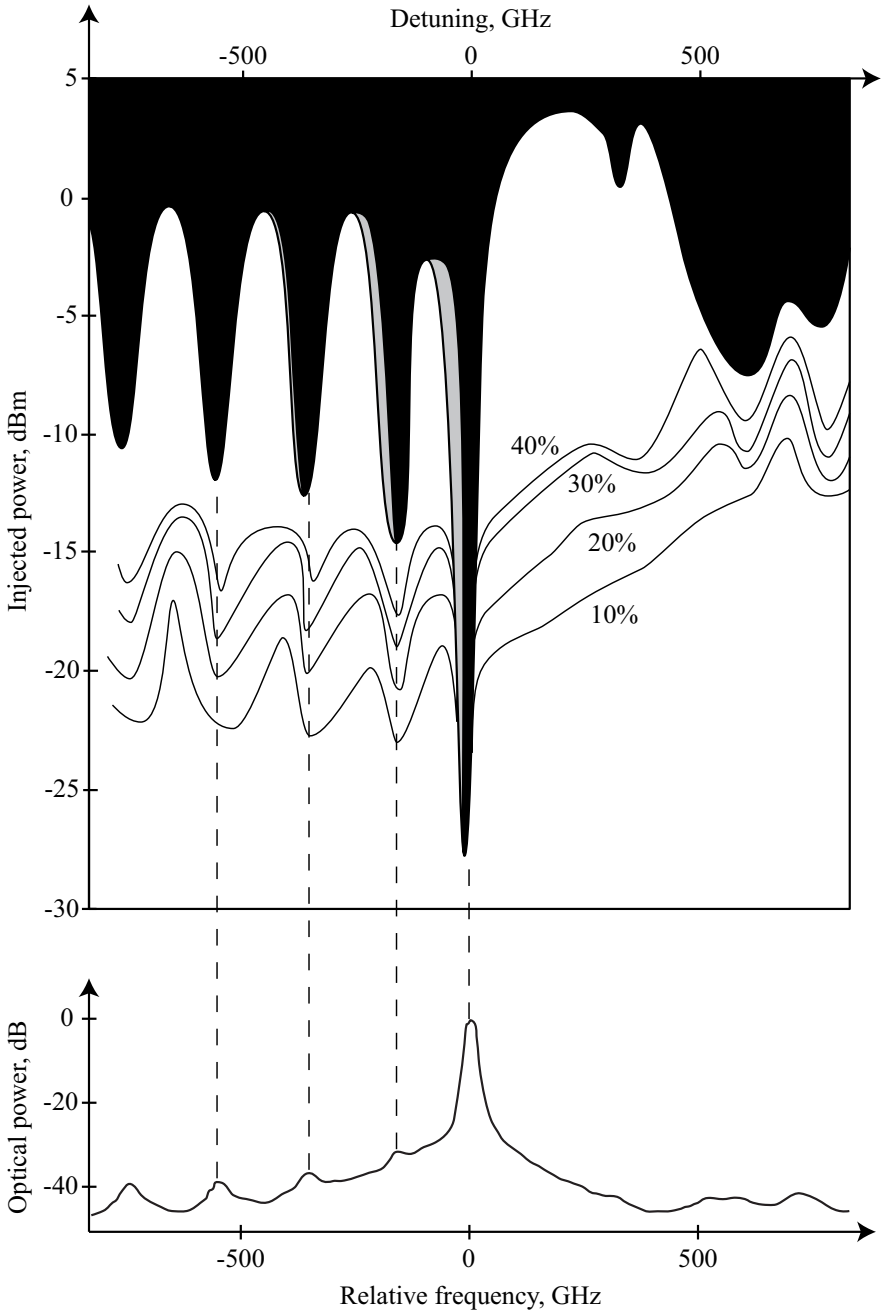

Fig. 3. (a) Experimental mapping and bistabilities of the intermodal injection for a slave laser pumped at 1.2 times its threshold. The black area represents the locking region. The white area represents the bimodal regime. The grey areas represent the bistable locking areas: The locking only occurs for decreasing detuning. Black lines represent the percentage of the power of the master peak when the injected slave is bimodal (100% corresponds to the locking regime). (b) Free slave laser spectrum.

#108455 - $15.00 USD Received 10 Mar 2009; revised 25 Apr 2009; accepted 10 May 2009; published 19 May 2009

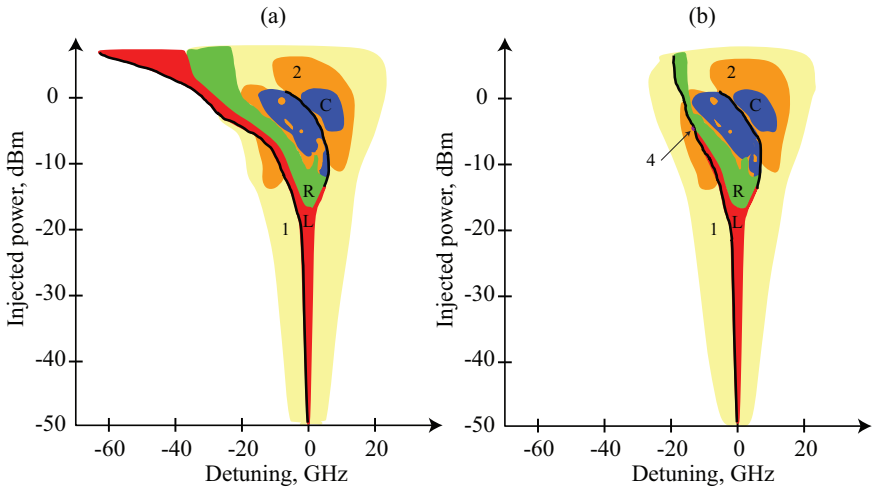

Fig. 4. Experimental mapping and bistabilities of the intramodal injection for a slave laser pumped at 4 times its threshold. "L" represents the locking area, "1" is for single wave mixing, "2" for period-doubling wave mixing, "4" for period-quadrupling wave mixing, "C" for chaos, "R" for undamped relaxation oscillation, and the white area represents the free slave injection regime. Thick black curves represent abrupt transitions of the injected slave spectra.

The bimodal regime is not observed anymore, the white area corresponds from now on to a free slave injection regime, i.e., the slave laser acts as if it was not injected. We observe that the map is less extended than the one close to threshold, except for the bistable area. Figure 4(a) is obtained for a decreasing detuning while Fig. 4(b) corresponds to an increasing one.

The FP spectrum of wave mixing (1) consists in a three-peak spectrum. The main peak is at the free slave frequency ν_s and has two satellites. One satellite is at the master frequency ν_m, the second one is the symmetric of ν_m with respect to ν_s and is usually less powerful. Note that the frequency pushing effect [4,26,28] appears, meaning a shift of the slave peak from the free slave frequency, far from the master frequency. A characteristic beating peak at the effective detuning (including frequency pushing effect) is observed at the Electrical Spectrum Analyzer (ESA). The region (2) consists in a period-doubling phenomenon: Peaks appear between lines of the single wave mixing (1), giving birth to sub-harmonic oscillations observed at the ESA. The region (2) arises from the region (1). Similarly, region (4) arises from region (2). This behavior is characteristic of a "period doubling bifurcation" phenomenon [29,30]. Note that chaos appears for quite high injected power (> -15 dBm), either for positive or negative detuning. Finally, the characteristics of undamped relaxation oscillation regime (R) are very similar to wave-mixing but in this case, the peak spacing is equal to the relaxation oscillation frequency (ROF) of the SL. Figure 5 illustrates the spectral properties of the possible injection regimes. A more complete description is given in Ref. [21,31–33].

Fig. 4 shows that, for an injected power lower than -17 dBm, the locking area is symmetric with respect to the null detuning axis. For higher injected powers, there is no locking at null detuning, but it exists at positive and mainly at negative detunings, as already reported in the literature [34]. The undamped relaxation oscillation regime takes place [32,35] between these two areas. One striking point about this map is the wide bistable area, in comparison to the dimensions of the map. The bistable area can be seen by comparing Figs. 4(a) and 4(b). As the close-to-threshold case, hysteresis can be revealed by either varying the detuning or the

#108455 - $15.00 USD Received 10 Mar 2009; revised 25 Apr 2009; accepted 10 May 2009; published 19 May 2009

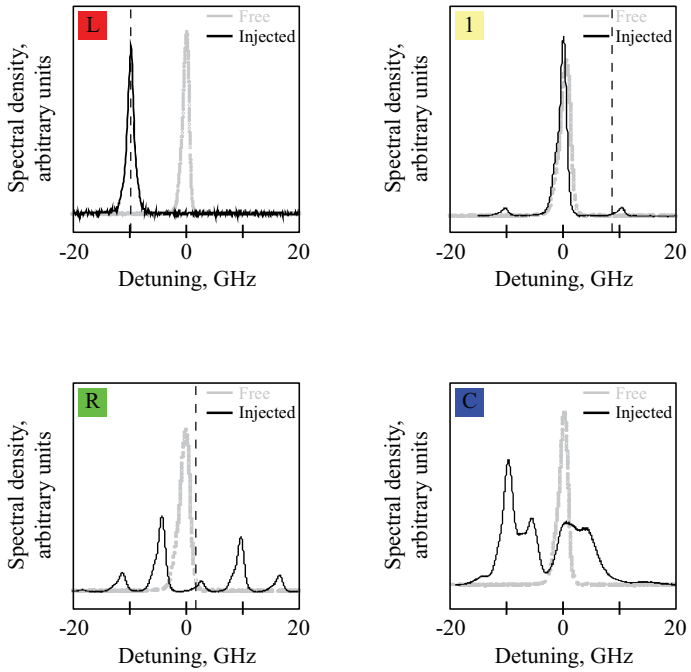

Fig. 5. Experimental FP spectra of different injected SL regimes. The broken vertical line indicates the ML optical frequency (ν_m).

injected power. The bistability between a locking regime (for decreasing detuning), and free-slave operation, wave mixing (1, 2, 4) or undamped relaxation oscillation regime (for increasing detuning), is clearly seen, especially at negative detuning, thus showing more bistable states than observed at lower pumping rate in Fig. 3. However bistability between different states (chaos-period doubling, undamped relaxation oscillation regime and wave-mixing) may also be observed as shown by the REC bar of fig. 6 (Media 1), which describes optical SL FP spectrum variation versus detuning, highlighting the hysteresis process.

3. Theory

3.1. Model

Various theoretical approaches have been proposed to numerically study optically-injected semiconductor lasers. Most studies are based on asymptotic analysis [17, 19] or bifurcation analysis [20, 36]. These methods have been largely described and we will focus on numerical simulations. The behavior of a single-mode injected laser can be described by the following normalized rate equations, which are given for the normalized carrier density $\Delta n(t)$ and for the complex electric field $E(t)$ [35] by:

$$\frac{dE}{dt} = \frac{1}{2\tau_c}(1+i\alpha_H)\, g_d\, \Delta n\, E + \kappa E_{inj} \tag{1}$$

$$\frac{d\Delta n}{dt} = \frac{1}{\tau_e}\left[j_b - \Delta n - \tau_e G_N \left(\Delta n + {}^1\!/_{n_{sp}}\right)|E|^2\right] \tag{2}$$

where E_{inj} is the complex electric field of the ML, which is injected in the SL cavity, τ_c is the

#108455 - $15.00 USD Received 10 Mar 2009; revised 25 Apr 2009; accepted 10 May 2009; published 19 May 2009

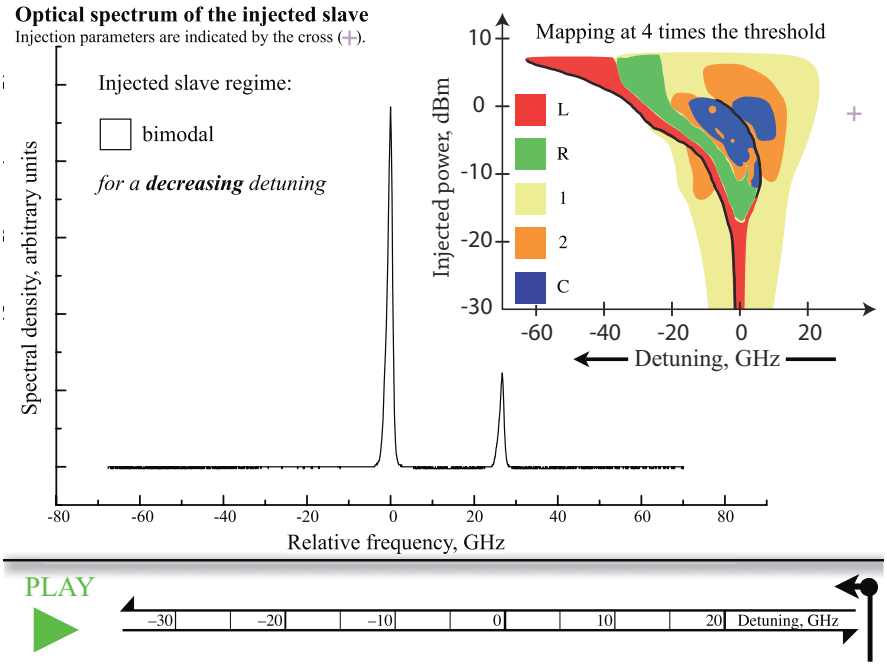

Fig. 6. Single frame movie (Media 1) of SL spectrum variation *vs* detuning. The top-right inset represents the previously described mapping at 4-times the threshold. The bottom bar indicates the different regimes for decreasing and increasing detuning at a glance.

round-trip time in the laser cavity, α_H is the linewidth-enhancement factor. The carrier lifetime τ_e is determined at threshold. G_N is the differential gain and g_d the normalized one. j_b is the normalized pumping rate of the SL ($j_b = r - 1$) and finally n_{sp} is the spontaneous emission rate.

Experimental measurements have been achieved in order to numerically determine parameter values [33]. A particular attention has been paid in order to perfectly fit the α_H parameter, the relative intensity noise versus the microwave frequency, the Light-Intensity curve as well as the dependency of the relaxation oscillation frequency on the bias current. This match has been done for the laser, which is mapped at 4 times its threshold. However, we have not used the same laser chip for mapping at 1.2 times due to a laser breakdown. Nevertheless, both lasers are of the same kind and have similar behavior when submitted to optical injection.

Table 1 sums up numerical values we use.

3.2. Numerical mapping

In this subsection, the nonlinear dynamics of the simulated injected laser is mapped as it has been done in Section 2. To this end, we numerically solve equations (1) and (2). Then, we compute the FFT of the electrical field $E(t)$ and we analyze it to determine in which injection regime the laser is. The overall result is shown in Figs. 7 and 8, when the SL pumping rate is respectively 1.3 and 4.

At low pumping rate (see Fig. 7), the injected laser mainly acts as an optical amplifier. As previously said (see Section 2), only frequency-locking or amplification are observed. Moreover, this figure shows that the hysteresis are well numerically reproduced. The SL is frequency-locked (grey area) only for a decreasing detuning. Note that the bistable area corresponding to

#108455 - $15.00 USD Received 10 Mar 2009; revised 25 Apr 2009; accepted 10 May 2009; published 19 May 2009

Table 1. Some parameters values for laser diode used.

Symbol	Physical constant	Value
L	Length of the active medium	200 μm
l	Width of the active medium	1 μm
e	Thickness of the active medium	0.1 μm
n	Group index of the active medium	3.75
Γ_C	Confinement factor	5 %
G_N	Differential gain	4.81×10^{-11} m^3.s^{-1}
N_t	Carrier density at transparency	$5.55 \times 10^{+21}$ m^{-3}
τ_e	Carrier lifetime at threshold	181 ps
τ_p	Photon lifetime	10 ps
τ_c	Round trip time in laser cavity	5 ps
α_H	Linewidth enhancement factor	6.5

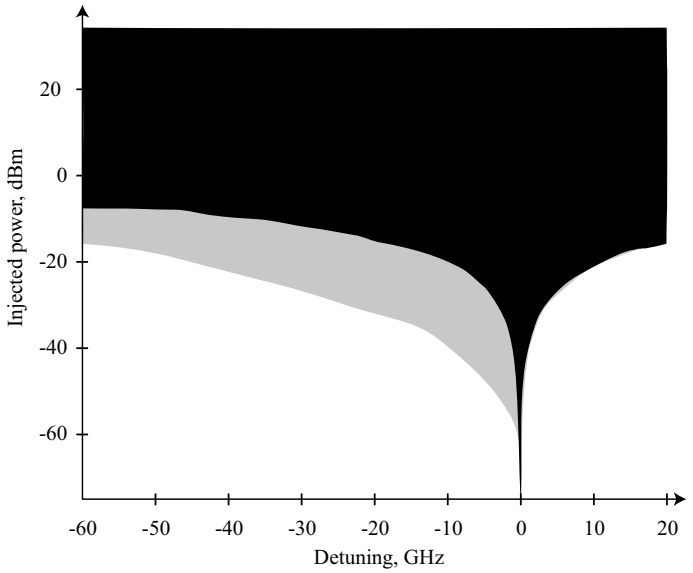

Fig. 7. Numerical mapping and bistabilities of the intramodal injection at 1.3 times its threshold. The black area represents the locking area. The grey area represents the bistable area: The injected SL is frequency-locked only for decreasing detuning.

the coexistence of a stationnary state and of a periodic orbit is observed at only one boundary, which corresponds to an abrupt transition between two regimes (locked-periodic), due to saddle-node bifurcation [20]. This property still remains at higher current. The bistable domain is presumably bounded at the right by an homoclinic bifurcation where the period of the bimodal or wave-mixing limit-cycle becomes infinite [20]. However further numerical and analytical work is needed to demonstrate that it is indeed the bifurcation mechanism.

By comparing this map with Fig. 2(c), a good qualitative agreement is achieved between experimental and numerical results. However, differences can be observed on the extension and location of the bistable area. As explained before, this mismatch is due to the fact that we do not measure the laser parameters before it broke down. Nevertheless, the general trend is observed.

#108455 - $15.00 USD Received 10 Mar 2009; revised 25 Apr 2009; accepted 10 May 2009; published 19 May 2009

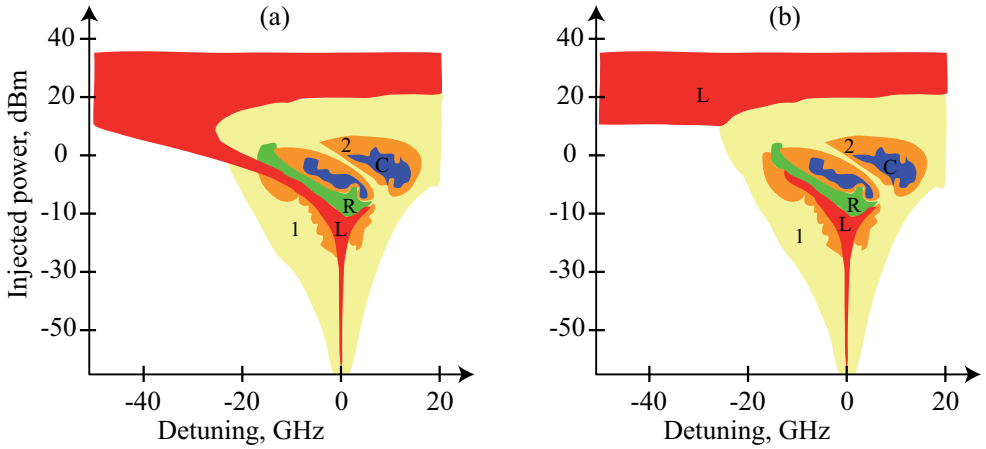

Fig. 8. Numerical mapping of the intramodal injection at 4 times its threshold. Symbols and colors are the same as in Fig. 4. Figure (a) is obtained for a decreasing detuning while Fig. (b) is for an increasing one.

For the SL biased at a higher current (4 times its threshold), numerical simulations lead to more complex dynamics (wave-mixing, chaos, etc.). Figure 8(a) gives the mapping for a decreasing detuning while Fig. 8(b) is obtained for an increasing one.

At this pumping rate, good qualitative and quantitative agreements are achieved between experimental and numerical maps. Such an adequation between experiments and simulation has already been reported in [37]. The original result of our paper is that the bistabilities are well numerically reproduced and that the effect of the slave laser pumping bias current is studied. As far as we know, it is the first demonstration of such a result. By comparing Figs. 4 and 8, minor differences on the extension and location of the different regimes can be seen. Small errors onto the value of the different parameters may explain these small discrepancies as well as the sensitivity of the maps to the injection bias current, as it can be experimentally checked.

4. Conclusion

In this paper, we investigated the bistability between different states and show that it leads to hysteresis when the detuning is driven back and forth. Major report concerns bistability between a locked steady state and pulsating intensity oscillations. This form of bistability typically appears near the steady state locking boundary at negative detuning. The pulsating intensities correspond to either a bimodal limit-cycle for low pumping rates or different forms of wave-mixing and relaxation oscillations at high pumping rates. Nevertheless, the areas of the bistable domain do not change significantly as the pumping rate is increased. From negative to positive detunings, the bistable domain is bounded at the left by the locking boundary of the steady state (saddle-node bifurcation point). This point is clearly noted as we decrease the detuning from positive values.

Acknowledgements

Authors would like to thank Guy Michel Stéphan and our “Laser Physics Group” colleagues from the lab FOTON-ENSSAT for helpful discussions.

#108455 - $15.00 USD Received 10 Mar 2009; revised 25 Apr 2009; accepted 10 May 2009; published 19 May 2009

Reduced Thermal Sensitivity of a Fiber-Optic Gyroscope Using an Air-Core Photonic-Bandgap Fiber

Stéphane Blin, Hyang Kyun Kim, *Member, IEEE*, Michel J. F. Digonnet, *Member, IEEE*, and Gordon S. Kino, *Life Fellow, IEEE*

***Abstract*—A 6.5-fold reduction in thermal sensitivity is demonstrated experimentally in a fiber-optic gyroscope made of a 235-m length of quadrupolar-wound air-core fiber, compared to the same gyro operated with a similar coil of conventional (SMF28) fiber. This result is in good agreement with the theoretical value of 6.6 and the value of 7.5 expected from independent thermal measurements carried out on short pieces of the same fibers.**

***Index Terms*—Air-core fiber, fiber-optic gyroscope (FOG), photonic-bandgap fiber (PBF), Shupe effect.**

I. Introduction

THE FIBER-OPTIC gyroscope (FOG) is now at a very advanced stage of production, having been researched, manufactured, and marketed by several companies around the world for at least two decades for a wide range of military and civilian applications. This success story was made possible by a combination of breakthroughs that occurred in the early research stages of the fiber gyro. The most important one was the use of a broadband light source to reduce phase errors due to coherent backscattering [1] and the nonreciprocal Kerr effect in the sensing coil [2]. Another key advance was winding the sensing coil in a special pattern, such as quadrupolar winding [3], to reduce phase errors caused by asymmetric perturbations of the sensing due to either temperature variations (a mechanism known as the Shupe effect [4]) or external acoustic waves. These solutions have effectively improved the FOG's phase stability to the point where it is now used in high-accuracy applications such as inertial aircraft navigation. However, they are not perfect, and they have also introduced other engineering complexities, such as the need to stabilize the mean wavelength of the broadband source to a very high degree [5]. They also increase the cost and probably reduce the manufacturing yield of the gyro.

We have recently proposed a new solution to further reduce the aforementioned deleterious effects that are fully compatible with the use of a broadband source and quadrupolar winding, which consists of replacing the conventional solid-core single-mode fiber used in an FOG by a single-mode air-core photonic-bandgap fiber (PBF) [6]. Because, in a PBF, most of the mode energy ($> 99\%$) travels in air, which has much weaker optical nonlinearities and refractive-index dependence on temperature than silica, in an air-core FOG, the Kerr and Shupe effects are anticipated to be considerably reduced. Combined to existing solutions, this novel approach is expected to further improve the gyro stability and relax some of its manufacturing requirements.

In a recent publication [7], we reported theoretical evidence that the Shupe constant S, which is defined as the relative change in propagation phase φ of the fundamental mode with temperature T, $S = (d\varphi/dT)/\varphi$, is about 3–6 times weaker in existing air-core fibers than in a conventional fiber. These predictions were confirmed with measurements performed on short lengths ($\sim$20 cm) of air-core and conventional fibers. As shown in [7], the thermal sensitivity of an optical fiber has two principal origins, namely a variation in the effective index of the fundamental mode, and an elongation of the fiber (mainly due to the polymer jacket of the fiber whose thermal expansion coefficient is dramatically larger than silica). We have shown that for an air-core fiber, the thermal sensitivity arises almost entirely from the elongation of the fiber jacket. With improved fiber design, namely increasing the outer cladding thickness and reducing the jacket thickness, we demonstrated that the Shupe constant of the air-core fiber could be reduced by a factor of $\sim$11 compared to a conventional solid-core fiber [7]. In this paper, we take this investigation one step further and report measurements of the thermal sensitivity of a complete FOG made of a 235-m quadrupolar-wound coil of air-core fiber. The objectives were to confirm the figures measured previously on short lengths of fiber, to evaluate the effect of the quadrupolar winding in an air-core fiber, and to quantify the reduction in the thermal sensitivity of an actual gyro operated with an air-core fiber. This paper confirms that the thermal sensitivity of an experimental FOG made up of a 235-m length of quadrupolar-wound air-core fiber is 6.5 times lower than that of the same gyro operated with a similar coil of conventional (SMF28) fiber.

II. Experimental Fiber Gyroscope

The fiber gyroscope that was tested had the standard configuration shown in Fig. 1. The optical source was a broadband

Manuscript received July 21, 2006; revised November 21, 2006. This work was supported by Litton Systems, Inc., a wholly owned subsidiary of Northrop Grumman Corporation.

S. Blin, M. J. F. Digonnet, and G. S. Kino are with the Edward L. Ginzton Laboratory, Stanford University, Stanford, CA 94305 USA (e-mail: sblin@stanford.edu; silurian@stanford.edu; kino@stanford.edu).

H. K. Kim was with the Edward L. Ginzton Laboratory, Stanford University, Stanford, CA 94305 USA. She is now with Nova Measuring Instruments Ltd., Sunnyvale, CA 94085 USA.

Color versions of one or more of the figures in this paper are available online at http://ieeexplore.ieee.org.

Digital Object Identifier 10.1109/JLT.2006.889658

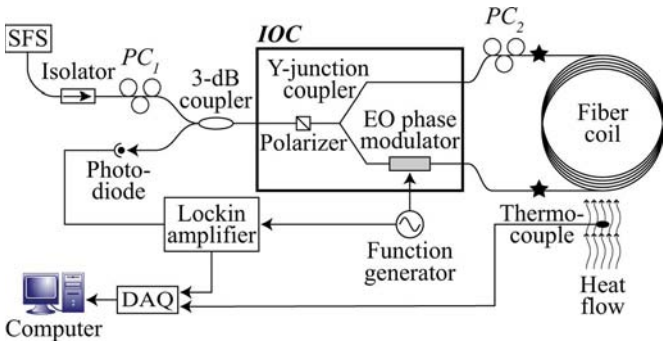

Fig. 1. Experimental setup used to test the temperature stability of the air-core FOG.

Er-doped superfluorescent fiber source. The Sagnac interferometer consisted of an input-output Y-junction coupler, a polarization controller PC_2, the fiber coil, and an electrooptic phase modulator (EO-PM). The polarizer, Y-junction, and EO-PM were all fabricated on an $LiNbO_3$ integrated-optic circuit (IOC), which was fiber-pigtailed to the 3-dB coupler and the coil. The Y-junction coupler splits the input light into two waves that propagate around the fiber loop in opposite directions. Rotating the coil around its main axis induces a phase shift $\Delta\phi$ between the counter-propagating waves (Sagnac effect) that is proportional to the rotation rate Ω. The latter parameter can be retrieved by measuring the power at the output port of the fiber coupler (see Fig. 1), which has a linear dependence on $\Delta\phi$ (for small rotation rates). The polarization controller PC_1 was adjusted to maximize the power entering the interferometer, and PC_2 to maximize the power returning from the interferometer. The gyroscope sensitivity was maximized by applying a sinusoidal phase modulation to the two waves at the loop proper frequency with the EO-PM. A lock-in detection was used to recover the return signal amplitude modulated at the proper frequency (100-ms integration time, 24-dB/octave filter slope).

Two different coils were tested, one was made up of a 300-m long SMF28 fiber from Corning, Inc., and the other of a 235-m long PBF from Blaze Photonics (HC-1550-02). Each fiber was wound in 16 layers on an 8-cm-diameter spool, using quadrupolar winding to reduce the thermal and acoustic sensitivities of the gyro [3]. Each layer was bonded to the one underneath it with a thin epoxy coating, and the outermost layer was also coated with epoxy. The standard fiber coil was connected to the IOC using angle-polished connectors ($\star$ in Fig. 1); these connections produced very little back reflection and negligible loss. In the case of the PBF coil, to reduce harmful back reflections from these connections, the PBF coil was cleaved at 90° and butt-coupled to the angle-polished fiber pigtails of the IOC, which resulted in a measured loss of $\sim$3 dB at each connection.

III. Model of Thermal Effects in the Fiber Gyroscope

As described by Shupe [4], a thermal transient is applied to a Sagnac loop anywhere, but at its midpoint from the coupler, it induces a phase-shift error $\Delta\phi_{\mathrm{E}}$ between the counter-propagating waves that is indistinguishable from a rotation-induced phase shift. If the temperature time derivative is $\dot{T}(z)$ in an element of fiber length dz located in a distance z from one end of the coiled fiber, the total phase-shift error in a fiber of total length L is

$$\Delta\phi_{\mathrm{E}} = \frac{2\pi}{\lambda_0 c} n^2 \int_0^L (L - 2z)\dot{T}(z)dz \tag{1}$$

where λ_0 is the wavelength, and c the velocity of light, both in a vacuum, n is the effective index of the fiber mode, and S is the Shupe constant defined earlier. This constant takes into account both the fiber elongation and the effective index variation with temperature. It is independent of fiber length. The phase-shift error defined in (1) induces a rotation-like signal Ω_{E} related to $\Delta\phi_{\mathrm{E}}$ by

$$\Delta\phi_{\mathrm{E}} = \frac{2\pi}{\lambda_0 c} LD\Omega_{\mathrm{E}} \tag{2}$$

where D is the coil diameter. Substituting (1) in (2), and using the new dimensionless variable $z' = z/L$, yield the following expression for the rotation-rate error induced by the transient temperature change $\dot{T}(z)$:

$$\Omega_{\mathrm{E}} = \frac{n^2 SL}{D} \int_0^1 (1 - 2z')\dot{T}(z')dz. \tag{3}$$

Equation (3) is important because it states that the thermal sensitivity of the FOG is proportional not only to the Shupe constant S, as expected, but also to n^2, which is the square of the mode index. Since the air-core fiber has a much smaller effective index ($n \approx 0.99$) than a standard fiber ($n \approx 1.44$), as well as a smaller Shupe constant, a dramatic reduction of the thermal sensitivity of the gyro is expected by using an air-core fiber. We measured $S = 7.9$ ppm/°C for the SMF28 fiber and $S = 2.2$ ppm/°C for the Blaze Photonics air-core fiber [7]. Combined with the additional benefit of this n^2 dependence, these values suggest that the Blaze Photonics PBF gyro should be $\sim$7.6 times less thermally sensitive than the solid-core fiber gyro, which constitutes a considerable stability improvement.

IV. FOG Thermal Stability Measurements

To confirm these predictions in an actual gyro, we measured the thermal sensitivity of the gyro coil by locally heating one side of the coil with a heat gun while keeping the gyro at rest and recording the resulting phase shift on the gyro output signal. We also placed a thermocouple close to the heated region to measure simultaneously the air temperature variations near the coil surface due to the heat source. Prior to these measurements, each gyro was carefully calibrated by placing it on a rotation table, applying known rotation rates, and measuring the lock-in output voltage dependence on rotation rate. The quantity we measured during the thermal measurements was therefore

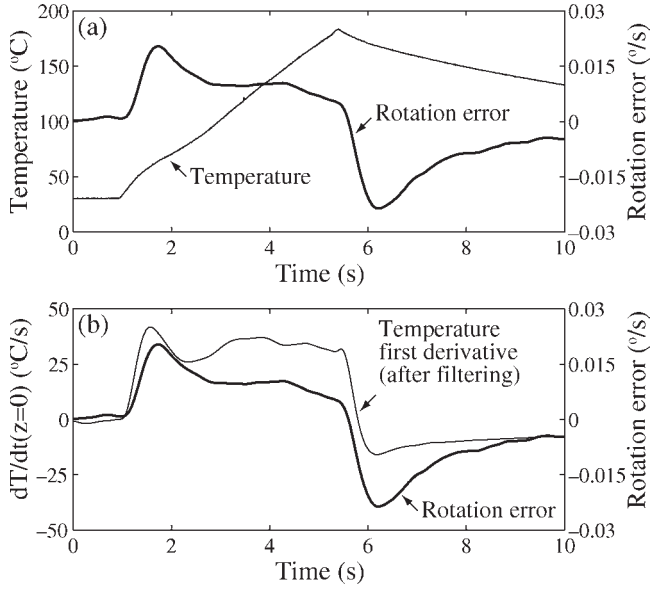

Fig. 2. (a) Temperature change applied to the air-core fiber gyroscope and measured resulting change in output signal. (b) Time derivative of the applied temperature change, shown together with the same measured output signal.

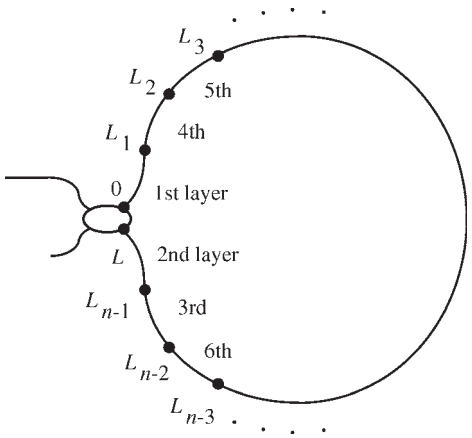

Fig. 3. Location in the Sagnac loop of the first few layers of an FOG's quadrupolar coil.

a rotation error signal Ω_{E}, from which we inferred $\Delta\phi_{\mathrm{E}}$ by making use of (2).

Fig. 2(a) shows an example of a measured temporal profile applied to one side of the air-core fiber gyro coil and the measured rotation error that it induced. Since the rotation error depends on the time derivative of the temperature [see (3)], we show in Fig. 2(b) the derivative of the applied temperature change. This derivative was calculated numerically from the measured temporal profile of Fig. 2(a) and then filtered numerically to simulate the four-stage 24-dB/octave low-pass filter of the lock-in amplifier. Compared to the measured rotation error reproduced in Fig. 2(b), a reasonable agreement between the two curves, as expected from (3), is shown. The relationship between these two curves in Fig. 2(b) agrees qualitatively well with the large body of literature on this subject [8]–[10].

In a quadrupolar winding [3], as illustrated in Fig. 3, the first (outermost) layer is comprised of a fiber located close to one of the two Sagnac loop ends closest to the coupler (between positions $z = 0$ and $z = L_1$). The second layer underneath it is comprised of the portion of the sensing fiber located at the opposite end of the coil ($L_{n-1} < z < L_n = L$). The third layer is comprised of a fiber located next to the second layer ($L_{n-2} < z < L_{n-1}$), etc. (see Fig. 3). In our experiment, just after the heat has been turned on, the first layer of the coil heats up first, and as a result, the differential phase between the counter-propagating waves changes (e.g., increases). As heat continues to be applied, it propagates radially into the coil, and the second layer, and then the third layer, start to warm up. In a quadrupolar or a bipolar winding, the first and second layers are located symmetrically in the Sagnac loop. Hence, as the second layer heats up, the thermal phase shift it induces begins to cancel that induced in the first layer. The same cancellation process takes place for the deeper layers. The total phase shift, however, continues to increase because the first layer heats up faster than the internal layers. Eventually, the temperature of the outer layer reaches some maximum value, and as more internal layers gradually heat up, the total thermal phase decreases. If heat is applied long enough, the temperature along the fiber reaches a steady-state distribution, and the thermal phase shift vanishes. This well-known explanation is consistent with the observed behavior of the thermally induced signal, which increases first and then decreases over time [Fig. 2(b)].

This physical behavior is consistent with the behavior of the measured thermal phase shift curve in Fig. 2(b). This curve closely follows the temperature derivative for about 1 s after the heat was turned on. For longer times, the two curves expectedly disagree (the measured rotation error curve drops below the temperature derivative curve) because by then, the heat has reached deep into the coil and the quadrupolar winding starts canceling the thermal phase shift. Just after the heat is turned off [around $t = 5.5$ s in Fig. 2(b)], the rotation error becomes negative. The reason is that at that time, the outermost layer starts to cool down [8]. Hence, the sign of the temperature gradient is reversed, and so is the sign of the rotation error.

When the air-core fiber was replaced by the solid-core fiber coil, the behavior of the gyro was similar (see Fig. 4), namely the rotation error increased just after the start of the heat pulse, then decreased, and finally became negative after the heat was turned off. However, the solid-core fiber gyro was clearly much more sensitive to asymmetric heating than the air-core FOG: for comparable applied peak derivative $\dot{T}$ (75.5 °C/s for the SMF28 versus 41.1 °C/s for the PBF), the error signal was about ten times larger for the solid-core fiber gyro [see Figs. 2(b) and 4].

From our measurements, the temperature derivative $\dot{T}(z)$ is known at all times but only at the surface of the coil ($z = 0$). It was consequently not possible to apply (3) and extract from the measured rotation error signals a value for the Shupe constant S of the two fiber coils. However, the thermal performance of the two gyros can still be compared by making two observations. First, because the two coils have identical diameter and thickness, we expect the rates of heat flow to be comparable in the two coils. Second, based on the above argument regarding the dynamic of heat flow in a quadrupolar coil, the total thermal phase shift is expected to reach its maximum shortly after

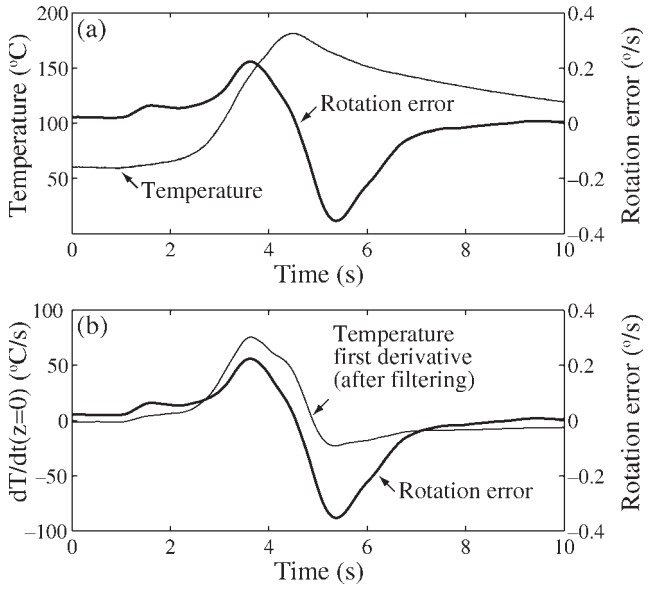

Fig. 4. (a) Temperature change applied to the conventional fiber gyroscope and measured resulting change in output signal. (b) Time derivative of the applied temperature change, shown together with the same measured output signal.

the first layer has started to heat up. The maximum thermally induced rotation error can therefore be approximated by

$$\Omega_{E,\max} \approx \frac{n^2 SL}{D} \int_0^{L_1/L} (1-2z')\dot{T}(z')dz. \tag{4}$$

Furthermore, the rate of temperature change of the outermost layer is expected to be close to the rate of temperature change measured at the surface of the coil and to be weakly dependent on z'. Hence, in (4), $\dot{T}(z')$ can be taken out of the integral, which shows that $\Omega_{\mathrm{E,max}}$ should scale approximately linearly with the measured surface temperature derivative.

To verify this approximation, we measured for each gyro the dependence of the maximum rotation-rate error on the applied temperature gradient. For example, in the measurement of Fig. 2(b), the maximum rotation-rate error is equal to 0.02 °/s, and at the time it occurred ($t \approx 1.8$ s), the applied temperature gradient was ∼41.1 °C/s. These data are plotted in Fig. 5. As expected, the maximum rotation-rate error increases roughly linearly with the applied temperature gradient, which confirms the validity of our approximation. The slopes of these dependences are 2.4×10^{-3} (°/s)/(°C/s) for the SMF28 fiber gyro, and 0.29×10^{-3} (°/s)/(°C/s) for the air-core fiber gyro. After correcting for the slightly different length of the two sensing fibers [factor L in (4)], we conclude that for identical coil lengths, the air-core fiber gyro is 6.5 times less sensitive to temperature gradients than the conventional FOG.

Independent thermal measurements performed on short pieces of the same fibers showed that the ratio of Shupe constants for the SMF28 and the Blaze PBF is 3.6 [7]. When using these values in (3), together with mode effective indexes of 0.99 and 1.44 for the two fibers, respectively, and assuming identical coils, we find that the air-core fiber is expected to be 7.6 times less sensitive than the solid-core fiber to thermal

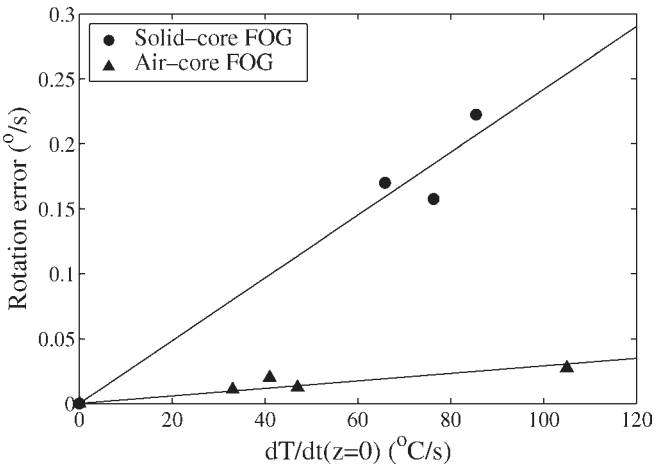

Fig. 5. Dependence of the maximum rotation-rate error on the applied temperature gradient measured in both the conventional and the air-core fiber gyro.

perturbations. This is in good agreement with our experimental value of 6.5. The small difference (∼13%) might be explained by slightly different heat propagation properties in the coils, which is expected since an air-core fiber constitutes a better thermal insulator [11], [12]. The measured value of 6.5 is also in excellent agreement with the theoretically predicted ratio for these two fibers (6.6) [8]. In any case, measured and theoretical values demonstrate unequivocally the significant advantage of using an air-core fiber in a FOG to reduce its thermal sensitivity—in addition to the other benefits pointed out elsewhere [6].

An asymmetric thermal transient in the Sagnac loop does not only induce a change in the propagation phase of the fundamental mode as described by the Shupe constant; it also induces a change in the state of polarization. Along with the input-output optical polarizer, such a polarization perturbation creates a variation in the return signal amplitude [13], thus adding a rotation error and also degrading the long-term drift performance of the gyro. The simplest solution to overcome this limitation is to use a polarization-maintaining fiber coil in the FOG. A further study would be to measure the thermal sensitivity of a polarization-maintaining FOG to evaluate the relative contribution of the Shupe effect in comparison to the thermally induced polarization instability.

V. Conclusion

In summary, we have demonstrated that using an air-core fiber instead of a solid-core fiber dramatically reduces the thermal sensitivity of a FOG, as a result of both the reductions in Shupe constant (relative change of propagation phase with temperature) and the lower mode effective index. A reduction of the thermal sensitivity by a factor of 6.5 has been demonstrated experimentally in a quadrupolar-wound air-core fiber compared to the same coil made of conventional SMF28 fiber. This result is in good agreement with the value of 7.5 expected from independent thermal measurements on short pieces of fibers and with the value of 6.6 predicted theoretically. Since the Shupe constant of an air-core fiber can be further reduced by another factor of ∼3 with improved fiber design [7], we predict that

the thermal sensitivity of the air-core fiber gyro can ultimately be made ∼23 times lower than that of a conventional FOG. This property constitutes a significant improvement for the fiber gyro. When combined to the other predicted benefits of air-core fibers, namely a substantial reduction in the Kerr and Faraday effects, it makes the air-core fiber an excellent candidate for this sensor technology.

REFERENCES

[1] C. C. Cutler, S. A. Newton, and H. J. Shaw, "Limitation of rotation sensing by scattering," *Opt. Lett.*, vol. 5, no. 11, pp. 488–490, Nov. 1980.

[2] S. Ezekiel, J. L. Davis, and R. W. Hellwarth, "Observation of intensity-induced nonreciprocity in a fiber-optic gyroscope," *Opt. Lett.*, vol. 7, no. 9, pp. 457–459, Sep. 1982.

[3] N. J. Frigo, "Compensation of linear sources of nonreciprocity in Sagnac interferometers," in *Proc. SPIE—Fiber Optic Laser Sensors*, 1983, vol. 412, pp. 268–271.

[4] D. M. Shupe, "Thermally induced nonreciprocity in the fiber-optic interferometer," *Appl. Opt.*, vol. 19, no. 5, pp. 654–655, 1980.

[5] J. L. Wagener, M. J. F. Digonnet, and H. J. Shaw, "A high-stability fiber amplifier source for the fiber optic gyroscope," *J. Lightw. Technol.*, vol. 15, no. 9, pp. 1689–1694, Sep. 1997.

[6] H. K. Kim, V. Dangui, M. Digonnet, and G. Kino, "Fiber-optic gyroscope using an air-core photonic-bandgap fiber," *Proc. SPIE*, vol. 5855, no. 1, pp. 198–201, 2005.

[7] V. Dangui, H. K. Kim, M. J. F. Digonnet, and G. S. Kino, "Phase sensitivity to temperature of the fundamental mode in air-guiding photonic-bandgap fibers," *Opt. Express*, vol. 13, no. 18, pp. 6669–6684, Sep. 2005.

[8] F. Mohr, "Thermooptically induced bias drift in fiber optical Sagnac interferometers," *J. Lightw. Technol.*, vol. 14, no. 1, pp. 27–41, Jan. 1996.

[9] O. F. Tirat and J.-M. Euverte, "Finite element model of thermal transient effect in fiber optic gyro," *Proc. SPIE*, vol. 2837, no. 1, pp. 230–238, 1996.

[10] C. M. Lofts, P. B. Ruffin, M. Parker, and C. C. Sung, "Investigation of the effects of temporal thermal gradients in fiber optic gyroscope sensing coils," *Opt. Eng.*, vol. 34, no. 10, pp. 2856–2863, 1995.

[11] J. Limpert, T. Schreiber, A. Liem, S. Nolte, H. Zellmer, T. Peschel, V. Guyenot, and A. Tunnermann, "Thermo-optical properties of air-clad photonic crystal fiber lasers in high power operation," *Opt. Express*, vol. 11, no. 22, pp. 2982–2990, Nov. 2003.

[12] K. Lyytikaïnen, J. Zagari, G. Barton, and J. Canning, "Heat transfer within a microstructured polymer optical fibre preform," *Model. Simul. Mater. Sci. Eng.*, vol. 12, no. 3, pp. S255–S265, May 2004.

[13] W. K. Burns, C.-L. Chen, and R. P. Moeller, "Fiber-optic gyroscopes with broad-band sources," *J. Lightw. Technol.*, vol. LT-1, no. 1, pp. 98–105, Mar. 1983.

Stéphane Blin received the degree of engineering in optronics and the Diplôme d'Etudes Approfondies in optronics/optical telecommunications from Ecole Nationale Supérieure des Sciences Appliquées et de Technologie, Lannion, France, in 2000, the Ph.D. degree in physics from Ecole Nationale Supérieure des Sciences Appliquées et de Technologie, Lannion, and the Ph.D. degree in electrical engineering from Université Laval, Québec, QC, Canada, in joint guardianship, in 2003.

Until 2004, he led optical injection experiments using semiconductor or fiber lasers, especially at very low injection levels (fW–pW), providing original metrological methods, e.g., spectral linewidth measurement of highly coherent lasers. He also studied the frequency noise of highly coherent lasers with DiCOS Technol., Québec. Since 2004, he has been a Postdoctoral Scholar with Edward L. Ginzton Laboratory, Stanford University, Stanford, CA. His current research interests include acoustic fiber sensor arrays and fiber-optic gyroscope using an air-core photonic-bandgap fiber.

Hyang Kyun Kim (M'03–A'04–M'04) received the B.S. degree from Yonsei University, Seoul, Korea, in 1987 and the M.S. and Ph.D. degrees from the Korea Advanced Institute of Science and Technology (KAIST), Daejon, Korea, in 1990 and 1994, respectively, all in physics.

From 1994 to 1999, she was a Senior Research Engineer with the Electronics and Telecommunication Research Institute (ETRI), Daejon. From 1999 to 2000, she was a member with the Technical Staff, Bell Labs., Lucent Technologies, Murray Hill, NJ. From 2001 to 2002, she was a Principal Staff Engineer with Novera Optics, Santa Clara, CA. From 2002 to 2005, she was a Research Associate with Edward L. Ginzton Laboratory, Stanford University, Stanford, CA. Her research interests include various aspects of fiber-optic communication systems and optical fiber sensors. With Stanford, her research focused on the design and characterization of photonic-crystal fibers and photonic-bandgap fiber components for applications to sensors and communication systems. She is currently with Nova Measuring Instruments Ltd., Sunnyvale, CA.

Michel J. F. Digonnet (M'01) received the degree in engineering from Ecole Supérieure de Physique et de Chimie de la Ville de Paris, Paris, France, the Diplome d'Etudes Approfondies in coherent optics from the University of Paris, Orsay, France, in 1978, and the M.S. and Ph.D. degrees from the Applied Physics Department, Stanford University, Stanford, CA, in 1980 and 1983, respectively. His doctoral research centered on WDM fiber couplers and single-crystal fibers.

From 1983 to 1986, he was a Visiting Scholar with Stanford, conducting research in miniature solid-state sources and integrated optics for fiber sensors. From 1986 to 1990, he was involved in the development of dye and 2-μm solid-state lasers, fiber sensors, and fiber delivery systems for laser angioplasty with the MCM Laboratories, Mountain View, CA. Since then, he has been a Senior Research Associate with the Applied Physics Department, Stanford University. His current research interests include photonic-bandgap fibers, fiber sensors and sensor arrays, high-power ceramic lasers, fiber lasers and amplifiers, fiber gratings, slow light, and optical microcavities. He has published 190 articles, been issued nearly 60 patents, edited several books, and chaired numerous conferences on optical fiber devices, sensors, and materials. He teaches a course entitled *Lasers* at Stanford, as well as short courses on fiber amplifiers and lasers and fiber sensors at international conferences.

Gordon S. Kino (S'52–A'54–SM'63–LF'94) received the B.Sc. and M.Sc. degrees in mathematics from London University, London, U.K., and the Ph.D. degree in electrical engineering from Stanford University, Stanford, CA.

He is the W. M. Keck Foundation Professor of electrical engineering, Emeritus, and Professor, by Courtesy, of applied physics, Emeritus. He was the Director with the Ginzton Laboratory, Stanford University. He has worked on microwave tubes, electron guns, plasmas, the Gunn effect, acoustic devices, acoustic imaging, nondestructive testing, fiber optics and microscopy. His current research interests are in various forms of near-field and scanning confocal microscopy, fiber optics, and optical antennas. He has published over 430 papers and has 47 patents. He and his students have developed new types of scanning optical microscopes and interferometric microscopes, and he and his students invented the *Real-Time Scanning Confocal Optical Microscope*, the *Mirau Correlation Microscope*, the *Solid Immersion Lens* for optical microscopy, and storage, and a *Micromachined Confocal Scanning Optical Microscope*. He and T. Corle have authored the *Confocal Optical Microscopy and Related Techniques* (New York: Academic, 1996). He has authored the *Acoustic Waves: Devices, Imaging, and Analog Signal Processing* (Englewood Cliffs, NJ: Prentice-Hall, 1987).

Dr. Kino was a Guggenheim Fellow in 1967 and is currently a Fellow of the American Physical Society and the AAAS and is a member of the National Academy of Engineering. In 1984, he received the IEEE Sonics and Ultrasonics Group Achievement Award and, in 1986, the ASNT Achievement Award in Applied Research.

Laser line shape and spectral density of frequency noise

G. M. Stéphan,[1] T. T. Tam,[2] S. Blin,[1] P. Besnard,[1] and M. Têtu[3]
[1]*Laboratoire d'Optronique associé au Centre National de la Recherche Scientifique, ENSSAT, 6 rue Kerampont, 22305 Lannion Cedex, France*
[2]*College of Applied Science and Technology, Vietnam National University, Hanoi (VNUH), 144 Xuan Thuy str., Building E3, Caugiay, Hanoi, Vietnam*
[3]*DiCOS Technologies, Boul. du Parc Technologique, Bureau 200, Québec, Canada G1K 7P4*
(Received 30 June 2004; published 11 April 2005)

Published experimental results show that single-mode laser light is characterized in the microwave range by a frequency noise which essentially includes a white part and a $1/f$ (flicker) part. We theoretically show that the spectral density (the line shape) which is compatible with these results is a Voigt profile whose Lorentzian part or homogeneous component is linked to the white noise and the Gaussian part to the $1/f$ noise. We measure semiconductor laser line profiles and verify that they can be fit with Voigt functions. It is also verified that the width of the Lorentzian part varies like $1/P$ where P is the laser power while the width of the Gaussian part is more of a constant. Finally, we theoretically show from first principles that laser line shapes are also described by Voigt functions where the Lorentzian part is the laser Airy function and the Gaussian part originates from population noise.

DOI: 10.1103/PhysRevA.71.043809 PACS number(s): 42.55.Ah, 42.55.Px

I. INTRODUCTION

Direct measurements of the power spectral density of frequency noise essentially characterize lasers having high spectral purities used in metrology or in optical telecommunication. They show that the main contributions in single-mode semiconductor lasers arise from white noise and $1/f$ noise (flicker noise) [1–3]. A flicker noise has also been measured [4,5] in the intensity fluctuations of a semiconductor laser and has been the subject of many studies [6–9]. A correlation was experimentally shown [10] to exist between this noise and frequency fluctuations in the optical emission. This correlation was theoretically understood [11–13] always in a semiconductor laser from the coupling between the index of refraction n and the fluctuations of the charge carriers N due to spontaneous emission.

Beside this $1/f$ noise due to charge carriers, the frequency white noise due to spontaneous emission is well known to be the primary origin of the laser linewidth [14]: It has been theoretically modeled in the Langevin equations of the laser as a time δ-correlated term, analogous to the random Brownian collision term in the motion equations of a particle in a gas. A comprehensive review of the understanding of laser spectra is given in Ref. [15].

However, while the laser linewidth has been the subject of many studies, the laser line shape was generally assumed to be described by a Lorentzian profile. The aim of our work is essentially to demonstrate that a Voigt profile is better adapted.

For this purpose, the relation between frequency noise and laser spectrum is described in Sec. II. We show and verify that the line shape, or the spectral distribution, of a single-mode laser which is compatible with both the white and flicker noises can essentially be described by a Voigt function. Many authors have already intuitively guessed that the laser line shape can be fit by a Voigt profile [16,17] and even described it by a convolution between a Lorentzian and a Gaussian [18], which is a Voigt function. However, no definite proof has been given up to now. In the following we first link the spectral density of the laser light to the noise spectrum: The white noise gives birth to the Lorentzian part and the $1/f$ noise is responsible for the Gaussian part. Then we verify that the Voigt function gives a nice fit to experimentally measured line shapes for a diode laser. The fit parameters are Γ, the half width at half maximum (HWHM) of the Lorentzian, and σ^2, the variance of the Gaussian. Our experimental results show that Γ follows a $1/P$ law, where P is the laser power, while σ^2 has a slower variation. We find the relation between the optical parameters Γ and σ^2 and the noise coefficients h_0 and h_{-1}. It follows that a measurement of h_0 and h_{-1} will allow one to characterize a laser line, which is otherwise difficult to measure directly from interference effects, especially for a laser used in metrology.

In Sec. III, we make the connection between the homogeneous laser line, which is described by the Airy function of the laser [19–21], and its inhomogeneous properties, which are included in the Gaussian distribution of the resonance frequency. Among its properties, this Airy function allows one to describe both the Fabry-Perot interferometer or the laser in a continuous way, when the gain is increased across the oscillation threshold.

During the course of this calculation, Lamb's solution for the laser intensity, Henry's factor, the role of the spontaneous emission, and "technical" or electronic noises naturally appear. It is thus believed that this synthesis gives a clear understanding of the single-mode laser line shape.

II. BROADBAND FREQUENCY NOISE AND LASER SPECTRAL DENSITY

A. Noise coefficients and laser Voigt spectrum

In this paper, we do not give any experimental result on the laser frequency noise (see Ref. [3]) but we want to make a clear connection between it and the optical spectrum. This is why we schematically describe both experiments in Fig. 1

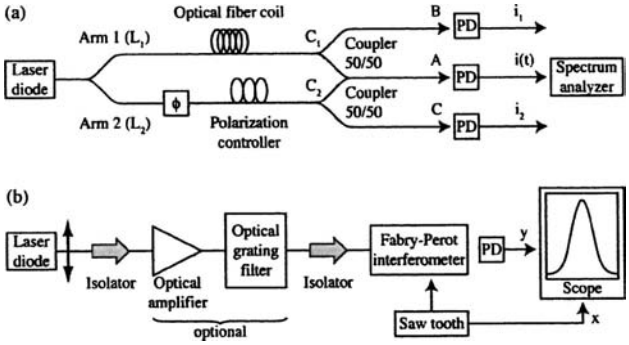

FIG. 1. (a) A practical Mach-Zehnder interferometer for the measurement of field noise properties. The fourth arms of the optical couplers are not shown. ϕ is the dephasor. (b) Optical spectrum analyzer based on a Fabry-Perot interferometer.

on noise and optical spectra and give some details on the measured quantities below.

The power density of frequency noise of a single-mode laser is measured in the standard experiment described in Fig. 1(a): A Mach-Zehnder interferometer splits the field into two parts which are directed into two different arms. A time delay τ_d is introduced with an optical fiber coil in one arm. The recombined field at the output is a function of time t and τ_d. For a fixed value of τ_d, the interferometer is used as a phase-amplitude convertor and the fringe system fluctuates in position and amplitude with time. The amplitude-converted phase noise is larger than the laser intensity noise which can be neglected in this kind of experiment. The larger τ_d is, the larger is the phase fluctuation. τ_d has to be optimized to have a comfortable signal, however in the limits of a linear approximation for a sine function (the fringe function around a zero). The optical signal is detected by a fast detector which delivers a current $i(t,\tau_d)$ which is proportional to the intensity of the field.

The output current of the detector (A) in Fig. 1(a) is written as

$$i(t,\tau_d) = i_1 + i_2 + 2\sqrt{i_1 i_2}\cos[\omega_0\tau_d + \phi(t+\tau_d) - \phi(t)], \quad (1)$$

where i_1 and i_2 are the currents detected by the photodiodes (B) and (C) in arms 1 and 2 as shown in Fig. 1(a). i_1 and i_2 can also be detected directly by the detector (A) simply by successively cutting out arms 1 and 2 of the interferometer. The time average of $i(t,\tau_d)$ corresponds to the interferogram. The amplitude noises in i_1 and i_2 are supposed to be negligible.[1] ω_0 is the central angular frequency of the field and $\phi(t)$ is the random phase.[2] The signal $i(t,\tau_d)$ where τ_d is kept fixed is sent into a spectrum analyzer which delivers as its output the spectral power of current noise $\tilde{S}_i(f)$. This quantity is linked to the spectral power of the frequency noise of the field $S_{\delta\nu}(f)$ through the relation [3]

$$\tilde{S}_i(f) = (i_1+i_2)^2\delta(f) + 16 i_1 i_2 S_{\delta\nu}(f)\frac{\sin^2(\pi f\tau_d)}{f^2}. \quad (2)$$

Here f is the Fourier frequency whose range generally extends from 10 kHz to 20 GHz. When $f \ll 1/\tau_d$, one notes that the second term has the asymptotic value $16 i_1 i_2 (\pi\tau_d)^2 S_{\delta\nu}(f)$. The coefficient $16 i_1 i_2 (\pi\tau_d)^2$ is a scale factor; it has to be experimentally measured. We give some definitions and steps of the calculation in Appendix A.

The optical spectrum of the field is denoted by $I_E(\omega) = \tilde{E}(\omega)\tilde{E}^*(\omega)$, where ω is the optical angular frequency and $\tilde{E}(\omega)$ the frequency component of the field. Figure 1(b) shows a sketch of the experiment which allowed us to measure $I_E(\omega)$ where the spectrometer is a scanning Fabry-Perot interferometer.

The relation between $S_{\delta\nu}(f)$ and $I_E(\omega)$ is written [16,22]

$$I_E(\omega) = E_0^2\int_0^\infty \cos[(\omega_0-\omega)\tau] \times\left\{\exp\left[-4\int_0^\infty S_{\delta\nu}(f)\frac{\sin^2(\pi f\tau)}{f^2}df\right]\right\}d\tau. \quad (3)$$

Again, some steps of the calculation are given in Appendix A.

The noise spectrum $S_{\delta\nu}(f)$ can generally be represented in a polynomial form in which the constant term h_0 (white noise) and the h_{-1}/f term are the main contributions.

When Eq. (3) is applied to the white noise case, $S_{\delta\nu}(f) = h_0$, and a Lorentzian function is obtained:

$$I_E(\omega) = \frac{E_0^2}{2}\frac{1}{i(\omega-\omega_0)+2\pi^2 h_0} + \text{c.c.} \quad (4)$$

The relation between Γ, the HWHM of the line, and the white noise coefficient h_0 is thus

$$\Gamma = 2\pi^2 h_0. \quad (5)$$

Here Γ is expressed in rad/s. When Eq. (3) is applied to the flicker noise case, $S_{\delta\nu}(f) = h_{-1}/f$, one obtains

$$I_E(\omega) = E_0^2\int_0^\infty \cos[(\omega_0-\omega)\tau] \times\left\{\exp\left[-4h_{-1}\int_0^\infty \frac{\sin^2(\pi f\tau)}{f^3}df\right]\right\}d\tau. \quad (6)$$

The problem here is that the integral $J = \int_0^\infty [\sin^2(\pi f\tau)/f^3]df$ is not convergent. The physical way to solve it is to notice that J is a function of time τ and that the minimum frequency which can be observed during this time is $1/\tau$. One thus obtains $J = (\pi\tau)^2 0.022\,561$ which gives the Gaussian function

[1] It follows that we are not considering any effect of the population relaxation resonance for example. Such effects are not preponderant and can be added easily in a more complete theory.

[2] The mean value $\bar{i}(\tau_d) = \langle i(t,\tau_d)\rangle$ with respect to time allows one to find the optical spectrum through the Wiener-Kintchin theorem. The measurement of $\bar{i}(\tau_d)$ is an easy task when the coherence length is not too large. This is not the case of metrological lasers.

$$I_E(\omega) = E_0^2 \frac{\sqrt{\pi}}{\sigma} e^{-(\omega_0 - \omega)^2/\sigma^2}. \quad (7)$$

The variance σ^2 is linked to h_{-1} by the relation

$$\sigma^2 = 3.56 h_{-1}. \quad (8)$$

When Eq. (3) is applied to the mixed case, $S_{\delta\nu}(f) = h_0 + h_{-1}/f$, one obtains

$$I_E(\omega) = \frac{E_0^2}{2} \int_0^\infty e^{i(\omega_0 - \omega)\tau - \Gamma\tau - (\sigma\tau/2)^2} d\tau + \text{c.c.} \quad (9)$$

This result can be manipulated to give

$$I_E(\omega) = E_0^2 \frac{\sqrt{\pi}}{\sigma} K(X,Y), \quad (10)$$

where $K(X,Y)$ is the Voigt function [23] defined by

$$K(X,Y) = \frac{Y}{\pi} \int_{-\infty}^{\infty} \frac{e^{-t^2} dt}{(X-t)^2 + Y^2}. \quad (11)$$

Here, $X = (\omega - \omega_0)/\sigma$, $Y = \Gamma/\sigma$, and $t = \sigma\tau/2 + iX + Y$, with the same relation between Γ and h_0, σ, and h_{-1} as before. Equation (10) allows us to compute the spectrum from h_0 and h_{-1} which are obtained from noise measurements. One originality of this article rests on formula (10), its subsequent experimental verification, and its demonstration from first principles.

B. Experimental test

In order to check the validity of the Voigt formula to describe the line shape, we have measured the spectrum of a standard single-mode distributed feedback (DFB) semiconductor laser[3] used in telecommunications at 1.55 μm. The experimental setup is schematically described in Fig. 1(b). The laser temperature is stabilized. The Fabry-Perot spectrometer has a sweep time of 9 ms and its feedback into the laser is kept as weak as possible ($<10^{-7}$). Its bandpass is 3.5 MHz and its free spectral range is 300 MHz. These characteristics add to the uncertainty of the measurements which essentially arises from the $1/f$ noise.

Figure 2 shows examples of a comparison between three measured line profiles and theoretical Voigt profiles.

The success in such fits for various values of the injection current (and also for different laser temperature T) led us to make several runs in order to draw curves like those represented in Fig. 3 which shows the variation of the fit parameters Γ and σ versus the laser power P for a fixed temperature. We have verified that σ slightly increases with temperature; however, the variation was too small to be really significant as compared to the uncertainty of our measurements. In our first verification of the validity of the description of laser lines by a Voigt function, the agreement between theory and experiment is satisfying: The experimental points in Fig. 3 show that Γ varies like $1/P$ in agreement with already known theory. It shows also that σ displays a slower decrease with the intensity, also in agreement with previously known behavior [15].

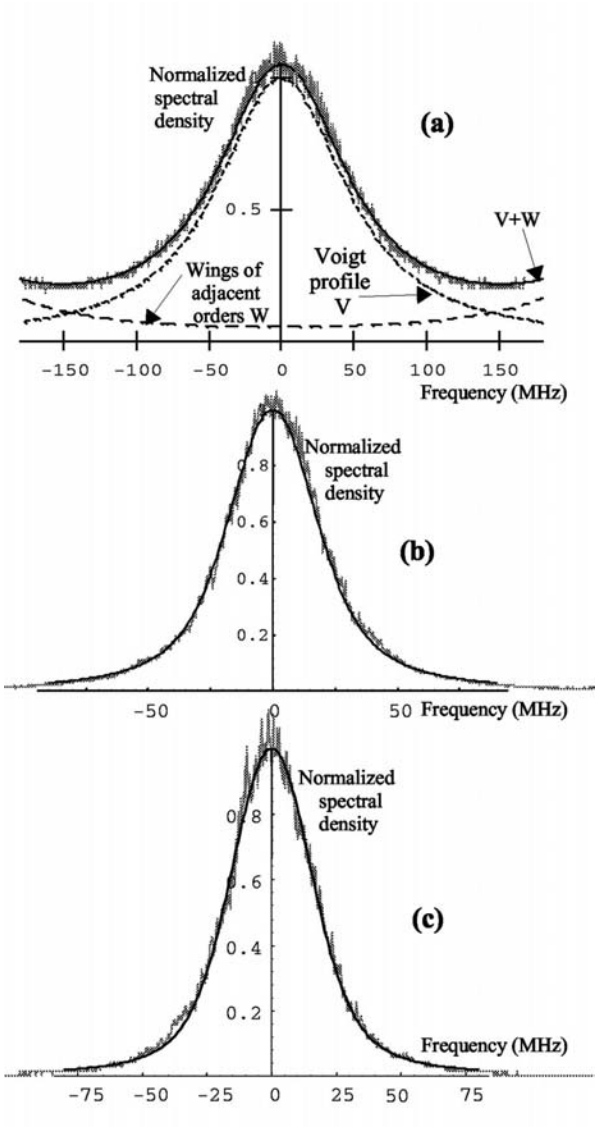

FIG. 2. Three examples of the line profile measured at $T \simeq 31\,^\circ$C, using the mounting in Fig. 1(b). The experimental result is the noisy line in gray; the theoretical fit is the black solid line. In (a), the full width at half maximum is FWHM=108 MHz, and the laser power is $P=307$ μW. The Fabry-Perot free spectral range being 300 MHz, the measured profile results from the sum of the Voigt function V and the wings W of the neighboring orders as indicated in the figure. In (b), FWHM=45 MHz and $P=835$ μW. In (c), FWHM=40 MHz and $P=1.55$ mW.

III. DESCRIPTION OF THE LASER SPECTRUM

Starting from frequency noise measurements, we have computed the laser line and found that a Voigt function is compatible with the simultaneous white and flicker noises.

[3]The laser is a massive InP/InGaAsP buried double-heterostructure distributed feedback laser.

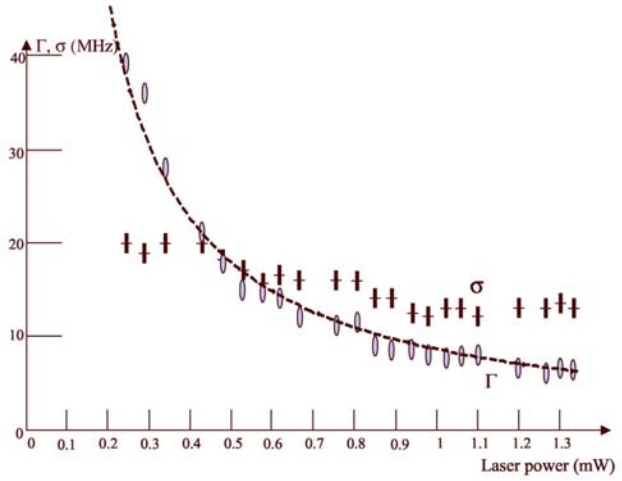

FIG. 3. Fit parameters Γ (ovals) and σ (crosses) in MHz vs the laser power P in mW. The variation of σ is not regular, while Γ follows the a/P curve, with $a \simeq 8.7$ mW MHz. Here $T \simeq 22$ °C. For $T \simeq 31$ °C, we found $a \simeq 11$ mW MHz.

We have then experimentally tested the formula and found a nice agreement with the line shapes and this Voigt profile. It remains now to find also that this Voigt function can be found from the electromagnetism of the laser. This is done below, where we show that the homogeneous part, the Lorentzian, is in fact the laser Airy function and the inhomogeneous part, the Gaussian, originates from the noise of the resonance frequency.

A. Laser Airy function

In the frequency domain, the laser field is the *response* of the device, the laser, to its sources. These sources are the spontaneous emission and the pumping process. It has already been demonstrated [20,21] that applying Maxwell equations and boundary conditions to a frequency component of the field gives the laser transfer function, or the laser Airy function:

$$\tilde{E} = \frac{\tilde{S}_e}{1 - e^{-L+g}e^{-i\phi}}. \tag{12}$$

$\tilde{E}$ represents a component at frequency ω of the laser field and $\tilde{S}_e$ the effective source at that frequency (amplified spontaneous emission). The loss term is written as e^{-L}. The active medium is represented by $\bar{\beta}$ including the dispersion and gain. ℓ being the laser length, the exponential term is split into its real and imaginary parts, $e^{-2i\bar{\beta}\ell} = e^{-2i\bar{\beta}^r\ell}e^{2\bar{\beta}^i\ell} = e^{-i\phi}e^{g}$ in order to explicitly show the gain g and the cumulated round trip phase ϕ:

$$\phi = 2\bar{\beta}^r\ell = 2\omega n\ell/c, \tag{13}$$

where n is the refraction index. The saturated quantities such as $\bar{\beta}$ have been averaged with respect to the saturating intensity.

The optical Airy function is easily calculated for a Fabry-Perot interferometer or a Fabry-Perot laser. It can also be obtained for DFB lasers (see Appendix B) and has the same basic structure. In the following, we will thus use the simple formula (12).

In the single-mode case, the spectrum is centered around the resonance angular frequency ω_0, which is given from $\phi = Q2\pi$ by

$$\omega_0 = Q2\pi\frac{c}{2n(\omega_0)\ell}. \tag{14}$$

The associated spectral density is

$$\tilde{I}(\omega) = \frac{|\tilde{S}_e|^2}{(1 - e^{-L+g})^2 + 4e^{-L+g}\sin^2(\phi/2)}. \tag{15}$$

If one considers the line shape of a single-mode laser around the central resonance frequency, ϕ remains very small and the approximation $4\sin^2(\phi/2) \simeq \phi^2$ can be used. In this case, expression (15) leads to the Lorentzian shape

$$\tilde{I} = \frac{c^2|\tilde{S}_e|^2}{4\ell^2 n_g^2 e^{-L+g}}\frac{1}{\Gamma^2 + (\omega - \omega_0)^2}, \tag{16}$$

where the half width at half maximum Γ is

$$\Gamma = \frac{c}{2\ell n_g}\frac{1 - e^{-L+g}}{e^{(-L+g)/2}}, \tag{17}$$

and n_g is the group index around ω_0. In the stationary regime, the saturating intensity $\mathbf{I}$ can be easily computed for a Lorentzian line [19,20]:

$$\mathbf{I} = \int \tilde{I}d\omega/2\pi = \frac{c^2|\tilde{S}_e|^2}{4\ell^2 n_g^2 e^{-L+g}}\frac{1}{2\Gamma}. \tag{18}$$

Note that $\mathbf{I}$ does not depend on the frequency. We will conform to the usage and introduce the saturation intensity I_s in order to work with a normalized quantity $P = \mathbf{I}/I_s$. I_s is such that the gain $g = g_0/(1 + \mathbf{I}/I_s)$ is divided by 2 when $\mathbf{I} = I_s$.

When the laser is far from the threshold, P is very close to the power P_L which is obtained when the saturated gain $g = g_0/(1+P)$ compensates exactly for losses ($P_L = g_0/L - 1$ can be termed Lamb's solution). In that case, the equality $g_0 = L$, where $P_L = 0$, defines the oscillation threshold of the laser. Anyway, even when the laser is close to the threshold, the gain g is very close to the losses L and the approximation $e^{-L+g} \simeq 1$ holds everywhere but in the expression $1 - e^{-L+g} \simeq L - g$.

Using Eq. (18), the approximated linewidth (17) is related to the saturating power P:

$$\Gamma \simeq \frac{c}{2\ell n_g}(L - g) = \frac{c^2}{(2\ell n_g)^2 2I_s}\frac{|\tilde{S}_e|^2}{P}. \tag{19}$$

It is inversely proportional to P.

When the source term is expressed as

$$|\tilde{S}_e|^2 = K\frac{g_0}{1+P}, \tag{20}$$

where K is a constant, one can easily compute P. The result is

$$P = \frac{g_0 - L}{2L} + \frac{1}{2L}\sqrt{(g_0 - L)^2 + \frac{cK}{\ell n_g I_s}Lg_0}. \tag{21}$$

This expression correctly describes the laser intensity. It can be tested around the threshold, especially for semiconductor lasers and for high-loss fiber lasers. Note that when the spontaneous emission is neglected ($K=0$), it gives back P_L.

B. Population fluctuations and the Voigt function

The homogeneous part of the line shape is described by the laser Airy function as shown above. This line is centered around the central frequency ω_0. Now this function has been calculated for a single value of N, the population difference. It should be recalled that N is a random variable with different realizations in the frequency domain, each realization having a statistical weight or a probability $\mathcal{P}(N)$. It follows that the line shape results from a convolution of the Airy function and the probability function corresponding to each of these realizations of N. These fluctuations introduce a noise on every physical quantity in the laser (gain, linewidth, for instance) but the stronger effect occurs on the position of the resonance frequency ω_0: For each value of N, the Airy function is centered around $\omega_0=\omega_0(N)$ with the probability $\mathcal{P}(N)$. This probability is essentially Gaussian, which corresponds to the intrinsic electronic $1/f$ noise and also to the different causes of technical noises [6].

The spectral profile (16) is then averaged over the different probabilities of N:

$$\langle\tilde{y}(N)\rangle_N = \int_{-\infty}^{\infty}\frac{c^2|\tilde{S}_e|^2}{4\ell^2 n_g^2 e^{-L+g}}\frac{\mathcal{P}(\delta N)d(\delta N)}{\Gamma^2 + [\omega - \omega_0(N)]^2}, \tag{22}$$

where $\delta N=N-\bar{N}$ and $\bar{N}$ is the most probable value.

Let us note that the laser intensity corresponding to the averaged value $\langle\tilde{y}(N)\rangle_N$ *remains the same* as the intensity before in Eq. (18), simply because $\mathcal{P}(\delta N)$ is a normalized probability. The saturating intensity is thus only due to the homogeneous part of the laser line. In order to see how δN acts on $\omega_0(N)$, let us first write the gain g and the refraction index n of the medium under the compact form

$$g = AN, \quad n = n_1 + BN, \tag{23}$$

where A, B, and n_1 are constants.

Now we assume the simple expression for the saturated population (for a homogeneous medium)

$$N = \frac{N_{ns}}{1+P}. \tag{24}$$

Here N_{ns} stands for the nonsaturated value of N. Note that in the laser regime $P\simeq P_L$. It follows that the saturated gain and the saturated index are written

$$g = A\frac{N_{ns}}{1+P}, \quad n = n_1 + B\frac{N_{ns}}{1+P}. \tag{25}$$

The angular frequency at resonance (always for the single mode laser) is written, for a given value of N [see Eq. (14)],

$$\omega_0(N) = Q2\pi\frac{c}{2\ell n(N)}, \tag{26}$$

where Q is an integer. The value of $\omega_0(N)$ around the reference $\omega_0(\bar{N})$ is obtained from a Taylor expansion:

$$\omega_0(N) = \omega_0(\bar{N}) - Q2\pi\frac{c}{2\ell}\frac{\delta n}{n^2(\bar{N})} = \omega_0(\bar{N})\left[1 - \frac{\delta n}{n(\bar{N})}\right]. \tag{27}$$

Let us note that a difference $\omega_0(N)-\omega_0(\bar{N})$ of the same order of magnitude as the laser linewidth is obtained for a very small variation of $\delta n/n(\bar{N})$ due to the large value of Q. For instance, if $\omega_Q(\bar{N})\simeq 10^{15}$ rad/s, a variation $\delta n/n(\bar{N})\simeq 10^{-8}$ only leads to $[\omega_0(N)-\omega_0(\bar{N})]/2\pi=10$ MHz. It is thus necessary to be very cautious in playing with approximations.

In order to obtain the variation δn of the index of refraction when N varies, one writes [see Eq. (19)]

$$n = n_1 + \frac{B}{A}g = n_1 + \frac{B}{A}\left[L - \frac{c|\tilde{S}_e|^2}{2\ell n_g 2I_s P}\right]. \tag{28}$$

It follows that the index variation δn is related to the variation $\delta N=N-\bar{N}$ of N around $\bar{N}$ by

$$\delta n = -\frac{B}{A}\frac{d}{dN}\left[\frac{c|\tilde{S}_e|^2}{2\ell n_g 2I_s P}\right]\delta N. \tag{29}$$

We are now in position to introduce Henry's factor [13,25,26]

$$\alpha_H = \frac{B}{A} \tag{30}$$

and another factor, which is also characteristic of the amplifying medium,

$$\alpha' = \frac{d}{dN}\left[\frac{c|\tilde{S}_e|^2}{2\ell n_g 2I_s P}\right], \tag{31}$$

in order to write the formula

$$\delta n = -\alpha_H\alpha'\delta N. \tag{32}$$

Let us note that a neglect of the spontaneous emission $|\tilde{S}_e|^2$ leads to $\alpha'=0$, or a zero variation of the refraction index. This is because P becomes P_L which clamps the saturated population $N/(1+P_L)$ from the relation $g=L$ in this case. One thus obtains

$$\omega_0(N) - \omega_0(\bar{N}) = \omega_0(\bar{N})\frac{\alpha_H\alpha'}{n(N_0)}\delta N. \tag{33}$$

We recover in formulas (32) and (33) the usual frequency shift from the transparency to the threshold. The index dif-

ference in Eq. (32) has been measured in [27] with a precision of 1%. Expression (33) is introduced in the equation for the mean profile (22) where we make the approximation $e^{-L+g} \simeq 1$:

$$\langle \tilde{y}(N) \rangle_N = \frac{c^2 |\tilde{S}_e|^2}{4\ell^2 n_g^2} \int_{-\infty}^{\infty} \frac{\mathcal{P}(\delta N) d(\delta N)}{\Gamma^2 + [\omega - \omega_0(\bar{N}) - \omega_0(\bar{N}) \alpha_H \alpha' / n(\bar{N}) \delta N]^2}. \tag{34}$$

Let us write now that δN follows a Gaussian probability law

$$\mathcal{P}(N) = \frac{e^{-(\delta N/\sigma_1)^2/2}}{\sigma_1 \sqrt{2\pi}}. \tag{35}$$

$\mathcal{P}(N)$ is characterized by its variance (or its second moment) σ_1^2. One sees now that $\langle \tilde{y}(N) \rangle_N$ is the convolution of a Lorentzian with a Gaussian—i.e., a Voigt profile.

In order to conform to the notation associated to the Voigt function, let us introduce

$$t = \frac{\delta N}{\sigma_1 \sqrt{2}} \tag{36}$$

and

$$d(\delta N) = \sigma_1 \sqrt{2} dt. \tag{37}$$

If we use the abbreviation

$$a = \frac{\omega_0(\bar{N}) \alpha_H \alpha'}{n(\bar{N})} \tag{38}$$

and the normalized variables:

$$Y \equiv \frac{\Gamma}{a \sigma_1 \sqrt{2}}, \quad X \equiv \frac{\omega - \omega_0(\bar{N})}{a \sigma_1 \sqrt{2}}, \tag{39}$$

the expression for the averaged spectral profile becomes

$$\langle \tilde{y}(N) \rangle_N = \frac{c^2 |\tilde{S}_e|^2}{4\ell^2 n_g^2} \frac{1}{2a^2 \sigma_1^2 \sqrt{\pi}} \int_{-\infty}^{\infty} \frac{e^{-t^2} dt}{Y^2 + [X - t]^2}. \tag{40}$$

In this formula, Y is the ratio of Lorentz to Gaussian widths. $\langle \tilde{y} \rangle$ is proportional to the Voigt function $K(X,Y)$ expressed in its standard form (11):

$$\langle \tilde{y}(N) \rangle_N = \frac{c^2 |\tilde{S}_e|^2}{4\ell^2 n_g^2} \frac{\sqrt{\pi}}{\sqrt{2} a \sigma_1 \Gamma} K(X,Y). \tag{41}$$

A comparison between Eqs. (10) and (41) and their associated symbols allows us to make the connection between the variance associated with population fluctuations and with the noise coefficient h_{-1}. However, it should be recalled that formula (41) contains more physics than formula (10) which expresses only the fact that the Voigt formula is compatible with the simultaneous white and $1/f$ noises.

The Voigt function usually characterizes spectral lines having an atomic origin; it follows that one can apply the same terminology to the laser line: (i) The "homogeneous" part of the laser line is represented by its Airy function which is a Lorentzian around a resonance. This part corresponds to a single realization of the pump. (ii) The "inhomogeneous" part of the laser line is the Gauss function which describes the random character of the pump.

We have thus attained our goal in demonstrating formula (41). The difficulty here in dealing with the Gaussian part is that the origins of its variance span from the fundamental properties of the pumping process to the "technical noise." It is well known that the linewidth is enlarged by a factor $(1 + \alpha_H^2)$ in the usual approximation of a Lorentzian line. In Eq. (41), we recover this broadening through the probabilistic nature of the resonant optical frequency. However, in Eq. (41), the factor is not as simple as before and could lead to another estimation of the α_H parameter. It is important to note that the uncertainty in measurements of α_H is usually bigger than 10% [15] which proves the limitations of the usual theory.

IV. CONCLUSION

In this paper we have first verified that a Voigt spectral profile is compatible with standard measurements of frequency noise in a single-mode laser: The Lorentzian part corresponds to the white noise part and the Gaussian part of the Voigt function corresponds to the $1/f$ noise part. The white noise arises from spontaneous emission and the flicker noise arises from fluctuations of the charge carriers or the pumping and from the "technical" noise. The formula does not include the intensity noise. We believe that the Voigt profile is characteristic of any single-mode laser. It follows that the spectrum of a metrological laser can be obtained from the measurement of the frequency noise coefficients.

We have then experimentally verified that the Voigt profile gives a very good fit to single-mode semiconductor lines and that the fit parameter Γ obeys an inverse power law while the second parameter σ varies more slowly with the power.

In the last section, we have put together the Airy function of the laser which becomes the homogeneous part of the Voigt function and the Gaussian probability distribution of the resonance frequency, which is its inhomogeneous part. In this work, only stationary lasers have been considered; the calculations are thus shorter, clearer, and more precise when they are done directly in the frequency domain. We have thus completed a synthesis of different phenomena all related to the spectral characteristics of the laser field.

It is clear from these results that a decrease of the laser spectral linewidth can be obtained only by a simultaneous and independent decrease of the noise coefficients h_0 and h_{-1}. h_0 can be decreased using high-quality resonators while h_{-1} can be decreased through mechanical, thermal, and acoustical stability, together with a pump process as stable as possible. In this respect, the electrical stability is fundamental. Our results confirm that the nature of the laser frequency noise depends upon the considered frequency band: (i) Essentially $1/f$ or white in frequency measurements and (ii) Gaussian near the center of the laser line spectrum, Lorentzian in the aisles. They also confirm that in some interfero-

metric experiments performed with the laser light, the result depends upon the measurement time, in agreement with Mercer [17].

APPENDIX A

The aim of this appendix is to describe the main steps which lead to Eqs. (2) and (3).

1. Relation between $S_{\delta\nu}(i)$ and $S_{\delta\nu}(f)$

The laser field is written in the scalar form

$$E(t) = E_0[1 + \varepsilon(t)]e^{i[\omega_0 t + \phi(t)]}. \tag{A1}$$

$\varepsilon(t)$ is the amplitude noise which will be neglected in the following. $\phi(t)$ is the phase noise which makes the instantaneous frequency wander around the nominal frequency $\nu_0 = \omega_0/(2\pi)$. This field is injected into the interferometer and split into two parts inside the two arms. Both arms contain an optical fiber of known length. One arm contains a dephasor for fine-tuning and a polarization controller. L_1 and L_2 are the optical lengths of arms 1 and 2. The path difference $L_1 - L_2$ results in a time shift τ_d between the recombined fields E_1 and E_2 at the interferometer output: $\tau_d = (L_1 - L_2)/c$. The polarization controller is used to set the same polarization for E_1 and E_2. The detector gives a signal which is proportional to the intensity of the interfering fields E_1 and E_2:

$$\begin{aligned} i(t) &= \frac{K_D}{2}|\vec{E}_1 + \vec{E}_2|^2 \\ &= i_1 + i_2 + 2\sqrt{i_1 i_2}\cos[\omega_0\tau_d + \phi(t+\tau_d) - \phi(t)]. \end{aligned} \tag{A2}$$

The current $i(t)$ is then processed by an electronic spectrum analyzer which delivers $\tilde{S}_i(f)$, the Fourier transform of the autocorrelation function $R_i(\tau)$ of $i(t)$:

$$\tilde{S}_i(f) = T_{\text{Fourier}}\{R_i(\tau)\}, \tag{A3}$$

with

$$R_i(\tau) = \langle i(t)i(t+\tau)\rangle. \tag{A4}$$

Note that $\tilde{S}_i(f)$ is also the modulus square of the Fourier transform of $i(t)$.

We are first looking at the relation between the power spectral density of frequency noise $S_{\delta\nu}(f)$ and the power spectral density of the input current $\tilde{S}_i(f)$ given by the spectrum analyzer.

The autocorrelation function $R_i(\tau)$ of the photocurrent $i(t) = i_1(t) + i_2(t)$ is obtained by computing the mean value over the time t of the following expression:

$$\begin{aligned} R_i(\tau) = (i_1+i_2)^2 &+ (i_1+i_2)\sqrt{i_1 i_2}\langle e^{i[\omega_0\tau_d+\upsilon]} + e^{-i[\omega_0\tau_d+\upsilon]} \\ &+ e^{i[\omega_0\tau_d+w]} + e^{-i[\omega_0\tau_d+w]}\rangle + i_1 i_2\langle\{e^{i[\omega_0\tau_d+\upsilon]} + e^{-i[\omega_0\tau_d+\upsilon]}\} \\ &\times\{e^{i[\omega_0\tau_d+w]} + e^{-i[\omega_0\tau_d+w]}\}\rangle, \end{aligned} \tag{A5}$$

with the notation

$$\upsilon = \phi(t+\tau_d) - \phi(t), \tag{A6}$$

$$w = \phi(t+\tau+\tau_d) - \phi(t+\tau). \tag{A7}$$

The reference angle $\omega_0\tau_d$ is adjusted in such a way that

$$\cos[\omega_0\tau_d + \phi(t+\tau_d) - \phi(t)] = \sin[\phi(t+\tau_d) - \phi(t)]. \tag{A8}$$

In this case, the interferometer is used as a phase-amplitude converter. We work also within the hypothesis of weak deviations υ and w. The experimental condition is $\tau_d \ll 1/\Gamma$.

The frequency deviation is linked to the phase variation during the time t by the relation

$$\delta\phi(t,\tau) = 2\pi\int_t^{t+\tau}\delta\nu(t')dt'. \tag{A9}$$

The correlation function of the frequency fluctuation $\delta\nu(t)$ is defined for a stationary process

$$R_{\delta\nu}(t',t'') = \langle\delta\nu(t')\delta\nu(t'')\rangle = R_{\delta\nu}(t'-t''). \tag{A10}$$

Note that the dimension of $R_{\delta\nu}(t'-t'')$ is Hz^2 or T^{-2}.

In the course of the calculation of $R_i(\tau)$, the following general identity is used:

$$\begin{aligned} &\int_a^b\int_c^d R_{\delta\nu}(t'-t'')dt'dt'' \\ &\quad= \int_0^{(a-b)} R_{\delta\nu}(-X-a+c)dX[(b-a+d-c)/2 - X] \\ &\qquad+ \int_0^{(d-c)} R_{\delta\nu}(X-a+c)dX[(b-a+d-c)/2 - X]. \end{aligned} \tag{A11}$$

We use also the familiar mean value for a Gaussian process:

$$\langle e^{i\phi(t)}\rangle = e^{-4\pi^2\langle\phi(t)\rangle^2/2}. \tag{A12}$$

After some calculations, one finds

$$\begin{aligned} R_i(\tau) = (i_1+i_2)^2 - 2i_1 i_2\Bigg[-8\pi^2\int_0^{\tau_d}[R_{\delta\nu}(X+\tau) \\ + R_{\delta\nu}(-X+\tau)][\tau_d - X]dX\Bigg]. \end{aligned} \tag{A13}$$

The spectrum analyzer gives, as a result, $\tilde{S}_i(f)$, the Fourier transform of $R_i(\tau)$:

$$\tilde{S}_i(f) = \int_{-\infty}^{\infty} R_i(\tau)e^{-2i\pi f\tau}d\tau. \tag{A14}$$

We will use the relation of the definition of the power spectral density of frequency noise (T_{Fourier} of the frequency fluctuation correlation):

$$S_{\delta\nu}(f) = \int_{-\infty}^{\infty} e^{-2i\pi f\tau} R_{\delta\nu}(\tau) d\tau. \quad \text{(A15)}$$

Note that the dimension of $S_{\delta\nu}(f)$ is in Hz or T^{-1} [$S_{\delta\nu}(f)$ is commonly expressed in Hz^2/Hz]. We obtain the desired result

$$\tilde{S}_i(f) = (i_1 + i_2)^2 \delta(f) + 16 i_1 i_2 S_{\delta\nu}(f) \frac{\sin^2(\pi f \tau_d)}{f^2}.$$

For $f \neq 0$,

$$S_{\delta\nu}(f) = \frac{1}{16 i_1 i_2} \frac{f^2}{\sin^2(\pi f \tau_d)} \tilde{S}_i(f). \quad \text{(A16)}$$

This result links the measured quantity $\tilde{S}_i(f)$ to the quantity $S_{\delta\nu}(f)$ which characterizes the frequency fluctuation of the field. It is clear that when the angle $\pi f \tau_d$ is small, the approximation $\sin^2(\pi f \tau_d) \simeq (\pi f \tau_d)^2$ can be used. In this case f^2 disappears and $S_{\delta\nu}(f)$ is directly represented by $\tilde{S}_i(f)$.

2. Relation between $S_{\delta\nu}(f)$ and the optical spectrum $I_E(\omega)$

We have used the relation between $S_{\delta\nu}(f)$ and the optical spectrum $I_E(\omega) = \tilde{E}(\omega)\tilde{E}^*(\omega)$, where ω is the optical frequency and $\tilde{E}(\omega)$ the frequency component of the field.

Let us give now the main steps which lead to this relation. The quantities which are used are the same as before.

The strategy is the following.

(i) $I_E(\omega)$ is linked to the temporal correlation $R_E(\tau)$ through the Fourier transform (Wiener-Khintchin theorem):

$$I_E(\omega) = \mathrm{Re}\left\{ \int_{-\infty}^{\infty} R_E(\tau) e^{-i\omega\tau} d\tau \right\} = \mathrm{Re}\left\{ \int_{-\infty}^{\infty} \langle E^*(t) E(t+\tau) \rangle e^{-i\omega\tau} d\tau \right\}. \quad \text{(A17)}$$

(ii) Now, for a Gaussian process, $R_E(\tau)$ can be written as

$$R_E(\tau) = \langle E^*(t) E(t+\tau) \rangle = e^{i\omega_0\tau} e^{-\sigma^2/2} \bar{I}, \quad \text{(A18)}$$

where

$$\sigma^2 = \sigma^2(\tau) = \langle [\phi(t+\tau) - \phi(t)]^2 \rangle, \quad \text{(A19)}$$

and $\bar{I}$ is the intensity. One obtains

$$I_E(\omega) = \bar{I} \int_{-\infty}^{\infty} e^{-\sigma^2/2} \cos[(\omega_0 - \omega)\tau] d\tau. \quad \text{(A20)}$$

(iii) The following step is to relate σ^2 to $R_{\delta\nu}(\tau)$, the temporal correlation of $\delta\nu(t)$. One obtains

$$\sigma^2 = 2 \int_0^{\tau} (\tau - t) R_{\delta\nu}(t) dt. \quad \text{(A21)}$$

(iv) Finally, one remembers that the power spectral density of frequency noise $S_{\delta\nu}(f)$ and the temporal correlation $R_{\delta\nu}(\tau)$ are Fourier transforms of each other.

When the calculation is performed following these steps, one finds the desired relation (3).

APPENDIX B

The aim of this appendix is to briefly describe the Airy function of the DFB laser.

The method is to start from the coupled wave theory [24] where a frequency component of the laser field is written with the standard notation:

$$\tilde{E}(z) = [A_1 e^{-iqz} + r B_2 e^{iqz}] e^{-i\beta_0 z} + s_1(z) + [r A_1 e^{-iqz} + B_2 e^{iqz}] e^{i\beta_0 z} + s_2(z). \quad \text{(B1)}$$

Here A_1, rB_2, rA_1, and B_2 are the progressive longitudinal slowly varying envelopes of the field, r the reflectance of the Bragg grating,

$$r = 2\beta \frac{q - \Delta\beta}{\kappa} = -\frac{\kappa}{2\beta} \frac{1}{q + \Delta\beta}, \quad \text{(B2)}$$

with $\Delta\beta = \beta^r - m\pi/\Lambda$, β^r being the real part of the propagation constant of the medium, Λ the grating period, and m an integer which minimizes $\Delta\beta$. One has also $\beta_0 = m\pi/\Lambda$ and

$$q = \left[\Delta\beta^2 - \frac{\kappa^2}{4\beta^2} \right]^{1/2}, \quad \text{(B3)}$$

κ being a coefficient which describes the coupling between the transverse and longitudinal parts of the field.

The symbols $s_1(z)$ and $s_2(z)$ represent the local spontaneous emission (source terms). When boundary conditions are applied, one finds

$$A_1 = \frac{S_1}{1 - r_1^2 e^{-2i(q-\beta_0)\ell}},$$

$$B_2 = \frac{S_2}{1 - r_1^2 e^{-2i(q-\beta_0)\ell}}, \quad \text{(B4)}$$

where r_1 is the complex effective reflectance:

$$r_1 = \frac{(\beta_{ext} - \beta_0 - q) + r(\beta_{ext} + \beta_0 - q) e^{i\beta_0\ell}}{\beta_{ext} + \beta_0 + q + r(\beta_{ext} - \beta_0 + q) e^{-i\beta_0\ell}}. \quad \text{(B5)}$$

Here β_{ext} is the propagation constant of the external medium (if this medium is air, $\beta_{ext} = \omega/c$). The source terms S_1 and S_2 in Eqs. (B4) depend in a complicated way on the laser structure: Their expressions are not important here. The main conclusion is that expressions (B4) have the same structure as Eq. (12).

[1] Y. Yamamoto, S. Saito, and T. Mukai, IEEE J. Quantum Electron. **QE-19**, 47 (1983).
[2] K. Kikuchi, IEEE J. Quantum Electron. **QE-25**, 684 (1989).
[3] P. Tremblay, C. S. Turcotte, M. Bondiou, J. Genest, M. Allard, P. Lévesque, J. P. Bouchard, C. Latrasse, M. Poulin, and M. Têtu, in Proceedings of the 6th Symposium on Frequency Standards and Metrology, 9–14 September 2001, Fife, Scotland, UK, edited by P. Gill (World Scientific, Singapore, 2002).
[4] J. J. Brophy, J. Appl. Phys. **38**, 2465 (1967).
[5] G. Tenchio, Electron. Lett. **12**, 562 (1976).
[6] R. J. Fronen, Ph.D. thesis, Eindhoven University, 1990.
[7] W. H. Burkett, B. Lü, and M. Xiao, IEEE J. Quantum Electron. **QE-33**, 2111 (1997).
[8] G. P. Agrawal and R. Roy, Phys. Rev. A **37**, 2495 (1988).
[9] Ph. Laurent, A. Clairon, and Ch. Bréant, IEEE J. Quantum Electron. **QE-25**, 1137 (1989).
[10] A. Dandridge and H. F. Taylor, IEEE J. Quantum Electron. **QE-18**, 1738 (1982).
[11] D. Welford and A. Mooradian, Appl. Phys. Lett. **40**, 560 (1982).
[12] K. Vahala and A. Yariv, Appl. Phys. Lett. **43**, 140 (1983).
[13] C. H. Henry, IEEE J. Quantum Electron. **QE-18**, 259 (1982).
[14] M. Sargent, M. O. Scully, and W. Lamb, Jr., *Laser Physics* (Addison-Wesley, Reading, MA, 1974).
[15] M. Osinski and J. Buus, IEEE J. Quantum Electron. **QE-23**, 9 (1987).
[16] B. Fermigier and M. Têtu, Proc. SPIE **3415**, 164(1998).
[17] L. D. Mercer, J. Lightwave Technol. **9**, 485 (1991).
[18] M. J. O'Mahony and I. D. Henning, Electron. Lett. **19**, 1000 (1983).
[19] G. M. Stéphan, Phys. Rev. A **55**, 1371 (1997).
[20] G. M. Stephan, Phys. Rev. A **58**, 2467 (1998).
[21] M. Bondiou, R. Gabet, G. M. Stéphan, and P. Besnard, J. Opt. Soc. Am. B **2**, 41 (2000).
[22] D. S. Elliot, R. Roy, and S. J. Smith, Phys. Rev. A **26**, 12 (1982).
[23] The Voigt function is the real part of the complex probability function. See V. N. Faddeyeva and N. M. Terent'ev, *Tables of the Function* $w(z)=e^{-z^2}[1+2i/\sqrt{\pi}\int_0^z e^{t^2}dt]$ *for Complex Argument* (Pergamont Press, Oxford, 1961). It is linked to the plasma dispersion function. See B. D. Fried and S. D. Conte, *The Plasma Dispersion Function, the Hilbert Transform of the Gaussian* (Academic Press, New York, 1961). See also B. H. Armstrong, J. Quant. Spectrosc. Radiat. Transf. **7**, 61 (1967).
[24] G. P. Agrawal and N. K. Dutta, *Semiconductor Lasers*, 2nd ed. (Van Nostrand Reinhold, New York, 1993), Chap. 7. Seminal papers are H. Kogelnik1 and C. V. Shank, Appl. Phys. Lett. **18**, 152 (1971); J. Appl. Phys. **43**, 2327 (1972).
[25] C. H. Henry, J. Lightwave Technol. **LT-4**, 298 (1986).
[26] K. Vahala, L. C. Chiu, S. Margalit, and A. Yariv, Appl. Phys. Lett. **42**, 631 (1983).
[27] C. H. Henry, R. A. Logan, and K. A. Bartness, J. Appl. Phys. **52**, 4457 (1981).